Replacing Metals with Organic Materials in Batteries

by

Julien Martin

BSc. (Chemistry), UNB Fredericton, 2010

A Thesis Submitted in Partial Fulfillment
of the Requirements for the Degree of

Master of Science

in the Graduate Academic Unit of Chemistry

Supervisor: C. Adam Dyker, PhD, Chemistry

Examining Board: Gilles Villemure, PhD, Chemistry (Chair)
David Lentz, PhD, Earth Sciences

This thesis is accepted by the
Dean of Graduate Studies

THE UNIVERSITY OF NEW BRUNSWICK

April, 2015

©Julien D. Martin, 2015

ABSTRACT

To face the challenge of climate change, our increasingly environmentally conscious society is seeking advanced energy systems which may help taper and eventually supplant our fossil fuel systems. In order to successfully displace fossil fuels, such systems need to be both economical and more environmentally-friendly. For batteries, much of the cost and environmental impact is caused by the use of metals in their various components. Organic materials may offer a solution to the necessity for metals, thanks to the development of many novel organic materials with select metallic properties. In the first part of this thesis, a conductive polymer paper composite was explored for application in lithium ion batteries as a current collector to supplant conventional aluminum foil current collectors. Higher current capacities and improved voltage efficiencies were obtained in cells utilizing the conductive composite compared to cells using aluminum as current collectors. However, the cells using conductive composite suffered from rapid deterioration in current capacity and operating voltage, becoming worse in performance compared to the aluminum current collector cells in less than 50 consecutive charge/discharge cycles. In the second part, alkyl substituted bis-pyridinium salts were synthesized with substantially improved solubility in dimethylformamide. The improved solubility could allow for higher loadings of the bis-pyridinium salts in the anolyte solutions of all-organic flow batteries, thereby increasing the energy densities that could be attained in these systems. In addition, four environmentally-sensitive bis-pyridinylidene compounds were also successfully isolated for the first time.

ACKNOWLEDGEMENTS

I offer my deepest gratitude to my project supervisor Professor C. Adam Dyker, for his support and counseling throughout my degree. This thesis would not have been possible without his patient guidance. Despite his many tasks and responsibilities, he was always able to make time to see me and entertain my innumerous questions and concerns.

I would like to thank my advisory committee members Doctors James Tait and Gilles Villemure for their invaluable recommendations throughout my degree. I would also like to thank my readers, Doctors James Tait and Larry Calhoun, for their advice and kind comments on my thesis.

I sincerely thank my parents René and Carmen for their love and support throughout my life and studies, my brother Raymond and sisters Nadine and Nicole for their unerring support, my dear friends Anasthasia and Thalie for their incredible kindness and encouragement, and my many other friends and colleagues who have been with me in this journey. This thesis would not have been possible without the influence and love of the great people that have enriched my life.

Table of Contents

ABSTRACT ii

ACKNOWLEDGEMENTS iii

List of Tables vi

List of Figures viii

List of Symbols and Abbreviations xx

Chapter 1 – Introduction 1

1.1 – Prevalence of Batteries 1
1.2 – Introduction to Electrochemistry 2
1.3 – Cell Potential 6
1.4 – Charge Capacity 9
1.5 – Cell Cycling 10
1.6 – Research Objective 17

Chapter 2 – Conductive Paper Current Collector 19

2.1 – Replacement of Aluminum with Conductive Paper in Li-Ion Cells 19
2.2 – Results and Discussion 22
2.2.1 – Conductivity Tests 24
2.2.2 – Coating the Current Collector Substrates 25
2.2.3 – Cell Cycling Tests 30
2.3 – Conclusions and Future Work 43
2.4 – Preparation, Materials, and Characterization 45

Chapter 3 – Bis-pyridinium Salts With Enhanced Solubilities for Applications in Redox Flow Cells 48

3.1 – Introduction to Redox Flow Cells 48
3.1.1 – Replacement of Metals in Flow Cells 52
3.2 – Results and Discussion 59

3.2.1 – Characteristics of the Pyridinium Bromide Precursors 59
3.2.2 – Characteristics of the N,N-Dialkylated Bis-Pyridinylidenes 63
3.2.3 – Characteristics of the N,N-Dialkylated Bis-Pyridinium Salts 83
3.2.4 – Characteristics of Asymmetric N-Alkyl-N′-Dodecyl Bis-Pyridinylidenes... 90
3.2.5 – Electrochemistry, Melting Point, and Solubility Tests 96
3.2 – Conclusions and Future Work 105
3.3 – Materials, Preparation, and Characterization 109
3.3.1 – N-Alkyl-4-Dimethylaminopyridinium Bromide Salts (2) 112
3.3.2 – N,N-Dialkyl and N-Alkyl-N′-Dodecyl Bis-Pyridinylidenes (3) 116
3.3.3 – N,N-Dialkyl and N-Alkyl-N'-Dodecyl Dichloride Salts (4) 122
3.3.4 – N,N-Dialkyl and N-Alkyl-N′-Dodecyl Hexafluorophosphate Salts (5) 127
3.3.5 – 2D NMR Assignments 132
3.3.6 – Cyclic Voltammetry Spectra 135
3.3.7 – Electrospray Ion Mass Spectra 140
3.3.8 – 1D and 2D NMR Spectra 150

Bibliography 210

Curriculum Vitae

List of Tables

Table 2.1: Measured resistivities for 5 by 5 cm sheets of PPyP, produced from pulps with varying reagent content. All compositions used 10 grams of virgin white pulp and 40 mL of water. 24

Table 2.2: Tabulation of aluminum and PPyP CC cell test results, with Max Q_{mDis} being the maxium gravimetric charge capacity achieved during a discharge half-cycle, Q_{mDis} Loss being the per-cycle loss of gravimetric charge capacity in discharge half-cycles after the 25th cycle, and 2nd and 75th cycle η_E being the cell discharge/charge potential efficiencies of the 2nd and 75th cycle, respectively, with $E_{discharge}$ and E_{charge} sampled at half-cycle capacities of 40 mA·h/g. 44

Table 3.1: Tabulated oxidation potentials ($E_{1/2}$) and peak separation potentials (E_{pc} - E_{pa}) of each individual salt **5a-d** and salt mixture **5e-g + 5a-c + 5d**, with respective peak separation potentials of their internal Fc reference. 98

Table 3.2: Calculated diffusion coefficients of $\mathbf{5a}^{\mathbf{0}}$ (D_{5a0}) and $\mathbf{5a}^{2+}$ (D_{5a2+}) at scan rates of 15, 25, 50, and 100 mV/s using Equation 3.2.2 – 2 in addition to the average diffusion coefficient with standard deviation (σ), relative standard deviation (*RSD%*), and corrective factor *b*. 101

Table 3.3: Melting point ranges of chloride salts and salt mixtures **4x** and hexafluorophosphate salts and salt mixtures **5x**..... 103

Table 3.4: Saturated solution concentrations of each salt and salt mixture in DMF..... 104

Table 3.5: ^{13}C, ^{1}H, ^{1}H-^{1}H COSY, and ^{1}H-^{13}C HMBC NMR Assignments for (*Z*)-N,N-dipropyl-bis-2-(4-dimethylamino)pyridinylidene (**3a**) in C_6D_6. VT - Found via Variable Temperature NMR. 132

Table 3.6: ^{13}C, ^{1}H, ^{1}H-^{1}H COSY, and ^{1}H-^{13}C HMBC NMR Assignments for (*E*)-N,N-dipropyl-bis-2-(4-dimethylamino)pyridinylidene (**3a**) in C_6D_6. HSQC - Found via ^{1}H-^{13}C Heteronuclear Single Quantum Coherence NMR. 133

Table 3.7: ^{13}C, ^{1}H, ^{1}H-^{1}H COSY, and ^{1}H-^{13}C HMBC NMR Assignments for N,N-dipropyl-2-(4-dimethylamino)pyridinium chloride (**4a**) in CD_3CN. 134

List of Figures

Figure 1.1: A lithium-ion cell with lithiated graphite (Li Grap) as the anode, and some lithiated metal oxide (Li MOx) as the cathode, internally separated by an organic solvent containing some Li-ion-based electrolyte (blue) and a polymer separator (hashed lines), and externally connected in an electronic circuit (grey) with a lightbulb. Hashed arrows show movement of charged species; solid arrows show chemical conversion of species. 3

Figure 1.2: Left (a); Cell operations when discharging. Right (b); Cell operations when charging (right, b). 5

Figure 1.3: Electrochemical potentials of some common reference half-cell reactions. ... 8

Figure 1.4: Cell-cycling profile for a single cycle assuming ideal behaviour, plotting voltage (in volts) against accumulated charge capacity (in ampere hours). 11

Figure 1.5: A discharge half-cycle of a cell with cell voltage versus current rate. The top hashed line represents the theoretical open-circuit voltage E_{OC}, the middle hashed line is the open-circuit voltage with ohmic polarization, the bottom hashed line is the open-circuit voltage with both ohmic and activation polarizations, and the solid line is the operating cell voltage E_{Cell} which constitutes E_{OC} and ohmic, activation, and concentration polarizations. 14

Figure 1.6: Example of a non-ideal cell cycle profile showing higher operating charging voltage (E_{Ch}) and lower operating discharging voltage (E_{Disch}) than the standard cell potential ($E°$) due to polarization effects, with η_{ECh} and η_{EDisch} being the charging and discharging half-cycle overvoltages, respectively. 16

Scheme 2.1: Left (a); short sections of polypyrrole in p-type conducting state. Right (b); short sections of polypyrrole in neutral non-conducting state. 22

Figure 2.1: Backscattered electron micrographs of drop-coated paper electrodes. Left (a); the side-view of a cross-cut electrode. Right (b); an overhead surface view of the same electrode at the edge of the coating. 28

Figure 2.2: Button cell assembly diagrams for a PPyP current-collector cell on the left (a) and an aluminum current-collector cell on the right (b). All components are assembled in bottom-up fashion. The bottom cap has a gasket-lined rim which forms the seal when the cell is crimped with 2000 psi pressure. 30

Figure 2.3: Representations of the capacities of charge and discharge half-cycles versus cycle number for cells which used $LiPF_6$ electrolyte, cycled at a rate of 1*C*. The orange series were cells that used paper CC, while the grey series used aluminum CC. Every 0.5 cycle number is a charge, while every whole unit cycle is a discharge. Left (a); average charge and discharge capacities with $\pm 1\sigma$ error bars for 3 cells from both cell series over 50 cycles. Right (b); best cells from both series. 31

Figure 2.4: Charge-discharge half-cycle profiles for best cells using $LiPF_6$ electrolyte from aluminum CC series on the left (a) and PPyP CC series on the right (b). 32

Figure 2.5: Illustrations of PPyP CC (black) with $LiFePO^4$ coating (green with lime filling) before cycling on the left (a) and after several cycles on the right (b). For representation purposes, gradual loss in the electrical conductivity of the PPyP fibres is shown as black → brown → orange → red. 33

Figure 2.6: Top (a); capacity graph for an aluminum CC and a PPyP CC cells. Bottom (b); the cycling profile graph of the PPyP CC cell. Both cells were cycled at 2*C*. 34

Figure 2.7: Capacity vs. cycle number graphs on the top (a) and corresponding cycling profiles on the bottom (b) for two different PPyP CC cells cycled at *C*/2, assembled within the same week, and tested on two different Keithley 2400 sourcemeters. The capacity graphs also contained an aluminum CC cell cycled at *C*/2 for comparison. 35

Figure 2.8: Top (a); capacity graph for previous aluminum CC (grey) and PPyP CC (orange) cell runs with 2.0-4.5 V cutoff points alongside an additional PPyP CC cell run with 3.0-4.5 V cutoff points (blue). Bottom (b); the cycling profile graph (bottom) of the PPyP CC cell run with 3.0-4.5 V cutoff points. All cells were cycled at 1*C*. .. 38

Figure 2.10: Charge-discharge half-cycle profiles of the first 75 cycles of an aluminum CC cell on the left (a) and of a PPyP CC cell on the right (b), using LiTFSI electrolyte. 42

Figure 3.1: A flow cell during electrochemical discharge, with anolyte (blue) and catholyte (orange) solutions, separated by an ion-selective membrane (fuschia). RAn and OAn are the reduced and oxidized anolyte species, while RCa and OCa are the reduced and oxidized catholyte species, respectively. The exchangeable electrolytic ion species can be one of El^+ or El^-. 50

Figure 3.2: Standard potential scale with redox couples inside and outside of water's thermodynamic stability window. All potentials are listed versus SHE. 53

Figure 3.3: Electrochemical potential window stability (black bars and upper y axis) values of electrolyte solutions of 1 M $CaClO_4$ in various organic solvents and solvent mixtures of ethylene carbonate (EC), diethyl carbonate (DEC), dimethyl carbonate (DMC), dimethoxyethane (DME), and propylene carbonate (PC). 54

Figure 3.4: Left (a); surfactant molecules forming a reverse-micelle in a non-polar solvent. Right (b); surfactant molecules forming a micelle in a polar solvent. 57

Figure 3.5: Left (a); structure of the asymmetrically di-alkylated viologen salt. Right (b); table of chain lengths (R,R') and corresponding transition temperatures from a solid crystal phase to a liquid crystal phase. 58

Figure 3.6: NMR spectra of N-propyl-4-dimethylaminopyridinium bromide salt **2a**. Top (a); the ^1H spectra taken in deuterated acetonitrile (300 MHz). Bottom (b); the ^{13}C spectra taken in deuterated chloroform (400 MHz). 61

Figure 3.7: Top (a); cyclic voltammograms of the 2nd cycle of ~0.0002 M of non-filtered **3a**. Bottom (b); the 1st cycle of ~0.001 M of **3a** (initial polarization current at -0.9 V). The working electrode potential (E_{we}) was recorded vs. a non-aqueous silver/silver$^+$ (Ag/Ag^+) reference electrode. The scan rate was 10 mV/s with "IR determination and compensation by impedance measurement technique" (ZIR correction) in the top

voltammogram and 50 mV/s without ZIR correction in the bottom voltammogram. The electrolyte used was 0.1 M TBAH DMF in both cases. 65

Figure 3.8: Top (a); cyclic voltammograms of the 2nd cycle of ~0.0002 M of non-filtered **3a** with ~0.0005 M ferrocene. Bottom (b); the 2nd cycle of ~0.001 M of **3a** with ~0.005 M ferrocene. The working electrode potential (E_{we}) was recorded vs. a non-aqueous silver/silver$^+$ (Ag/Ag^+) reference electrode. The scan rate was 10 mV/s with ZIR correction in the top voltammogram and 50 mV/s without ZIR correction in the bottom voltammogram. The electrolyte used was 0.1 M TBAH DMF in both cases. 66

Figure 3.9: Top (a); CV spectrum of KBr in 0.1 M TBAH in DMF at 10 mV/s with ZIR correction. Bottom (b); CV spectrum of KBr + Fc in 0.1 M TBAH in DMF at 10 mV/s with ZIR correction. 68

Figure 3.10: Top (a); CV spectrum of **2a** in 0.1 M TBAH in DMF at 10 mV/s with ZIR correction. Bottom (b); CV spectrum of **2a** + Fc in 0.1 M TBAH in DMF at 10 mV/s with ZIR correction. 69

Figure 3.11: ^{1}H NMR spectra of N,N-dipropyl-bis-2-(4-dimethylamino)pyridinylidene **3a** in C_6D_6 (400 MHz). 70

Figure 3.12: The structural labeling of the hydrogen nuclei in the *E*/*Z* isomers of **3a**. ... 72

Figure 3.13: ^{1}H-^{1}H correlation spectroscopy (COSY) spectrum of **3a** in C_6D_6, with both the f1 and f2 traces representing the ^{1}H spectrum of **3a**. 74

Figure 3.14: Top (a); ^{13}C NMR spectra of N,N-dipropyl-bis-2-(4-dimethylamino)pyridinylidene **3a** in deuterated benzene. Bottom (b); the structural labeling of the carbon nuclei in the *E*/*Z* isomers of **3a**. 75

Figure 3.15: ^{1}H-^{13}C heteronuclear single quantum coherence spectroscopy (HSQC) spectrum of **3a** in C_6D_6 with the f1 and f2 traces representing the ^{13}C and ^{1}H spectra of **3a**, respectively. 77

Figure 3.16: ^{1}H-^{13}C heteronuclear multiple-bond correlation (HMBC) spectrum of **3a** in C_6D_6, with the f1 and f2 traces representing the ^{13}C and ^{1}H spectra of **3a**, respectively. 79

Figure 3.17: Variable temperature ^{1}H NMR of **3a** in C_6D_6 at temperatures of 60, 50, 40, and 20°C (top to bottom). 81

Figure 3.18: ^{1}H-^{1}H COSY (top, a) and ^{1}H-^{13}C HSQC (bottom, b) of **3a** in C_6D_6 at 50°C. Decoupling was not performed in the HSQC study. 82

Figure 3.19: Top; ^{1}H NMR spectrum of **4a** recorded in CD_3CN (a). Middle; ^{13}C NMR spectrum of **4a** recorded in CD_3CN (b). Bottom; structure of N,N-dipropyl-bis-2-(4-dimethylamino)pyridinium chloride **4a** with labelled hydrogen nuclei on the left (c) and carbon nuclei on the right (d). 85

Figure 3.20: The two resonance structures of N,N-dialkyl-bis-2-(4-dimethylamino)pyridinium chloride derivatives **4**. 86

Figure 3.21: Top; ^{1}H NMR spectrum of 5a in CD_3CN (a). Middle; ^{13}C NMR spectrum of 5a in CD_3CN (b). Bottom; Structure of N,N-dipropyl-bis-2-(4-dimethylamino)pyridinium hexafluorophosphate **5a** with labelled hydrogen nuclei on the left (c) and carbon nuclei on the right (d). 89

Figure 3.22: ^{1}H (top, a) and ^{13}C (bottom, b) NMR spectra of the product mixture containing **3e** in C_6D_6. 92

Figure 3.23: ESI-MS of chloride salt mixture **4e** + **4a** + **4d**. 94

Figure 3.24: Cyclic voltammogram of 0.002 M **5a** with 0.001 M Ferrocene, recorded with 10 mV/s scan rate and ZIR correction, using a Ag/Ag+ reference electrode. 97

Figure 3.25: Cyclic voltammogram of 0.002 M **5a**, recorded at various scan rates between -2 and -1 V, using a Ag/Ag+ reference electrode. The 10 mV/s scan had ZIR correction applied to it. 99

Figure 3.26: Structure of N-propyl (**2a**), N-butyl (**2b**), N-hexyl (**2c**), and N-dodecyl (**2d**) -4-dimethylaminopyridinium Bromide. 112

Figure 3.27: N-propyl-4-dimethylaminopyridinium bromide salt (**2a**) crystals grown in a cold mixture of isopropanol and diethyl ether. 113

Figure 3.28: Structures of N,N-dipropyl (**3a**), N,N-dibutyl (**3b**), N,N-dihexyl (**3c**), and N,N-didodecyl (**3d**) -bis-2-(4-dimethylamino)pyridinylidene..... 116

Figure 3.29: Structures of N-propyl-N′-dodecyl (**3e**), N-butyl-N′-dodecyl (**3f**), and N-hexyl-N′-dodecyl (**3g**) -bis-2-(4-dimethylamino)pyridinylidene in mixtures with **3a**, **3b**, and **3c**, respectively, and with **3d**. 117

Figure 3.30: Left (a), structures of N,N-dipropyl (**4a**), N,N-dibutyl (**4b**), N,N-dihexyl (**4c**), and N,N-didodecyl (**4d**) -bis-2-(4-dimethylamino)pyridinium. Right (b), structures of N-propyl-N′-dodecyl (**4e**), N-butyl-N′-dodecyl (**4f**), and N-hexyl-N′-dodecyl (**4g**) -bis-2-(4-dimethylamino)pyridinium chloride in mixtures with **4a**, **4b**, and **4c**, respectively, and with **4d**..... 122

Figure 3.31: Left (a), structures of N,N-dipropyl (**5a**), N,N-dibutyl (**5b**), N,N-dihexyl (**5c**), and N,N-didodecyl (**5d**) -bis-2-(4-dimethylamino)pyridinium. Right (b), structures of N-propyl-N′-dodecyl (**5e**), N-butyl-N′-dodecyl (**5f**), and N-hexyl-N′-dodecyl (**5g**) -bis-2-(4-dimethylamino)pyridinium chloride in mixtures with **5a**, **5b**, and **5c**, respectively, and with **5d**..... 127

Figure 3.32: Structure of **(*Z*)-3a** illustrating all assigned 2D NMR correlations for ^{1}H-^{1}H COSY and ^{1}H-^{13}C HMBC. 132

Figure 3.33: Structure of **(*E*)-3a** illustrating all assigned 2D NMR correlations for ^{1}H-^{1}H COSY and ^{1}H-^{13}C HMBC. 133

Figure 3.34: Structure of **4a** illustrating all assigned 2D NMR correlations for ^{1}H-^{1}H COSY and ^{1}H-^{13}C HMBC. 134

Figure 3.35: CV spectrum of **4a** + Fc in 0.1 M TBAH in DMF at 50 mV/s. 135

Figure 3.36: CV spectrum of **4b** + Fc in 0.1 M TBAH in DMF at 50 mV/s. 135

Figure 3.37: CV spectrum of **4c** + Fc in 0.1 M TBAH in DMF at 50 mV/s..... 136

Figure 3.38: CV spectrum of **5a** + Fc in 0.1 M TBAH in DMF at 10 mV/s with ZIR correction. 136

Figure 3.39: CV spectrum of **5b** + Fc in 0.1 M TBAH in DMF at 10 mV/s with ZIR correction. 137

Figure 3.40: CV spectrum of **5c** + Fc in 0.1 M TBAH in DMF at 10 mV/s with ZIR correction. 137

Figure 3.41: CV spectrum of **5d** + Fc in 0.1 M TBAH in DMF at 10 mV/s with ZIR correction. 138

Figure 3.42: CV spectrum of **5e+5a+5d** + Fc in 0.1 M TBAH in DMF at 10 mV/s with ZIR correction. 138

Figure 3.43: CV spectrum of **5f+5b+5d** + Fc in 0.1 M TBAH in DMF at 10 mV/s with ZIR correction. 139

Figure 3.44: CV spectrum of **5g+5c+5d** + Fc in 0.1 M TBAH in DMF at 10 mV/s with ZIR correction. 139

Figure 3.45: Top (a); Low-resolution mass spectrum of **4a**. Bottom (b); High-resolution mass spectrum of **4a**..... 140

Figure 3.46: Top (a); Low-resolution mass spectrum of **4b**. Bottom (b); High-resolution mass spectrum of **4b**. 141

Figure 3.47: Top (a); Low-resolution mass spectrum of **4c**. Bottom (b); High-resolution mass spectrum of **4c**. 142

Figure 3.48: Top (a); Low-resolution mass spectrum of **4d**. Bottom (b); High-resolution mass spectrum of **4d**. 143

Figure 3.49: Top (a); Low-resolution mass spectrum of **4e+4a+4d**. Bottom (b); High-resolution mass spectrum of **4a** in sample **4e+4a+4d**..... 144

Figure 3.50: Top (a); High-resolution mass spectrum of **4d** in sample **4e+4a+4d**. Bottom (b); High-resolution mass spectrum of **4e** in sample **4e+4a+4d**. 145

Figure 3.51: Top (a); Low-resolution mass spectrum of **4f+4b+4d**. Bottom (b); High-resolution mass spectrum of **4b** in sample **4f+4b+4d**..... 146

Figure 3.52: Top (a); High-resolution mass spectrum of **4d** in sample **4f+4b+4d**. Bottom (b); High-resolution mass spectrum of **4f** in sample **4f+4b+4d**. 147

Figure 3.53: Top (a); Low-resolution mass spectrum of **4g+4c+4d**. Bottom (b); High-resolution mass spectrum of **4c** in sample **4g+4c+4d**. 148

Figure 3.54: Top (a); High-resolution mass spectrum of **4d** in sample **4g+4c+4d**. Bottom (b); High-resolution mass spectrum of **4g** in sample **4g+4c+4d**. 149

Figure 3.55: ^{1}H NMR spectrum of **2a** in CD_3CN (300 MHz). 150

Figure 3.56: ^{1}H NMR spectrum of **2a** in $CDCl_3$ (400 MHz). 151

Figure 3.57: ^{13}C NMR spectrum of **2a** in $CDCl_3$ (400 MHz). 152

Figure 3.58: ^{1}H NMR spectrum of **2b** in CD_3CN (300 MHz). 153

Figure 3.59: ^{1}H NMR spectrum of **2b** in $CDCl_3$ (400 MHz). 154

Figure 3.60: ^{13}C NMR spectrum of **2b** in $CDCl_3$ (400 MHz). 155

Figure 3.61: ^{1}H NMR spectrum of **2c** in CD_3CN (300 MHz)..... 156

Figure 3.62: ^{1}H NMR spectrum of **2c** in $CDCl_3$ (400 MHz). 157

Figure 3.63: ^{13}C NMR spectrum of **2c** in $CDCl_3$ (400 MHz). 158

Figure 3.64: ^{1}H NMR spectrum of **2d** in CD_3CN (300 MHz). 159

Figure 3.65: ^{1}H NMR spectrum of **2d** in $CDCl_3$ (400 MHz). 160

Figure 3.66: ^{13}C NMR spectrum of **2d** in $CDCl_3$ (400 MHz). 161

Figure 3.67: ^{1}H NMR spectrum of **3a** in C_6D_6 (400 MHz)..... 162

Figure 3.68: ^{13}C NMR spectrum of **3a** in C_6D_6 (400 MHz). 163

Figure 3.69: ^{1}H-^{1}H COSY NMR spectrum of **3a** in C_6D_6 (400 MHz). 164

Figure 3.70: ^{1}H-^{13}C HSQC NMR spectrum of **3a** in C_6D_6 (400 MHz). 165

Figure 3.71: ^{1}H-^{13}C HMBC NMR spectrum of **3a** in C_6D_6 (400 MHz). 166

Figure 3.72: ^{1}H NMR spectrum of **3b** in C_6D_6 (400 MHz). 167

Figure 3.73: ^{13}C NMR spectrum of **3b** in C_6D_6 (400 MHz). 168

Figure 3.74: ^{1}H NMR spectrum of **3c** in C_6D_6 (400 MHz). 169

Figure 3.75: ^{13}C NMR spectrum of **3c** in C_6D_6 (400 MHz). 170

Figure 3.76: ^{1}H NMR spectrum of **3d** in C_6D_6 (400 MHz). 171

Figure 3.77: ^{13}C NMR spectrum of **3d** in C_6D_6 (400 MHz). 172

Figure 3.78: ^{1}H NMR spectrum of **3a**, **3d**, and **3e** unknown mixture in C_6D_6 (400 MHz). 173

Figure 3.79: ^{13}C NMR spectrum of **3a**, **3d**, and **3e** unknown mixture in C_6D_6 (400 MHz). 174

Figure 3.80: ^{1}H NMR spectrum of **3b**, **3d**, and **3f** unknown mixture in C_6D_6 (400 MHz). 175

Figure 3.81: ^{13}C NMR spectrum of **3b**, **3d**, and **3f** unknown mixture in C_6D_6 (400 MHz). 176

Figure 3.82: ^{1}H NMR spectrum of **3c**, **3d**, and **3g** unknown mixture in C_6D_6 (400 MHz). 177

Figure 3.83: ^{13}C NMR spectrum of **3c**, **3d**, and **3g** unknown mixture in C_6D_6 (400 MHz). 178

Figure 3.84: ^{1}H NMR spectrum of **4a** in CD_3CN (400 MHz). 179

Figure 3.85: ^{13}C NMR spectrum of **4a** in CD_3CN (400 MHz). 180

Figure 3.86: ^{1}H-^{1}H COSY NMR spectrum of **4a** in CD_3CN (400 MHz). 181

Figure 3.87: ^{1}H-^{13}C HSQC NMR spectrum of **4a** in CD_3CN (400 MHz). 182

Figure 3.88: ^{1}H-^{13}C HMBC NMR spectrum of **4a** in CD_3CN (400 MHz). 183

Figure 3.89: ^{1}H NMR spectrum of **4b** in CD_3CN (400 MHz). 184

Figure 3.90: ^{13}C NMR spectrum of **4b** in CD_3CN (400 MHz). 185

Figure 3.91: ^{1}H NMR spectrum of **4c** in CD_3CN (400 MHz). 186

Figure 3.92: ^{13}C NMR spectrum of **4c** in CD_3CN (400 MHz). 187

Figure 3.93: ^{1}H NMR spectrum of **4d** in CD_3CN (400 MHz). 188

Figure 3.94: ^{13}C NMR spectrum of **4d** in CD_3CN (400 MHz). 189

Figure 3.95: ^{1}H NMR spectrum of **4a**, **4d**, and **4e** unknown mixture in C_6D_6 (400 MHz). 190

Figure 3.96: ^{13}C NMR spectrum of **4a**, **4d**, and **4e** unknown mixture in C_6D_6 (400 MHz). 191

Figure 3.97: ^{1}H NMR spectrum of **4b**, **4d**, and **4f** unknown mixture in C_6D_6 (400 MHz). 192

Figure 3.98: ^{13}C NMR spectrum of **4b**, **4d**, and **4f** unknown mixture in C_6D_6 (400 MHz). 193

Figure 3.99: ^{1}H NMR spectrum of **4c**, **4d**, and **4g** unknown mixture in C_6D_6 (400 MHz). 194

Figure 3.100: ^{13}C NMR spectrum of **4c**, **4d**, and **4g** unknown mixture in C_6D_6 (400 MHz). 195

Figure 3.101: ^{1}H NMR spectrum of **5a** in CD_3CN (400 MHz). 196

Figure 3.102: ^{13}C NMR spectrum of **5a** in CD_3CN (400 MHz). 197

Figure 3.103: ^{1}H NMR spectrum of **5b** in CD_3CN (400 MHz). 198

Figure 3.104: ^{13}C NMR spectrum of **5b** in CD_3CN (400 MHz). 199

Figure 3.105: ^{1}H NMR spectrum of **5c** in CD_3CN (400 MHz)..... 200

Figure 3.106: ^{13}C NMR spectrum of **5c** in CD_3CN (400 MHz). 201

Figure 3.107: ^{1}H NMR spectrum of **5d** in CD_3CN (400 MHz). 202

Figure 3.108: ^{13}C NMR spectrum of **5d** in CD_3CN (400 MHz). 203

Figure 3.109: ^{1}H NMR spectrum of **5a**, **5d**, and **5e** unknown mixture in C_6D_6 (400 MHz). 204

Figure 3.110: ^{13}C NMR spectrum of **5a**, **5d**, and **5e** unknown mixture in C_6D_6 (400 MHz). 205

Figure 3.111: ^{1}H NMR spectrum of **5b**, **5d**, and **5f** unknown mixture in C_6D_6 (400 MHz). 206

Figure 3.112: ^{13}C NMR spectrum of **5b**, **5d**, and **5f** unknown mixture in C_6D_6 (400 MHz). 207

Figure 3.113: ^{1}H NMR spectrum of **5c**, **5d**, and **5g** unknown mixture in C_6D_6 (400 MHz). 208

Figure 3.114: ^{13}C NMR spectrum of **5c**, **5d**, and **5g** unknown mixture in C_6D_6 (400 MHz). 209

List of Schemes

Scheme 2.1: Left (a); short sections of polypyrrole in p-type conducting state. Right (b); short sections of polypyrrole in neutral non-conducting state. 22

Scheme 3.1: Top (a); the electrochemical oxidation of N,N-dimethyl-bis-2-(4-dimethylamino)pyridinylidene **1** to the corresponding bis-pyridinium dication $\mathbf{1}^{2+}$. Bottom (b); the resonance structures of the bis-pyridinium $\mathbf{1}^{2+}$. 55

Scheme 3.2: The synthesis of the N-alkyl-4-dimethylaminopyridinium bromide precursor salts **2a-d** with the accompanying final yields for each precursor..... 60

Scheme 3.3: The synthetic scheme for generating the N,N-dialkyl-bis-2-(4-dimethylamino)pyridinylidene electron donors **3a-d**, with accompanying isolated yields and *Z*/*E* isomer ratios..... 63

Scheme 3.4: Preparation of N,N-dialkyl-bis-2-(4-dimethylamino)pyridinium chloride salts **4a-d** with accompanying yields. 83

Scheme 3.5: Preparation of N,N-dialkyl-bis-2-(4-dimethylamino)pyridinium hexafluorophosphate salts **5a-d** with accompanying yields. 88

Scheme 3.6: Synthetic scheme for generating the mixtures of **3a-c**, **3d**, and corresponding N-alkyl-N′-dodecyl-bis-2-(4-dimethylamino)pyridinylidene (**3e-g**), with accompanying yields assuming only **3e-g** were generated (m = 0). 91

Scheme 3.7: The synthetic scheme for generating the mixtures of **4a-c**, **4d**, and corresponding N-alkyl-N′-dodecyl-bis-2-(4-dimethylamino)pyridinium chloride (**4e-g**), with accompanying yields assuming only **4e-g** were generated (m = 0)..... 93

Scheme 3.8: The synthetic scheme for generating the mixtures of **5a-c**, **5d**, and corresponding N-alkyl-N′-dodecyl-bis-2-(4-dimethylamino)pyridinium hexafluorophosphate (**5e-g**), with accompanying yields assuming only **5e-g** were generated (m = 0). 95

List of Symbols and Abbreviations

1D	One-dimensional
2D	Two-dimensional
3D	Three-dimensional
4DMAP	4-dimethylaminopyridine
α_i	Chemical activity of the i^{th} electroactive species
A	Electrode surface area (μm^2)
AQSA	Anthraquinone-2-sulfonic acid
b	Sum of current factors for a non-idealized cell at rest (mA)
BSE	Back-scattered electron
BuBr	Butylbromide
C	Concentration (mmol / mL)
CC	Current collector
COSY	Correlation spectroscopy
CV	Cyclic voltammetry
d	Density (mg / mm^3)
D	Diffusion coefficient (cm^2 / s)
DEC	Diethyl carbonate
DMSO	Dimethyl sulfoxide
DodeBr	Dodecylbromide
σ	Standard deviation

E°	Standard potential of a cell (V)
$E_{1/2}$	Half-cell potential (V)
E_{Cell}	Cell voltage or operating cell voltage (V)
E_{Ch}	Charging voltage (V)
E_{Disch}	Discharging voltage (V)
E_{ox}	Oxidation potential (V)
E°_{ox}	Standard oxidation potential of a half-cell (V)
$E^\circ_{ox,\ Anode}$	Standard oxidation potential of the anode half-cell (V)
E_{OC}	Open-circuit potential of a cell (V)
E_{re}	Reduction potential (V)
E^o_{red}	Standard reduction potential of a half-cell (V)
$E^\circ_{red,\ Cathode}$	Standard reduction potential of the cathode half-cell (V)
$E^\circ_{red,\ Anode}$	Standard reduction potential of the anode half-cell (V)
E_{we}	Working electrode potential (V)
EC	Ethyl carbonate
El	Exchangeable electrolytic ion species
ESI-MS	Electrospray ion mass spectrometry
F	Faraday's constant (26.801 A·h / mol e^-)
Fc	Ferrocene
Fc^+	Ferrocenium
ΔG°	Standard Gibbs free energy available from a system (J)
h	Thickness (mm)
HexBr	Hexylbromide

HMBC	Heteronuclear multiple bond correlation spectroscopy
HMDS	Bis(trimethylsilyl)amine
HOMO	Highest occupied molecular orbital
HSQC	Heteronuclear single quantum coherence spectroscopy
I	Electric current (A)
I_p	Peak current (mA)
I_{pa}	Reduction wave peak current (mA)
I_{pc}	Oxidation wave peak current (mA)
J	Scalar coupling (Hz)
k_{ex}	Chemical exchange rate
KHMDS	Potassium bis(trimethylsilyl)amide
LiGraph	Lithiated graphite
Li-ion	Lithium ion
LiMOx	Lithium metal oxide
LiTFSI	Lithium bis-(trifluoromethylsulfonyl)imide
m	Mass of electroactive material, whole electrode, or entire cell (g)
m_{active}	Mass of electroactive material (mg)
m_{Al}	Mass of aluminum in an electrode disk (mg)
m_{barePa}	Mass of uncoated polypyrrole paper composite current collector (mg)
$m_{graphite}$	Mass of graphite (mg)
m_l	Mass of the limiting electroactive material (g)
$m_{LiFePO4}$	Mass of lithium iron phosphate (mg)
m_{PVDF}	Mass of polyvinylidene fluoride (mg)

m_{total}	Total mass of an electrode (mg)
m_{wetPa}	Mass of freshly-coated polypyrrole paper composite current collector (mg)
MS	Mass spectrometry
$\eta_{E\,Ch}$	Charging half-cycle overpotential or overvoltage (V)
$\eta_{E\,Disch}$	Discharging half-cycle overpotential or overvoltage (V)
$\Delta\eta_E$	Voltage difference between charging and discharging voltages (V)
$\%\eta_E$	Voltage efficiency (%)
n	Number of moles of electrons (mol)
NMP	N-methyl-2-pyrrolidone
NMR	Nuclear magnetic resonance
OAn	Oxidized anolyte species
OCa	Oxidized catholyte species
ppm	Parts per million
PPy	Polypyrrole
PPyP	Polypyrrole-coated paper composite
PrBr	Propylbromide
PVDF	Polyvinylidene fluoride
Q	Charge capacity (A·h or mA·h)
Q_{Ch}	Charge capacity stored in a charge half-cycle (mA·h)
Q_{Disch}	Charge capacity released in a discharge half-cycle (mA·h)
Q_m	Gravimetric charge capacity (mA·h / g)
Q_{mDis}	Gravimetric current capacity of a discharge half-cycle (mA·h / g)
Q_{ml}	Gravimetric capacity of the limiting electroactive material (mA·h / g)

$Q_{\Delta T}$	Charge capacity for a specified time interval (mA·h)
Q_v	Volumetric charge capacity (mA·h / mL)
r	Radius (mm)
R	Electrical resistance or internal cell resistance (Ω)
R	Gas constant (8314.46 mVm·C / K·mmol)
R_{dry}	Dry electrode coating ratio
$R_{LiFePO4}$	Lithium iron phosphate content ratio of an electrode coating
RAn	Reduced anolyte species
RCa	Reduced catholyte species
RE	Reference electrode
RSD%	Relative standard deviation (%)
SCE	Saturated calomel electrode
SED	Super electron donor
SEM	Scanning electron micrography
SHE	Standard hydrogen electrode
SLI	Starting, lighting, ignition
T	Temperature (K)
ΔT	Specific time interval (h)
TBAH	Tetrabutylammonium hexafluorophosphate
THF	Tetrahydrofuran
v	Volume of electroactive material, whole electrode, or entire cell (mL)
v	Scan rate (mV / s)
Δv	Frequency difference between conformers

$V(acac)_3$	Vanadium acetylacetonate
VT	Variable temperature
WE	Working electrode
x	Number of moles of limiting electroactive species (mol)
ZIR	Current-resistance determination and compensation by impedance measurement technique

Chapter 1 – Introduction

1.1 – Prevalence of Batteries

A battery is a device that converts the chemical energy contained in its active materials directly into electrical energy by means of an electrochemical oxidation-reduction (redox) reaction.[1] The first battery, called the voltaic pile, was invented in 1799 by Allesandro Volta.[2] The system was crude but versatile, with a voltaic pile consisting of 2000 cells having been used by Sir Humphry Davy to isolate elemental barium, calcium, strontium, boron, and magnesium for the first time in 1808.[3,4] The next major innovation in electrochemical storage technology was the invention of the lead-acid battery by Gaston Planté in 1859.[5] The lead-acid system was the first kind of battery that could be recharged by passing a current through it. Many more systems have since been devised, with the lithium battery being conceptualized in the 1970s for tasks requiring high energy density.[6] The pursuit of rechargeable batteries using lithium metal was wrought with challenges that limited their commercial use[7] until 1990 when Sony Corporation revealed a "lithium-ion" battery using lithiated graphite instead of lithium metal.[6]

Today, batteries play an important role in powering consumer electronics, and are gaining increasing interest in powering vehicles[8] and grid energy storage, as well as some more specialized applications.[9] World demand for batteries is projected to increase by

8.1% per year to a total of 132 billion USD by 2016.[10] As an energy storage system, batteries can be very energy-efficient, scalar, and modular. In addition, batteries usually have lower CO_2 emission footprints compared to fossil fuel systems.[11] There is also a wide variety of different battery types with specific strengths and weaknesses from which to choose from when an energy storage system is needed for some specific application. For example, lead-acid batteries see prominent use in automobiles as SLI (starting, lighting, ignition) batteries or as fast-response stationary batteries for emergencies[12] and for stabilizing and regulating electrical transmission[12,13] as these systems meet the high charge-discharge rate capability and cycling stability necessitated by these applications.[12,14] Meanwhile, lithium-ion batteries have high energy densities that make them very practical for powering portable electronics.[15,16] Indeed, there is an ever-increasing effort in battery R&D not only to improve existing battery technology but also to develop new, more suitable systems that may better meet the requirements of our society's technological needs.[17,18]

1.2 – Introduction to Electrochemistry

Electrochemistry is concerned with the interrelation of electrical and chemical effects.[19] Electrochemical reactions are processes that transport charged species, either electrons or ions, across interfaces between two different chemical phases. In cells, the interfaces of interest are those formed between an ionically conducting phase, called an electrolyte, and an electrically conducting phase, called the electrode. The most basic

electrochemical reactions involve an electroactive species either being oxidized by producing an electron or reduced by accepting an electron at this interface. The entire system consisting of the electrode immersed in an electrolyte, with either containing an electroactive species, is called a half-cell.[20] Full electrochemical cells are built from at least two half cells in order to utilize oxidation and reduction reactions to interconvert electrical and chemical energy. Batteries can be either single cells or many electrochemical cells electrically connected in series and/or parallel arrangements.[1]

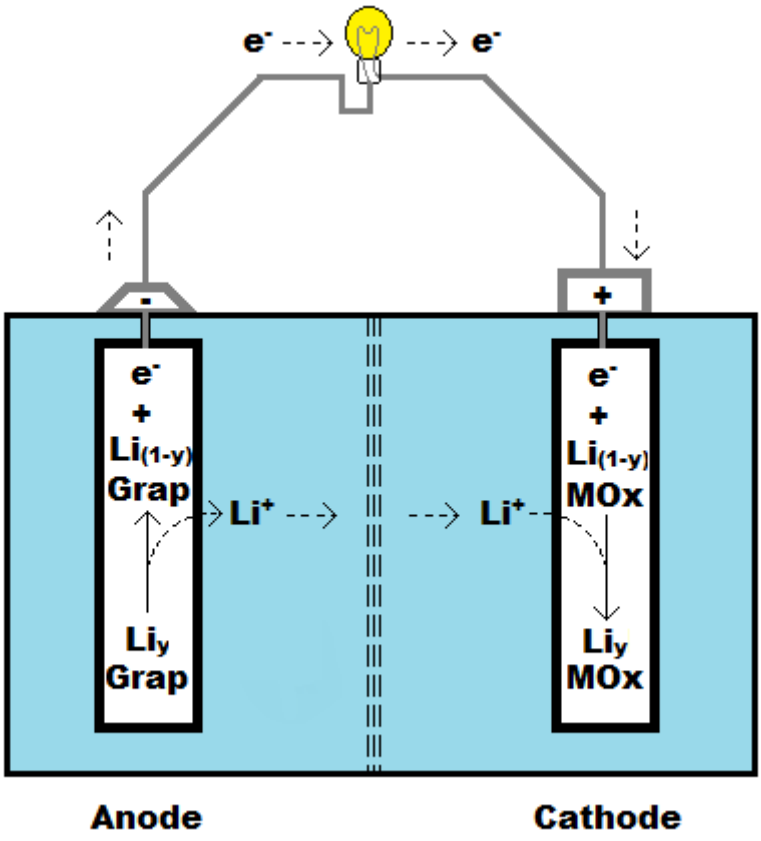


Figure 1.1: A lithium-ion cell with lithiated graphite (Li Grap) as the anode, and some lithiated metal oxide (Li MOx) as the cathode, internally separated by an organic solvent containing some Li-ion-based electrolyte (blue) and a polymer separator (hashed lines), and externally connected in an electronic circuit (grey) with a lightbulb. Hashed arrows show movement of charged species; solid arrows show chemical conversion of species.

In order to interconvert chemical and electrical energies, an electrochemical cell requires some key structures and mediums. Figure 1.1 shows a typical lithium ion (Li-ion) cell based on graphite and metal oxide active materials. Oxidation takes place at the anode, while reduction takes place at the cathode. As such, lithiated graphite (LiGrap) is the anodic material; it's being oxidized to produce lithium ions (which are released by de-intercalation) and electrons. The lithiated metal oxide (LiMOx) is the cathodic material; it is being reduced by accepting lithium ions (via intercalation) and electrons. These two reactions can be written as individual half-cell reactions and then combined together to give the full-cell reaction:

$Li_yGrap \rightarrow Li_{(1-y)}Grap + y\ e^- + y\ Li^+$	Anode
$Li_{(1-y)}MOx + y\ e^- + y\ Li^+ \rightarrow Li_yMOx$	Cathode
$Li_yGrap + Li_{(1-y)}MOx \rightarrow Li_{(1-y)}Grap + Li_yMOx$	Full Cell

where "y" denotes the amount of lithium, and thus lithium ions and electrons, being exchanged between the electrodes. LiGrap and LiMOx participate in the full-cell reaction and are thus called electroactive materials. All other materials and components of the cell which are not included in the full-cell reaction are called inactive materials. Ideally, the electroactive materials should not travel across the electrode-electrolyte interface. Only charged species should be exchanged between electrodes, i.e. lithium ions and electrons.

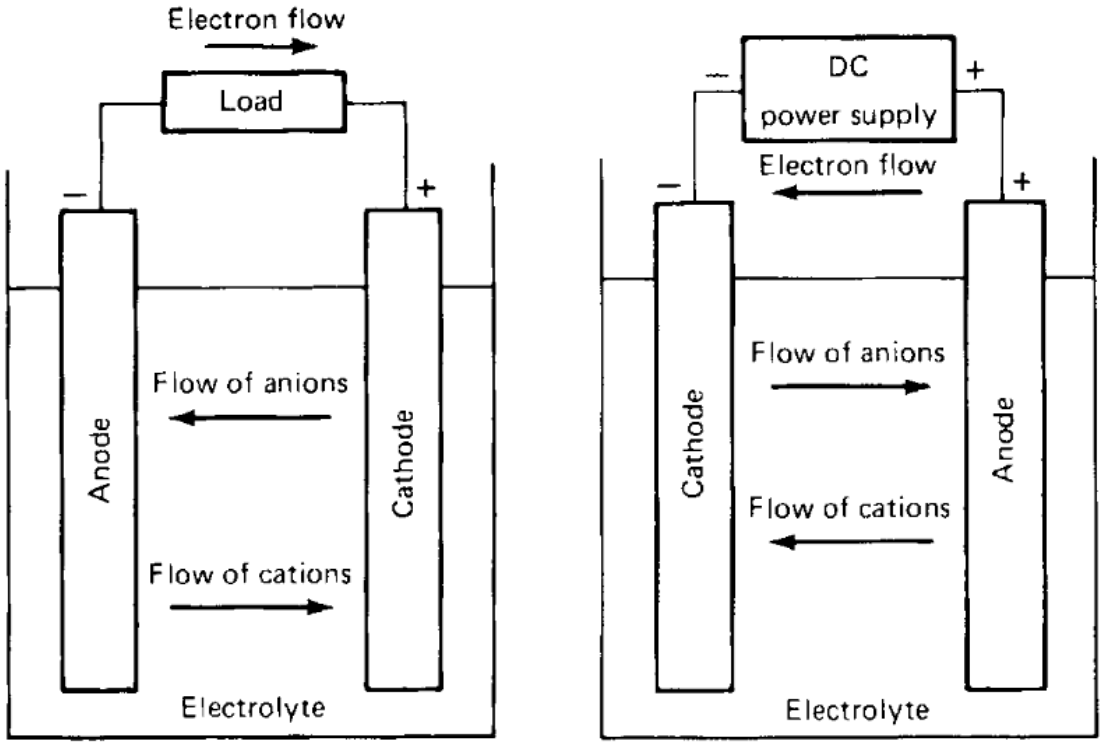


Figure 1.2: Left (a); Cell operations when discharging. Right (b); Cell operations when charging (right, b).[1]

The cell systems in Figures 1.1 and 1.2a are shown to be undergoing discharge, a spontaneous process that generates a useful electric current, driven by the electrochemical potential difference between the two electrode reactions. The contrasting process is "charging" (Figure 1.2b), wherein an electric current is supplied in the opposing direction in order to reverse the full-cell reaction and regenerate the charged state of the electroactive materials. Charging is only possible in systems encompassing electrode reactions that are both chemically and practically reversible;[12] the commercial name of this capability is called "rechargeable". Cells that can be charged / recharged are called secondary cell systems, while cells that cannot be charged / recharged are called primary cells, with the latter cells typically being discarded after they are fully discharged.

1.3 – Cell Potential

Electrochemical cells are similar to typical chemical reactions, in that the state of the active materials in a cell will spontaneously shift towards chemical and thermodynamic equilibrium by reacting with each other.[21] Cell systems differ from conventional chemical reactions in that rather than having the reagents react with each other directly; their reaction is carried out via the exchange of charged species while keeping the reactants physically separate from each other in two half-cell systems. The exchange of charge is segregated into an external electric current and an internal ionic current. Because the exchanged species are charged, these two exchange paths can be understood as an electric "circuit" with the charge exchange through both paths being driven by the difference in thermodynamic potential between the cell's two connected half-cells.[1] This potential difference gives the generated parallel ionic and electric current a specific electric potential which, under standard conditions (T = 25°C, 1:1 activity ratio of reduced and oxidized species at the electrode interface, ambient pressure of 1 atm), is called the standard potential of the cell system $E°$.[1] The standard potential is related to the standard Gibbs free energy change of the system through the following equation:

$$E° = -\frac{\Delta G°}{nF} \qquad (\mathbf{1.3 - 1})$$

where $\Delta G°$ is the standard Gibbs free energy change, n is the number of electrons involved in the reaction, F is Faraday's constant, and the ° sign denotes standard conditions. Spontaneous reactions have a positive potential and produce net free energy (negative $\Delta G°$), and hence can perform useful work. Whereas non-spontaneous reactions

will have a negative potential and need energy (positive ΔG°), consequently requiring some form of work to be driven.

The standard potential of a cell E° can be expressed in volts (V) or joules per coulomb (J/C) and describes the amount of energy produced when the cell is being discharged or consumed when the cell is being charged per unit electric charge exchanged between two half-cells. The magnitude and sign of E° can be determined by measuring the voltage and direction of the electric current generated between the half-cells when they are in circuit,[1]

$$E^\circ = E^\circ_{red,\ Cathode} + E^\circ_{ox,\ Anode} \qquad (\mathbf{1.3-2})$$

where E°_{red} and E°_{ox} are the standard reduction and oxidation potentials of the half-cells and "Anode" and "Cathode" designate the anodic and cathodic half-cells, respectively. If the half-cell reactions are reversible, then $E^\circ_{red} = -E^\circ_{ox}$, and the following equation is also true,

$$E^\circ = E^\circ_{red,\ Cathode} - E^\circ_{red,\ Anode} \qquad (\mathbf{1.3-3})$$

The magnitude of E° is particularly important in energy applications, as a higher voltage current is capable of accomplishing more work. For this reason, chemically-compatible half-cells of high E^o_{Red} and E°_{ox} are favored when assembling high-energy batteries.

In order to measure the potential of a specific half-cell for comparison against other half-cells, it is typically paired up with complimentary reference half-cells which are called reference electrodes[22] with these reference electrodes exhibiting a very stable half-cell potential under standard conditions. The standard hydrogen electrode (SHE)

reaction $2H^+ + 2e^- \rightarrow H_2$ is defined as having a standard potential of zero volts[23] for both oxidation and reduction reactions. The difficulties associated with incorporating an SHE in a cell for experimental measurements[19] have made its real-world use somewhat limited. Instead, other electrodes[24] or internal reactants[25] with established standard potentials vs. SHE are used as reference systems.[22]

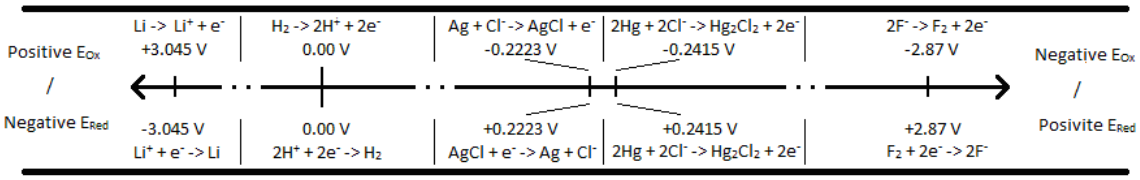


Figure 1.3: Electrochemical potentials of some common reference half-cell reactions.

Several reference half-cell reactions with standardized reduction potentials, sometimes called redox potentials,[26] and oxidation potentials are shown in Figure 1.3 (bottom and top, respectively), with the SHE being the origin on the scale. For reversible half-cell reactions it is common practice to report the reduction potential of the oxidized species rather than the oxidation potential of the reduced species. Standard reduction potential tables can be found in the literature for a wide variety of half-cells.[27]

1.4 – Charge Capacity

Half-cells are chemically finite systems, meaning the electroactive species can eventually be either fully oxidized or fully reduced.[1] Therefore, half-cells contain a finite amount of exchangeable charge. In electrochemical cells, this quantity is called charge capacity, commonly expressed in ampere hours (A·h) which may be converted into coulombs (1 A·h = 3600 C). The charge capacity of a half-cell can be determined using the following equation:

$$Q = xnF \qquad (\mathbf{1.4 - 1})$$

where Q is the charge capacity, x is the number of moles of the limiting electroactive species, n is the number of electrons produced per mole of limiting electroactive species, and F is Faraday's constant (26.801 A·h / mol e^-).

Charge capacity does not give any information about the mass or volume of the half-cell which can be important factors when drawing comparisons against other half-cells for use in energy storage systems. Gravimetric charge capacity, Q_m, is the charge capacity of a half-cell per unit mass, whereas volumetric charge capacity, Q_v, is the charge capacity per unit volume:

$$Q_m = xnF/m \qquad (\mathbf{1.4 - 2})$$

$$Q_v = xnF/v \qquad (\mathbf{1.4 - 3})$$

where m can be the mass of the electroactive material, the electrode, or the entire cell system, and v can be the volume of those same components, as specified. For comparing

the performance of solid electroactive materials, it is typical to use gravimetric capacity of the active material.[28]

With both charge capacity and cell potential, the net energy content of a cell may be calculated from the voltage (1 V = 1 J/C) and capacity (1 A·h = 3600 C) using an equation derived from the Gibbs free energy change equation (1.3 – 1):

$\Delta G^\circ = 3600 \times Q \times E^\circ$ (**1.4 – 4**)

where ΔG° is the available Gibbs energy from the system in joules. Specific energy, the energy content-per-mass of a component or system, and energy density, the energy content-per-volume of a component or system, may also be calculated the same way by substituting Q for Q_m and Q_v respectively. Equation 1.4 – 4 demonstrates the importance of seeking cells with increasingly higher cell potential while also minimizing the mass or volume of the system in order to maximize the available energy of the system.

1.5 – Cell Cycling

Thus far, ideal cell behavior has been assumed in the calculation and understanding of both cell potential and charge capacity. Real cells are non-ideal systems that require testing in order to better ascertain their real-world behavior. One of the staple tests for secondary cells is cell-cycling.[22,29] This is a cyclic electroanalytical experiment where a constant current is applied in such a way as to charge and discharge the cell repeatedly while monitoring the cell's voltage with respect to the accumulated charge

capacity Q, with the latter measurement being the product of the cycling time and the current applied to the cell. Cell-cycling typically takes place between minimum and maximum cutoff voltages; once a cutoff voltage is met, the current is reversed in order to begin the next half-cycle. As such, the cell is effectively charged and discharged repeatedly.

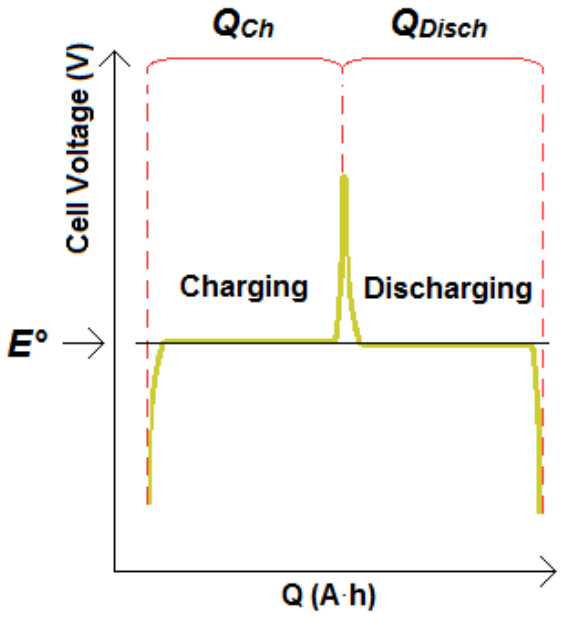


Figure 1.4: Cell-cycling profile for a single cycle assuming ideal behaviour, plotting voltage (in volts) against accumulated charge capacity (in ampere hours).

An example plot of cell voltage vs. charge capacity of the first charge and discharge for an idealized cell is depicted in Figure 1.4. Most of a half-cycle's profile forms a "plateau" wherein the cell voltage varies by very little (see Figure 1.4). However, at the beginning and end of each half-cycle there is an abrupt change in potential between this plateau region and the cutoff voltages. The drastic change can be explained via the Nernst equation applied to both half-cell reactions in the battery.[21]

$$E_{OC} = E^\circ - \frac{RT}{nF} \ln \frac{\alpha_C^c \alpha_D^d}{\alpha_A^a \alpha_B^b} \qquad \textbf{(1.5 – 1)}$$

where E_{OC} is the open-circuit potential of the cell, E° is the standard cell potential, R is the universal gas constant (8.314 J K-1 mol-1), T is temperature in Kelvin, n is the number of electrons being transferred between the electrode and the electroactive species in the full cell reaction, F is the Faraday constant (96485 C / mol), and α_i is the chemical activity of the ith electroactive species. Equation 1.5 – 1 can be simplified when assuming $T = 25^\circ$C,

$$E_{OC} = E^\circ - \frac{0.05916\ \text{V}}{n} \log_{10} \frac{\alpha_C^c \alpha_D^d}{\alpha_A^a \alpha_B^b} \qquad \textbf{(1.5 – 2)}$$

The exponents of the electroactive species activities are representative of the amounts of electroactive species required in a full cell reaction,

$$aA + bB \leftrightharpoons cC + dD \qquad \textbf{(1.5 – 3)}$$

with a, b, c, and d being the number of molecules of A, B, C, and D required for a single reaction, respectively, with each pair of $A – C$ and $B – D$ being constituents of two separate half-cells.

In both equations 1.5 – 1 and 1.5 – 2, the second term's magnitude depends exponentially on the quotient of the chemical activities of the electroactive species of the cell system. Chemical activity is a function of the activity coefficient and the concentration of the species in question. At the beginning and end of each half-cycle, the difference in concentration between the reduced and oxidized species in either or both

half-cells is large enough to create the notable sharp incline or decline in voltage at these points.

The electric current rate I (in amperes, A) is the rate of flow of electric charge. In a battery, an electric current will be supplied to or drawn from the battery's electrodes in order to charge or discharge it, respectively. Cycling time can be multiplied by the applied electric current exhibited by the battery during a specific period of time in order to yield the charge capacity $Q_{\Delta T}$ achieved by the battery during a specified time interval ΔT (in hours, h), with typical measurements including the determination of the total charge capacity stored in a charge half-cycle (Q_{Ch}) or the charge capacity released in a discharge half-cycle (Q_{Disch}). An ideal cell can be fully charged and fully discharged in terms of its theoretical charge capacity at any current I, with this current exhibiting the open-circuit voltage of the cell E_{OC} which depends exclusively on the changes in activities of the electroactive species. The only electrochemical processes involved would be those governed by Faraday's law (i.e. Faradaic processes), in which "the amount of chemical reaction caused by the flow of current is proportional to the amount of electricity passing through the system".[19] However, real electrochemical systems also exhibit a number of phenomena which do not involve electrochemical reactions and therefore do not obey Faraday's law, and as such these phenomena are called non-Faradaic processes. The most widely encountered types of non-Faradaic processes are polarization effects[19] which cause buildup of charge at interfaces that lead to losses in energy to such things as Joule heating.[30]

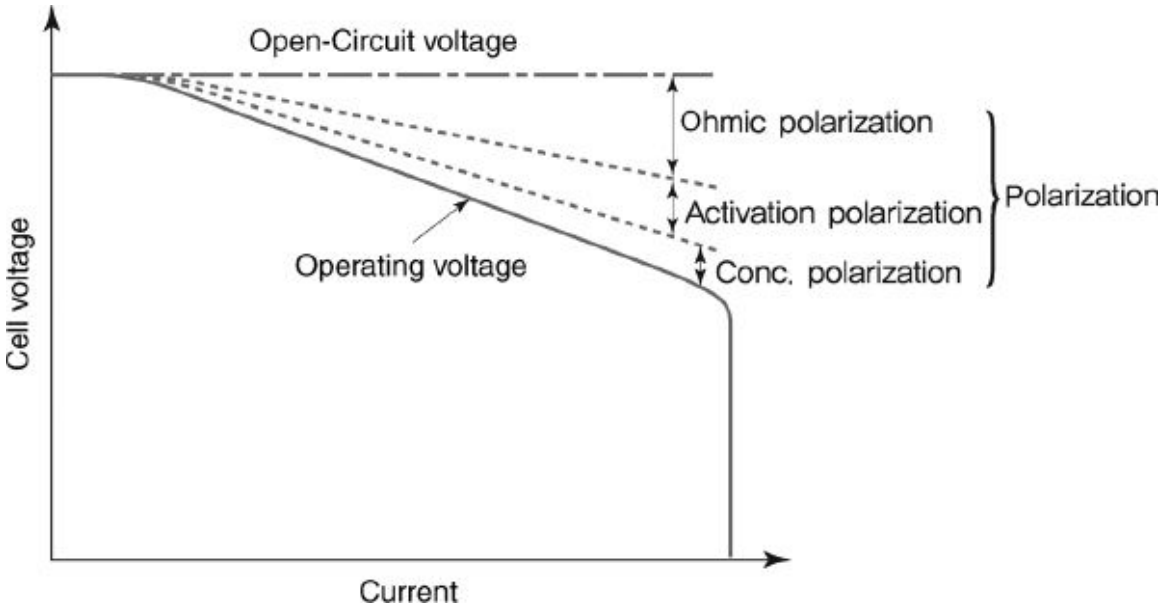


Figure 1.5: A discharge half-cycle of a cell with cell voltage versus current rate. The top hashed line represents the theoretical open-circuit voltage E_{OC}, the middle hashed line is the open-circuit voltage with ohmic polarization, the bottom hashed line is the open-circuit voltage with both ohmic and activation polarizations, and the solid line is the operating cell voltage E_{Cell} which constitutes E_{OC} and ohmic, activation, and concentration polarizations.[31]

Figure 1.5 visually demonstrates the most common non-Faradaic processes encountered in batteries and their effect on the resulting cell voltage E_{Cell} as a function of increasing current rate. The simplest non-Faradaic process is ohmic polarization, which results in a net drop in operating voltage that is equal to the product of the sum total internal resistance of the cell, R (in ohms, Ω), and the applied current, I. As such it is commonly called the "IR drop" or "IR loss".[21] Activation polarization is caused by ionic adsorption and formation/maintenance of the electrical double-layer at the electrode-electrolyte interfaces in cells.[21] Finally, voltage loss from concentration polarization is related to mass-transport of electroactive species between the cell electrodes and electrolyte,[21] with its effect progressively increasing as the charge carriers at the electrode

interfaces become depleted. Ohmic polarization is a current-dependant process, while the activation and concentration polarizations are rate-dependant processes, and so the effects of these polarizations on the operating voltage of the cell can be diminished by using slower current rates. Indeed, the open-circuit voltage E_{OC} is typically estimated experimentally by subjecting cells to very low current rates,[32] wherein polarization effects become negligible.

Because the magnitude of these polarizations is often related to the magnitude of the current applied to the system, it is imperative to control and measure the current used when testing the cycling behavior of a battery. A common practice in battery research and development is to use currents based on the amount of electroactive materials involved in cell systems, with these specific currents being called *C* rates.[33] For example, 1*C* is the current required to completely charge or completely discharge a cell system in 1 hour. A *C* rate of *C*/2 is half the current of 1*C*, and so defines the current required for complete charge or discharge in 2 hours. 2*C* or *C*/0.5 is double the current of 1*C*, and so on.

There are two ways of determining *C* rates for a cell. The first is to calculate it based on the mass and theoretical capacity of the limiting electroactive material in the cell:

$$C = Q_{ml} \times m_l \qquad (\mathbf{1.5 - 4})$$

where m_l is the mass of the limiting material. For example, a lithium cell with an excess of lithium metal at the anode, and 1 gram of lithium iron phosphate ($LiFePO_4$) which has

a theoretical capacity of 170 mAh/g at the cathode, will have *C* rates of:

C = 170 mA·h/g x 1 g = 170 mAh

$C/2$ = 85 mA, $1C$ = 170 mA, $2C$ = 340 mA

The other method is to cycle a cell using a very low current (~$C/20$ or less) to mitigate the effects of polarization, with the capacity of a resulting discharge being the near-theoretical capacity of the cell system. Then one can use *C* rates for similar cell systems based on this experimentally-determined theoretical capacity. In this thesis, the former approach based on calculated theoretical capacity was used to determine the *C* rates for testing cells.

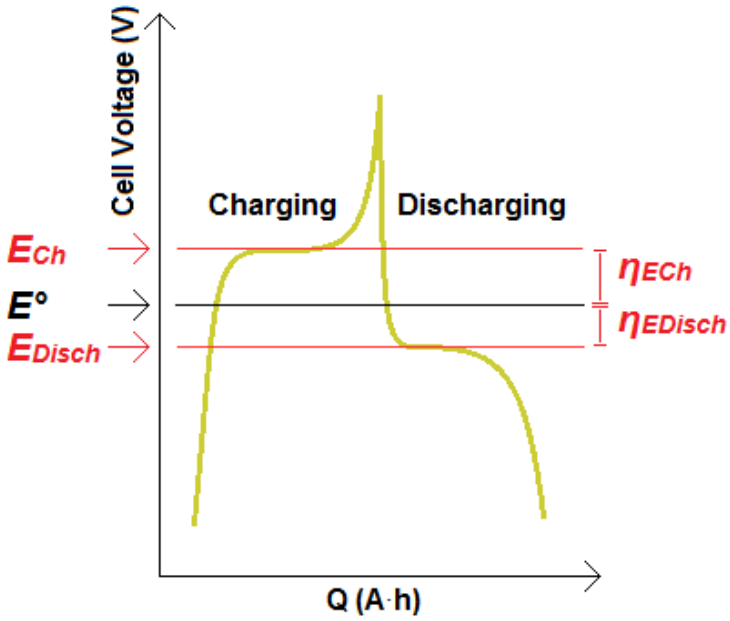


Figure 1.6: Example of a non-ideal cell cycle profile showing higher operating charging voltage (E_{Ch}) and lower operating discharging voltage (E_{Disch}) than the standard cell potential ($E°$) due to polarization effects, with η_{ECh} and η_{EDisch} being the charging and discharging half-cycle overvoltages, respectively.

The sum effect of these non-Faradaic processes can severely impair the cell voltage performance of a battery as well (Figure 1.6). The current needed for charging carries a higher voltage requirement E_{Ch} while the current produced when discharging carries a lower voltage E_{Disch}. The overvoltage[21] of a charge or discharge half-cycle can be calculated via the following:

$$\eta_{E\,Ch\,/\,Disch} = | E^{\circ} - E_{\,Ch\,/\,Disch} | \qquad (\mathbf{1.5 - 5})$$

where $\eta_{E\,Ch\,/\,Disch}$ is the overvoltage of the charge or discharge half-cycle and $E_{\,Ch\,/\,Disch}$ is the operating cell voltage during the same charge or discharge half-cycle. The sum of the charge and discharge overvoltages is called the voltage difference $\Delta\eta_E$:

$$\Delta\eta_E = \eta_{E\,Ch} + \eta_{E\,Disch} = E_{Ch} - E_{Disch} \qquad (\mathbf{1.5 - 6})$$

Furthermore, the potential difference measurement can be accompanied by the voltage efficiency of the cell $\%\eta_E$, which can be calculated as:

$$\%\eta_E = (E_{Disch} / E_{Ch}) \text{ x } 100\% \qquad (\mathbf{1.5 - 7})$$

In addition to Q_{Ch} and Q_{Disch}, both $\Delta\eta_E$ and $\%\eta_E$ serve as means to compare different batteries. For this reason, the cell voltages required in calculating both the overvoltages $\eta_{E\,Ch\,/\,Disch}$ and the voltage efficiency $\%\eta_E$ must be sampled at consistent times or accumulated capacities during the charge and discharge steps in a battery cycle.

1.6 – Research Objective

This thesis's research objective was the replacement of metallic elements in batteries with organic alternatives. To that end, two research projects were conducted: 1)

the replacement of metallic current collectors with conductive paper current collectors in Li-ion batteries, and 2) preparing new organic electroactive materials with increased solubility as alternatives to inorganic and organometallic electroactive materials for redox flow batteries.

In order to be competitive, these organic alternatives needed to either perform on par with or better than conventional commercial materials in some aspect(s). A conductive paper current collector was synthesized and tested in Li-ion batteries in hopes of achieving higher capacities and/or better voltage efficiencies than cells using aluminum as a current collector. Testing took place at multiple *C* rates and compared the capacity of paper current collector cells to those of cells using aluminum. The conductive paper could potentially be applied to electrochemical cells based on other chemistries as well. In addition, some exceptionally good organic reducing agents called "super-electron donors" (SEDs)[34] were synthesized with improved properties for use in redox flow batteries. These SEDs were altered to have higher solubilities in organic electrolyte solvents without negatively affecting their electrochemical behavior. This work could be adapted to other organic compounds for redox flow batteries, with the ultimate goal being the development of all-organic flow batteries of equal or better operating voltages and volumetric capacities as compared to traditional inorganic flow batteries.

Chapter 2 – Conductive Paper Current Collector

2.1 – Replacement of Aluminum with Conductive Paper in Li-Ion Cells

Lithium-ion cells have become a dominant energy storage choice for portable electronics thanks to technological advances since their first commercial appearance in 1991.[35] These cells utilize a low-affinity lithium intercalating material as the anodic material and a high-affinity material as the cathodic material, separated by an electrolyte that allows the diffusion of lithium ions from one electrode to the other.[36] The major advantage of these systems is the use of low mass and high oxidation potential anodic materials. Lithium metal, for instance, boasts a theoretical gravimetric capacity of 3.86 A·h/g due to its extremely low atomic mass, in addition to exhibiting a standard oxidation potential of +3.01 V[1] which is exceptionally high. However, the use of lithium metal, especially in rechargeable batteries, presents substantial safety hazards,[37,38] therefore lithiated graphite and other compounds that can intercalate lithium at a low potential are typically used instead, with the resulting cells being classified as lithium-ion cells[6] often abbreviated as Li-ion cells. Lithiated graphite has a much lower theoretical capacity of 0.372 A·h/g but a comparable oxidation potential of +2.8 V versus SHE.[1] These advantages give Li-ion systems much higher energy densities and specific energies (400 W·h/L and 150 W·h/kg, respectively) than what is possible with competing rechargeable cell systems of nickel-cadmium (100 W·h/L, 35 W·h/kg) and nickel-metal-hydride (240 W·h/L, 75 W·h/kg).[39]

Although there have been many improvements in Li-ion cell technology in terms of developing superior cathode and anode active materials,[40,41] electrolyte compositions,[42] and methods of enhancing electrode conductivities and stability through modifications in their morphology,[43,44] very little attention has been given, relatively-speaking, to the non-active components of Li-ion cells or of other cells in general. Non-active components are required for electric and/or structural purposes in electrochemical cells but do not play a direct role in their electrochemical reactions,[45] with these components including cell casings, metallic spacers and springs, and current collectors. Reducing the mass of a battery's non-active components is indirectly effective in increasing the cell's gravimetric capacity and specific energy by allowing for the incorporation of more active material within the cell without changing its total mass. Because non-active component technologies are independent of cell chemistry, such technologies can be utilized in other types of galvanic cells,[46,47] fuel cells,[48] and other electrochemical energy systems,[49,50] if such technologies confer a weight, performance, cost, or other advantage without compromising the system.

Current collectors are the elements onto or into which electroactive material composites are deposited. These non-active components contribute as much as 25% of a battery's total mass,[51] making them good targets for weight-reduction through use of lighter electrically-conducting alternatives. Current collectors are also critical for providing electrical contact between the active materials and the cell's leads. Conventional current collectors are usually flat two-dimensional metallic foils,[52] with aluminum metal foil being the preferred current collector for the cathode in Li-ion

batteries, due to its light weight and ability to form a protective chemical film under cell-cycling conditions, which inhibits its corrosion.[53] As some active materials are not very conductive themselves, the geometry of a current collector becomes important in order to achieve higher electrical access to all active sites in the material. Improved electrical contact has shown increases in achievable cycling rates, cycle stability, and charge capacities in various cell systems.[54-57]

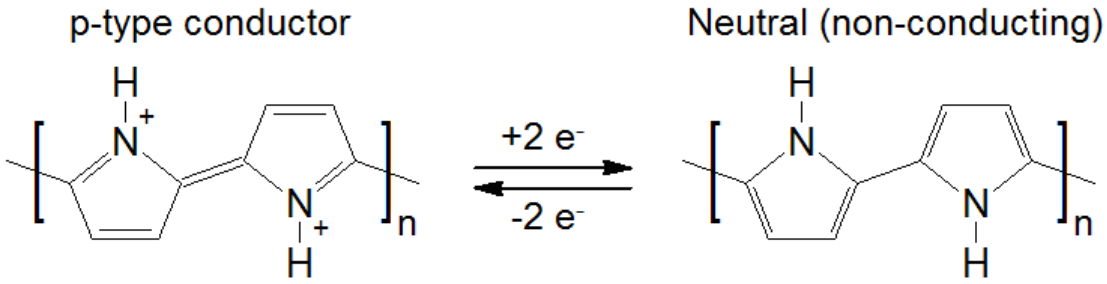
There are numerous examples of alternative current collectors in the literature that have been shown to enhance the performance of electrochemical cells via superior electrical contact with the active materials,[58] including conductive polymers,[59,60] metallic foams,[61] carbon paper,[62] and carbon nanotube inked cellulose paper.[63] Polypyrrole-coated cellulose designed by Yonghao Ni *et al.*[64] combines the simple and effective conductive polymer aspect of polypyrrole with a low-cost cellulose scaffolding, yielding a lightweight metal-free conductive polymer-coated cellulose material. In addition to being a non-metallic alternative to aluminum, it was hoped that the conductive polymer-paper composite's three-dimensional morphology would provide enhanced electrical contact for electroactive materials coated on it.

In this research, conductive polypyrrole-coated cellulose was synthesized and tested as a replacement for aluminum foil current collectors for cathode materials. Lithium iron phosphate ($LiFePO_4$) is used as the cathode active material due, in part, to its cycle durability and reliable cycling behavior,[65] making it highly suitable for testing electrode additives and alternative cell components.[66] $LiFePO_4$ has an adequate operating

voltage of 3.45 V versus Li/Li^+, a gravimetric capacity of 170 mA·h/g, and is inexpensive relative to other cathodic materials used in Li-ion cells.[67] The major drawback of $LiFePO_4$ is its poor electric conductivity,[68] which can be remedied to some degree by mixing in carbon black,[69] as was done in this research. Other improvements include altering the size[70] and morphology[71] of the $LiFePO_4$ grains, and the coating of individual grains with conductive materials.[72] These additional measures were not used in this research, but have nevertheless allowed for the increasing use of $LiFePO_4$ in high-power commercial applications such as electric vehicles.[73]

2.2 – Results and Discussion

Polypyrrole (PPy) is classified as a p-type conductive polymer, which is to say that it has relatively good electric conductivity only when positively charged.



Scheme 2.1: Left (a); short sections of polypyrrole in p-type conducting state. Right (b); short sections of polypyrrole in neutral non-conducting state.

In the neutral state (Scheme 2.1b), the polymer is electrically insulating.[74] When the polymer is oxidized however, a radical-polaron (not shown) or bi-polaron (Scheme 2.1a) forms in the π-system of the polymer which can travel across the chain via π-bond

delocalization, effectively transporting an electric charge across the chain.[75,76] The neutral state is unstable and prone to degradation both through chemical attack[77] and electrochemical decomposition.[74] Anthraquinone-2-sulfonic acid (AQSA) is typically used as a dopant to stabilize the oxidized form of the polymer[78] with the additional benefit of improving its electrical conductivity.[79]

To coat cellulose in conductive polypyrrole, the polymer was synthesized in the presence of an AQSA–cellulose pulp mixture in water. Afterwards, the conductive pulp was pressed into handsheets of polypyrrole paper composite (PPyP). Because residual water would lead to contamination of the electrolyte and cause reactions with anodic electroactive materials such as lithium and lithiated graphite[80] which can lead to a shortened cell life,[81] the water content of the PPyP needed to be reduced. Adequate drying of the PPyP was difficult in part due to slow decomposition of PPy when exposed to ambient air[82] as well as the decomposition of PPy at drying temperatures[83] which meant that any heat-drying techniques or heat-treatments of coatings on the PPyP had to be avoided. Therefore, vacuum-drying techniques and desiccants were utilized to achieve passable levels of dryness in the synthesized PPyP, and the handsheets were stored in a glovebox under argon until they were needed.

2.2.1 – Conductivity Tests

In principle, the PPyP developed in Dr. Ni's work offered improved electric contact over that of metallic foils as a current collector, owing to the porosity of the cellulose, but remained at a severe disadvantage in terms of electric conductivity due to the inherently poorer conductivity of organic polymers as compared to metals.[84] In order to obtain better conductivities, multiple same-mass batches of virgin pulp were mixed using incrementally higher amounts of AQSA, pyrrole, iron chloride ($FeCl_3$), and ice in the pulp making process in order to prepare PPyP with higher PPy loadings. The resulting PPyP handsheets were clamped in a custom-made surface conductivity testing apparatus and their electrical resistivities were recorded.

Table 2.1: Measured resistivities for 5 by 5 cm sheets of PPyP, produced from pulps with varying reagent content. All compositions used 10 grams of virgin white pulp and 40 mL of water.

Handsheet composition	Resistivity (Ω)	Mass (g)	(Ω·g)
Basic recipe	2105	0.159	334
Double recipe (2x all reagents)	240	0.154	37.0
4x all reagents	760	0.141	107
6x all reagents	162	0.182	29.5
8x all reagents	69.4	0.162	11.2
10x all reagents	259.5	0.149	38.7

As shown in Table 2.1, increasing the reagents in double, quadruple, etc. quantities generally produced less resistive batches of PPyP, with the highest conductivity increase having occurred with the initial doubling of reagents compared to the original recipe batch. The 4x and 10x recipes were outliers to the general trend of increasing conductivities, with their unexpectedly high resistivities being ascribed to a lack of control over the homogeneity of the pulp when mixing and pressing, an experimental factor which is reported to play an important role in the resulting conductivity of the PPyP.[85] It is also worth noting that the higher the reagent quantities used, the more fragile the handsheets became, with the 8x and 10x reagent recipes producing sheets of paper that were too fragile to use in batteries. It was concluded that the "double recipe" PPyP was satisfactory for use in batteries in terms of conductivity and robustness, and so this composition was used in all further testing.

2.2.2 – Coating the Current Collector Substrates

Two methods were used for coating the current collectors with the $LiFePO_4$ electrode composite in a way that would allow for the precise determination of the mass of the $LiFePO_4$ loadings. Generally, the current collector substrates (conductive paper or aluminum foil) were coated with a N-methyl-2-pyrrolidone (NMP) -based slurry which contained $LifePO_4$, polyvinylidene fluoride polymer binder (PVDF) and conductive carbon black. These substrates could be used as cathode disks in button cells after drying.

Aluminum-based cathode disks were produced via thin-film deposition of a 5 mm-thick coating of electrode casting slurry on 15 micron-thick aluminum sheets using an applicator, with the sheets then being air-dried for 48 hours before being cut into disks of 1.50 cm diameter. The mass of the aluminum in each electrode disk m_{Al} (mg) was determined indirectly as the calculated product of the thickness h (mm), radius r (mm), and the density d (2.70 mg/mm^3) of the aluminum in the dry, cut cathode disks:

$$m_{Al} = \pi \text{ x } r^2 \text{ x } h \text{ x } d \qquad (\mathbf{2.2 - 1})$$

The $LiFePO_4$ loading m_{active} was determined by subtracting the mass of the bare aluminum from the total mass m_{total}, the latter being measured immediately before cell assembly. The result was then multiplied by the expected $LiFePO_4$ mass ratio in the coating, according to the reagent masses used in making the original slurry:

$$m_{active} = (m_{total} - m_{Al}) \; x \; R_{LiFePO4} \qquad (\mathbf{2.2 - 2})$$

with the $LiFePO_4$ content ratio $R_{LiFePO4}$ being determined from

$$R_{LiFePO4} = [m_{LiFePO4} / (m_{LiFePO4} + m_{PVDF} + m_{graphite})] \qquad (\mathbf{2.2 - 3})$$

with $m_{LiFePO4}$, m_{PVDF}, and $m_{graphite}$ being the masses of $LiFePO_4$, PVDF, and graphite used in making the NMP-based slurry, respectively.

In the case of the PPyP, thin-film application was impractical due to the variable thickness and density of the PPyP throughout the handsheets, and so we could not use an equation analogous to Equation 2.2 – 2 to assess the mass of bare PPyP cathode disks cut from coated PPyP sheets. Furthermore, obtaining a reliable dry mass m_{total} for each PPyP disk was experimentally difficult. The aforementioned heat-sensitivity barred the usage of heat-drying techniques to completely eliminate NMP, and instead prompted the use of

room-temperature air-drying and vacuum-drying. Neither of these drying techniques could ensure the complete removal of NMP in the coated electrode disks, which was concerning because any residual NMP would have lead to overestimation of the amount of $LiFePO_4$ in the PPyP cathode disks. In addition, the moisture level in the PPyP was subject to variation under vacuum. An undeterminable amount of water was lost when drying the electrodes *in vacuo* and also when bringing the dry coated PPyP electrodes into the glovebox as this required several evacuate-and-refill cycles.

In order to avoid these issues, drop-wise deposition of wet slurry was used for coating pre-weighed 1.50 cm diameter PPyP disks along with 4-5 pre-weighed dummy aluminum disks. Using an Eppendorf pipette, approximately 60 microliters of the slurry was applied to PPyP and aluminum disks directly on a balance so their masses could be recorded quickly to avoid measurement errors from losses in NMP to evaporation. The aluminum disks were then completely dried in an oven before being reweighed, and the averaged difference in mass of the coated aluminum disks before and after drying was used for the estimation of the mass of the coatings deposited on the PPyP using the following equation:

$$m_{active} = (m_{wetPa} - m_{barePa}) \text{ x } R_{LiFePO4} \text{ x } R_{dry} \qquad (\mathbf{2.2-4})$$

where m_{wetPa} is the mass of the freshly coated PPyP, m_{barePa} is the mass of the PPyP before coating, and the mean ratio R_{dry} is:

$$R_{dry} = \sum_{i=1}^{n} \frac{\left[\left(m_{i\,dryAl} - m_{i\,bareAl}\right)/\left(m_{i\,wetAl} - m_{i\,bareAl}\right)\right]}{n} \qquad (\mathbf{2.2-5})$$

in which $m_{i\,dryAl}$, $m_{i\,bareAl}$, and $m_{i\,wetAl}$ are the masses of the i^{th} dry coated, bare un-coated,

and freshly coated aluminum disks, respectively. The relative standard deviation of the mean R_{dry} was below 5.0 parts per thousand for the average batch of electrodes coated this way, and so this method was deemed precise enough for the purposes of determining the $LiFePO_4$ loadings of the PPyP electrodes.

The thin-film deposition method could only be used on aluminum substrate sheets, whereas the drop-wise method could be used on either sheets or pre-cut disks of either aluminum or PPyP. However, the drop-wise method produced composite coatings of noticeably lowered durability on aluminum disks compared to their thin-film coated counterparts, leading to extreme cracking and chipping.

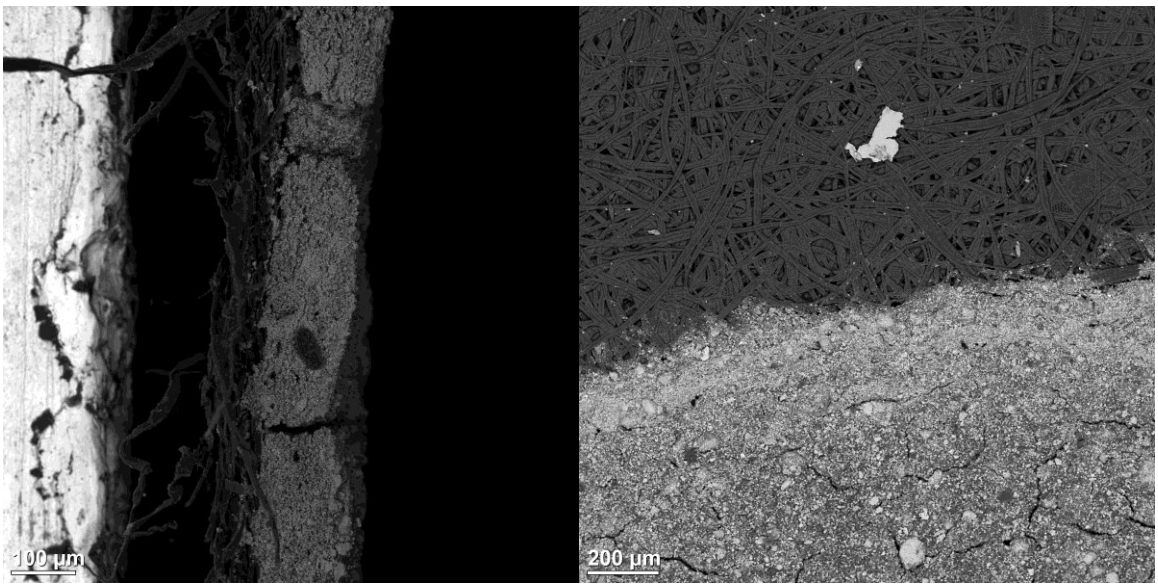


Figure 2.1: Backscattered electron micrographs of drop-coated paper electrodes. Left (a); the side-view of a cross-cut electrode. Right (b); an overhead surface view of the same electrode at the edge of the coating.

In contrast, the drop-applied composite coatings on PPyP were very durable and did not crumble or chip even when the PPyP disks were bent, despite the cracks. In order to determine the cause of this robustness, a coated PPyP electrode disk was cut in half and studied with scanning backscattered electron (BSE) micrography, wherein the dense $LiFePO_4$ composite appeared white while the lightweight paper fibers appeared dark (Figure 2.1). Figure 2.1a showed a single large conductive PPyP fiber woven into the coating (near the bottom of the image), which made the idea of structural support from interwoven fibres a possibility. Figure 2.1b was taken at the edge of the coating where thinner parts of the $LiFePO_4$ coating were adhering to the paper fibers, suggesting that the robustness of the coatings could also be attributed to enhanced adhesion with the paper fibres.

Assembly of the electrode disks into lithium cells was conducted in a bottom-up assemblage method. The assembly process for cells featuring both PPyP and aluminium – based cathodes is depicted in Figures 2.2a and b, respectively (*vide infra*). A thick lithium disk was used as the anode. Cells were assembled using one of two different salts in the electrolyte: lithium hexafluorophosohate ($LiPF_6$) or bis-(trifluoromethylsulfonyl)imide (LiTFSI). Cells bearing $LiPF_6$ electrolyte were tested at rates of *C*/2, 1*C*, and 2*C*, while the cells that contained LiTFSI electrolyte were tested at 1*C*. In total, eight cell test series were explored, divided by the type of current collector, electrolyte salt, and *C* rate that were used, in an attempt to elucidate under which conditions the paper was comparable or better than aluminum. Henceforth, current collector will be abbreviated as CC.

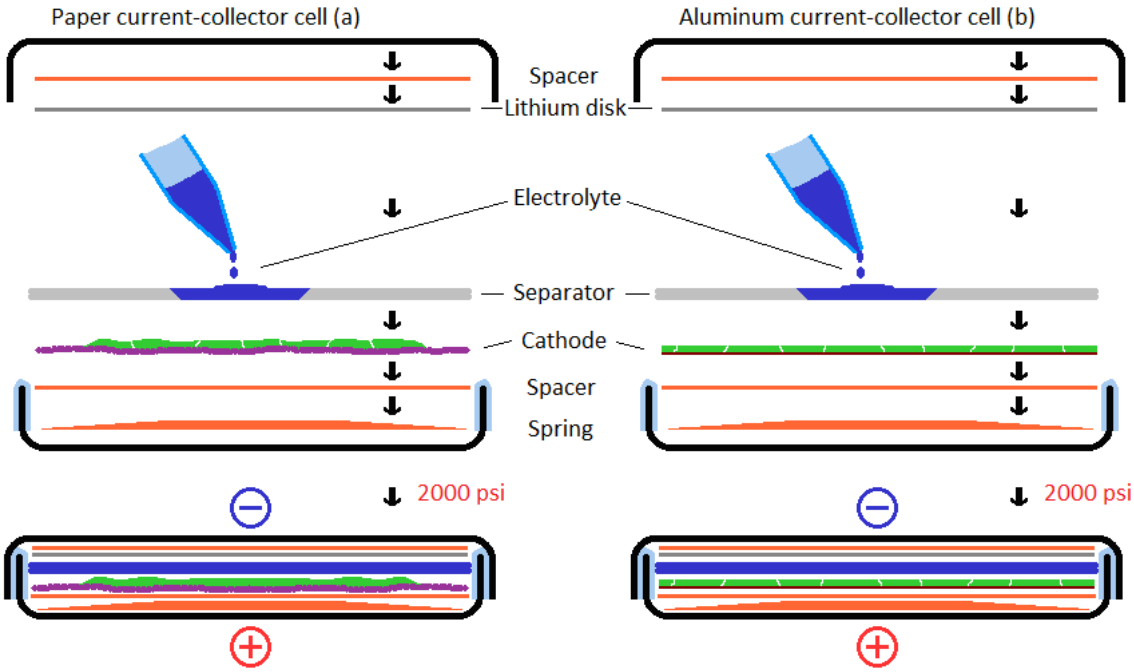


Figure 2.2: Button cell assembly diagrams for a PPyP current-collector cell on the left (a) and an aluminum current-collector cell on the right (b). All components are assembled in bottom-up fashion. The bottom cap has a gasket-lined rim which forms the seal when the cell is crimped with 2000 psi pressure.

2.2.3 – Cell Cycling Tests

As a preliminary test, the two kinds of coated CC were cycled in lithium cells using lithium hexafluorophosphate salt in the electrolyte. Lithium hexafluorophosphate is a well-explored electrolyte that is commonly used in both commercial and research cells based on lithium-ion technology[15,86] owing to its inertness with respect to Li-ion cell electrodes[42,87] and high ionic conductivity when dissolved in organic solvents.[88]

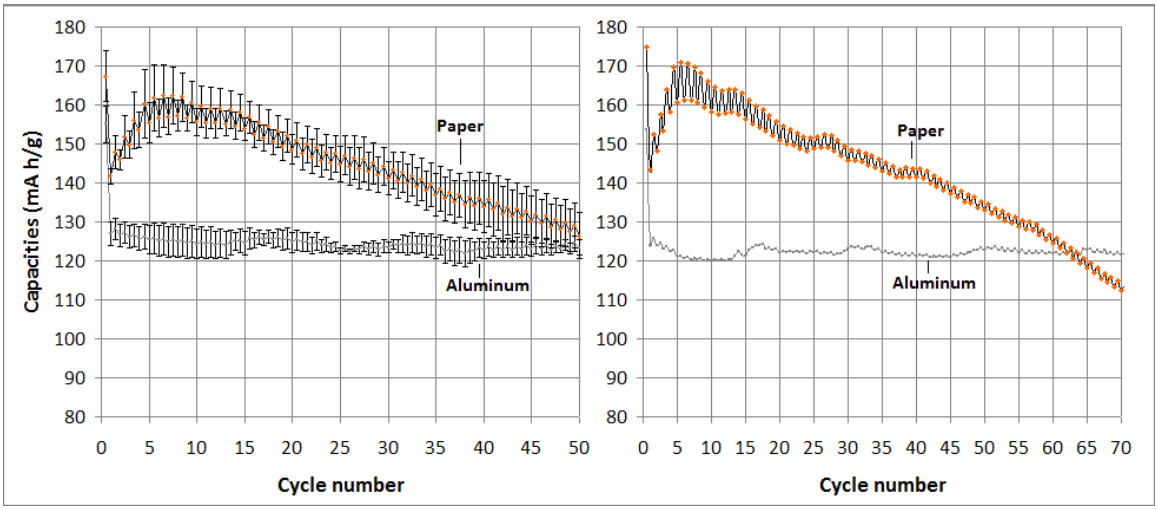


Figure 2.3: Representations of the capacities of charge and discharge half-cycles versus cycle number for cells which used $LiPF_6$ electrolyte, cycled at a rate of 1*C*. The orange series were cells that used paper CC, while the grey series used aluminum CC. Every 0.5 cycle number is a charge, while every whole unit cycle is a discharge. Left (a); average charge and discharge capacities with ±1σ error bars for 3 cells from both cell series over 50 cycles. Right (b); best cells from both series.

Aluminum CC cells exhibited good cycle stability over 70 cycles along with discharge capacities between 120 and 125 mA·h/g (Figure 2.3). In contrast, PPyP CC cells exhibited an initial steep increase in capacities, up to 170 and 160 mA·h/g for charge and discharge half-cycles, respectively, followed by rapid deterioration of 0.8 mA·h/g per cycle after the 25^{th} cycle. This general behavior was reproduced in three PPyP CC cells and resulted in an increase in discharge half-cycle capacities of as much as 28% higher for PPyP CC cells as compared to aluminum CC cells

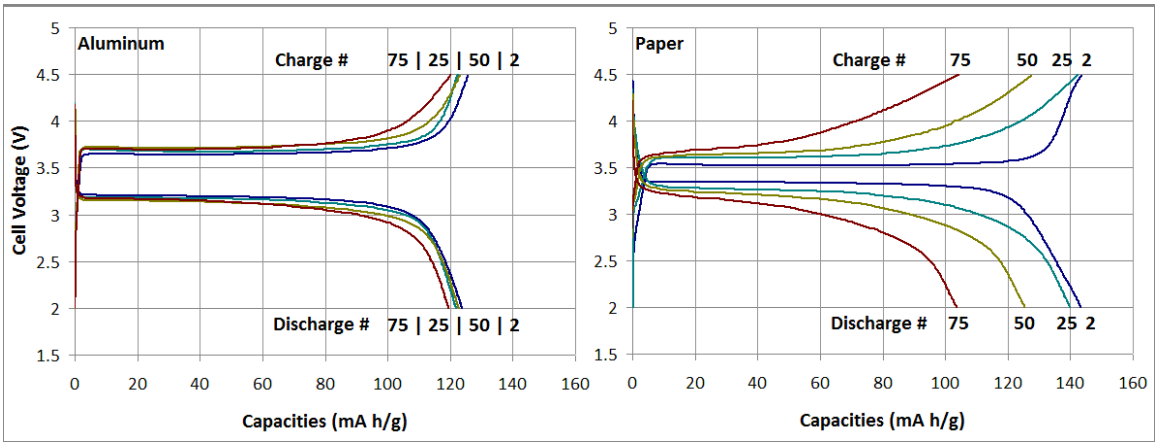


Figure 2.4: Charge-discharge half-cycle profiles for best cells using $LiPF_6$ electrolyte from aluminum CC series on the left (a) and PPyP CC series on the right (b).

The individual charge and discharge half-cycles of the best aluminum and PPyP CC cells, seen in Figure 2.4a and b respectively, showed that the PPyP's superior gravimetric capacity during the first cycles was attributed to a narrower potential difference between the charge and discharge profiles (i.e. better voltage efficiency), which suggested that PPyP suffered lower IR losses compared to aluminum. Superior voltage efficiency meant that the PPyP CC cells could be charged or discharged for longer periods of time before reaching the cutoff potential, leading to higher capacities for the PPyP CC cells over the first 25 cycles.

However, the next 50 cycles were mired with rapid deterioration in capacity accompanied by decreasing voltage efficiency over time for PPyP CC cells. The potential difference between the flattest parts of the charge-discharge half-cycle plateaus increased from 0.20 V between the 2^{nd} charge and discharge half-cycles to 0.75 V at the 75^{th} cycle for a total increase of 0.55 V (+275%) in the PPyP cell. The aluminum CC cell had a

potential difference of 0.44 V for the 2nd cycle, but this difference only increased to 0.51 V at the 75th cycle, for a total increase of only 0.06 V (+14%). This dramatic increase in voltage difference between the charge and discharge plateaus was indicative of rapidly increasing internal cell resistance in PPyP CC cells.



Figure 2.5: Illustrations of PPyP CC (black) with $LiFePO^4$ coating (green with lime filling) before cycling on the left (a) and after several cycles on the right (b). For representation purposes, gradual loss in the electrical conductivity of the PPyP fibres is shown as black → brown → orange → red.

Another form of deterioration seen in PPyP CC cells was the increasing/decreasing slope in the tail-end of the half-cycle profiles. This sloping of the profile was highly reminiscent of charge polarization. A possible cause could be heterogeneous losses of electrical conductivity in the PPyP fibers, as illustrated in Figure 2.5.

Further experiments were performed in order to shed more light on these deteriorations in the PPyP CC cells' performances. Additional aluminum and PPyP CC cells were fabricated using $LiPF_6$ as the electrolyte. Some were cycled at a faster rate of 2*C* while others were cycled at a slower rate of *C*/2.

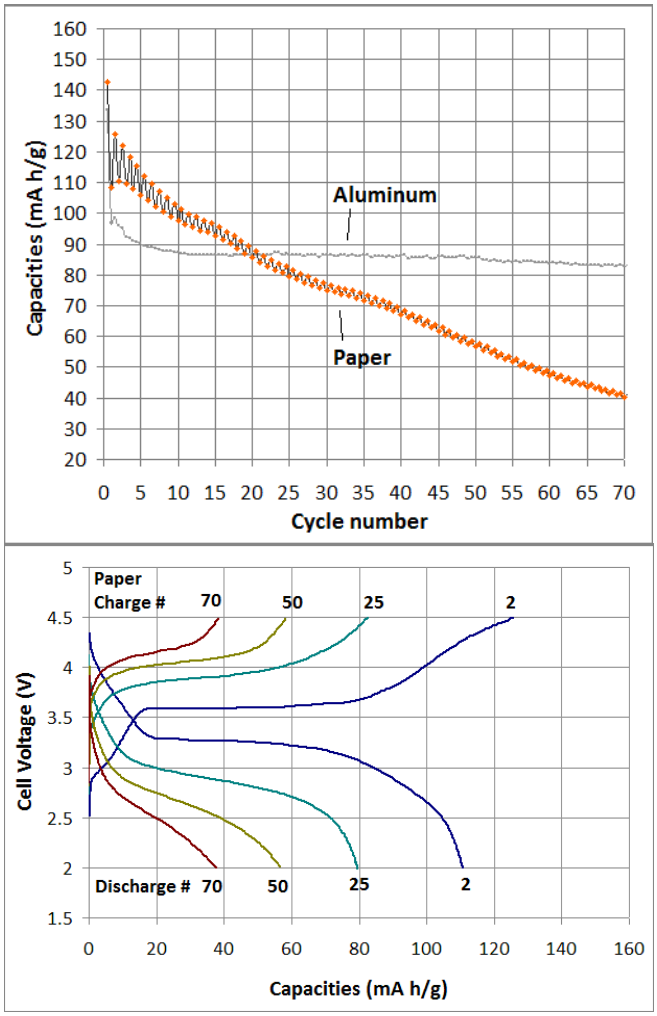


Figure 2.6: Top (a); capacity graph for an aluminum CC and a PPyP CC cells. Bottom (b); the cycling profile graph of the PPyP CC cell. Both cells were cycled at 2*C*.

At 2*C* current rates, the PPyP CC cells outperformed aluminum CC cells in terms of gravimetric capacity for only 15-20 cycles, as seen in Figure 2.6a. The highest discharge capacity for this PPyP cell was 110 mA·h/g on the 2nd cycle, with a steady degradation rate of approximately 1.0 mA·h/g thereafter. In contrast, the aluminum CC cell cycled at 2*C* suffered from a much slower degradation rate in its capacity and lost a mere 0.06 mA·h/g per cycle from the 10th cycle to the 70th cycle. The cycling profile of the PPyP CC cell (Figure 2.6b) revealed a severe increase in potential difference between the

charge and discharge half-cycles as the number of cycles increased, from 0.30 V for the 2nd cycle to 1.35 V for the 70th cycle (+350%). What's more, the slopes of the profiles increased more rapidly in the PPyP CC cell at 2*C* as compared to the PPyP cell at 1*C*, which demonstrated the negative effects of increased resistance (resulting from higher current rates) on charge polarization.

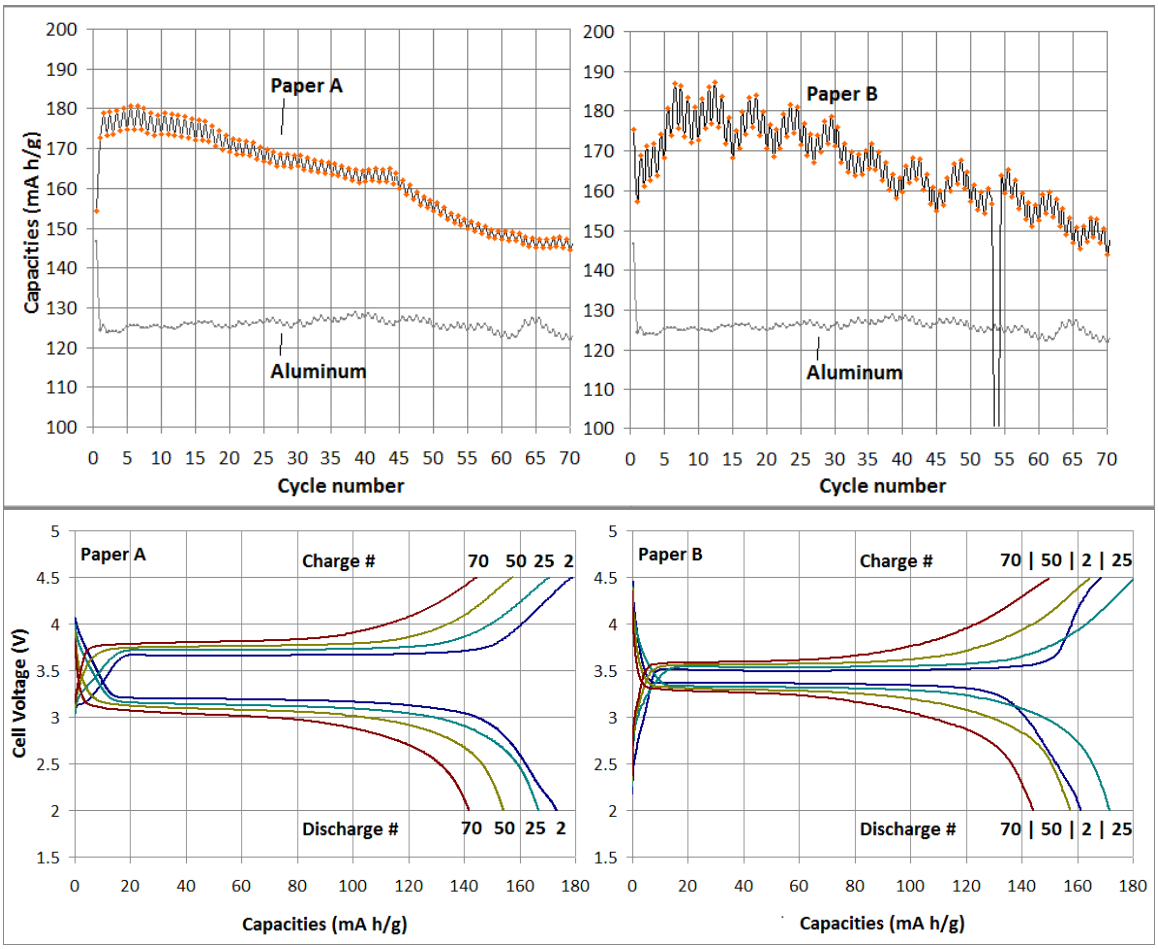


Figure 2.7: Capacity vs. cycle number graphs on the top (a) and corresponding cycling profiles on the bottom (b) for two different PPyP CC cells cycled at *C*/2, assembled within the same week, and tested on two different Keithley 2400 sourcemeters. The capacity graphs also contained an aluminum CC cell cycled at *C*/2 for comparison.

The PPyP CC cell *C*/2 runs produced mixed results in terms of stable capacity (Figure 2.7a) and cycling profile (Figure 2.7b). While Paper A (left) produced a straight-line trend in terms of capacity, its cycling profile yielded a much greater potential difference compared to 1*C* PPyP runs despite the lower current, which may have been attributed to some experimental flaw in cell assembly that resulted in much higher-than-usual internal resistance. Paper B (right) produced a saw-tooth trend in capacity, which was later determined to be caused by a defect in the instrument. Despite this issue, Paper B had a normal cycling profile showing the expected higher voltage efficiency than the 1*C* paper CC cells. For comparison purposes, the capacity trend of Paper A and cycling profile of Paper B were used to represent a problem-less PPyP cell cycled at *C*/2.

The PPyP CC cells outperformed the aluminum CC cell in terms of capacity at *C*/2, but again this only held true for a limited number of cycles. The degradation in capacity was still present but at a much-reduced rate of 0.5 mA·h/g after the 25th cycle for PPyP CC cells, which was a little more than half the rate of degradation found in PPyP CC cells cycled at 1*C*. Furthermore, the cycling profile of Paper B showed narrower potential difference between charge and discharge half-cycles and smaller increases in potential difference with subsequent cycling compared to 1*C* PPyP CC cells, with a potential difference of 0.14 V for the 2nd cycle's plateaus versus 0.20 V at 1*C*, increasing to 0.34 V at the 70th cycle versus 0.51 V at the 75th cycle at 1*C* (+143% at *C*/2 versus +275% at 1*C*). The slower loss of capacity, better voltage efficiency, and less severe sloping of the profiles over longer periods of time hinted that the degradation of the PPyP

CC cells was current-dependant rather than time-dependant, with the greater currents used at higher *C* rates leading to an acceleration of the degradation seen in these cells.

Another difference from the previous 1*C* runs was that the PPyP CC cells cycled at *C*/2 demonstrated both charge and discharge half-cycle capacities that were higher than $LiFePO_4$'s theoretical capacity (170 mA·h/g), with peak capacities of 181 mA·h/g for the 6^{th} charge and 175 mA·h/g for the 5^{th} discharge half-cycles. This extra capacity could have been caused by a poorly-reversible redox reaction involving the polypyrrole in the PPyP CC cells. The redox mechanism of polypyrrole is well-explored with its complete reduction taking place at -0.8 V vs. SCE (~ +2.4 V vs. lithium) and complete oxidation taking place at +0.4 V vs. SCE (~ +3.6 V vs. lithium) in PPy films.[89] As mentioned in Section 2.2, PPy is not electrically conductive in the reduced state and most of the change in electrical conductivity is reported to occur between -0.2 and +0.2 V vs. SCE (~ +3.0 to +3.4 V vs. lithium).[89] Furthermore, PPy is reportedly prone to permanent degradation of its electrical conductivity upon being fully-reduced[82] due to a combination of electrical and electrochemical changes that occur in the PPy in this state,[90] and as such discharging cells to a 2.0 V cutoff point may have led to permanent losses in the electrical conductivity of the PPyP CC. It was subsequently hypothesized that increasing the discharge cutoff voltage from 2.0 to 3.0 V might mitigate this degradation in the PPyP CC's electrical conductivity.

To test this, a PPyP CC cell was assembled using $LiPF_6$ electrolyte and cycled between 3.0-4.5 V.

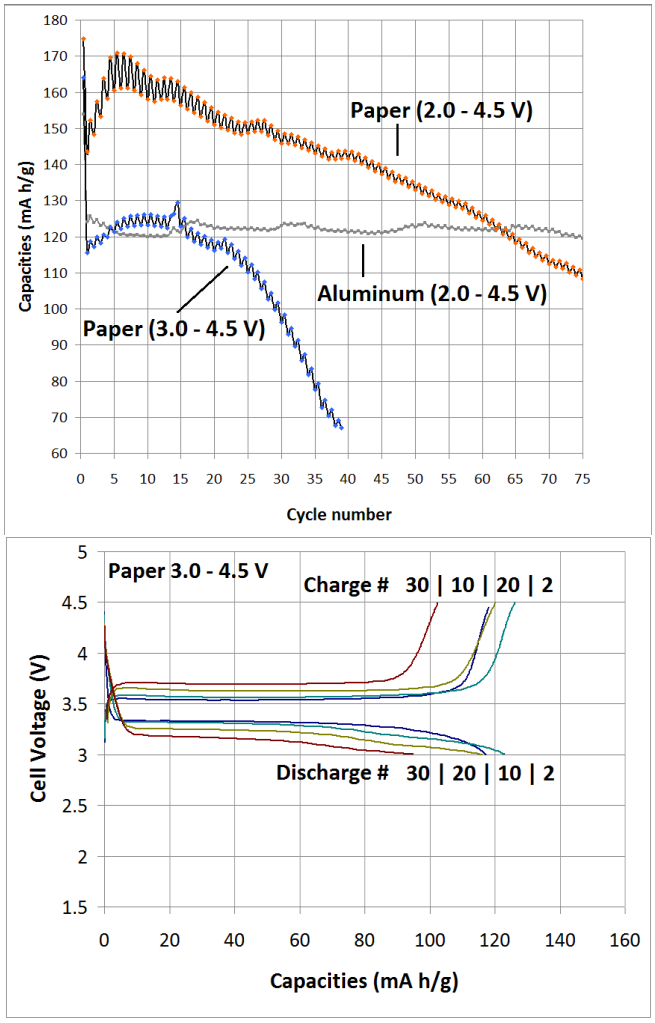


Figure 2.8: Top (a); capacity graph for previous aluminum CC (grey) and PPyP CC (orange) cell runs with 2.0-4.5 V cutoff points alongside an additional PPyP CC cell run with 3.0-4.5 V cutoff points (blue). Bottom (b); the cycling profile graph (bottom) of the PPyP CC cell run with 3.0-4.5 V cutoff points. All cells were cycled at 1*C*.

The PPyP CC cell attained much lower charge and discharge capacities of 126 and 123 mA·h/g when cycled between 3.0-4.5 V (Figure 2.8a) when compared to the previous PPyP CC cell cycled between 2.0-4.5 V which had charge and discharge capacities of 170 and 160 mA·h/g, respectively. Cycling the PPyP CC cell between 3.0 and 4.5 V also increased the rate of capacity loss to 2.3 mA·h/g between cycles 20 and 39, versus 0.8 mA·h/g between cycles 25 and 75 for PPyP CC cycled between 2.0-4.5 V.

The cause of the deterioration of capacity appeared to be due to the rapid increase in voltage difference between charge and discharge half-cycles (Figure 2.8b) with an initial difference of 0.20 V for the 2nd cycle which increased to 0.52 V for the 30th cycle for a total increase of 0.32 V (+160%). Despite the rapid loss in capacity with cycling, the profile of the 3.0-4.5 V PPyP CC cell maintained the same general shape and slope over the first 30 cycles. This was consistent with the previous hypothesis of PPy suffering from heterogeneous losses in electrical conductivity, specifically in PPyP CC cells that are discharged too deeply.

The increase in potential difference between charge and discharge half-cycles over time at all *C* rates was also a serious concern for applications of the PPyP in practical Li-ion batteries and was thought to be caused by depletion of the $LiPF_6$ electrolyte. It was possible that corrosive hydrofluoric acid (HF) was being formed via the reaction of dissolved $LiPF_6$ with dissolved water in the electrolyte solvent,[91] with the water in question coming from the PPyP CC which could not be completely dried. When dissolved in organic solvents such as the ethylene carbonate and diethyl carbonate solvent mixture used in our cells, $LiPF_6$ partially dissociates into lithium fluoride (LiF) and phosphorous pentafluoride (PF_5).[92] Once formed, the PF_5 can react with moisture present in the organic solvent to form HF and phosphoryl fluoride (POF_3):[91]

$LiPF_6 \rightarrow LiF + PF_5$

$PF_5 + H_2O \rightarrow POF_3 + 2\ HF$

This HF-forming process, if it was occurring, would be highly problematic. In addition to being corrosive towards both the active electrode materials[93] and inactive components[94] inside the cells, HF formation comes at the expense of the $LiPF_6$ salt. The reduction in total $LiPF_6$ concentration could lead to a rising internal cell resistance, thus increasing IR losses and subsequently decreasing the voltage efficiency which was consistent with what was seen in the cycling profiles of PPyP CC cells at all *C* rates (refer to Figures 2.4, 2.6b, and 2.7b). Furthermore, the formation of HF was reported to be accelerated at higher temperatures[95] from such effects as joule heating at higher current rates,[96] which agreed with the faster degradation found in PPyP CC cells cycled at higher *C* rates.

If HF formation was indeed occurring due to the use of $LiPF_6$ as the electrolyte salt, it could be mitigated in the PPyP CC cells by simply using a different salt. Lithium bis(trifluoromethanesulfonyl)imide, often abbreviated as LiTFSI, is stable towards moisture in organic solvents[92] and is often used independently or in combination with other salts as the electrolyte in order to produce batteries with extended cycle durability.[97] Thus, some aluminum CC and PPyP CC cells were assembled using LiTFSI electrolyte solution instead of $LiPF_6$ and cycled at rates of 1*C*.

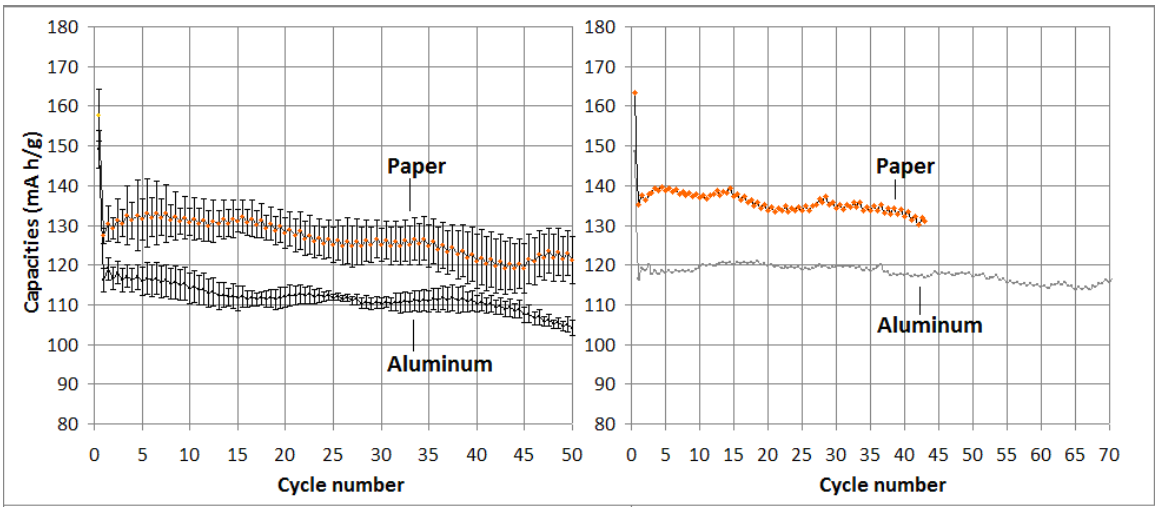


Figure 2.9: Representations of the capacities of charge and discharge half-cycles for cells which used LiTFSI electrolyte, cycled at a rate of 1*C*. Left (a); average charge and discharge capacities with ±1σ error bars for 7 cells from the aluminum CC cell series and 5 cells from the PPyP CC cell series over 50 cycles. Right (b); best cells from both series.

Both the PPyP and aluminum CC cells achieved inferior capacities overall with LiTFSI at 1*C* than they did with $LiPF_6$ (Figure 2.9), a consequence of the lower ionic conductivity of the LiTFSI electrolyte.[98] The average PPyP CC cell using LiTFSI suffered from capacity degradation of 0.2 mA·h/g per cycle, which was 1/4th the rate of degradation found with similar cells using $LiPF_6$ cycled at 1*C*. Aluminum CC cells also suffered from degradation in capacity of 0.2 mA·h/g on average. The PPyP still outperformed aluminum with peak discharge capacities of 138 mA·h/g for the best PPyP CC cell compared to 120 mA·h/g for the best aluminum CC cell, resulting in a capacity enhancement of 15% when using PPyP.

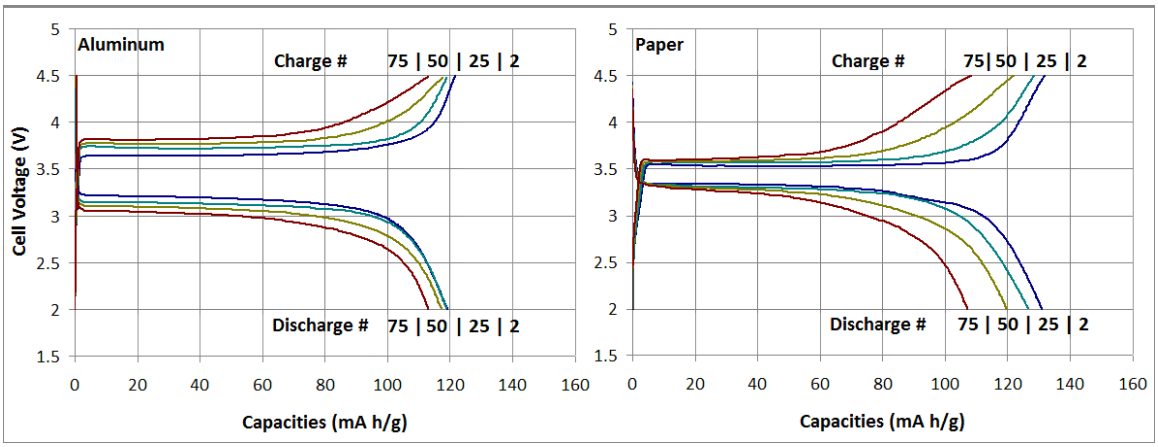


Figure 2.10: Charge-discharge half-cycle profiles of the first 75 cycles of an aluminum CC cell on the left (a) and of a PPyP CC cell on the right (b), using LiTFSI electrolyte.

The degradation of voltage efficiency with cycling increased drastically in aluminum CC cells using LiTFSI (Figure 2.10a), with the 2nd cycle carrying a potential difference of 0.44 V which increased to 0.91 V at the 75th cycle for a total increase of 0.47 V (+107%). This was prescribed to LiTFSI's reactivity with the pure aluminum CC,[99,100] which would cause electrolyte concentration depletion similar to what was postulated to be occurring in the PPyP CC cells using $LiPF_6$. In contrast, the PPyP CC cells using LiTFSI suffered a minimal decrease in voltage efficiency with cycle number (Figure 2.10b), with the 2nd cycle carrying a potential difference of 0.20 V which increased to only 0.30 V by the 75th cycle for a total increase of only 0.10 V (+50% when using LiTFSI versus +275% when using $LiPF_6$ in PPyP CC cells cycled at 1*C*). Although electrolyte depletion appeared to be somewhat remedied in PPyP CC cells when using LiTFSI, the cycling profiles still showed gradual change in profile slope towards the end of charge and discharge half-cycles as the number of cycles increased, indicating that the

PPyP CC was still suffering heterogeneous losses in electrical conductivity.

2.3 – Conclusions and Future Work

Polypyrrole-coated cellulose paper (PPyP) composites were optimized for superior electrical conductivities per unit mass and investigated as replacement cathode current collectors (CC) in lithium batteries. The performance of the PPyP CC was generally superior to that of conventional aluminum CC, with PPyP CC cells exhibiting better discharge capacities and narrower charge-discharge half-cycle potential differences compared to aluminum CC cells over a small number of cycles. As seen in Table 2.2 (*vide infra*), the PPyP CC cells achieved higher maximum discharge capacities, Q_{mDis}, compared to aluminum CC cells in all test series. However, the per-cycle losses in discharge capacities when using lithium hexafluorophosphate ($LiPF_6$) electrolyte were very severe for PPyP CC cells in addition to exhibiting severe losses in discharge/charge efficiencies ($\%\eta_E$). The capacity loss problem was somewhat resolved in PPyP CC cells by using more chemically-stable lithium bis-(trifluoromethanesulfonyl)imide (LiTFSI) electrolyte, which avoids the formation of corrosive hydrofluoric acid (HF). The discharge/charge efficiency $\%\eta_E$ was still observed to be decreasing at a steady rate even with the use of LiTFSI, however, with its cause being thought to be attributed to heterogeneous losses in electrical conductivity in the PPyP upon cycling.

Table 2.2: Tabulation of aluminum and PPyP CC cell test results, with Max Q_{mDis} being the maxium gravimetric charge capacity achieved during a discharge half-cycle, Q_{mDis} Loss being the per-cycle loss of gravimetric charge capacity in discharge half-cycles after the 25th cycle, and 2nd and 75th cycle η_E being the cell discharge/charge potential efficiencies of the 2nd and 75th cycle, respectively, with $E_{discharge}$ and E_{charge} sampled at half-cycle capacities of 40 mA·h/g.

Electrolyte and *C* rate	CC type	Max Q_{mDis} (mA·h/g)	Q_{mDis} Loss (mA·h/g)	2nd cycle $\%\eta_E$ (%)	75th cycle $\%\eta_E$ (%)
$LiPF_6$ 2C	Aluminum	96.7	0.1	76	68*
	PPyP	109.2	0.9	91	61*
$LiPF_6$ 1C	Aluminum	123.8	negligible	88	85
	PPyP	161.1	0.8	95	84
$LiPF_6$ C/2	Aluminum	127.1	negligible	77	86
	PPyP	174.7	0.5	97	87
LiTFSI 1C	Aluminum	120.9	0.2	88	79
	PPyP	138.8	0.1	95	90

(*) – E_{charge} and $E_{discharge}$ sampled at 20 mA·h/g

In future work, the decomposition of the $LiPF_6$ electrolyte in lithium batteries using PPyP could potentially be monitored via ^{19}F NMR, through which fluorine-containing decomposition products, such as HF, could be detected and measured.[101] The other decomposition mechanisms of batteries utilizing PPyP could be studied using electrochemical impedance spectroscopy, which can accurately detect and measure the internal resistance effects of batteries with minimal disturbance to the system.[102] In addition, the performance of the PPyP CC might be improved by better integrating the

active material into the meshwork, thereby increasing electrical contact between the PPyP and the active material. The PPyP could also be tested with other cathode materials and electrolytes in lithium ion batteries in order to further study its range of applications. One could also explore the viability of other conductive polymers in making conductive paper composites for use as current collectors,[103] with some polymers reportedly being more stable under battery cycling conditions compared to polypyrrole.[104]

2.4 – Preparation, Materials, and Characterization

Conductive polymer paper items: Pyrrole, 40% aqueous iron chloride, anthraquinone-2-sulfonic acid sodium salt (AQSA), and dry white cellulose pulp were supplied by Knowcharge, Inc (Fredericton, NB). The pyrrole was distilled prior to use, and kept refrigerated at -32^{o}C to limit decomposition.[105]

Battery items: $LiFePO_4$, polyvinylidene fluoride (PVDF) binder, lithium disks, and aluminium foil, and slurry applicator were purchased from MTIxtl. C2032 coin cell components were also obtained from MTIxtl. Super P Li grade conductive carbon black was obtained from TIMCAL. N-methylpirolidinone (NMP) was obtained from Alfa-Aesar. Lithium hexafluorophosphate ($LiPF_6$), lithium bis(trifluoromethanesulfonyl)imide (LiTFSI), ethylene carbonate (EC) and diethyl carbonate (DEC) were obtained from Novolyte. All chemicals and components were used as purchased.

The conductive paper composite synthesis was adopted from a patent.[106] Small scale batches were made using 10 grams of dry white pulp and 40 mL of tap water, mixed together using a hand-held electric egg beater in a 1000 mL beaker. A typical batch would also include the addition of 1.4 grams of AQSA, 1.2 grams pyrrole, and 16.5 grams of 40% $FeCl_3$, respectively, with each chemical being added to and mixed with the pulp and water in that order. Ice (14.0 g) was also added quickly after the addition of iron chloride. As the ingredients were mixed, the color of the pulp changed from dark orange due to the coloration of iron chloride, to dark green, and finally black. Mixing after addition of all chemicals was carried out for 5 to 10 minutes. The conductive paper pulp is then washed with tap water and pressed into handsheets at the Limerick Pulp and Paper Center at the University of New Brunswick in Fredericton, NB, Canada. The handsheets were dried in a humidity controlled room for at least 24 hours.

The $LiFePO_4$ slurry used to coat either aluminum CC or paper CC was 83% $LiFePO_4$, 7% PVDF binder, and 10% Super P Li carbon black, plus an amount of NMP. For coating aluminum, 2.25 mL of NMP was added for every 1 gram total of chemicals. For coating paper, 5 mL of NMP was added for every 1 gram of chemicals. In both cases, the slurry was thoroughly mixed for 30 minutes in a mortar with a pestle until the slurry became smooth and homogeneous.

All of the following procedures were conducted in a glovebox under argon atmosphere. Electrolyte solutions containing $LiPF_6$ and LiTFSI were prepared by dissolving the required amount of ethylene carbonate (solid below 36.4°C[107]) in diethyl

carbonate in a 1 : 0.75 mass ratio, which was then added to the required amount of salt to yield a 1 molar solution. The electrolytes were swirled prior to each use. C2032 coin cells were assembled in bottom-up fashion, using a current collector coated with $LiFePO_4$ as the cathode and lithium metal disks as the anode, with a 1.8 cm separator disk (purchased from MTIxtl) wet with 100-200 microliters of electrolyte sandwiched in-between the two electrodes. Cells were crimped with 2000 psi of pressure using a custom-made coin cell-crimper. The rims of the crimped cells were wiped dry with a kimwipe immediately after assembly to remove any excess electrolyte.

A single-channel Keithley 2400 sourcemeter and a 4-channel Arbin battery test station were used to cycle prepared cells. Cells were cycled in the same week they were crimped. The Keithley instrument was also used to perform two-point sheet resistivity measurements on 5 by 5 cm cut paper sheets, using a custom-made clamp holder for even distribution of electrical contact along the two opposing edges of the sheets. SEM and related microscopy of the paper and coatings were performed with the help of the Microscopy and Microanalysis group in the University of New Brunswick in Fredericton, NB, Canada, using a JEOL 6400 SEM instrument. No conductive coating was required for SEM, and the beam was set at 15 eV for all measurements.

Chapter 3 – Bis-pyridinium Salts With Enhanced Solubilities for Applications in Redox Flow Cells

3.1 – Introduction to Redox Flow Cells

Climate change continues to be an extremely complicated and threatening problem for modern civilization.[108] Climate change itself is attributed to the presence of greenhouse gasses in the Earth's atmosphere, such as CO_2 and methane, which "impede the outward flow of infrared radiation more effectively than they impede incoming solar radiation", causing a greenhouse effect.[109] As such, initiatives to replace fossil fuels and other CO_2 emission sources with carbon-neutral alternatives have grown intensely in our time.[110] In 2010, electricity and heat production accounted for 41.2% of the world's CO_2 emissions,[111] with electricity alone accounting for 12.8% of Canada's CO_2 emissions in 2011.[112] Of the potential energy sources for electrical generation, nuclear, hydroelectric, wind, solar, and geothermal are often cited as the best contenders for replacing coal and diesel in electricity production.[113] Natural gas acts as a bridge between more emissive fossil fuels and the minimally-emissive renewables and nuclear, acting as an economical alternative,[114,115] but supply uncertainties often lead to poor energy security when heavily relied upon.[116] While the impediments to using nuclear are largely political in nature,[117] and hydroelectric is dependent on the availability of strong water drainage,[118] the overwhelming obstacle in large-scale implementations of solar and wind renewables presents itself as a myriad of physical source-related restrictions which translate to higher

costs relative to using other energy sources.[119]

One key limitation of wind and solar, which urgently requires a solution, is their intermittent nature.[120] The electrical production of wind/solar plants is tied to the periodic availability of wind and sunlight, respectively. The variability of these energy sources causes the electrical output of wind/solar plants to be variable, which can lead to serious strain and damage on electrical grids.[121] It is theorized that this problem may become especially severe after a certain level of wind and solar incorporation in the grid[122] and so several remedial measures are already being investigated to resolve their intermittency. In a few instances, an entire retooling of the grid into "smart grids" has begun to take place, and while smart grids can help address the intermittent nature of renewables via a number of proactive measures not available with our current grids[123] such undertakings are proving to be daunting due to the shear magnitude of infrastructural changes required to implement them.[124]

A more rapid solution to both of these issues would be better storage of energy from these intermittent sources,[125] in which large thermoelectric, hydroelectric, or electrochemical energy storage facilities are used to store excess electrical capacity and subsequently release it on demand.[126] Among the electrochemical storage options, flow batteries stand out as a leading technology based on longevity and design flexibility to fulfill power plant load-leveling roles.[127] First patented in 1970 by Lawrence H. Thaller,[128] aqueous flow batteries have already begun seeing application as large-scale energy storage systems, especially for renewables.[129]

In flow batteries, the anodic and cathodic materials are dissolved in the electrolyte solutions rather than being incorporated in solid form in the cell's electrodes.[130] These catholyte and anolyte solutions[131] are stored in large tanks and pumped into a redox flow cell, where the electrochemical cycling processes take place. The cell chamber contains current-collecting electrodes, which are connected to an outside electrical circuit, and on which the reduction and oxidation of the electroactive species take place.

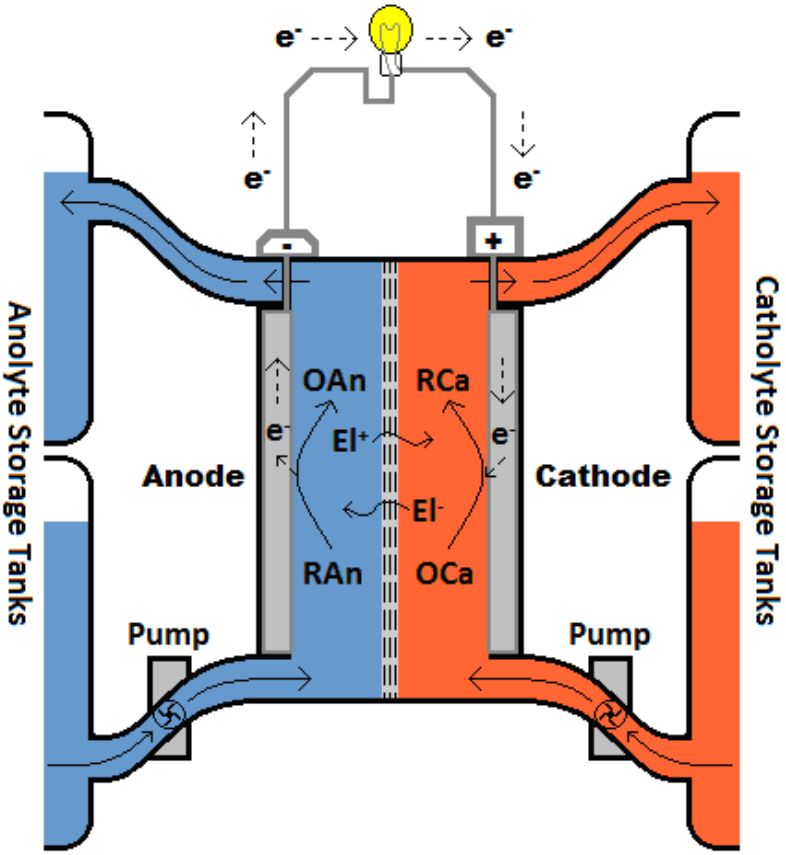


Figure 3.1: A flow cell during electrochemical discharge, with anolyte (blue) and catholyte (orange) solutions, separated by an ion-selective membrane (fuschia). RAn and OAn are the reduced and oxidized anolyte species, while RCa and OCa are the reduced and oxidized catholyte species, respectively. The exchangeable electrolytic ion species can be one of El^+ or El^-.

During the discharge process, as depicted in Figure 3.1, anolyte species in reduced state (RAn) are oxidized at the anodic current collector's surface to produce the oxidized species (OAn) and an electron. Simultaneously, catholyte species in oxidized state (OCa) are reduced in the cathodic chamber, consuming an electron and producing the reduced catholyte species (RCa). Within these redox flow cells, the dissolved cathodic and anodic species are kept separate by a membrane, which only allows the free passage of exchangeable electrolytic ions (El^+ or El^-) to balance the charge and complete the charge-transfer process when cycling the cell.

The separation of electroactive material storage from the cell modules makes flow batteries extremely flexible secondary energy systems. Unlike solid electrode cells, the storage capacity and current rate (or power) produced from flow batteries can be changed independently of each other.[132] The size of the storage tanks can be increased in order to increase the capacity of the system, while increasing the number of cell chambers, using bigger cells, and increasing flow rate will all lead to higher current rates from flow batteries with minimal dependence of the size of the storage tanks. Dissolving the electroactive materials in solution also eliminates solid-solid phase transitions, which mitigates much of the cycling wear-and-tear seen in other cell systems.[133]

For all their advantages, flow batteries are not without their set of challenges, especially in regards to cost.[134] While not important factors when considering stationary applications, maintaining low volume and weight remains paramount for energy systems destined for transportation and portable electric applications.[135] The high use of solvent in

flow batteries makes them heavy and bulky. Consequently, flow batteries have only achieved gravimetric capacities of up to 50 W·h/kg,[136] which is respectable, but still remains a far-cry from the ~100 W·h/kg capacities that are easily achievable in current lithium iron phosphate batteries.[137] This is further complicated by concerns over the operational temperature dependence of flow batteries, with these systems exhibiting greater problems than most other battery systems when operating outside ideal temperature ranges.[138] Still, flow batteries lend themselves well towards the eventual realization of a library of different electrochemical energy systems, each with a set of advantages that make them more suitable for specific tasks than the others. As such, the development of flow batteries has been primarily aimed at improvements for their use in stationary applications.

3.1.1 – Replacement of Metals in Flow Cells

One significant limitation of conventional flow batteries is their reliance on inorganic electroactive species, usually metal or metal oxide ions.[138] These inorganic species necessitate the use of water as the electrolyte solvent, with pure water having a fairly narrow thermodynamic stability window of 1.23 V.[139] Although the window of stability can be increased with the addition of solutes that help stabilize water, the resulting stability increases come with many other disadvantages.[140]

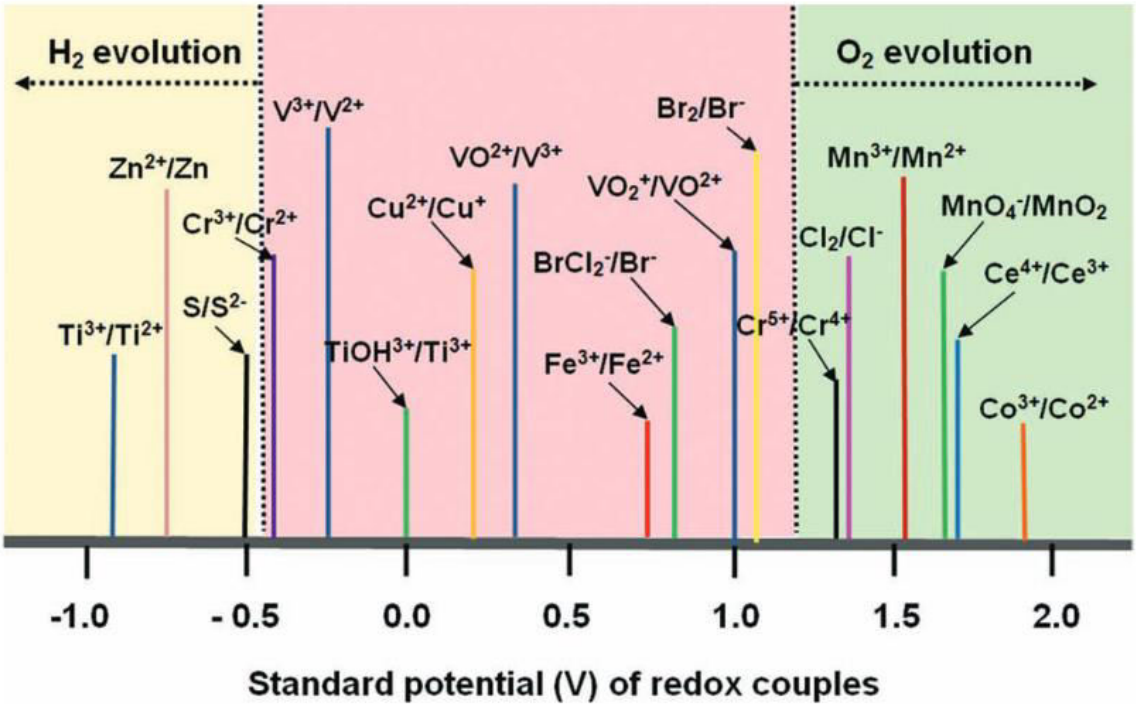


Figure 3.2: Standard potential scale with redox couples inside and outside of water's thermodynamic stability window. All potentials are listed versus SHE.[140]

The narrow stability window of water puts a hard cap on the cell potentials that can be achieved by flow batteries (Figure 3.2), effectively limiting the selection of catholyte and anolyte to species with relatively weak oxidizing and reducing potentials, respectively. Alternatively, organic solvents have much wider electrochemical potential windows than water (Figure 3.3, *vide infra*). The wider electrochemical stability of organic solvents allows for the use of organometallic complexes[142] or organic compounds[143] with redox potentials outside the potential stability window of water, thereby allowing the pairing of anodic and cathodic redox couples with more extreme redox potentials in order to yield batteries with higher cell potentials[144]

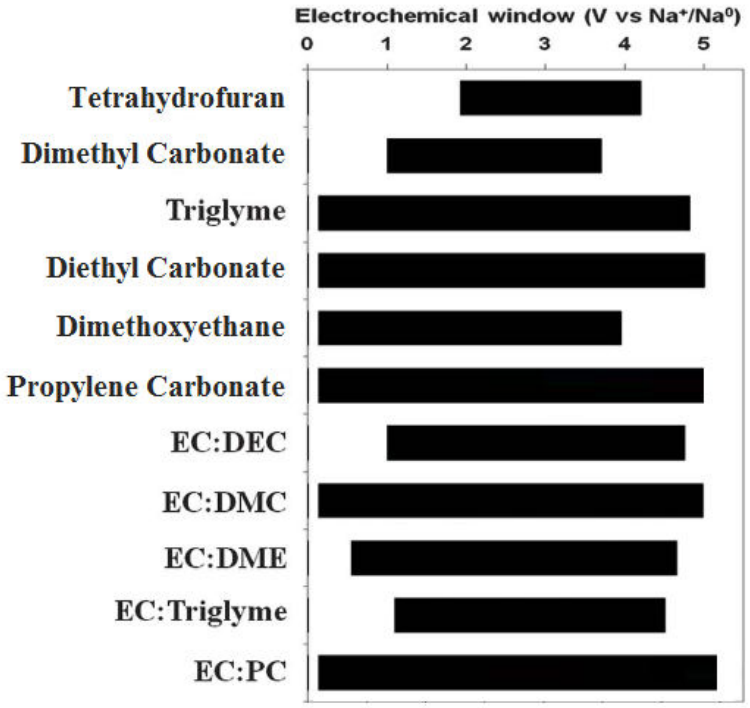


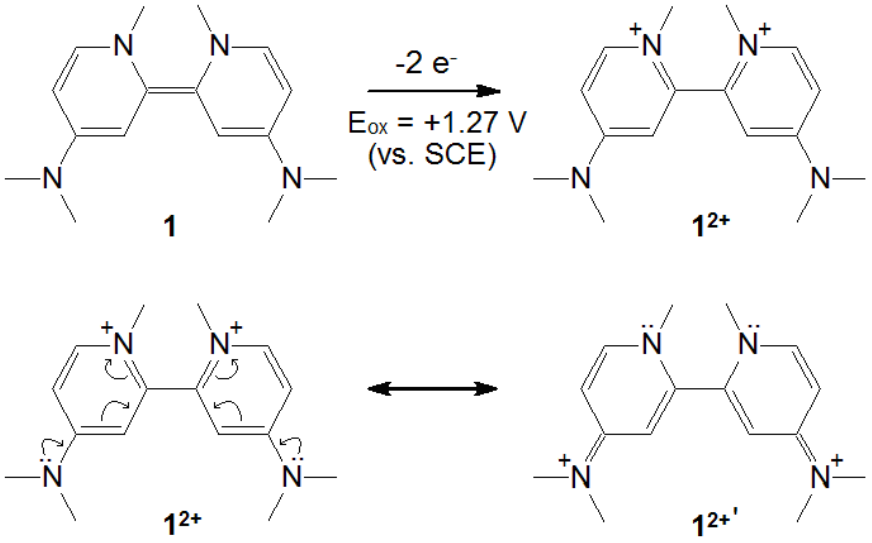
Figure 3.3: Electrochemical potential window stability (black bars and upper y axis) values of electrolyte solutions of 1 M $CaClO_4$ in various organic solvents and solvent mixtures of ethylene carbonate (EC), diethyl carbonate (DEC), dimethyl carbonate (DMC), dimethoxyethane (DME), and propylene carbonate (PC).[141]

Indeed, the vanadium acetylacetonate [$V(acac)_3$] flow batteries utilizing acetonitrile solvent are reportedly capable of achieving cell potentials of 2.2 V,[142] which is much higher than what is possible with aqueous solvents.

A notable disadvantage of using organic solvents instead of water comes from the increase in weight, volume, and cost. Current non-aqueous flow batteries frequently see the use of electroactive solute concentrations in the 0.01-0.2 molar range,[145] a far-cry from the > 1 molar solutions seen in aqueous flow batteries,[146] which forces the use of more solvent in organic flow-cells. The limitations in electroactive species concentration

are typically attributed to the poor solubility of either or both the organic anodic and cathodic species in their charged ion states.

The bis-pyridinylidenes, first characterized by John A. Murphy,[34] are examples of potentially excellent electroactive materials for organic flow batteries which are unfortunately limited in those applications due to solubility issues. Indeed, all-organic redox flow battery research conducted by Fahad M. Alkhayri had only achieved bis-pyridinium concentrations of ~0.04 M in the anodic electrolyte, which severely limited the energy density of the resulting flow battery.[147] Bis-pyridinylidenes are currently some of the strongest organic reducing agents reported in literature[148] and are consequently considered some of the strongest candidate anolytes for organic flow batteries.



Scheme 3.1: Top (a); the electrochemical oxidation of N,N-dimethyl-bis-2-(4-dimethylamino)pyridinylidene **1** to the corresponding bis-pyridinium dication $\mathbf{1}^{2+}$. Bottom (b); the resonance structures of the bis-pyridinium $\mathbf{1}^{2+}$.

In particular, N,N-dimethyl-bis-2-(4-dimethylamino)pyridinylidene **1** (Scheme 3.1a) is one of the strongest known organic reducing agents with an oxidation potential of +1.27 V vs. SCE in a single two-electron process.[149] The strength of **1** as a reducing agent is owed in large part to the resonance stability of its oxidized form, N,N-dimethyl-bis-2-(4-dimethylamino)pyridinium $\mathbf{1}^{2+}$, which is stabilized by aromaticity and by π-electron donation into the ring systems by the dimethylamino substituents which results in contribution of resonance structure $\mathbf{1}^{2+\prime}$ to the overall stability of the compound (Scheme 3.1b). Derivatives of **1** and $\mathbf{1}^{2+}$ are often abbreviated as bis-pyridinylidene and bis-pyridinium compounds, respectively.

The difficulties of using bis-pyridinylidenes such as **1** in organic flow batteries arise from the poor solubility of their oxidized state, $\mathbf{1}^{2+}$ in this case. Making bis-pyridinium salts more amphiphilic[150] could be one method of improving their solubility in non-polar media. Amphiphilic compounds, such as surfactants,[151] contain both polar and apolar characteristics that allow them to be dissolved in both low and high polarity solvents, with their solubility resulting in the formation of soluble micelles and reverse-micelles (Figures 3.4a and 3.4b, respectively, *vide infra*). Bis-pyridinium compounds are already highly-polar, so in order to make them amphiphilic one could synthetically attach to them non-polar groups, such as long alkyl chains.

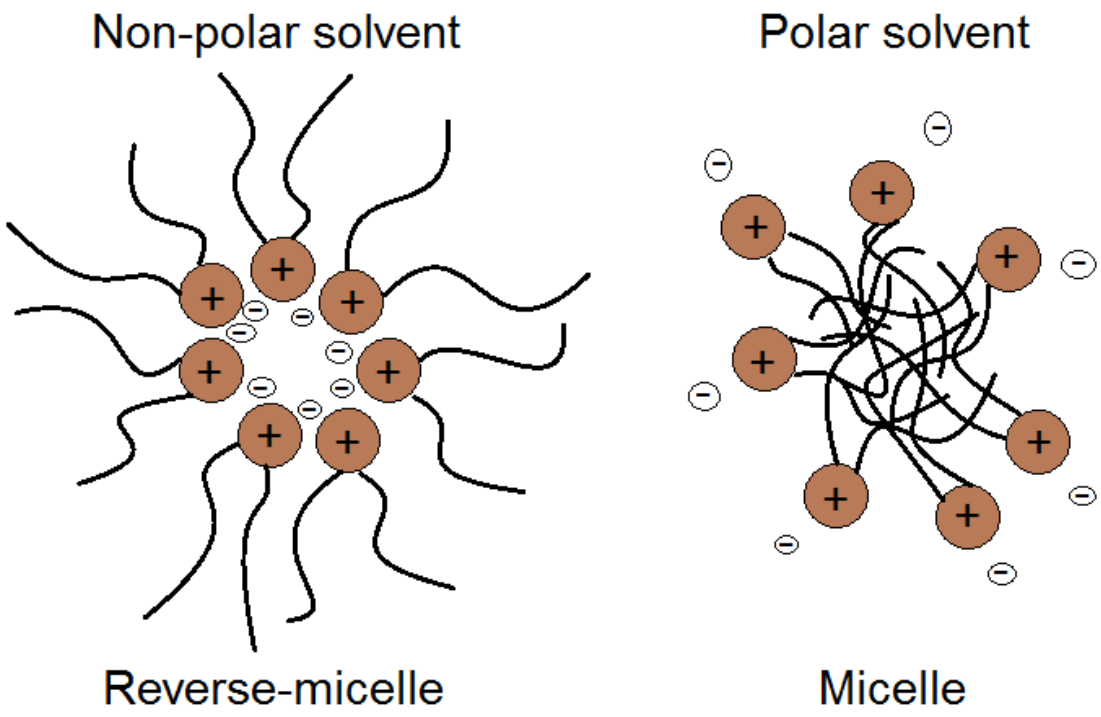
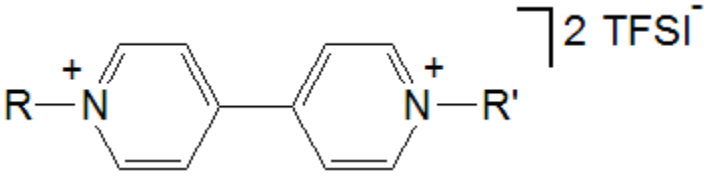


Figure 3.4: Left (a); surfactant molecules forming a reverse-micelle in a non-polar solvent. Right (b); surfactant molecules forming a micelle in a polar solvent.

Another possible method of improving the solubility of the bis-pyridinium salts could be to synthesize these compounds with alkyl substitutents of differing chain length on each pyridinium ring. The concept of "asymmetric" di-alkylated bis-pyridinium salts was inspired by a study on very similar organic compounds called viologens,[152] which were also di-alkylated dicationic salts with bipyridinium ring systems.



R,R'	$T_{C \rightarrow M}$
8,8	37.0°C
8,9	24.8°C
8,10	4.4°C
8,11	3.9°C
7,11	-0.4°C

Figure 3.5: Left (a); structure of the asymmetrically di-alkylated viologen salt. Right (b); table of chain lengths (R,R') and corresponding transition temperatures from a solid crystal phase to a liquid crystal phase.

The study found that viologens (Figure 3.5a) exhibited demonstrably lower transition temperatures to a liquid crystal phase when their alkyl chains were asymmetric in length, as compared to cases where their alkyl chains were more symmetric in length (Figure 3.5b). The association between symmetry and transition temperatures in these asymmetric viologens follow Carnelley's rule, which states that "high molecular symmetry is associated with high melting point".[153] In this case, the study moved in the opposite direction of Carnelley's rule by purposely introducing asymmetry to achieve viologens with lower transition points, which were more desirable for liquid crystal applications.

In terms of solubility, lowering the transition point of a compound typically does so by lowering the strength of the intermolecular forces that keep the compound in solid state,[154] with these same intermolecular forces playing a role in the solubility of the compound.[155] Indeed, theoretical studies have used the melting point of compounds in order to estimate their solubility in aqueous and non-aqueous media.[156] Asymmetric di-alkylated bis-pyridinium salts could therefore exhibit even higher solubilities than what

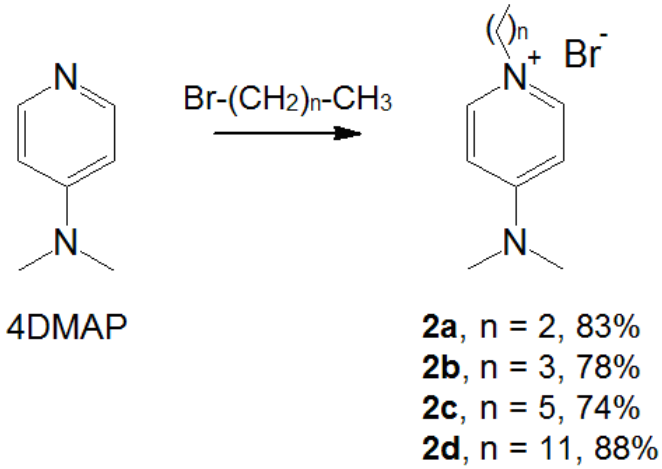
may be achieved in the symmetric bis-pyridinium salts by virtue of potentially having weaker lattice energies as a result of the asymmetry.

It was hoped that greater solubilities for the oxidized form of the resulting bis-pyridinylidenes could be achieved via either of these aforementioned methods, without adversely affecting the oxidation potentials of the bis-pyridinylidenes. If proven successful, similar synthetic alterations could be adapted to other organic anolytes or even catholytes in order to improve the solubility of their ionic forms in organic flow battery solvents.

3.2 – Results and Discussion

3.2.1 – Characteristics of the Pyridinium Bromide Precursors

The complete synthesis of symmetrical di-alkylated bis-pyridinium salts began with the synthesis of the N-alkyl-4-dimethylaminopyridinium bromide precursors.



Scheme 3.2: The synthesis of the N-alkyl-4-dimethylaminopyridinium bromide precursor salts **2a-d** with the accompanying final yields for each precursor.

Precursor salts **2a**, **2b**, **2c**, and **2d** were prepared (Scheme 3.2) via reactions of propylbromide (PrBr, n=2), butylbromide (BuBr, n=3), hexylbromide (HexBr, n=5), and dodecyl bromide (DodeBr, n=11), respectively, with 4-dimethylaminopyridine (4DMAP). The purity of **2a-d** was determined using ^{1}H and ^{13}C nuclear magnetic resonance (NMR) spectroscopy and melting point determination. The yields of the precursors ranged from 74-88% after recrystallization.

After purification, the precursor salts showed little or no traces of remaining 4DMAP, bromoalkane, or residual solvents, such as non-deuterated acetonitrile, ethanol, iso-propanol, diethyl ether, and water, in ^{1}H NMR in CD_3CN (Figure 3.6a, *vide infra*).

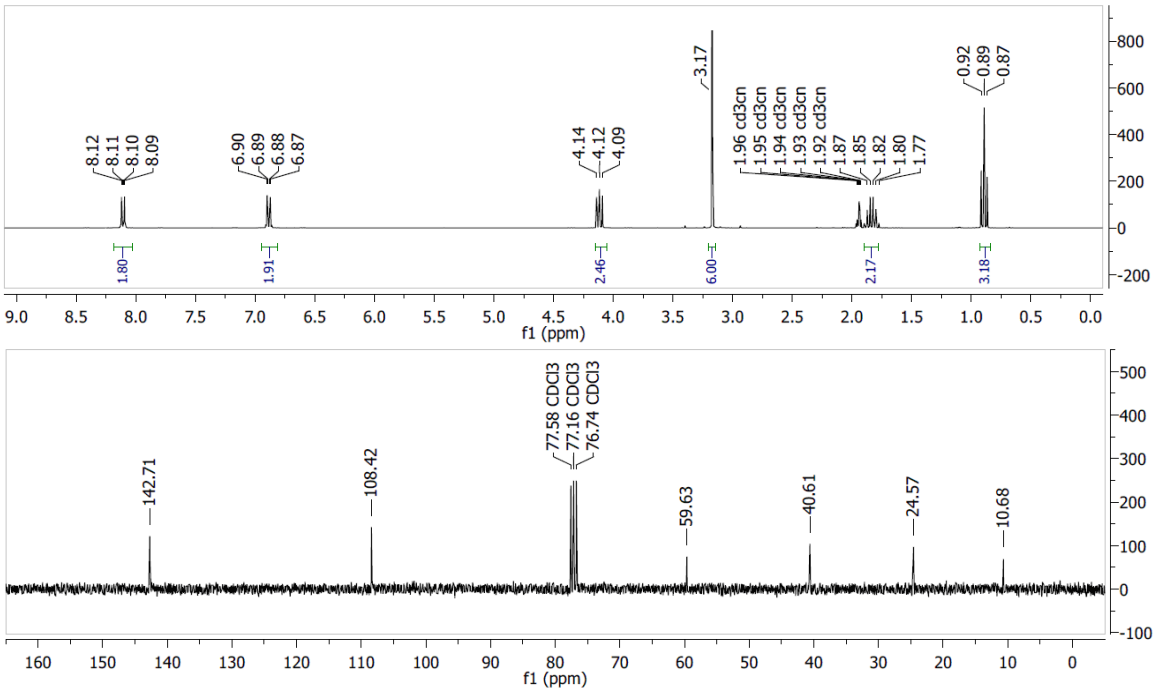


Figure 3.6: NMR spectra of N-propyl-4-dimethylaminopyridinium bromide salt **2a**. Top (a); the ^{1}H spectra taken in deuterated acetonitrile (300 MHz). Bottom (b); the ^{13}C spectra taken in deuterated chloroform (400 MHz).

Peak assignments for **2a-d** were carried out using the J-couplings and integrations of the peaks in ^{1}H NMR, in addition to comparisons with the shifts of 4DMAP and the individual bromoalkanes. Although complete ^{1}H NMR assignments were conducted for **2a-d** in both $CDCl_3$ and CD_3CN (see Section 3.3.8), only the characterization of **2a** via CD_3CN is considered in this section, as its peak assignments are similar to those of **2b-d**, and because the assignments in CD_3CN are relevant in the identification of the precursor salts as reaction byproducts in the preparation of bis-pyridinium chloride salts (see Section 3.2.3).

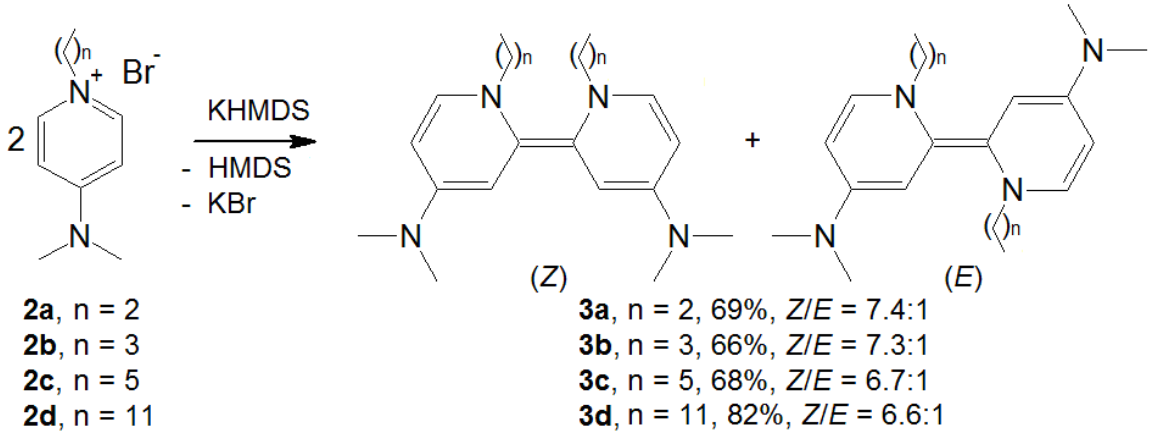
The characteristic ^{1}H-NMR chemical shifts of **2a** (Figure 3.6a) included the pyridinium ring C-*H* doublets at 8.11 and 6.89 parts per million (ppm) for the 2 and 3 ring positions, respectively, which moved from their original chemical shifts of 8.13 and 6.55 ppm in the 4DMAP pyridine ring in CD_3CN (8.21 and 6.46 ppm in $CDCl_3$[157]). The pyridinium alkyl substituent N-C*H*$_2$- was assigned to the triplet with a chemical shift of 4.12 ppm, which is farther downfield compared to the alkyl bromide triplet at 3.386 ppm triplet.[158] The large singlet found at 3.17 ppm was assigned to N(C*H*$_3$)$_2$ in **2a**, being downfield from the 2.98 ppm singlet assigned to the 4DMAP in CD_3CN (2.96 ppm in $CDCl_3$[157]).

The characteristic chemical shifts in the ^{13}C spectra of **2a** (Figure 3.6b) included the shifts at 142.7 ppm and 108.4 ppm assigned to the pyridinium ring 2 and 3 position *C*-H, respectively, which would be near the original 149.7 and 106.5 ppm peaks assigned to the same positions in 4DMAP.[157] The 40.6 ppm peak was assigned to N(*C*H$_3$)$_2$ in **2a**, being slightly downfield from the 38.9 ppm peak expected for the N(*C*H$_3$)$_2$ group in 4DMAP.[157] Lastly, the peak at 40.6 ppm was assigned to N-*C*H$_2$- in the precursor salts, farther upfield compared to the 35.76 ppm peak expected for the Br-*C*H$_2$- in the corresponding BrPr reagent, with the other bromoalkanes also exhibiting this peak in the 34-37 ppm range.[158-161]

The synthesized precursor salts exhibited very sharp melting points with melting ranges between 1-2°C, indicating that they were fairly pure,[162] and these matched closely with their literature values. The precursor salts exhibited a trend of lower melting point

from **2b** to **2d**, going from a melting range of 218-220°C for **2b** to 70-71°C for **2d**. In contrast to this trend, the propylated salt **2a** had a melting point of 162-163°C, which was much lower than that of **2b**.

3.2.2 – Characteristics of the N,N-Dialkylated Bis-Pyridinylidenes



Scheme 3.3: The synthetic scheme for generating the N,N-dialkyl-bis-2-(4-dimethylamino)pyridinylidene electron donors **3a-d**, with accompanying isolated yields and *Z*/*E* isomer ratios.

The second synthetic step was the generation of the symmetrical alkyl-substituted bis-pyridinylidene super electron donors via reaction of the precursor salts with potassium bis(trimethylsilyl)amide (KHMDS), a strong base, yielding *Z*/*E* isomer mixtures of **3a**-**d** (Scheme 3.3) with the *Z*/*E* isomers being identified via ^{1}H NMR. This step was carried out under moisture and air -free conditions due to the sensitivity of the bis-pyridinylidene products towards air.[163] The *Z*/*E* isomer ratios found to be 6.7-7.4 : 1 via ^{1}H NMR signal integration ratios of the peaks assigned to the H_a and H_b nuclei in both isomers, with the reported *Z*/*E* isomer ratios being averages of the (*Z*)-H_a / (*E*)-H_a

and (*Z*)-H_b / (*E*)-H_a ratios (see Figure 3.12). Despite their isomerically-impure state, **3a-d** were considered isolates by virtue of being almost entirely devoid of other impurities.

The level of purity afforded by the isolation process, detailed in the experimental section (see Section 3.3.2), was partially qualified via cyclic voltammetry (CV) of a sample of **3a**. The objective of the CV experiment is to study electron transfer processes in an analyte solution by incrementing and decrementing the working electrode potential in cyclical fashion. A potentiostat is used to record the working electrode (WE) potential E_{we} (volts) against a reference electrode (RE), in addition to supplying and measuring the necessary electric current I (mA) required for incrementing or decrementing E_{we}. When E_{we} reaches an experimentally-specified value, the current is reversed and the potential is swept in the reverse direction, with the completion of both a forward and a reverse sweep constituting a "cycle". Electroactive species in the analyte solution undergo oxidation or reduction at the WE-solution interface as E_{we} is incremented or decremented, leading to the formation of current-positive or current-negative events, respectively, which manifest as "waves" in the resulting spectra. Information about the oxidation/reduction processes can be extracted from the peaks, areas, and shapes of these CV waves. Note that all presented CV spectra herein were recorded with E_{we} being incremented during the oxidation step to yield current-positive peaks as oxidation events and decremented during the reduction step to yield current-negative peaks as reduction events.

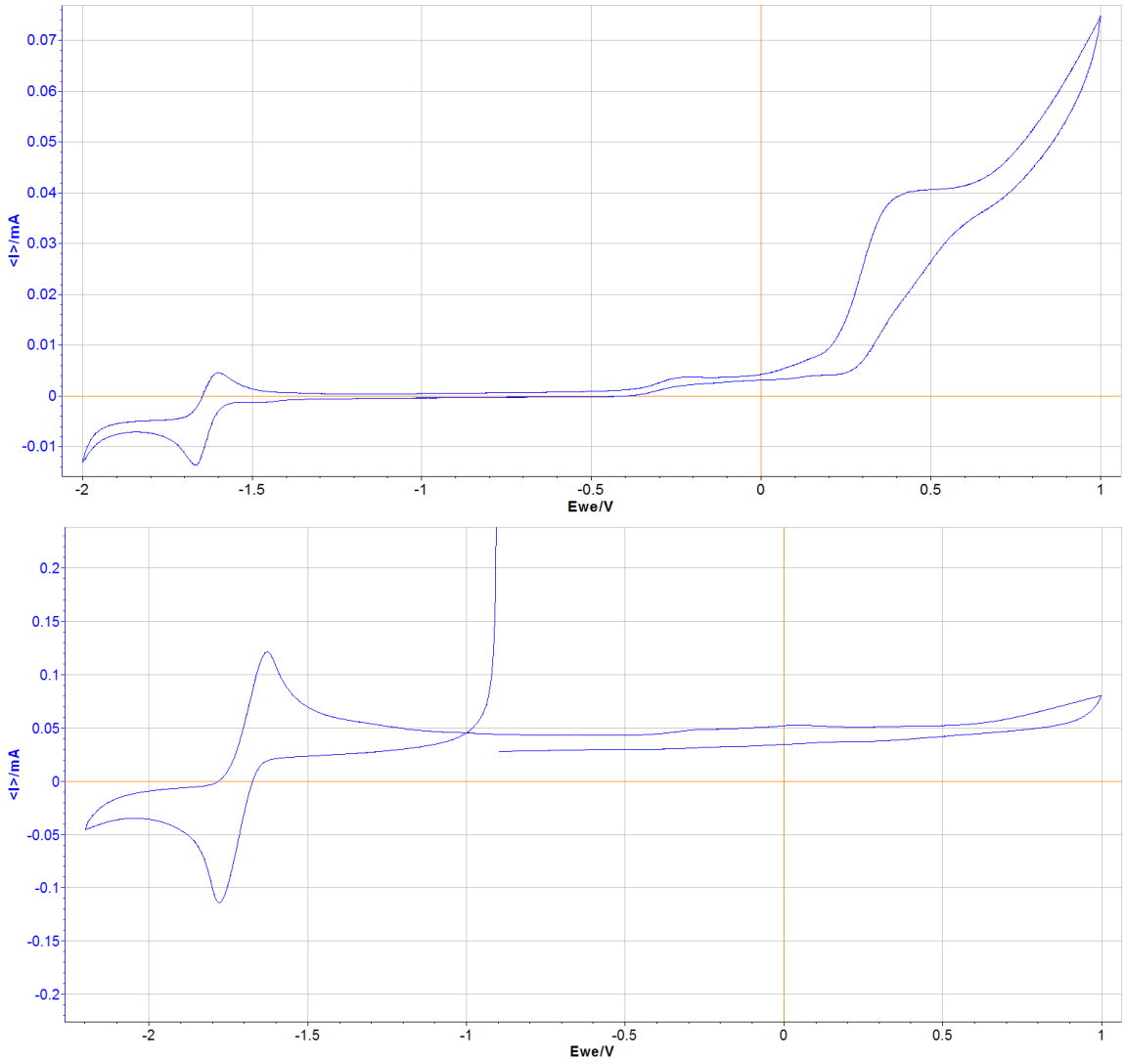


Figure 3.7: Top (a); cyclic voltammograms of the 2nd cycle of ~0.0002 M of non-filtered **3a**. Bottom (b); the 1st cycle of ~0.001 M of **3a** (initial polarization current at -0.9 V). The working electrode potential (E_{we}) was recorded vs. a non-aqueous silver/silver^{+} (Ag/Ag^{+}) reference electrode. The scan rate was 10 mV/s with "IR determination and compensation by impedance measurement technique" (ZIR correction) in the top voltammogram and 50 mV/s without ZIR correction in the bottom voltammogram. The electrolyte used was 0.1 M TBAH DMF in both cases.

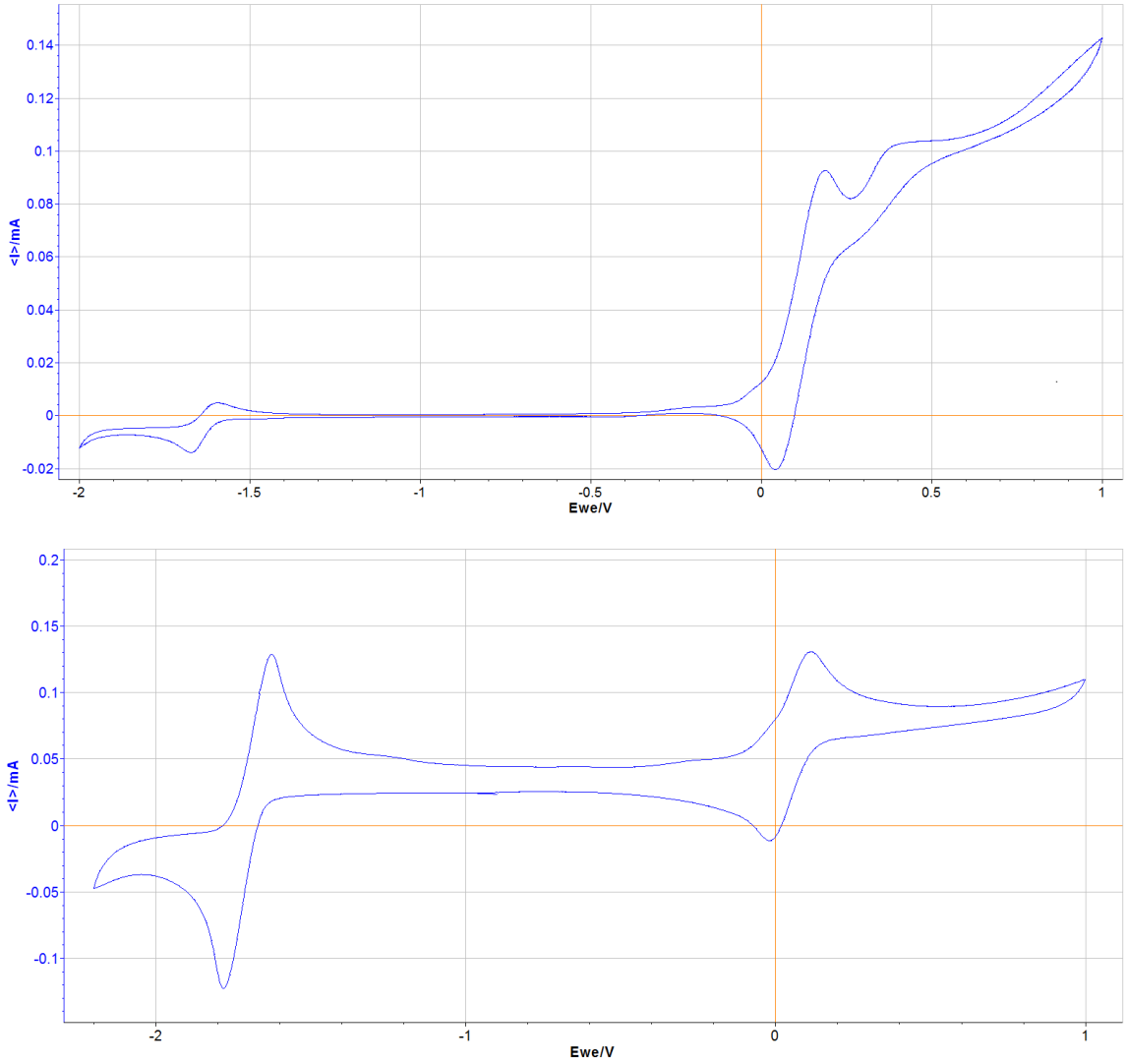


Figure 3.8: Top (a); cyclic voltammograms of the 2nd cycle of ~0.0002 M of non-filtered **3a** with ~0.0005 M ferrocene. Bottom (b); the 2nd cycle of ~0.001 M of **3a** with ~0.005 M ferrocene. The working electrode potential (E_{we}) was recorded vs. a non-aqueous silver/silver^{+} (Ag/Ag^{+}) reference electrode. The scan rate was 10 mV/s with ZIR correction in the top voltammogram and 50 mV/s without ZIR correction in the bottom voltammogram. The electrolyte used was 0.1 M TBAH DMF in both cases.

In order to draw comparisons between **3a** before and after isolation, CV experiments were performed on a non-filtered sample of **3a**, which had merely been dried *in vacuo* and on **3a** that had been double-filtered using the experimental procedure (see Section 3.3.2). The experiments included non-filtered **3a** with and without ferrocene

(Figures 3.7a and 3.8a, respectively) and double-filtered **3a** with and without ferrocene (Figures 3.7b and 3.8b, respectively), with ferrocene (Fc) acting as an internal reference compound (+0.470 V vs. SCE in DMF[164]) owing to its more stable oxidation, reduction, and half-cell potentials (E_{ox}, E_{re}, and $E_{1/2}$, respectively) compared to the voltammetry cell's Ag/Ag^+ reference electrode. In all four cyclic voltammograms, the $\mathbf{3a}^{2+} + 2e^- \leftrightharpoons \mathbf{3a}$ redox couple wave was observed at half-cell potentials of $E_{1/2}$ = -1.64 and -1.71 V vs. the Ag/Ag^+ reference electrode for the non-filtered and filtered samples without Fc, and $E_{1/2}$ = -1.73 V vs. Fc (-1.28 V vs. SCE) in both cases with Fc.

The CV spectrum of non-filtered **3a** without Fc exhibited three non-reversible waves appearing at -0.21 V (oxidation event), +0.26 V (reduction event), and +0.42 V (oxidation event) vs. Ag/Ag^+, with the wave at +0.42 V being especially intense. In comparison, this same region was very clean in the CV spectrum of double-filtered **3a** (Figure 3.7b). In the spectrum of the non-filtered **3a** with Fc, this particular oxidation wave was found to have an oxidation potential of +0.62 vs. SCE, which was near the oxidation potential of bromide in organic media (+0.45 V vs. SCE in CH_3CN[164]).

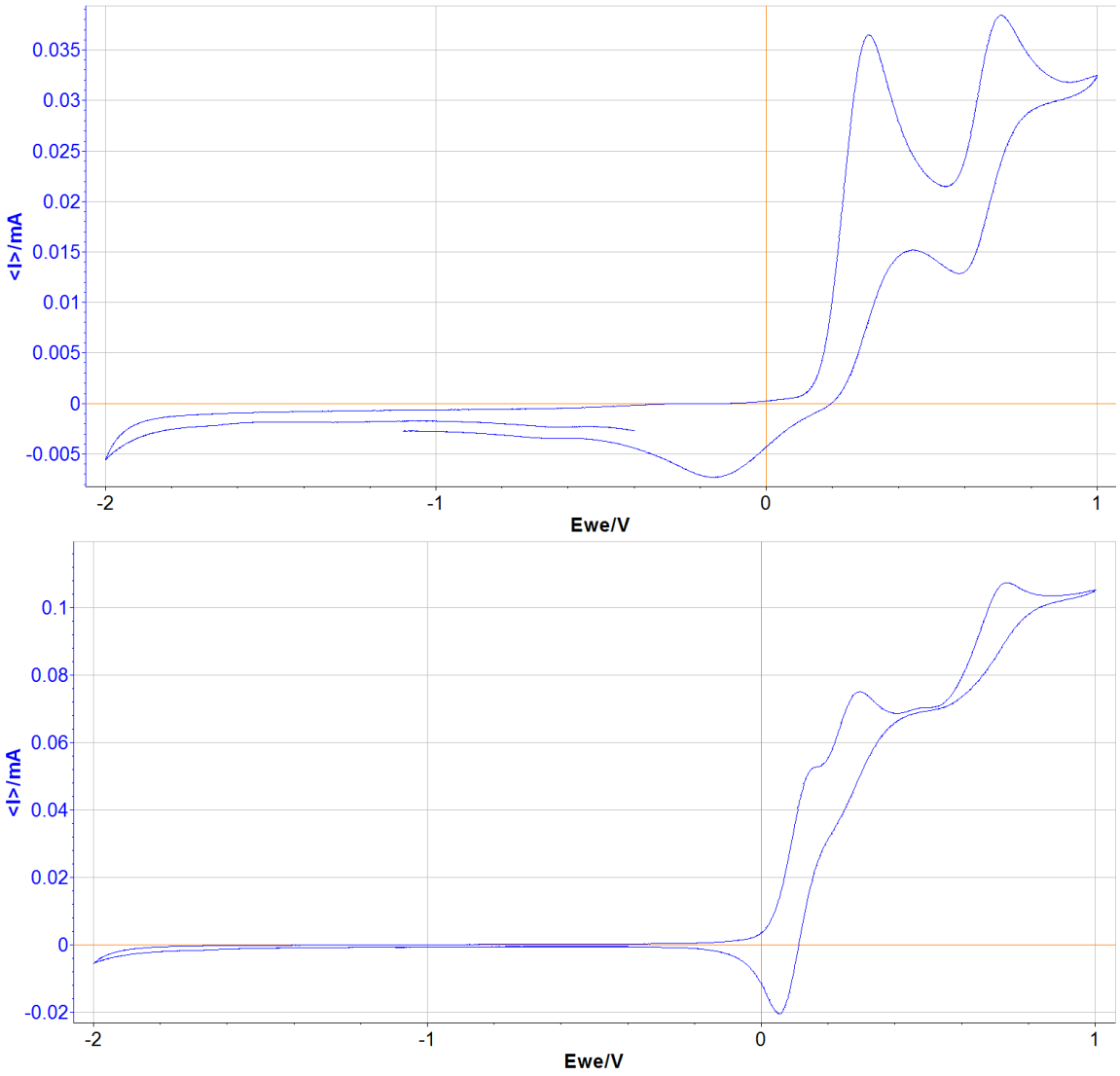


Figure 3.9: Top (a); CV spectrum of KBr in 0.1 M TBAH in DMF at 10 mV/s with ZIR correction. Bottom (b); CV spectrum of KBr + Fc in 0.1 M TBAH in DMF at 10 mV/s with ZIR correction.

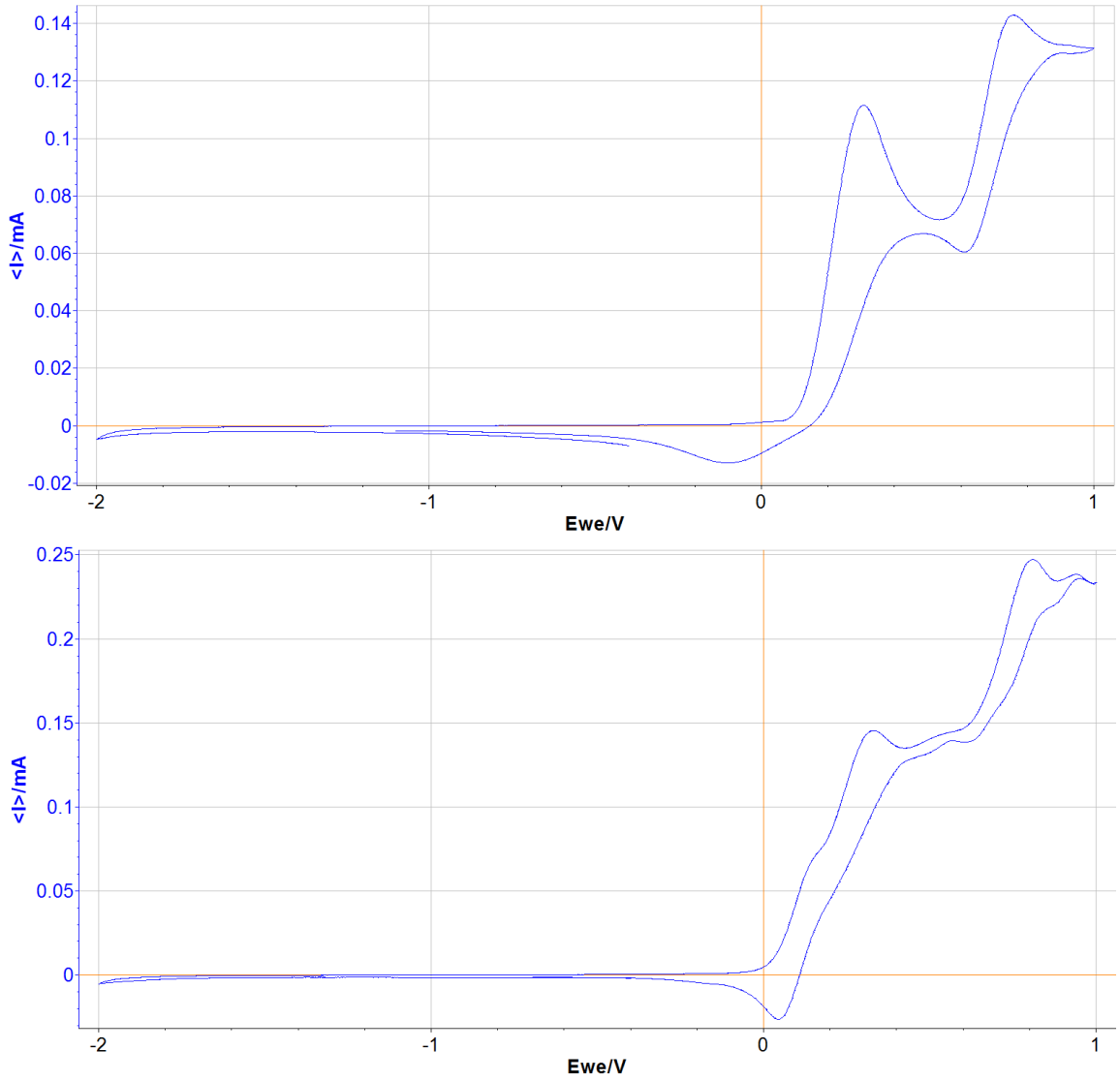


Figure 3.10: Top (a); CV spectrum of **2a** in 0.1 M TBAH in DMF at 10 mV/s with ZIR correction. Bottom (b); CV spectrum of **2a** + Fc in 0.1 M TBAH in DMF at 10 mV/s with ZIR correction.

This same wave was also present in the CV spectra of KBr and **2a** at E_{ox} = 0.31 V vs. Ag/Ag^{+} in both cases without Fc (Figures 3.9a and 3.10a), and E_{ox} = 0.10 and 0.13 V vs. Fc (+0.55 and +0.58 V vs. SCE) in cases with Fc (Figures 3.9b and 3.10b), respectively, with its presence in bromide salts corroborating its assignment to the bromide oxidation process $2Br^{-} \rightarrow Br_2 + 2e^{-}$. The lack of reduction wave may have been due to the high

reactivity of the produced bromine (Br_2), making it too short-lived at the electrolyte-electrode interface for the process to be reversible. In conclusion, the isolation process was deemed successful in eliminating KBr, **2a**, and other bromide salt impurities by virtue of the lack of the assigned bromide oxidation wave in the isolated **3a**.

The purity of the bis-pyridinylidenes **3a-d** was also verified via ^{1}H NMR in C_6D_6 in which proton signals from non-ionic impurities and residual solvent would be seen if these were present in notable quantities.

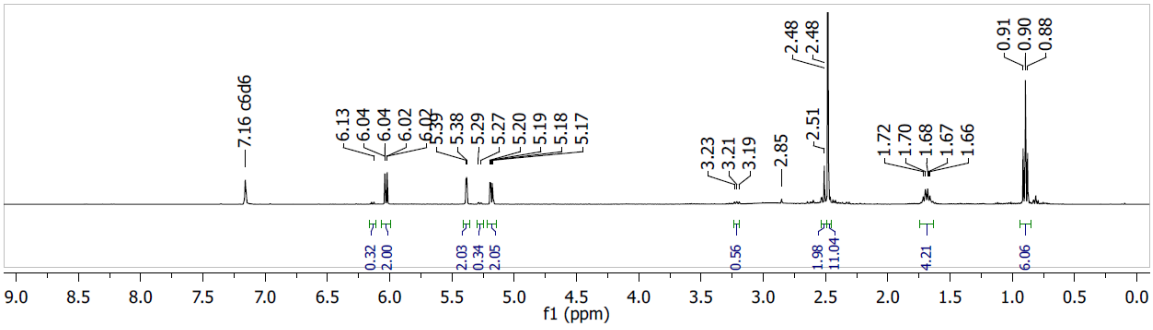


Figure 3.11: ^{1}H NMR spectra of N,N-dipropyl-bis-2-(4-dimethylamino)pyridinylidene **3a** in C_6D_6 (400 MHz).

Amongst the possible impurities, the bis(trimethylsilyl)amine (HMDS) reaction byproduct would have been the most prominent with its trimethylsilyl hydrogen signal reportedly appearing as a singlet with a chemical shift of 0.013 ppm in DMSO-d_6.[165] The isolation method was successful in eliminating this impurity from **3a-d** (Figure 3.11), with only trace amounts of HMDS and indiscernible amounts of KHMDS remaining at worst. The isolation process also eliminated tetrahydrofuran (THF) and n-hexanes as possible residual solvent impurities, signified by the lack of multiplets at 3.27 and 1.40

ppm in the case of the former and lack of multiplet at 1.24 and triplet at 0.89 pm in the case of the latter in C_6D_6.[166] Lastly, only trace amounts of decomposition products could be seen in some of the bis-pyridinylidene spectra, signified by the small sharp singlets sometimes seen in the 2.7-3.0 ppm region. The peaks were assigned to as-of-yet unidentified decomposition products of **3a-d**.

Despite the high purity of **3a-d**, some additional small peaks remained detectable in both ^{1}H and ^{13}C NMRs of all the derivatives (Section 3.3.8). In ^{1}H spectra, it was found that the integrations of the smaller peaks were well-correlated with each other, and so it was possible that the smaller peaks all belonged to the same compound. As an explanation for the NMR data, it was rationalized that these bis-pyridinylidenes were exhibitting *E/Z* isomerism around the double bond, and as a result each set of peaks belonged to one of the two possible isomers. Computational calculations by Clennan *et al.*[167] suggested that the *Z* isomer of the di-methylated bis-pyridinylidene **1** should be the favored product, which led to the hypothesis that the set of major peaks seen in ^{1}H and ^{13}C NMRs of **3a-d** belonged to the *Z* isomer while the set of small peaks belonged to the *E* isomer.

A complete characterization of all the ^{1}H and ^{13}C NMR peaks to their respective nuclei was conducted for the *Z* and *E* isomers of **3a** via one-dimensional ^{1}H and ^{13}C NMR assisted by two-dimensional COSY, HSQC, and HMBC NMR experiments and variable temperature NMR experiments. Owing to the high degree of similarity found between bis-pyridinylidenes **3a-d**, the ^{1}H and ^{13}C peak assignments for **3a** were then used

as reference in the characterizations of **3b-d** based solely on their one-dimensional ^{1}H and ^{13}C NMR spectra. With the lack of 2D NMR in the cases of **3b-d**, some of their *E* isomer ^{1}H signals could not be assigned due to some of the *E* isomer peaks being buried by overlapping *Z* isomer peaks.

The details and justifications for the ^{1}H peak assignments for the di-propyl bis-pyridinylidene isomers **(*Z*)-3a** and **(*E*)-3a** are presented below.

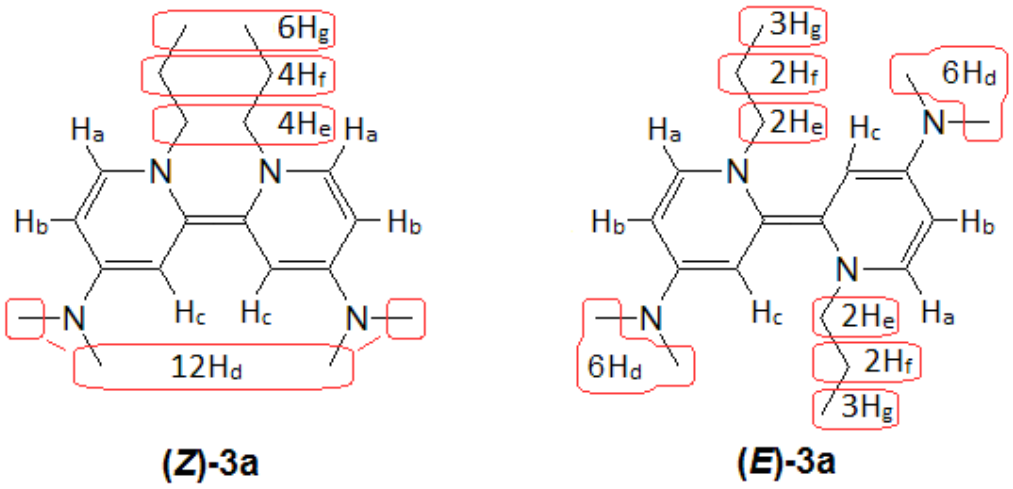


Figure 3.12: The structural labeling of the hydrogen nuclei in the *E*/*Z* isomers of **3a**.

The bis-pyridinylidene ring (*Z*)-H_a, (*Z*)-H_b, and (*Z*)-H_c (Figure 3.12) were assigned to the doublet at 6.03 ppm, the doublet at 5.19 ppm, and the singlet at 5.39 ppm, respectively, as this region is typically populated by chemical shifts from hydrogen nuclei belonging to alkene groups.[168] The (*E*)-H_a and (*E*)-H_b nuclei were assigned to the doublet at 6.13 ppm and the doublet at 5.28 ppm, respectively, while the peak from (*E*)-H_c was not observed in the ^{1}H NMR because of overlap with the (*Z*)-H_c peak, as confirmed by

HSQC experiments (Figure 3.15, *vide infra*). Farther upfield from the alkene region, a small multiplet was found at 3.21 ppm and was assigned to the (*E*)-H_e nuclei. The broad peak at ~2.9 ppm was assigned to the (*Z*)-H_e nuclei in **3a-d**. This peak was broadened into the baseline of the ^{1}H NMR spectrum due to the (*Z*)-H_e nuclei exhibiting atropisomerism with intermediate chemical exchange rates, which was later resolved using variable temperature (VT) NMR experiments. A prominent singlet peak could be found at 2.48 ppm and was assigned to the (*Z*)-H_d nuclei, while the smaller singlet peak on the shoulder at 2.51 was assigned to the (*E*)-H_d nuclei, with this region typically being populated by chemical shifts from alkylamine protons. The (*Z*)-H_f, (*Z*)-H_g, and (*E*)-H_g nuclei were assigned to the multiplet at 1.68 ppm, the triplet at 0.90 ppm, and the small triplet at 0.81 ppm, respectively, while the (*E*)-H_f peak was later found via 2D NMR to be buried in the (*Z*)-H_f peak with a chemical shift of 1.69 ppm.

A ^{1}H-^{1}H correlation spectroscopy (COSY) experiment was conducted on **3a** and supported some of the previous ^{1}H assignments. In COSY spectra, the off-diagonal peaks reveal J-coupling connectivity between the hydrogen nuclei in the 1D traces along the f1 and f2 axes.[169] All of the observable ^{1}H-^{1}H COSY NMR cross-couplings for the *Z* and *E* isomers of **3a** are listed in Tables 3.5 and 3.6 (see Section 3.3.5).

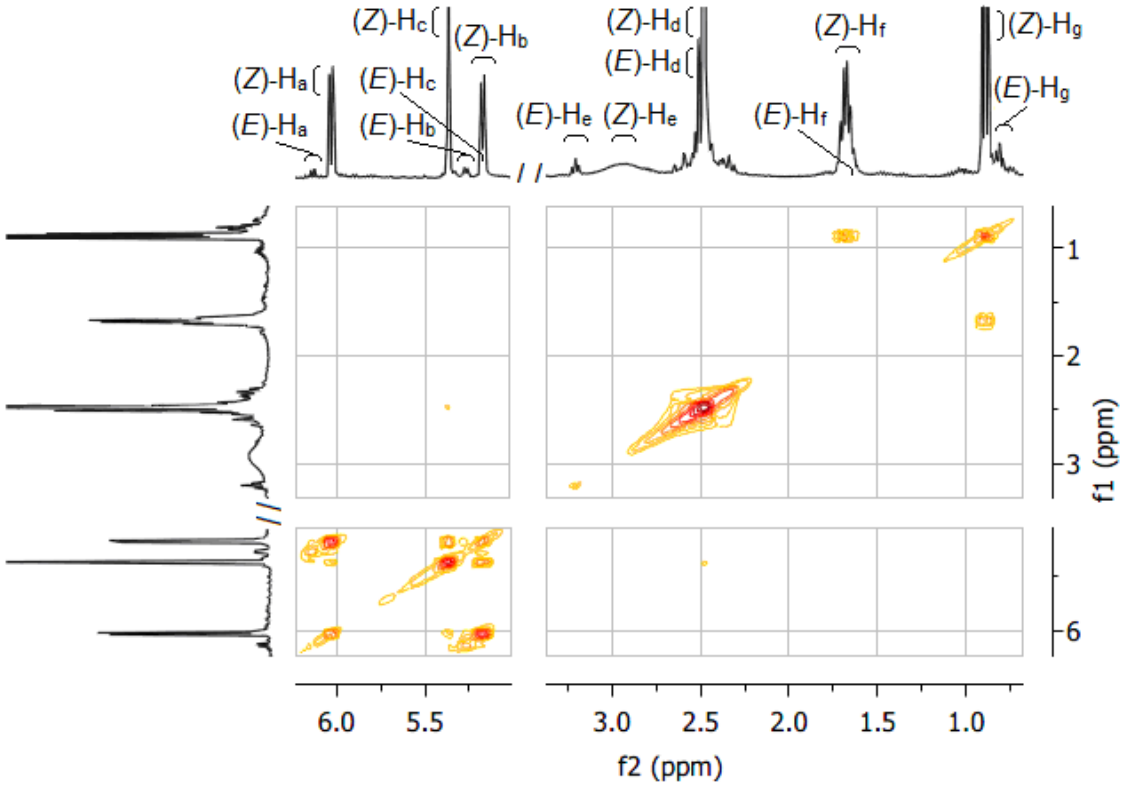


Figure 3.13: ^{1}H-^{1}H correlation spectroscopy (COSY) spectrum of **3a** in C_6D_6, with both the f1 and f2 traces representing the ^{1}H spectrum of **3a**.

In the COSY spectrum of **3a** (Figure 3.13), the broad peak at ~2.9 ppm lacked both cross coupling and diagonal coupling peaks. The lack of coupling was reasoned to be a consequence of intermediate chemical exchange, which is known to eliminate any observable coupling between the involved nuclei.[170] While not shown here, weak coupling could be observed between the multiplet at 3.21 ppm assigned to (*E*)-H_e and a peak buried under the multiplet at 1.69 ppm assigned to (*Z*)-H_f in the COSY spectrum at higher scaling. The buried peak was also coupled to the (*E*)-H_g peak, and so it was assigned to (*E*)-H_f.

The characterization of **3a-d** continued with the assignment of ^{13}C NMR spectra. The resolution of the 1D ^{13}C spectra made possible the assignment of all the *Z* and *E* isomer ^{13}C signals, with 2D HSQC (Figure 3.15) and HMBC (Figure 3.16) experiments supporting these 1D ^{13}C NMR peak assignments and further corroborating the ^{1}H NMR peak assignments. The complete ^{13}C NMR characterization of **3a** via both 1D NMR and 2D NMR experiments was used as a guide in characterizing **3b-d** through 1D ^{13}C NMR.

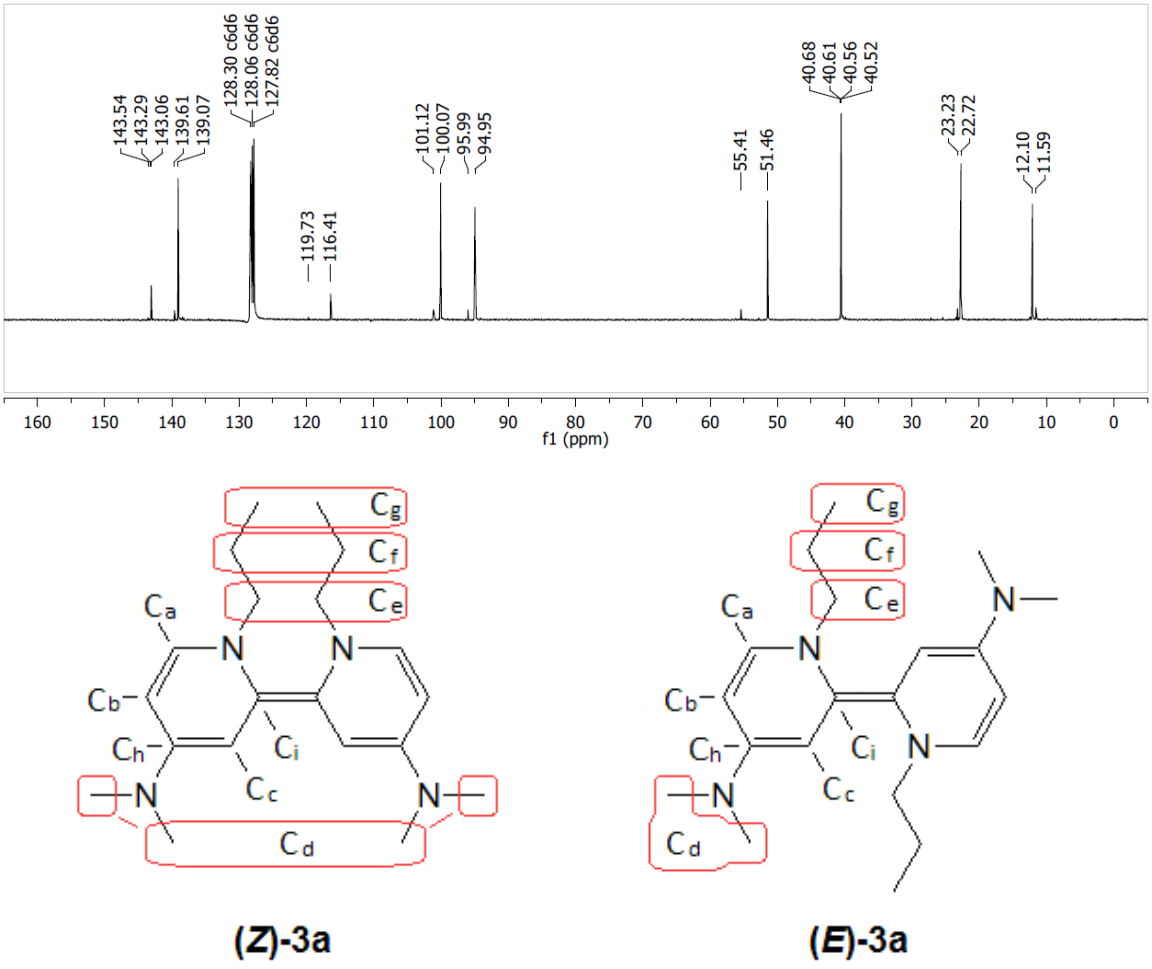


Figure 3.14: Top (a); ^{13}C NMR spectra of N,N-dipropyl-bis-2-(4-dimethylamino)pyridinylidene **3a** in deuterated benzene. Bottom (b); the structural labeling of the carbon nuclei in the *E*/*Z* isomers of **3a**.

From the ^{13}C NMR spectrum of **3a** (Figure 3.14a), the large singlets at 138.7, 100.1, and 95.0 ppm were assigned to the (*Z*)-C_a, (*Z*)-C_b, and (*Z*)-C_c nuclei (Figure 3.14b), respectively, while the smaller peaks at 143.1 and 116.4 ppm were assigned to the (*Z*)-C_h and (*Z*)-C_i nuclei, respectively, with this region usually being populated by ^{13}C nuclei belonging to alkene systems.[171] The intensities of the peaks supported these assignments, as less-intense peaks were expected for ^{13}C such as C_h and C_i that have no other nearby ^{1}H nuclei. The much smaller peaks at 143.5, 139.6, 119.7, 101.1, and 96.0 ppm were also assigned to the (*E*)-C_h, (*E*)-C_a, (*E*)-C_i, (*E*)-C_b, and (*E*)-C_c nuclei, respectively, following after the assignments of the *Z* isomer ^{13}C nuclei. The large peak at 51.5 ppm and smaller peak at 55.4 ppm were assigned to (*Z*)-C_e and (*E*)-C_e, respectively, conforming to this region typically being populated by peaks from alkylamine ^{13}C nuclei. In addition, another peak was present in this same region at 40.6 ppm and was assigned to both (*Z*)-C_d and (*E*)-C_d, with the latter being buried in the former. The remaining large peaks at 23.2 and 12.1 ppm and the small peaks at 22.7 and 11.5 ppm were assigned to (*Z*)-C_f, (*Z*)-C_g, (*E*)-C_f, and (*E*)-C_g, respectively.

The ^{1}H-^{13}C heteronuclear single quantum coherence experiment (HSQC) yields 2D spectra depicting cross-coupled peaks between ^{1}H nuclei and the aliphatic ^{13}C nucleus they are directly bonded to.

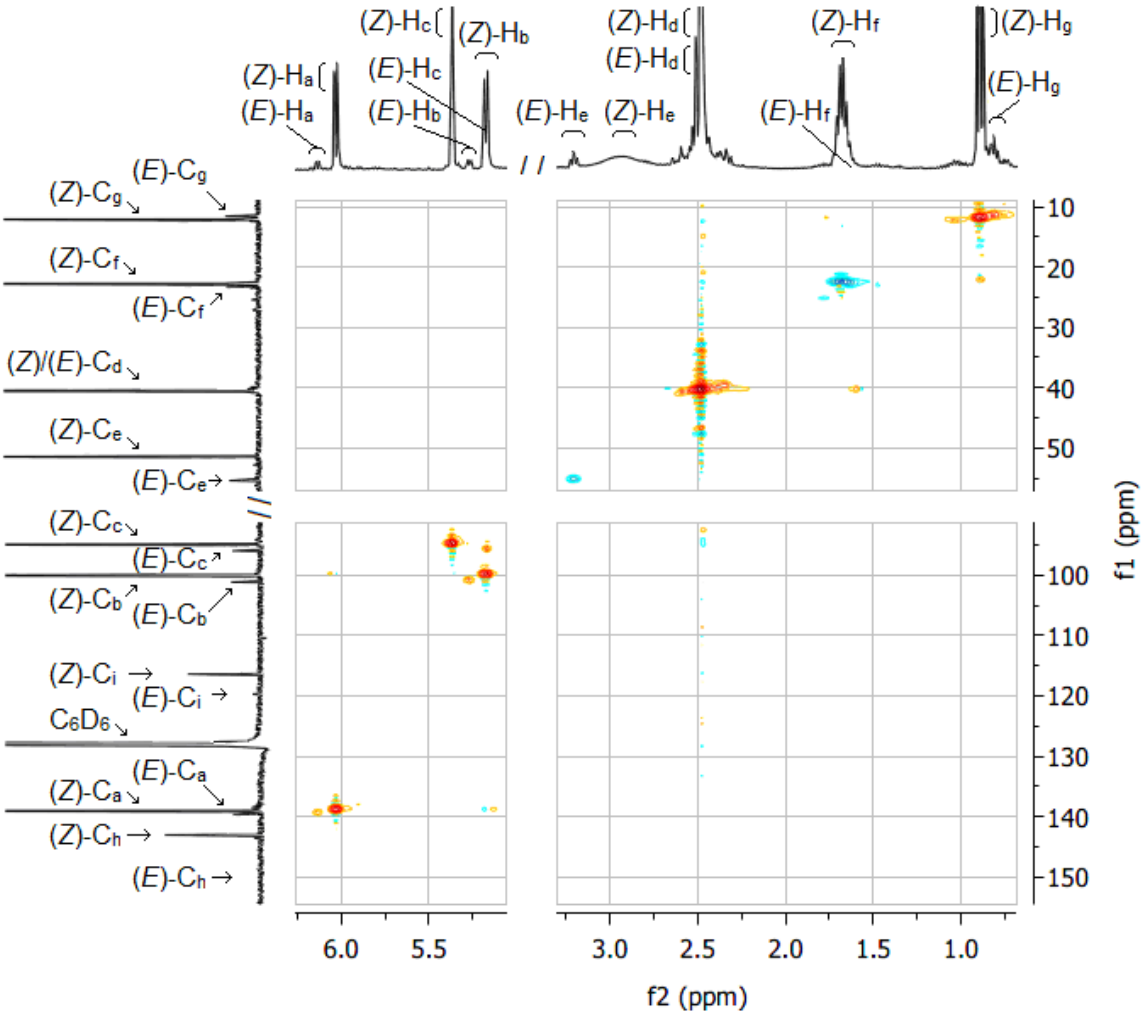


Figure 3.15: ^{1}H-^{13}C heteronuclear single quantum coherence spectroscopy (HSQC) spectrum of **3a** in C_6D_6 with the f1 and f2 traces representing the ^{13}C and ^{1}H spectra of **3a**, respectively.

The HSQC spectrum of **3a** (Figure 3.15) supported the previous ^{1}H and aliphatic ^{13}C assignments for both the *Z* and *E* isomers. The HSQC spectrum also showed that the peaks assigned to (*Z*)-C_h, (*E*)-C_h, (*Z*)-C_i, and (*E*)-C_i did not exhibit coupling to any of the ^{1}H peaks, which helped confirm that these peaks were from quaternary ^{13}C, with the only such nuclei being found in the ring system. It was also revealed that a peak was buried inside the peak assigned to (*Z*)-H_b. This buried peak was subsequently assigned to (*E*)-H_c

due to its coupling to the peak assigned to (*E*)-C_c. The lack of observable coupling between the broad peak at ~2.9 ppm assigned to (*Z*)-H_e with the peak at 51.5 ppm assigned to (*Z*)-C_e was consistent with the previously mentioned intermediate chemical exchange thought to be exhibited by the (*Z*)-H_e, which should eliminate all coupling between (*Z*)-H_e and other ^1H and ^{13}C nuclei.

To complement the HSQC spectrum, a ^1H-^{13}C heteronuclear multiple-bond quantum correlation experiment (HMBC) was also conducted on **3a**. The HMBC experiment yields a 2D spectrum depicting cross-coupled peaks between each ^1H nucleus and any nearby ^{13}C nuclei which are separated by two, three, or (rarely) four chemical bonds. In contrast to HSQC, the HMBC technique omits couplings from ^1H directly bonded to ^{13}C from its spectra. The HMBC spectrum of **3a** (Figure 3.16, *vide infra*) provided sufficient structural information to finalize the ^1H and ^{13}C NMR peak assignments in both the *Z* and *E* isomers. However, there was an anomaly in the HMBC spectrum as the H_b - C_a and H_b - C_h coupling peaks for both *Z* and *E* isomers were either very weak (H_b - C_a for the *E* isomer) or entirely absent (H_b - C_a for the *E* isomer and H_b - C_h for both isomers).

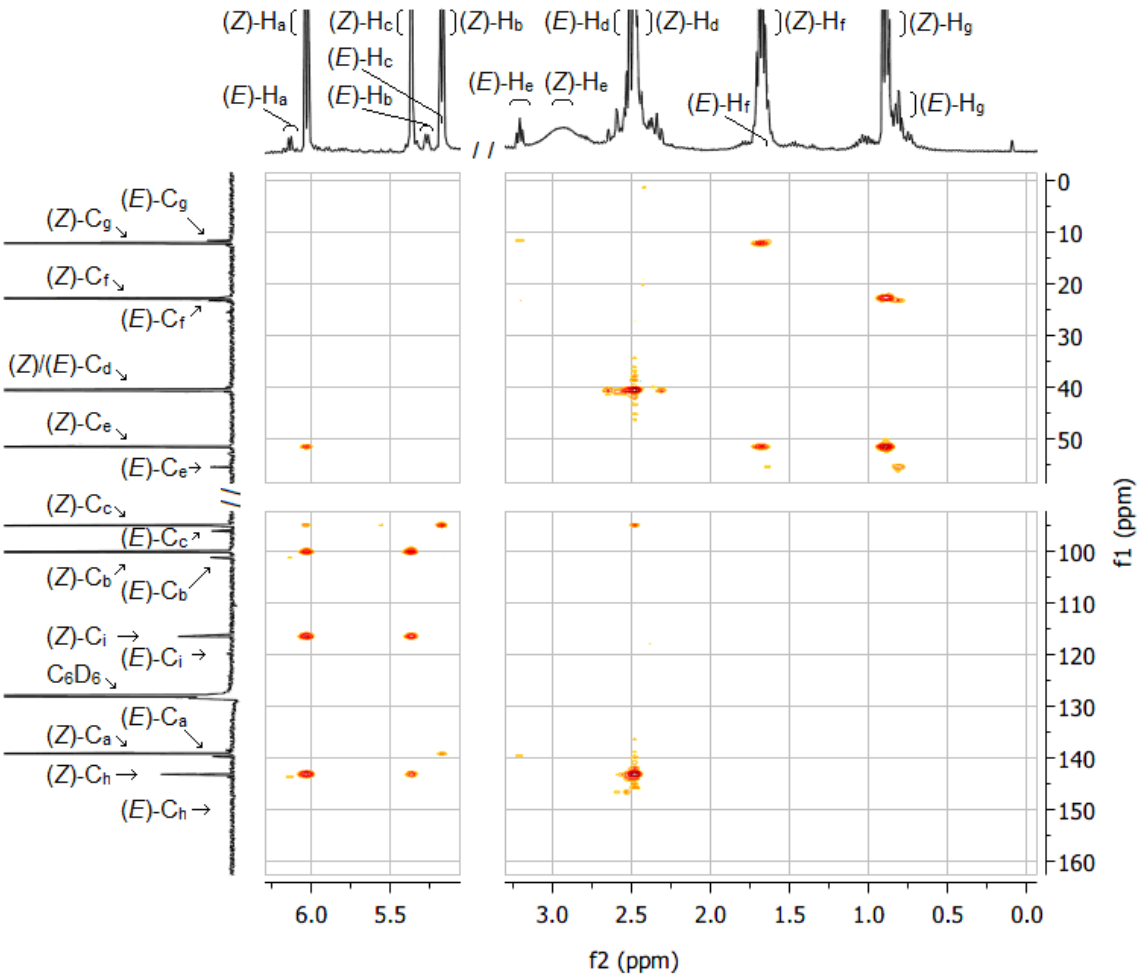


Figure 3.16: ^{1}H-^{13}C heteronuclear multiple-bond correlation (HMBC) spectrum of **3a** in C_6D_6, with the f1 and f2 traces representing the ^{13}C and ^{1}H spectra of **3a**, respectively.

It was thought that the structural dihedral angles between the H_b nuclei and nearby C_a and C_h were unfavorable for coupling as described by the Karplus relationship.[172,173] Furthermore, the peak assigned to C_h was not very intense due to the lack of surrounding ^{1}H nuclei, which further reduced the intensities of its coupling peaks. The lack of both couplings in the Z isomer was also a result of its lower relative abundance.

Thus far, the ^{1}H, ^{13}C, COSY, HSQC, and HMBC spectra supported all but one peak assignment: that of the (*Z*)-H_e nuclei, which had been assigned to the broad peak at ~2.9 ppm. Based on later findings for the bis-pyridinium salts (see Section 3.2.3), it was reasoned that the N-C_e bonds in the Z isomer could be experiencing hindered rotation due to the spatial proximity of the two N-CH_2- to each other, which would make the (*Z*)-H_e nuclei atropisomeric.[174] This would consequently lead to two or more chemically-distinct (*Z*)-H_e and thus two or more distinct peak sets in ^{1}H NMR spectra. Consequently, these nuclei should exhibit some degree of chemical exchange.[175]

The lack of coupling peaks between the ~2.9 ppm peak and other peaks in COSY, HSQC, and HMBC could be theorized to be a result of the chemical exchange rate (k_{ex}) and the difference in frequency between individual conformer signals ($|\Delta v|$) being almost equivalent ($k_{ex} \approx |\Delta v|$) in which case the chemical exchange rate is said to be "intermediate".[176] The complete set of ^{1}H signals becomes observable when the frequency difference between the peaks is much larger than the chemical exchange rate ($k_{ex} << |\Delta v|$) typically achieved by increasing the NMR instrument's field strength (B_0) or more conventionally by cooling the sample. Observing the set of distinct peaks is useful for determining the chemical exchange rate of the (*Z*)-H_e nuclei.[177] However for the purposes of demonstrating 2D NMR coupling peaks to corroborate the NMR assignments, the signals could just as well be made to coalesce into a single peak by conducting NMR experiments at higher temperatures and/or in a weaker field, with coalescence occurring when the chemical exchange rate becomes much faster than the frequency difference between conformers ($k_{ex} >> |\Delta v|$). As a preliminary experiment, the

~2.9 ppm peak was made to coalesce in the ^{1}H spectra of **3a** by recording spectra at temperature increments between 20 and 60°C. This was then followed by a series of 1D ^{13}C NMR, 2D ^{1}H-^{1}H COSY, and 2D ^{1}H-^{13}C HSQC experiments at 50°C.

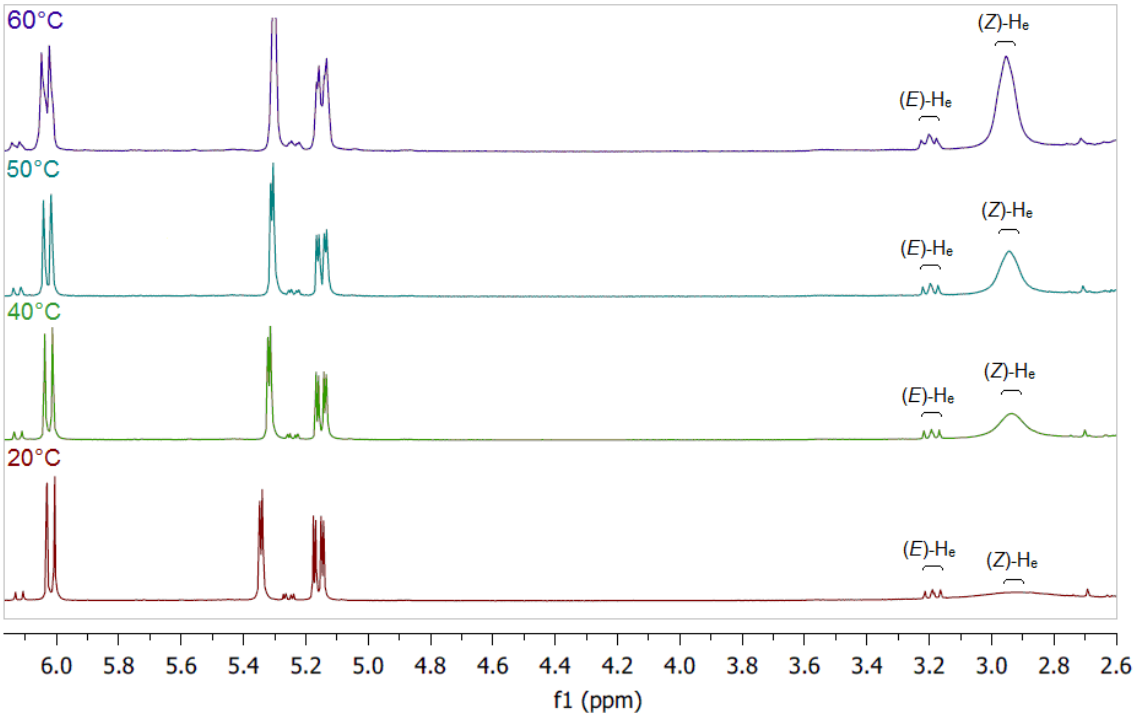


Figure 3.17: Variable temperature ^{1}H NMR of **3a** in C_6D_6 at temperatures of 60, 50, 40, and 20°C (top to bottom).

Acquiring ^{1}H NMR spectra of **3a** at higher temperatures lead to a prominent increase in the intensity of the 2.92 ppm peak (Figure 3.17), as expected from a coalescence effect. A 25°C ^{1}H NMR spectrum was also taken after the VT experiments in which the signal had broadened back into the baseline (not shown), which eliminated the possibility of the peak being from a different compound generated via a non-reversible heat-driven phenomenon such as decomposition.

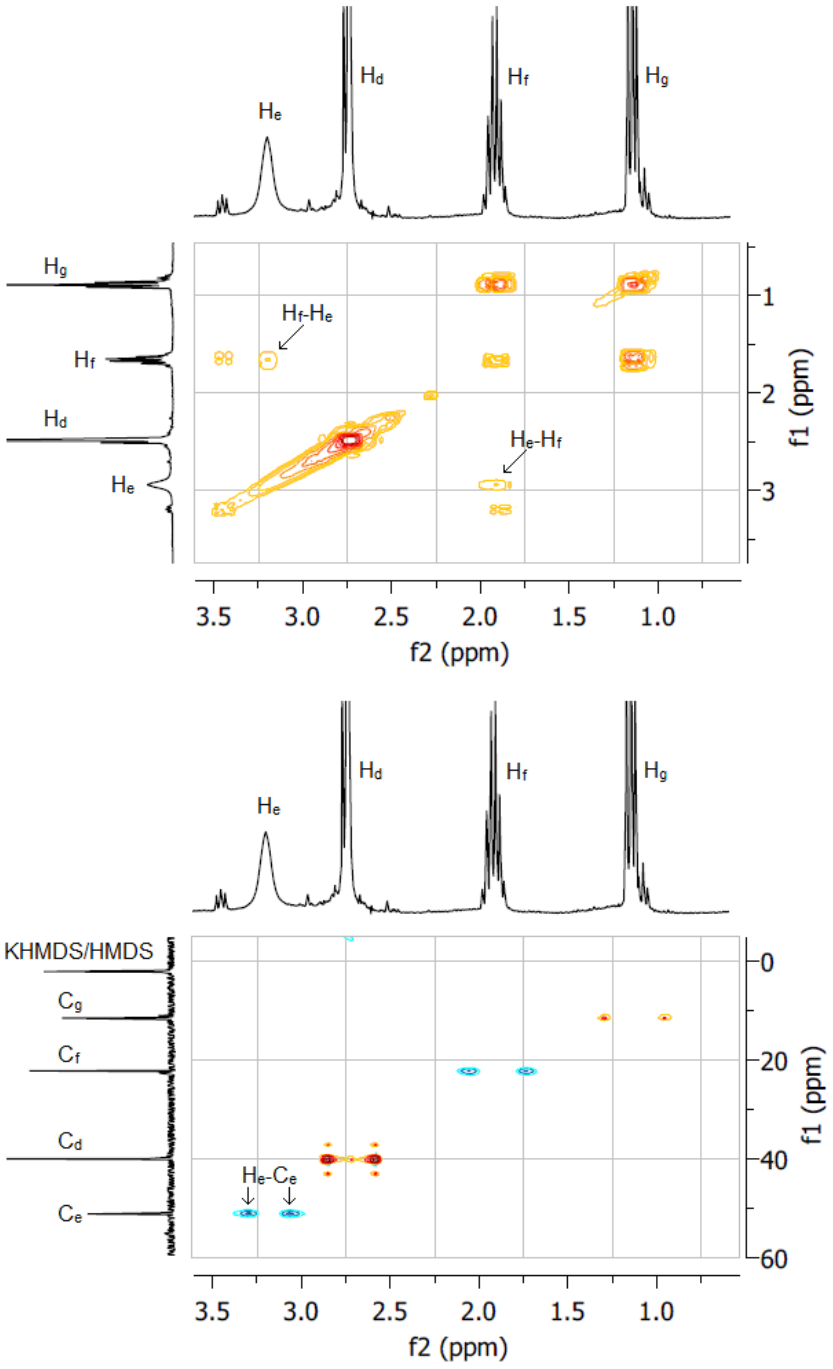
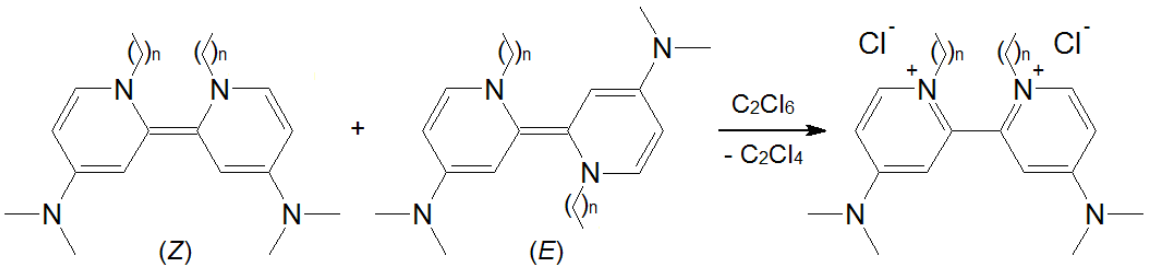


Figure 3.18: ^{1}H-^{1}H COSY (top, a) and ^{1}H-^{13}C HSQC (bottom, b) of **3a** in C_6D_6 at 50°C. Decoupling was not performed in the HSQC study.

The case for the peak being assigned to the atropisomeric (*Z*)-H_e nuclei was made strongest in the 50°C 2D NMR experiments of **3a**. A weak correlation was observed between the peak assigned to (*Z*)-H_f and the coalesced peak in the 50°C COSY spectrum (Figure 3.18a). In addition, a coupling peak was found between the coalesced peak at 2.92 ppm and the peak assigned to (*Z*)-C_e in the 50°C HSQC spectrum (Figure 3.18b). It was reasoned that the peak assigned to the (*E*)-H_e nuclei was spared from the atropisomeric effects afflicting the peak assigned to the (*Z*)-H_e nuclei because the N-CH_2- groups in the *E* isomer were too far away from each other as well as from the N-$(CH_3)_2$ groups to suffer from steric hindrance effects. This distinction between hindered and non-hindered N-CH_2- in the *Z* and *E* isomers, respectively, supported the hypothesis that the major isomer was the *Z* isomer and that the minor isomer was the *E* isomer.

3.2.3 – Characteristics of the N,N-Dialkylated Bis-Pyridinium Salts



Scheme 3.4: Preparation of N,N-dialkyl-bis-2-(4-dimethylamino)pyridinium chloride salts **4a-d** with accompanying yields.

The third synthetic step was the generation of the bis-pyridinium chloride salts (**4a-d**) via reaction of the bis-pyridinylidenes **3a-d** with hexachloroethane (C_2Cl_6), as described in Scheme 3.4, with yields ranging from 79-93%. Because **4a-d** were hygroscopic, air-free techniques were exercised in all stages of their synthesis and handling. The characterization of **4a-d** was conducted via ^1H and ^{13}C NMR, electrospray ionization mass spectrometry (ESI-MS), and melting point determination, while the purity of the chloride salts was assessed via ^1H NMR and melting point determination.

As in the cases of **3a-d**, the complete assignment of **4a** via ^1H, ^{13}C, ^1H-^1H COSY, ^1H-^{13}C HSQC, and ^1H-^{13}C HMBC NMR experiments (Table 3.7) was used as a reference in the ^1H and ^{13}C NMR peak assignments of the remaining **4b-d**. The diagnostic ^1H NMR peaks of **4a** (Figure 3.19a, *vide infra*) included the doublet, doublet of smaller J-value, and doublet of doublets at 8.44, 7.26, and 7.11 ppm which were assigned to the bis-pyridinium ring H_a, H_c, and H_b (Figure 3.19c), respectively. Of interest was the observation of the peak sets at 3.68-4.11 ppm and at 3.24-3.27 ppm. The 3.68-4.11 ppm peak set was assigned to the diastereomeric H_{e1} and H_{e2} nuclei, forming two overlapping doublets of smaller triplets with chemical shifts of 3.88 and 3.91 ppm, respectively, and with coupling constants of $^2J_{e1\ e2}$ = 13.5 Hz and $^3J_{e1\ d}$ = $^3J_{e2\ d}$ = 7.6 Hz.

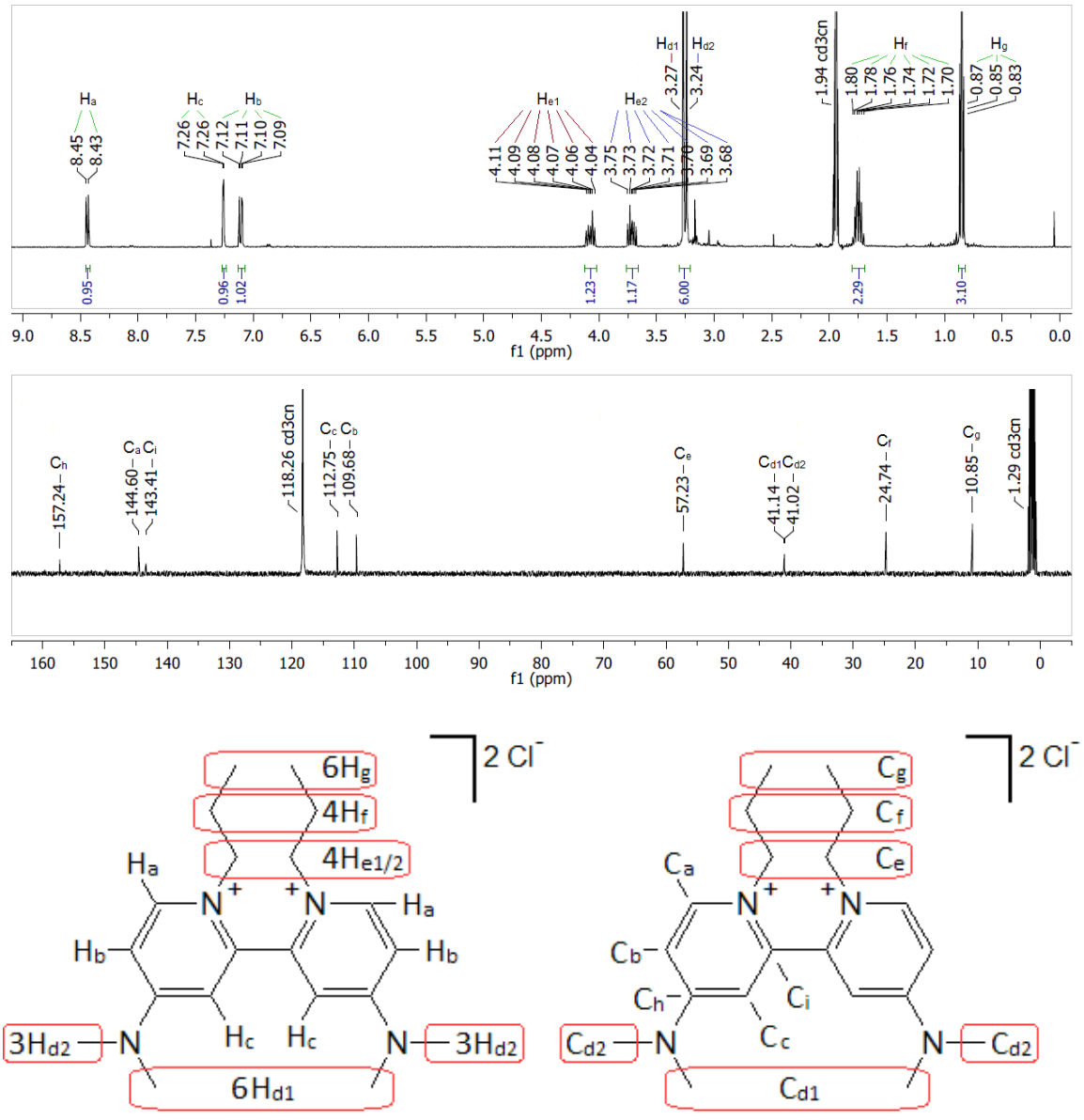


Figure 3.19: Top; ^{1}H NMR spectrum of **4a** recorded in CD_3CN (a). Middle; ^{13}C NMR spectrum of **4a** recorded in CD_3CN (b). Bottom; structure of N,N-dipropyl-bis-2-(4-dimethylamino)pyridinium chloride **4a** with labelled hydrogen nuclei on the left (c) and carbon nuclei on the right (d).

In the cases of H_{e1} and H_{e2}, splitting was occurring due to twisting of the two pyridinium rings which causes two distinct chemical environments (internal and external) for the H_e protons.

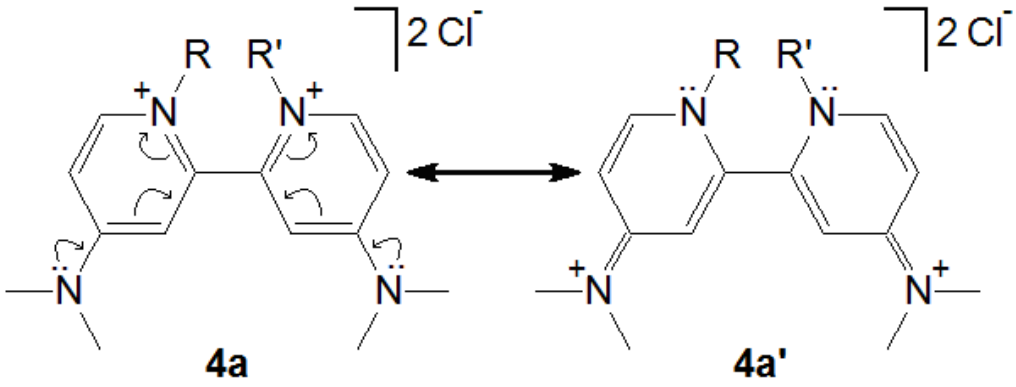


Figure 3.20: The two resonance structures of N,N-dialkyl-bis-2-(4-dimethylamino)pyridinium chloride derivatives **4**.

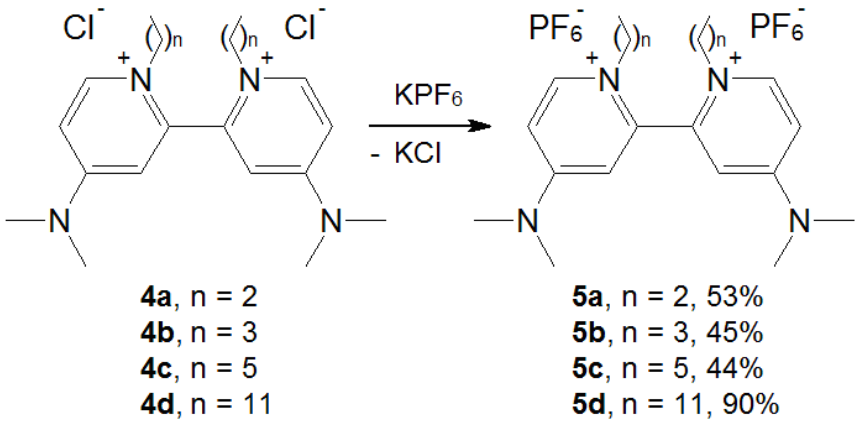
The two singlets at 3.27 and 3.24 ppm were assigned to the H_{d1} and H_{d2} nuclei, respectively, in the $N(CH_3)_2$ group. The observation of the two singlets for the $N(CH_3)_2$ was a consequence of the non-equivalence of the methyl groups due to substantial double bond character and hindered rotation about the N-C_{ring} bond, leaving one methyl group pointing towards the center of the molecule and one pointing away from it. This phenomenon could be explained by the contribution of resonance structure **4a′** (Figure 3.20). The remaining multiplet at 1.75 and triplet at 0.85 ppm were assigned to H_f and H_g, respectively.

The ^{13}C NMR characteristic peaks of **4a** (Figure 3.19b) included those at 157.2, 144.6, 143.4, 112.8, and 109.7 ppm, which were assigned to the bis-pyridinium ring C_h,

C_a, C_i, C_c, and C_b (Figure 3.19d), respectively. The two peaks found at 41.1 and 41.0 ppm were assigned to C_{d1} and C_{d2}, respectively, with these carbon nuclei being made chemically non-equivalent by the aforementioned restricted rotation of the C_{ring}-N bond, which caused one of the methyl groups to point internally and the other to point externally. The three remaining peaks at 57.2, 24.7, and 10.9 ppm were assigned to the N-alkyl C_e, C_f, and C_g, respectively.

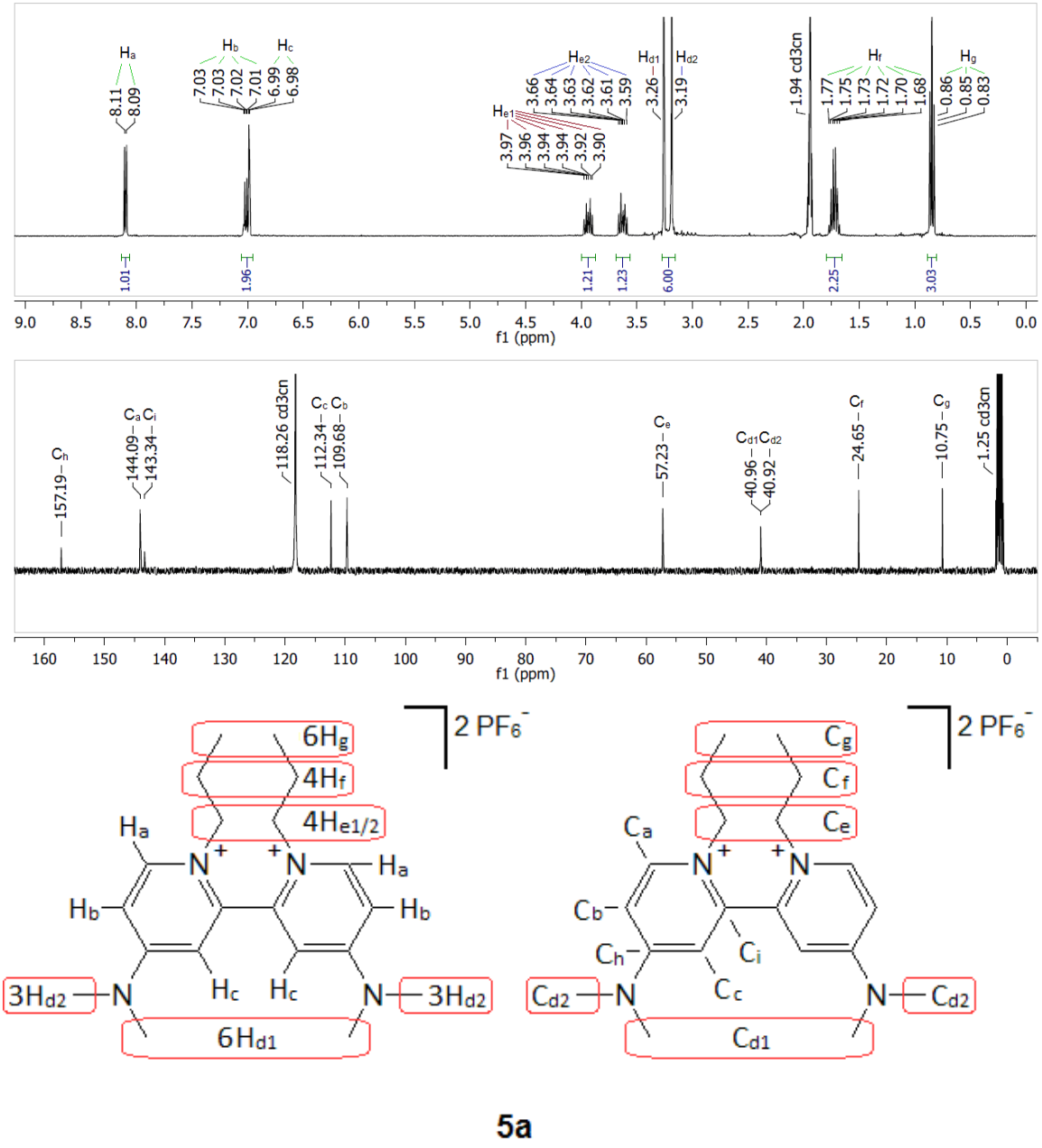
The chloride salts **4a-d** were shown to contain minor amounts of some impurity via ^{1}H NMR. Two small doublet peaks were always observed in the aromatic region at 8.1 and 6.9 ppm which were later found to be coupled together in the COSY spectrum. These peaks were highly reminiscent of the 8.11 and 6.89 ppm peaks assigned to the **2a-d** precursor salt aromatic 2 and 3 position C-*H*. A prominent singlet peak could also be observed at 3.17 ppm in **4a-d** and this too was nearly identical to the peak assigned to $N(CH_3)_2$ in **2a**-**d**. In light of these similarities, it was reasoned that the impurities from which these peaks manifested in the ^{1}H NMR of **4a-d** were analogues of **2a-d** with chloride anions instead of bromide ions. The emergence of these pyridinium salts may have been caused by thermal decomposition of the bis-pyridinylidenes upon addition of C_2Cl_6, being consistent with the exothermicity of the reaction (see Section 3.3.2). The heat-sensitivity of bis-pyridinylidenes **3a-d** was first observed when some of these compounds were found to have decomposed after heating *in vacuo* during the isolation process.

The melting point ranges of **4a-d** were also indicative of the impure nature of these salts, ranging between 3-7°C. The low purity of **4a-d** posed a number of issues, with the impurities being present in large enough quantities to complicate cyclic voltammetry experiments and solubility testing. To avoid these issues, the corresponding hexafluorophosphate analogues **5a-d** were prepared via metathesis of **4a-d** with potassium hexafluorophosphate (KPF_6) as a final synthetic step.



Scheme 3.5: Preparation of N,N-dialkyl-bis-2-(4-dimethylamino)pyridinium hexafluorophosphate salts **5a-d** with accompanying yields.

The hexafluorophosphate salts were produced in varying yields (Scheme 3.5) due to the small quantities of **4a-d** used for the metathesis and the variable effectiveness of the purification method (see Section 3.3.4). However, **5a-d** were hydrophobic rather than hygroscopic, which made their handling and purification much simpler compared to **4a-d**. Each salt was subjected to ^{19}F NMR in order to confirm the presence of hexafluorophosphate anions (not shown). The purity of **5a-d** was assessed via ^{1}H NMR and melting point determination, when applicable.



5a

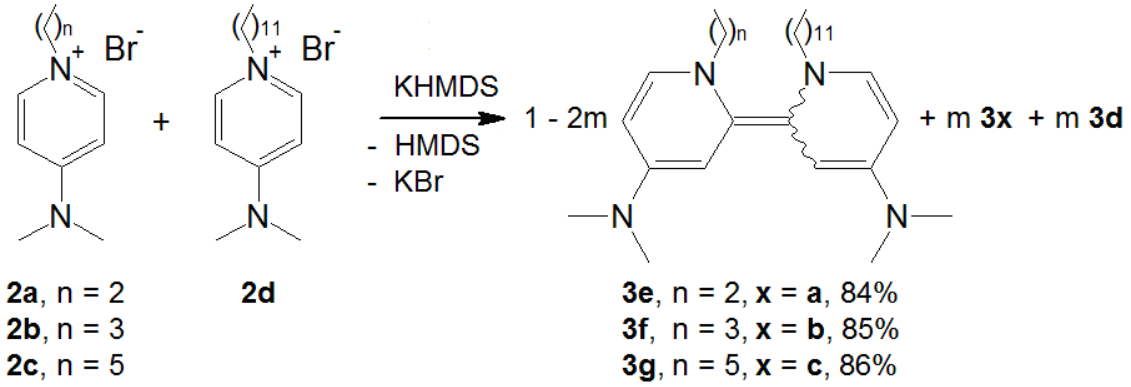
Figure 3.21: Top; ^{1}H NMR spectrum of 5a in CD_3CN (a). Middle; ^{13}C NMR spectrum of 5a in CD_3CN (b). Bottom; Structure of N,N-dipropyl-bis-2-(4-dimethylamino)pyridinium hexafluorophosphate **5a** with labelled hydrogen nuclei on the left (c) and carbon nuclei on the right (d).

The hexafluorophosphate salts **5a-d** appeared clean via ^{1}H NMR (see Section 3.3.8), showing only trace amounts of **2a-d** derivatives. The melting ranges were also

much narrower for **5c-d** as compared to **4c-d**, lying between 2-3°C in the former cases. Melting point ranges could not be determined for **5a** and **5b** as they decomposed before reaching their melting points. The ^{1}H and ^{13}C NMR assignments of **5a-d** were similar to those of **4a-d** with slight variability in the chemical shifts. Most of the peaks were found to have shifted upfield in **5a-d** compared to **4a-d**. The most dramatic movements in the ^{1}H NMR spectrum included that of the doublet assigned to H_a (Figure 3.21c), which had shifted from 8.44 ppm in **4a** to 8.10 ppm in **5a**, and that of the small doublet assigned to H_c which was found farther upfield from the doublet of small doublets assigned to H_b in **5a**. In the ^{13}C NMR spectrum of **5a** (Figure 3.21b), the only notable upfield shifts were those of the peaks assigned to C_a and C_c (Figure 3.21d) moving from 144.6 and 112.8 ppm to 144.1 and 112.3 ppm, respectively.

3.2.4 – Characteristics of Asymmetric N-Alkyl-N′-Dodecyl Bis-Pyridinylidenes

Some asymmetric N-alkyl-N′-dodecyl bis-pyridinylidenes **3e-g** were prepared in mixtures with **3a-c**, respectively, and **3d** via a route similar to **3a-d**, with the main distinction being the use of a 50:50 mix of **2d** and one of **2a-c**. The procedure also required homogenization of the salt mixtures via stirring in tetrahydrofuran (THF) overnight before the addition of potassium bis-(trimethylsilyl)amide (KHMDS).



Scheme 3.6: Synthetic scheme for generating the mixtures of **3a-c**, **3d**, and corresponding N-alkyl-N′-dodecyl-bis-2-(4-dimethylamino)pyridinylidene (**3e-g**), with accompanying yields assuming only **3e-g** were generated (m = 0).

The yields ranged from 84-86% and were reported with the assumption that only the asymmetrical **3e-g** were generated. The *E*/*Z* isomer ratios were not determined due to the complexity of the ^{1}H NMR spectra of these products (*vide infra*).

As seen in Figure 3.22a (*vide infra*), the product mixtures were relatively clean via ^{1}H NMR, with only traces of HMDS remaining after drying along with minimal amounts of decomposition products. However, the NMR characteristics were inconclusive as to the constitution of the products, being consistent with either **3e-g** or mixtures of **3d** and **3a-c**, respectively. This was due to the similarities for the expected ^{1}H and ^{13}C NMR signals of **3e-g** to the signals from **3d** and **3a-c**, which prevented the definitive assignment of the products in the mixtures.

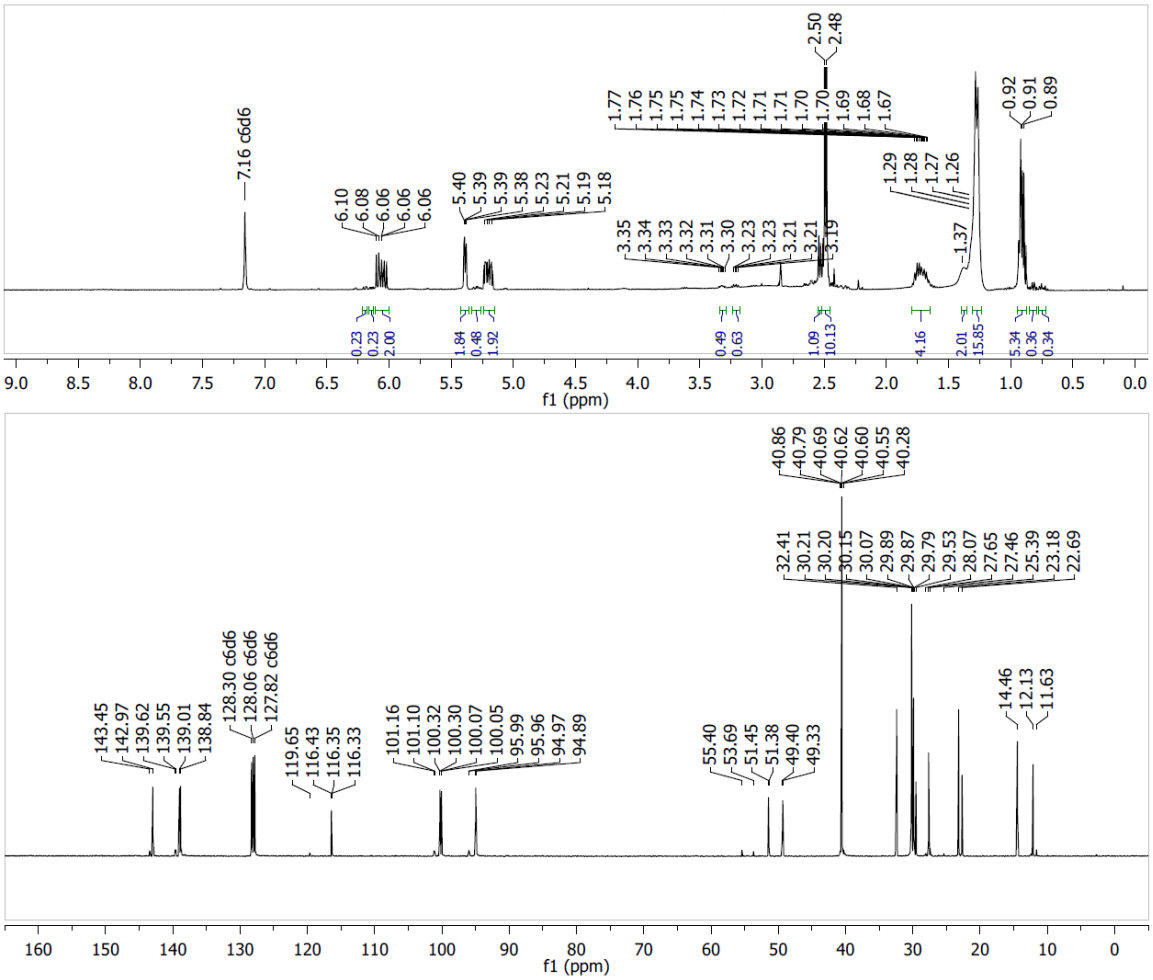
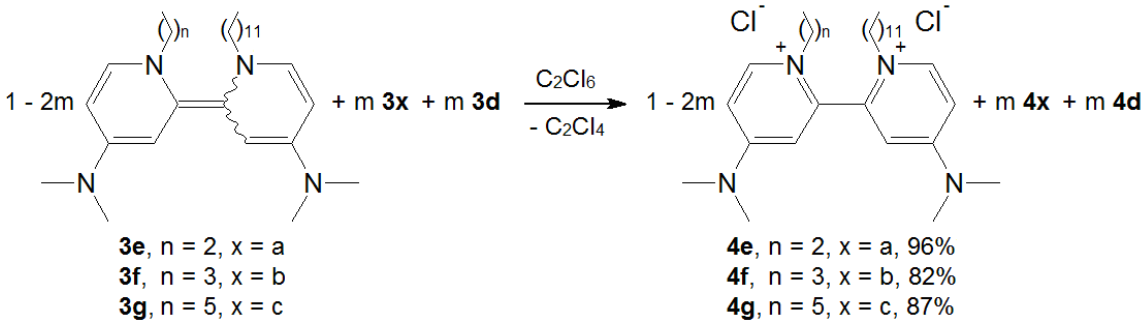


Figure 3.22: ^{1}H (top, a) and ^{13}C (bottom, b) NMR spectra of the product mixture containing **3e** in C_6D_6.

After attempts using column chromatography, the physical separation of the asymmetric **3e-g** from the symmetric **3d** and **3a-c** was deemed infeasible due to the assumed physical similarities of these compounds, so instead, mass spectrometry was considered for determining whether the asymmetric derivatives were indeed present. For this, the oxidation of the bis-pyridinylidene products into more stable chloride salts was required.



Scheme 3.7: The synthetic scheme for generating the mixtures of **4a-c**, **4d**, and corresponding N-alkyl-N′-dodecyl-bis-2-(4-dimethylamino)pyridinium chloride (**4e-g**), with accompanying yields assuming only **4e-g** were generated (m = 0).

The process for converting the mixtures of **3e-g** + **3a-c** + **3d** into chloride salts (Scheme 3.7) was identical to the procedure used for converting **3a-d** into chlorides (see Section 3.2.3) and afforded the mixtures of **4e-g** + **4a-c** + **4d** in yields of 82-96% (with yield calculations assuming the products were comprised solely of **4e-g**). Again several additional peaks were observed in the ^{1}H and ^{13}C NMR spectra of the chloride salts (see Section 3.3.8), but not enough to completely assign all the nuclei of the asymmetric compounds.

For the purposes of detecting the asymmetric compounds in the chloride mixtures, Electrospray Ion Mass Spectrometry (ESI-MS) was used because it is a “soft ionization” technique that induces very little fragmentation.[178]

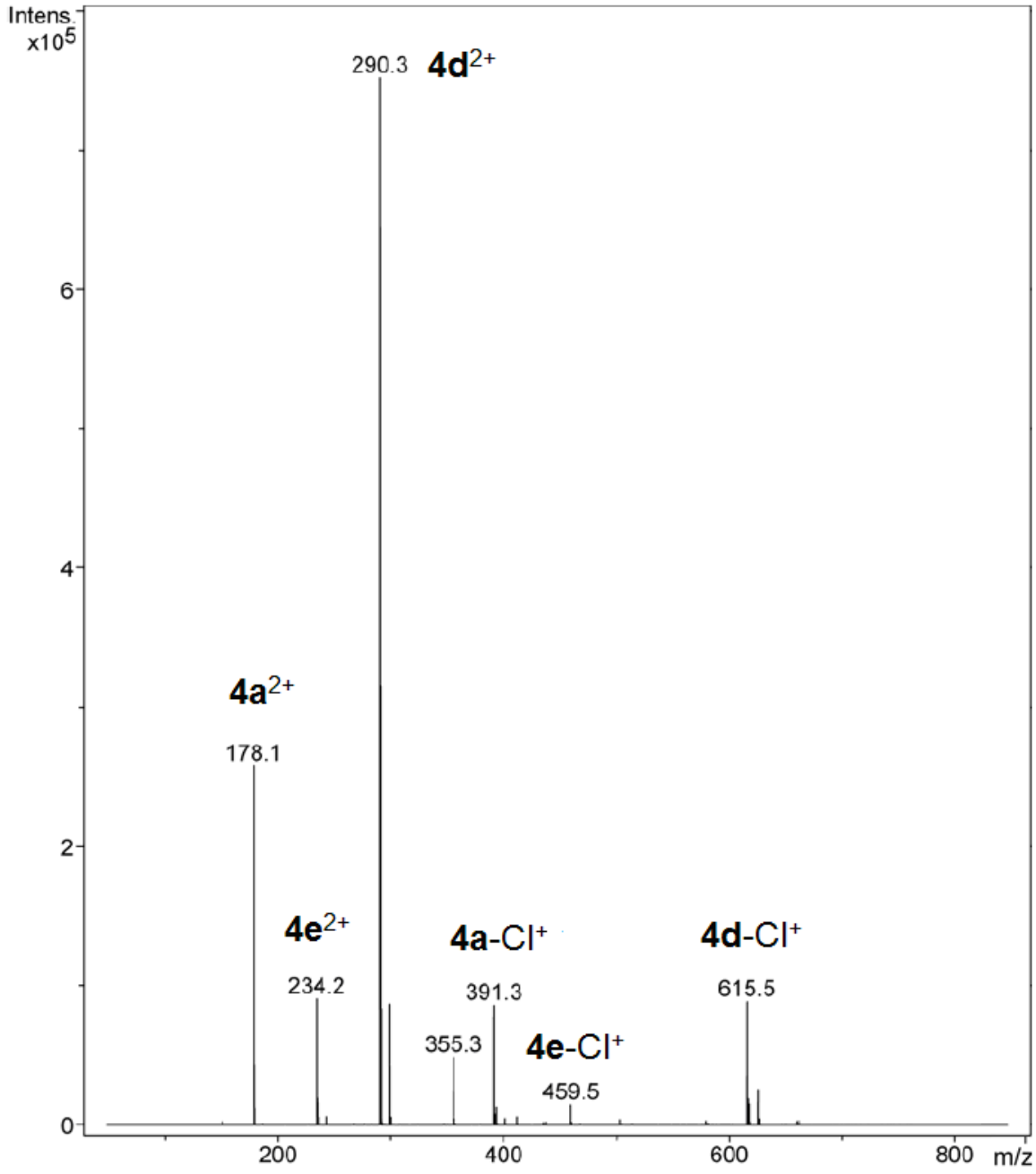
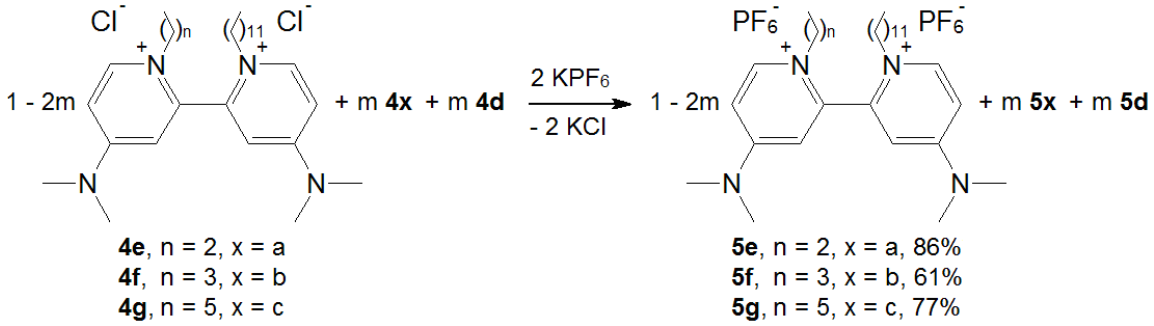


Figure 3.23: ESI-MS of chloride salt mixture **4e** + **4a** + **4d**.

The mass spectra of the chloride product mixtures (see Section 3.3.7) revealed the products to indeed be mixtures of **4e-g** + **4a-c** + **4d**, with high-resolution masses being

found for all three asymmetric compounds. However, the samples were not standardized, and therefore the mass-ratio of each salt in the mixtures could not be elucidated.

The chloride salt mixtures exhibited melting point ranges of 5-8°C due to them being mixtures. The chloride salt mixtures were also hygroscopic, and so metathesis of the chloride salt mixtures to hexafluorophosphate salt mixtures was performed in order to prepare the less hygroscopic hexafluorophosphate salt mixtures.



Scheme 3.8: The synthetic scheme for generating the mixtures of **5a-c**, **5d**, and corresponding N-alkyl-N′-dodecyl-bis-2-(4-dimethylamino)pyridinium hexafluorophosphate (**5e-g**), with accompanying yields assuming only **5e-g** were generated (m = 0).

The procedure for converting the chloride salt mixtures **4e-g** + **4a-c** + **4d** into hexafluorophosphate salt mixtures (Scheme 3.8) was identical to the procedure used for converting **4a-d** into **5a-d**, and afforded mixtures **5e-g** + **5a-c** + **5d** in yields ranging from 61-86% (yield calculated assuming the products were comprised solely of **5e-g**). The ^{1}H NMR spectra of the hexafluorophosphate salt mixtures (see Section 3.3.8) appeared relatively clean compared to those of the chloride salt mixtures, exhibiting much narrower melting point ranges of 1-2°C. As such, the hexafluorophosphate salt mixtures

containing **5e-g** were further analyzed in CV and solubility experiments.

3.2.5 – Electrochemistry, Melting Point, and Solubility Tests

The cyclic voltammetry (CV) experiment, as discussed previously (see Section 3.2.2), is a useful electroanalytical experiment for studying electron transfer processes in analytes of interest. The CV experiment can be used for elucidating such things as the redox potentials of novel compounds[179], in addition to thermodynamic information about these systems and involved species such as electron transfer kinetics and diffusion behavior.[180] Bis-pyridinylidene/bis-pyridinium redox couples tend to yield very low reduction potentials relative to other organic compounds, making them very attractive for potential applications as organic reducing agents and as anolytes in organic redox flow batteries.

The high oxidation potentials of bis-pyridinylidene compounds are a result of several stabilizing effects in the bis-pyridinium ions and destabilizing effects in the bis-pyridinylidenes. Stabilization of the bis-pyridinium ions is mainly from the aforementioned contribution of resonance stabilization from the labile π electrons of the NMe_2 groups into the aromatic rings, as supported by the restricted rotation of the C_{ring}-$N(CH_3)_2$ bond seen in the room temperature ^1H and ^{13}C NMR spectra. These same π electron effects raise the energy of the HOMO of the bis-pyridinylidene. In addition, the

bis-pyridinylidene suffers from steric effects that strain its geometry from the ideal planar arrangement, further raising the energy of the HOMO.[167]

While bridging together the two N_{ring} of bis-pyridinylidene/pyridinium compounds with alkyl chains has been studied in literature,[181] the effects of free elongated alkyl-chain substituents on the N_{ring} on the electrochemical properties of the bis-pyridinylidenes/pyridinium compounds had yet to be elucidated. Herein, the electrochemical effects of having alkyl-chain substituents on the N_{ring} of salts and salt mixtures of **5** were investigated.

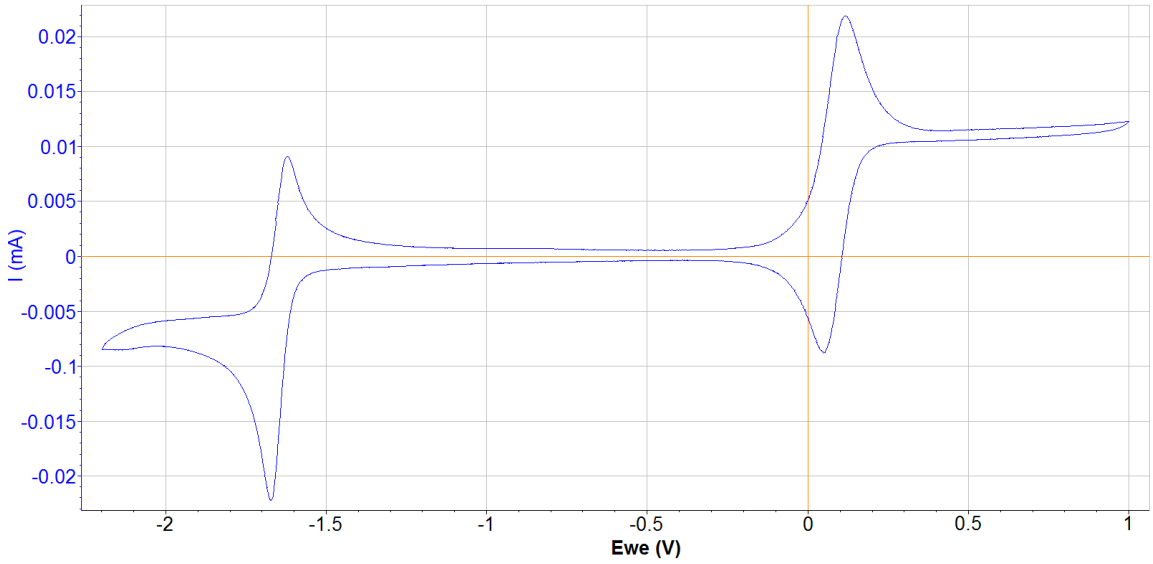


Figure 3.24: Cyclic voltammogram of 0.002 M **5a** with 0.001 M Ferrocene, recorded with 10 mV/s scan rate and ZIR correction, using a Ag/Ag+ reference electrode.

Firstly, the cyclic voltammograms of salts **5a-d** and salt mixtures **5e-g** + **5a-c** + **5d** (see Section 3.3.6) were exceptionally clean, showing no sign of chloride or bromide contamination in the +0.25-1.00 V region. Ferrocene was added as an internal reference

against which the $\mathbf{5^0/5^{2+}}$ redox couple potentials were measured, in which $\mathbf{5^0}$ is the neutral state of the species (analogous to species **3**). Ferrocene has a redox potential of 0.470 V vs. SCE in DMF,[164] and from this the redox potential of each salt was converted into potential vs. SCE (Table 3.1).

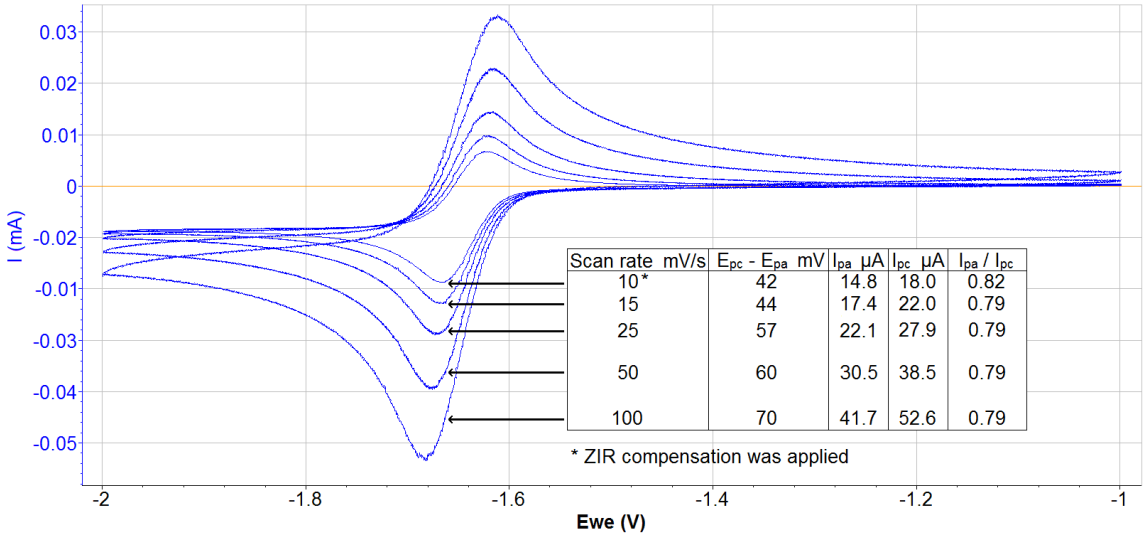
Table 3.1: Tabulated oxidation potentials ($E_{1/2}$) and peak separation potentials (E_{pc} - E_{pa}) of each individual salt **5a-d** and salt mixture **5e-g + 5a-c + 5d**, with respective peak separation potentials of their internal Fc reference.

Compound	$E_{1/2}$ vs. SCE (V)	E_{pc} - E_{pa} (mV) of **5**	E_{pc} - E_{pa} (mV) of Fc
5a	1.26	50	66
5b	1.26	54	65
5c	1.27	45	78
5d	1.26	51	65
5e + 5a + 5d	1.27	62	66
5f + 5b + 5d	1.26	62	77
5g + 5c + 5d	1.27	67	75

All compounds displayed oxidation potentials $E_{1/2}$ (Table 3.1) of 1.26 and 1.27 V vs. SCE, which were in-line with the methyl-substituted bis-pyridinylidene/bis-pyridinium $\mathbf{1/1^{2+}}$ redox couple $E_{1/2}$ of 1.27 vs. SCE,[148] and so it appeared that the addition of longer alkyl chain substituents did not have any discernible impact on the redox potentials of bis-pyridinylidene/bis-pyridinium couples. All bis-pyridinium hexafluorophosphate salts and salt mixtures exhibited 2-electron waves as evidenced by the peak separations which were between the ideal values of 29.6 mV for 2-electron

processes and 59.2 mV for 1-electron processes (actual values of 45-54 mV). The salt mixtures containing asymmetrically substituted derivatives exhibited wider peak separations outside of the 29.6-59.2 mV range (62-67 mV), but were still narrower than the peak separations found in the 1-electron wave for the ferrocene redox couple (65-78 mV), still supporting two-electron behavior. All of the salts and salt mixtures also exhibited larger peak currents for their reduction wave (I_{pa}) compared to those of their oxidation waves (I_{pc}), signifying that the bis-pyridinium/bis-pyridinylidene redox process was not completely reversibile.[182]

In order to better evaluate the nature of the issue of reversibility, several CV experiments were conducted on **5a** at different scan rates.



Scan rate mV/s	E_{pc} - E_{pa} mV	I_{pa} µA	I_{pc} µA	I_{pa} / I_{pc}
10*	42	14.8	18.0	0.82
15	44	17.4	22.0	0.79
25	57	22.1	27.9	0.79
50	60	30.5	38.5	0.79
100	70	41.7	52.6	0.79

Figure 3.25: Cyclic voltammogram of 0.002 M **5a**, recorded at various scan rates between -2 and -1 V, using a Ag/Ag+ reference electrode. The 10 mV/s scan had ZIR correction applied to it.

The different scan rates (Figure 3.25) caused a widening of the electrochemical potential gap between the reduction and oxidation peaks of the **5a^0/5a^{2+}** couple (E_{pc} - E_{pa}). In addition, the I_{pa} and I_{pc} were found to increase linearly for the 15-100 mV/s scan rates, with the 10 mV/s sweep being excluded due to ZIR correction effects. The increase in E_{pc} - E_{pa} and linear increase in both I_{pa} and I_{pc} with the square-root of the scan rate was indicative that the process was limited by diffusion.[183] However, the ratio of the anodic and cathodic peak currents (I_{pa}/I_{pc}) was a constant 0.79 at 15, 25, 50, and 100 mV/s scan rates, while being 0.82 at 10 mV/s with ZIR correction. The straying of I_{pa}/I_{pc} from unity corresponded with this redox couple system having "limited reversibility" under these conditions.[184] The I_{pa} being smaller than the I_{pc} of the **5a^0/5a^{2+}** couple linearly at all scan rates would indicate that the process responsible for the limited reversibility of the **5a^0/5a^{2+}** redox process may have been due to a difference in diffusion coefficients between **5a^{2+}** and **5a^0**.

To verify this, the Randles-Sevcik equation[185] was used to determine the diffusion coefficients D (cm^2/s) of the oxidized **5a^{2+}** and reduced **5a^0** species in the 0.1 M TBAH in DMF electrolyte used in these experiments,

$$I_p = 0.4463\, nFAC\sqrt{\frac{nFvD}{RT}} + b \qquad (\mathbf{3.2.2-1})$$

where I_p is the peak current (mA), n is the number of electrons transferred during redox, A is the surface area of the electrode (μm^2), F is the Faraday Constant (96483.6 mA·s/mmol), C is the concentration (mmol/mL), v is the scan rate (mV/s), R is the Gas Constant (8314.46 mVm·C/K·mmol), T is the temperature (K), and b is the sum of

corrective current factors for a non-idealized cell system at rest (mA). The diffusion coefficient of an electroactive species is typically calculated from the slope of I_p vs. $v^{1/2}$. In this experiment, $n = 2$, $A = 0.2827$ cm^2, $C = 0.002$ mmol/cm^3, and T = 298 K, so equation 3.2.2 – 1 could be simplified to

$$D = 0.0054138\left(\frac{I_p - b}{v^{1/2}}\right)^2 \qquad (\mathbf{3.2.2 - 2})$$

in order to solve for diffusion coefficient D.

Table 3.2: Calculated diffusion coefficients of **5a^0** (D_{5a0}) and **5a^{2+}** (D_{5a2+}) at scan rates of 15, 25, 50, and 100 mV/s using Equation 3.2.2 – 2 in addition to the average diffusion coefficient with standard deviation (σ), relative standard deviation ($RSD\%$), and corrective factor b.

v (mV/s)	D_{5a0} (cm^2/s)	D_{5a2+} (cm^2/s)
15	8.3 x 10^{-8}	1.33 x 10^{-7}
25	8.6 x 10^{-8}	1.36 x 10^{-7}
50	8.7 x 10^{-8}	1.37 x 10^{-7}
100	8.4 x 10^{-8}	1.35 x 10^{-7}
Slope-derived D	8.4 x 10^{-8} cm^2/s	1.35 x 10^{-7} cm^2/s
σ	±0.15 x 10^{-8} cm^2/s	±0.023 x 10^{-7} cm^2/s
$RSD\%$	1.8 %	1.7 %
Corrective factor b	2.23 x 10^{-3} mA	2.89 x 10^{-3} mA

The slope-calculated diffusion coefficients revealed that the diffusion of the reduced **5a^0** was 38% slower than that of the oxidized **5a^{2+}**. It was reasoned that the limited diffusion

of **5a**^{0} may have accounted for the limited reversibility of the **5a**$^{0/}$**5a**$^{2+}$ redox couple by causing a disproportionately lower quantity of **5a**^{0} to return to the electrode to be re-oxidized into **5a**$^{2+}$ compared to the amount of **5a**$^{2+}$ that could reach the electrode during the reduction phase. The corrective factor *b* was the approximate sum of peak current effects from other phenomena that did not follow Fick's laws of diffusion[186] from which Randles-Sevcik equation was derived. Such phenomena could include the cell system being perturbed by vibrations or shocks, or undesirable side reactions that depleted **5a**^{0} or **5a**$^{2+}$ at the WE interface in which case *b* would stray from a constant value to instead become a complex value that better reflects the kinetics of these side reactions. Consequently, a complex factor *b* should have made Equation 3.2.2 – 2 insufficient for solving the diffusion coefficients of **5a**^{0} and **5a**$^{2+}$. In this case, the factor *b* was a smaller value for **5a**^{0} compared to **5a**$^{2+}$, which could have indicated that **5a**^{0} was involved in a side-reaction that was causing its depletion at the WE interface. However, the factors of both **5a**^{0} and **5a**$^{2+}$ both appeared to be constant, and so it was concluded that any side-reactions involving **5a**^{0} were too insignificant to warrant a non-constant *b* if these side-reactions were indeed present at all. Therefore, it was reasoned that the predominant effect which led to the lowered reversibility of the **5a**$^{0/}$**5a**$^{2+}$ redox couple was the difference in diffusion coefficient between **5a**^{0} and **5a**$^{2+}$.

Melting points were also carried out on all chloride and hexafluorophosphate salts and salt mixtures (Table 3.3), with the melting of the chlorides having been carried out under argon atmosphere in sealed capillary tubes due to the hygroscopic nature of these salts and salt mixtures.

Table 3.3: Melting point ranges of chloride salts and salt mixtures **4x** and hexafluorophosphate salts and salt mixtures **5x**.

Substituents (**x**)	Melting point - **4x** (°C)	Melting point - **5x** (°C)
a	152-155	>220 (decomposed)
b	130-133	>220 (decomposed
c	115-119	77-79
d	65-67	65-68
e + a + d	65-70	75-77
f + b + d	116-123	72-74
g + c + d	119-124	74-76

A clear trend in lowering melting range was seen in the symmetric chloride and hexafluorophosphate salts of **a-d**, with compounds having longer alkyl groups exhibiting the lowest melting points, down to ranges of 65-67 and 65-68°C, respectively (Table 3.3). The chloride salt mixtures of **4e-g + 4a-c + 4d** exhibited broad melting ranges, likely due to containing both **2a-c** and **2d** chloride derivative impurities, respectively. In addition, the melting ranges of **e-g + a-c + d** in both chloride and hexafluorophosphate forms were higher than the symmetric didodecyl salts, which was counter to the reported trend of lowering melting point with higher difference in N-alkyl substituent chain lengths in viologens.[152]

The solubility of each chloride and hexafluorophosphate salt and salt mixture was assessed in dimethylformamide (DMF), a common organic solvent for redox flow battery

electrolyte solvents.[133] The tests were carried out via the addition of small amounts of DMF to excesses of each salt (~50 µL DMF per 50 mg of salt). The resulting mixtures were stirred for 5 minutes and then allowed to settle for 10-15 minutes. An Eppendorf micropipette was used to transfer a fixed volume of each solution (200 µL for chlorides **4**, 50 µL for hexafluorophosphates **5**) into vials which were placed under high vacuum with >100°C heating from a heatgun for short 1-2 minute lapses. The vials were pre-weighed beforehand, weighed again immediately after the addition of the solutions, and then weighed several times in between drying until their masses remained unchanged. The dry salts and salt mixtures were found to contain very little residual DMF, or moisture in the chlorides, via ^{1}H NMR in dry CD_3CN (not shown).

Table 3.4: Saturated solution concentrations of each salt and salt mixture in DMF.

Substituents (**x**)	Molarity - **4x** (mmol/mL)	Molarity - **5x** (mmol/mL)
a	0.18	0.67
b	0.26	0.60
c	0.41	0.70
d	0.45	0.57
e + a + d	0.58	0.69
f + b + d	0.52	0.92
g + c + d	0.51	0.84

In the **4x** series, a clear trend of higher saturated solution concentrations was observed in salts with increasing alkyl chain length (Table 3.4), while a trend of

increasing concentration with increasing difference in chain length was also observed in the mixtures containing **4e-g**. Both of these trends were in agreement with the initial hypotheses of this research (see Section 3.1.1). The **5x** salts yielded even higher solution concentrations than what was achievable in the chlorides. The variability in **5x** concentrations was likely due to measurement uncertainty arising from the much smaller scale of these experiments. The smaller scale was necessitated by the much smaller amounts of hexafluorophosphate salts available for solubility tests, as compared to the chloride salts. Of note were the unprecedented solution concentrations achieved in hexafluorophosphate salt mixtures 5**f** + 5**b** + 5**d** and 5**g** + 5**c** + 5**d**, which could be dissolved in concentrations of up to 0.92 and 0.84 M in DMF, respectively. These values are much higher than any reported concentration of organic active material in a redox flow battery, and make these compounds promising candidate as anolyte materials.

3.2 – Conclusions and Future Work

In this work, four novel N,N-dialkyl-bis-2-(4-dimethylamino)pyridinylidene compounds **3a-d** have been synthesized and successfully isolated for the first time, with their purities being certified via ^{1}H NMR and cyclic voltammetry experiments. These bis-pyridinylidenes exhibited *E*/*Z* isomerism about the C_{ring}=C_{ring} double bond, with a *E*/*Z* isomer ratio of 1 to 6.6-7.4. All four bis-pyridinylidenes were fully-characterized via both ^{1}H and ^{13}C NMR. Of these four, only the N,N-dipropyl bis-pyridinylidene **3a** was fully assigned in regards to both *E* and *Z* isomers via ^{1}H with the use of 2D NMR and variable

temperature NMR experiments. The unresolved N-CH_2 peak was made to coalesce in high temperature VT NMR experiments in **3a**, and found to couple to peaks belonging to the major isomer. It was reasoned that the N-CH_2- could only be diastereomeric in the *Z* isomer where steric hindrance of the alkyl groups was most likely to be occurring, and as such it was concluded that the *Z* isomer was the major isomer in **3a** and further reasoned to be the major isomer in **3b-d** as well. In addition, three mixtures containing N-alkyl-N′-dodecyl-bis-2-(4-dimethylamino)pyridinylidene, the appropriate N,N-dialkyl bis-pyridinylidene, and N,N-didodecyl bis-pyridinylidene, were generated.

From the bis-pyridinylidene isolates and pure mixtures were prepared N,N-dialkyl-2-(4-dimethylamino)pyridinium chloride salts **4a-d** and N-alkyl-N′-dodecyl-bis-2-(4-dimethylamino)pyridinium chloride salt mixtures **4e-g + 4a-c + 4d**, respectively, with the pure salts being fully characterized via ^{1}H NMR, ^{13}C NMR, and melting point, while the salt mixtures could only be partially characterized via ^{1}H NMR, ^{13}C NMR, and melting point. Electrospray ionization mass spectrometry (ESI-MS) experiments were conducted on the chloride salt mixtures and confirmed the presence of the asymmetric derivatives in these mixtures. The chloride salts and salt mixtures were hygroscopic, so they were subsequently metathesised into hexafluorophosphate salts **5a-d** and salt mixtures **5e-g + 5a-c + 5d** for the purposes of CV and solubility determination experiments.

Cyclic voltammetry experiments of the hexafluorophosphate salts and salt mixtures revealed that these compounds exhibited 2-electron redox waves with $E_{1/2}$

between -1.26 and -1.27 V vs. SCE in DMF electrolyte, which agreed closely with the redox potential of -1.27 V vs. SCE reported for the N,N-dimethyl-bis-2-(4-dimethylamino)pyridinylidene/pyridinium couple under the same conditions in literature.[148] As such it was concluded that the addition of longer alkyl chains had insignificant effect on the electrochemical potentials of the resulting bis-pyridinylidene/pyridinium redox couples. It was also found that the hexafluorophosphate salts and salt mixtures exhibited limited redox wave reversibility, which was reasoned to be due to differences between the diffusion rates of the reduced $\mathbf{5}^{\mathbf{0}}$ and the oxidized $\mathbf{5}^{\mathbf{2+}}$ under these cyclic voltammetry experimental conditions.

The saturated DMF concentrations of the symmetric chloride salts **4a-d** increased with chain length in the symmetric chloride salts **4a-d** from 0.18 to 0.45 M for **4a** and **4d**, respectively. The achievable saturated concentrations also increased with the difference in chain length of the asymmetric chloride salt mixtures **4e-g** + **4a-c** + **4d** from 0.51 to 0.58 M for mixtures containing **4g** and **4e**, respectively. The hexafluorophosphate salts exhibited saturated concentrations in excess of 0.55 M. Even so, the mixture of **5f** + **5b** + **5d**, could be dissolved in concentrations of up to 0.92 M in DMF, a 2300% increase over the solution concentration of the N,N-dimethyl-bis-2-(4-dimethylamino)pyridinium hexafluorophosphate salt of 0.04 M in DMF, used in all-organic flow cells.[147]

The addition of alkyl chain substituents has proven to be a simple and effective method of drastically improving the solubility of bis-pyridinium salts in organic solvents. The enhanced solubilities of the alkylated bis-pyridinium salts will yield flow batteries

with higher energy densities. Indeed, salts of N,N-dihexyl bis-pyridinium are already undergoing tests in flow batteries, with these experiments being conducted by Hillary Christina Wheeler of UNB, Fredericton, *circa* 2015. The addition of long alkyl chains to the pyridine ring N site could also be applied to other super electron donors in order to improve their solubilities for application in flow batteries.

The diffusion of the neutral bis-pyridinylidene species through the flow battery's ion-selective membrane separator[147] is an ongoing issue, however, with this effect resulting in rapid degradation in the performance of the cell. In order to limit such behavior, bis-pyridinium/pyridinylidene compounds with alkylammonium substituents are also being designed and tested in flow batteries as part of Hillary's work, with such compounds maintaining ionic character even when reduced to the bis-pyridinylidene species. In other future work, asymmetrically substituted bis-pyridinium/pyridinylidenes with an akyl chain on one ring and an alkylammonium chain on the other could be synthesized and more easily separated from the mixtures of symmetrically substituted derivatives. These asymmetric compounds might boast further-enhanced solubilities while also maintaining their ionic character in the neutral bis-pyridinylidene state. If successful, such improvements could be explored for other organic electroactive materials for use in flow batteries as well.

3.3 – Materials, Preparation, and Characterization

Reagents used in synthesis: Bromopropane, bromobutane, bromohexane, bromododecane, and potassium hexafluorophosphate were bought from Alfa Aesar and used as purchased. 4-dimethylaminopyridine, potassium bis(trimethylsilyl)amide, and hexachloroethane were bought from Sigma Aldrich and used as purchased. Silica gel was bought from VWR Scientific Products and dried at 200°C under vacuum before use. 4Å-pore 1-2 mm pellet molecular sieves purchased from Alfa Aesar and flame-dried under vacuum before use. Calcium hydride (92%) was purchased from Alfa Aesar.

Reagents used in electrochemical analysis: Tetrabutyl ammonium hexafluorophosphate (TBAHP, 99+% ACS grade) and silver nitrate (99+% ACS grade) were purchased from Sigma Aldrich and used without any further purification. Ferrocene was purchased from Sigma Aldrich and recrystallized from hot n-hexanes, powdered, and dried under vacuum before use.

Dry solvents: All the following solvents were degassed via freeze-pump-thaw and stored over molecular sieves inside a glovebox under argon atmosphere before use. Anhydrous tetrahydrofuran and diethyl ether were acquired from a Glass Contour Solvent Purification System supplied by Pure Process Technology. Acetonitrile, n-hexanes, and benzene-d6 (99.6% Deuterium) were purchased from Sigma Aldrich, dried over calcium hydride, and distilled before use. Acetonitrile-d3 (99.8% Deuterium) was purchased from Cambridge Isotope Laboratories, Inc., dried over calcium hydride, and distilled before

use. Anhydrous dimethylformamide (99.8%) was purchased from EMD Millipore and simply stored over molecular sieves under argon atmosphere for drying before use.

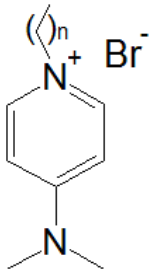
Other solvents: 95% ethanol was purchased from Greenfield Specialty Alcohols Inc.. Isopropanol was purchased from Sigma Aldrich.

Instruments: The Glass Contour Solvent Purification System was department-shared and supplied by Pure Process Technology. The 300 and 400 MHz NMR magnets were supplied by Oxford Instruments and used Unity Inova Varian and Agilent Technologies 400NMR operating systems, respectively. The glovebox was a Pure Lab PL-HE-4GB-2400 system from Innovative Technology. The melting point apparatus was a DigiMelt MPA160 produced by Stanford Research Systems, Inc. (a temperature ramp rate of 2°C/min was used in all melts). Mass spectra were acquired at Dalhousie University's Maritime Mass Spectrometry Laboratory by Xiao Feng using a Bruker microTOF Focus Mass Spectrometer for both low-resolution and high-resolution spectra.

Cyclic Voltammetry procedure: All reagents and solvents were stored and all experiments were performed inside a glovebox under argon atmosphere at 28 ± 1°C. All solvents used in electrochemical experiments were dry and oxygen-free. The instrument used to conduct cyclic voltammetry was a Biologic SP-150 Research Grade Potentiostat/Galvanostat, equipped with Electrochemical Impedance Specstroscopy capability. Where noted, "current-resistance determination and compensation by impedance measurement technique" (ZIR) was applied in the cyclic voltammetry

experiments as a built-in instrumental technique. The experimental setup was a three-electrode system comprised of LPTE platinum working electrode (exposed Pt disk surface diameter of 3 mm), platinum wire counter electrode, and a non-aqueous silver/silver chloride reference electrode. Before each experiment, the platinum disk working electrode was polished and wiped clean using a kimwipe. A fresh reference electrode was prepared one day before each series of experiments and comprised of a silver wire, shine-polished with oven-dried glass filter paper, submerged in an acetonitrile solution of 0.1 M tetrabutylammonium hexafluorophosphate (TBAPF) - 0.01 M AgCl inside a porous-glass-tip electrode. When not used, the reference electrode was stored with the tip submerged in a 0.1 M TBAPF acetonitrile solution inside a freezer at -38°C. The electrolyte used in the the cyclic voltammetry experiments was 0.1 M TBAPF in DMF, and all electrodes were thoroughly rinsed with 0.1 M TBAPF in DMF just prior to each experiment. Cyclic voltammetry was performed using 3 mL of 0.1 M TBAPF in DMF, using 0.001-0.002 M of the analyte compounds and 0.001-0.002 M of ferrocene, unless otherwise specified.

3.3.1 – N-Alkyl-4-Dimethylaminopyridinium Bromide Salts (2)



2a, n = 2
2b, n = 3
2c, n = 5
2d, n = 11

Figure 3.26: Structure of N-propyl (**2a**), N-butyl (**2b**), N-hexyl (**2c**), and N-dodecyl (**2d**) -4-dimethylaminopyridinium Bromide.

To an acetonitrile solution of 4-dimethylaminopyridine was added 1.6 equivalents of bromoalkane (~5 mL of acetonitrile per gram of 4DMAP) of appropriate alkyl chain length. The resulting reaction mixtures were stirred at room temperature until the reaction mixtures no longer contained any 4DMAP via ^{1}H NMR. The product salts then were precipitated using ~3 mL of cold diethyl ether per gram of 4DMAP originally used, the precipitates then being collected via filtration and washed with three portions (each ~1 mL per gram of 4DMAP originally used) cold diethyl ether. The product salts were recrystallized from a mixture of hot diethyl ether - propanol for **2** and hot diethyl ether – ethanol for **3-5**, vigorously stirring the alcohol solutions of the product salts with heating while adding small amounts of diethyl ether. The solutions eventually became cloudy, at which point no further diethyl ether was added and the solutions were merely stirred and heated up until they became clear. At that point, stirring and heating were stopped and

further disturbances were kept to a minimum, the solutions were sealed and allowed to cool to room temperature, and then stored in a fridge set at -25°C for 24-48 hours in order to grow the crystals.



Figure 3.27: N-propyl-4-dimethylaminopyridinium bromide salt (**2a**) crystals grown in a cold mixture of isopropanol and diethyl ether.

The resulting clear colorless crystallized salts (Figure 3.27) were filtered and washed several more times with cold diethyl ether (~1 mL per gram of 4DMAP originally used). The process yielded beautiful crystals which were then unceremoniously crushed into fine powder using an oven-dried mortar and pestle. The resulting powders were dried under high vacuum with periodic heating using a heat-gun. Finally, the dry white powder products were brought into a glovebox for weighing and then characterized

via ^{1}H and ^{13}C NMRs and melting point determination. The final yield for this step ranged from 74-88%.

2a: 4-dimethylaminopyridine (4.00 g, 32.8 mmol) and 1-bromopropane (6.45 g, 52.4 mmol) were used; Reaction mixture was stirred for 4 days. The product was crystallized from Et_2O/iPrOH mixture (10 mL/ 5 mL). Yield: 6.62 g (83%); mp: 162-163°C (146-148°C[187]); ^{1}H NMR (300 MHz, CD_3CN) δ 0.89 (3H, t, CH_3), 1.84 (2H, m, CH_2), 3.17 (6H, s, $N(CH_3)_2$), 4.12 (2H,t, NCH_2), 6.89 (2H, d, J = 6.0 Hz, ArH), 8.11 (2H, d, J = 6.0 Hz, ArH); ^{1}H NMR (400 MHz, $CDCl_3$) δ 0.94 (3H, t, CH_3), 1.91 (2H, m, CH_2), 3.26 (6H, s, $N(CH_3)_2$), 4.31 (2H,t, NCH_2), 7.01 (2H, d, J = 7.6 Hz, ArH), 8.53 (2H, d, J = 7.6 Hz, ArH); ^{13}C NMR (400 MHz, $CDCl_3$) δ 10.5 (CH_3), 24.4 (CH_2), 40.5 (NCH_3), 59.4 (NCH_2), 108.3 (CH), 142.6 (CH), 156.2 (C).

2b: 4-dimethylaminopyridine (4.00 g, 32.8 mmol) and 1-bromobutane (7.07 g, 57.5 mmol) were used; Reaction mixture was stirred for 4 days. The product was crystallized from Et_2O/EtOH mixture (10 mL/ 5 mL). Yield: 6.60 g (78%); mp: 218-220°C (lit. 221.85°C[188]); ^{1}H NMR (300 MHz, CD_3CN) δ 0.93 (3H, t, CH_3), 1.31 (2H, m, CH_2), 1.78 (2H, m, CH_2), 3.16 (6H, s, $N(CH_3)_2$), 4.10 (2H, t, NCH_2), 6.85 (2H, d, J = 7.8 Hz, ArH), 8.00 (2H, d, J = 7.8 Hz, ArH); ^{1}H NMR (400 MHz, $CDCl_3$) δ 0.83 (3H, t, CH_3), 1.26 (2H, m, CH_2), 1.77 (2H, m, CH_2), 3.18 (6H, s, $N(CH_3)_2$), 4.26 (2H, t, NCH_2), 6.96 (2H, d, J = 7.5 Hz, ArH), 8.45 (2H, d, J = 7.5 Hz, ArH); ^{13}C NMR (400 MHz, $CDCl_3$) δ 13.6 (CH_3), 19.3 (CH_2), 33.1 (CH_2), 40.5 (NCH_3), 57.9 (NCH_2), 108.4 (CH), 142.6 (CH), 156.2 (C).

2c: 4-dimethylaminopyridine (4.00 g, 32.8 mmol) and 1-bromohexane (8.62 g, 52.2 mmol) were used; Reaction mixture was stirred for 4 days. The product was crystallized from Et_2O/EtOH mixture (10 mL/ 5 mL). Yield: 6.92 g (74%); mp: 194-195°C (lit. 195.85°C[188]); ^{1}H NMR (300 MHz, CD_3CN) δ 0.88 (3H, t, CH_3), 1.29 to 1.32 (6H, broad m, $(CH_2)_3$), 1.80 (2H, m, CH_2), 3.16 (6H, s, $N(CH_3)_2$), 4.09 (2H, t, NCH_2), 6.85 (2H, d, J = 7.8 Hz, ArH), 7.99 (2H, d, J = 7.8 Hz, ArH); ^{1}H NMR (400 MHz, $CDCl_3$) δ 0.72 (3H, t, CH_3), 1.29 to 1.34 (6H, broad m, $(CH_2)_3$), 1.75 (2H, m, CH_2), 3.16 (6H, s, $N(CH_3)_2$), 4.22 (2H, t, NCH_2), 6.96 (2H, d, J = 7.5 Hz, ArH), 8.41 (2H, d, J = 7.5 Hz, ArH); ^{13}C NMR (400 MHz, $CDCl_3$) δ 13.9 (CH_3), 22.3 (CH_2), 25.7 (CH_2), 31.1 (CH_2), 31.1 (CH_2), 40.5 (NCH_3), 58.2 (NCH_2), 108.4 (CH), 142.5 (CH), 156.2 (C).

2d: 4-dimethylaminopyridine (4.00 g, 32.8 mmol) and 1-bromododecane (12.79 g, 51.3 mmol) were used; Reaction mixture was stirred for 2 days. The product was crystallized from Et_2O/EtOH mixture (10 mL/ 5 mL). Yield: 10.71 g (88%); mp: 70-71°C (lit. 72°C[189]); ^{1}H NMR (300 MHz, CD_3CN) δ 0.88 (3H, t, CH_3), 1.27 (18H, broad m, $(CH_2)_9$), 1.79 (2H, m, CH_2), 3.16 (6H, s, $N(CH_3)_2$), 4.06 (2H, t, NCH_2), 6.83 (2H, d, J = 5.9 Hz, ArH), 7.94 (2H, d, J = 5.9 Hz, ArH); ^{1}H NMR (400 MHz, $CDCl_3$) δ 0.87 (3H, t, CH_3), 1.23 to 1.30 (18H, broad m, $(CH_2)_9$), 1.87 (2H, m, CH_2), 3.27 (6H, s, $N(CH_3)_2$), 4.33 (2H, t, NCH_2), 7.02 (2H, d, J = 7.6 Hz, ArH), 8.44 (2H, d, J = 7.6 Hz, ArH); ^{13}C NMR (400 MHz, $CDCl_3$) δ 14.03 (CH_3), 22.6 (CH_2), 26.0 (CH_2), 29.0 (CH_2), 29.2 (CH_2), 29.3 (CH_2), 29.4 (CH_2), 29.5 (CH_2), 29.5 (CH_2), 31.1 (CH_2), 31.8 (CH_2), 40.5 (NCH_3), 58.2 (NCH_2), 108.4 (CH), 142.4 (CH), 156.2 (C).

3.3.2 – N,N-Dialkyl and N-Alkyl-N′-Dodecyl Bis-Pyridinylidenes (3)

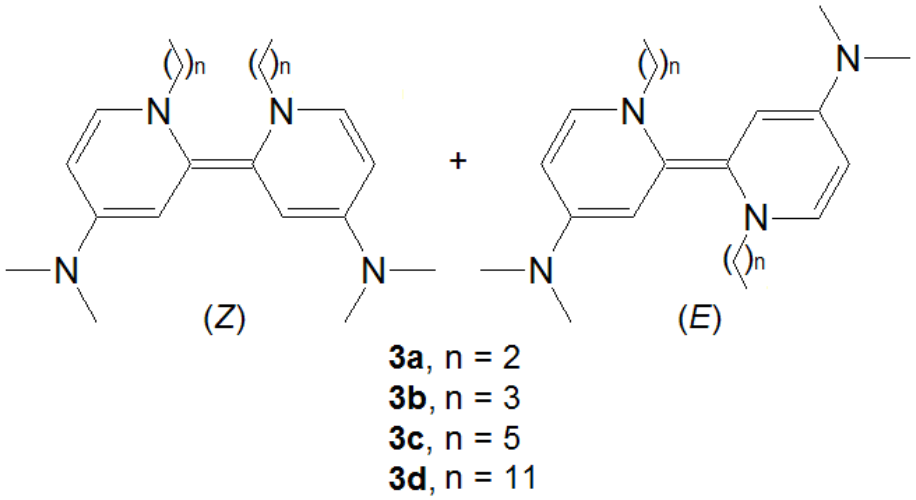


Figure 3.28: Structures of N,N-dipropyl (**3a**), N,N-dibutyl (**3b**), N,N-dihexyl (**3c**), and N,N-didodecyl (**3d**) -bis-2-(4-dimethylamino)pyridinylidene.

This step needed to be conducted entirely inside a glovebox using oven-dried glassware. Solvents used in this step also needed to be moisture/oxygen-free. To a tetrahydrofuran solution of the appropriate precursor salt in tetrahydrofuran (~4 mL of THF per gram of KHMDS used) was added 1.05-1.10 equivalents of bis(trimethylsilyl)amide (KHMDS). The resulting mixture immediately changed to an opaque red-tinted liquid, and was stirred overnight. To protonate residual KHMDS into HMDS to be later removed through heating *in vacuoo*, the product mixtures were vacuum-filtered through a bed of silica gel in a fine grade glass-sintered funnel with three THF washings (10 mL each). The product mixtures were then concentrated under vacuum with stirring and gentle heating (~50 °C) for up to an hour. Care was taken not to overheat the products as they were heat-sensitive. After drying, ^{1}H NMR showed that the product mixtures contained only the bis-pyridinylidene and HMDS.

Each product was filtered once more through dry silica gel using n-hexanes as solvent (8 mL). The filter was then washed with n-hexanes (3 portions of 5 mL), and the resulting filtrates were re-concentrated *in vacuo* with stirring and gentle heating (~50°C) for up to 6 hours to remove volatile HMDS. The removal of HMDS with this method was deemed complete when the product liquids stopped bubbling, with its absence being verified via ^{1}H NMR of the products. The total process afforded isolates of **3a-d** as viscous black red-tinted liquids in yields of 66-82%.

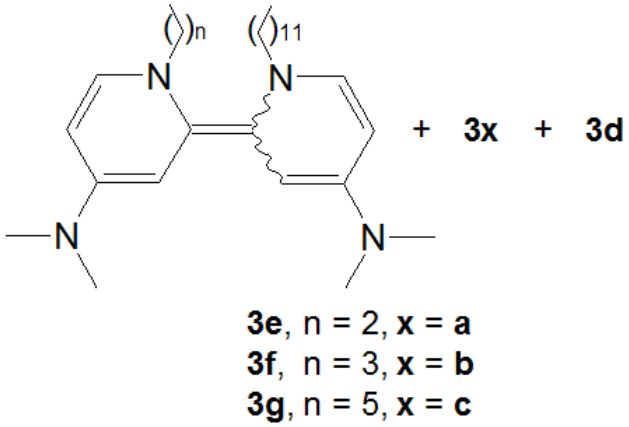


Figure 3.29: Structures of N-propyl-N′-dodecyl (**3e**), N-butyl-N′-dodecyl (**3f**), and N-hexyl-N′-dodecyl (**3g**) -bis-2-(4-dimethylamino)pyridinylidene in mixtures with **3a**, **3b**, and **3c**, respectively, and with **3d**.

The N-alkyl-N′-dodecyl bis-pyridinylidenes were prepared in mixtures which also contained **3a-c** and **3d** (Figure 3.29) by using 0.5 equivalents of dodecyl precursor **2d** with 0.5 equivalents of either the propyl (**2a**), butyl (**2b**), or hexyl (**2c**) precursor, respectively. The equimolar precursor salt mixtures were first stirred overnight in THF (2 mL THF per gram of KHMDS to be used). Then, 1.1 equivalents of KHMDS was added along with additional THF (2 mL THF per gram KHMDS) followed by stirring of the

reaction mixture for 2-3 days. The subsequent purification steps for the bis-pyridinylidene mixtures containing **3e-g** were identical to those of **3a-d** and afforded viscous black red-tinted liquids as the products in yields of 84-86% (calculated by assuming only **3e-g** are present).

3a: **2a** (1.18 g, 4.80 mmol, 1.00 eq.) and KHMDS (1.09 g, 5.45 mmol, 1.14 eq.) were used. Yield: 0.547 g (69%); ^{1}H NMR (400 MHz, C_6D_6), (major isomer) δ 0.90 (6H, t, CH_3), 1.69 (4H, m, CH_2), 2.48 (12H, s, $N(CH_3)_2$), 2.92 (4H, br$^{25°C}$, s$^{50°C}$, NCH_2) 5.18 (2H, dd, J = 7.2, 2.2 Hz, CH), 5.38 (2H, d, J = 2.2 Hz, CH), 6.03 (2H, d, J = 7.2 Hz, CH), (minor isomer) δ 0.81 (6H, t, CH_3), 1.62 (4H, m, CH_2), 2.51 (6H, s, $N(CH_3)_2$), 3.21 (4H, m, NCH_2), 5.28 (2H, dd, J = 7.5, 2.6 Hz, CH), 6.14 (2H, d, J = 7.5 Hz, CH); ^{13}C NMR (400 MHz, C_6D_6) (major isomer) δ 12.1 (CH_3), 22.7 (CH_2), 40.6 (NCH_3), 51.5 (NCH_2), 95.0 (CH), 100.1 (CH), 116.4 (C), 138.7 (CH), 143.1 (C), (minor isomer) δ 11.6 (CH_3), 23.2 (CH_2), 40.6 (NCH_3), 55.4 (NCH_2), 96.0 (CH), 101.1 (CH), 119.7(C), 139.6 (CH), 143.5 (C).

3b: **2b** (1.26 g, 4.87 mmol, 1.00 eq.) and KHMDS (1.09 g, 5.44 mmol, 1.12 eq.) were used. Yield: 0.572 g (66%); ^{1}H NMR (400 MHz, C_6D_6), (major isomer) δ 0.82 (6H, t, CH_3), 1.35 (4H, m, CH_2), 1.67 (4H, m, CH_2), 2.48 (12H, s, $N(CH_3)_2$), 5.21 (2H, dd, J = 7.4, 2.4 Hz, CH), 5.39 (2H, d, J = 2.4 Hz, CH), 6.04 (2H, d, J = 7.4 Hz, CH), (minor isomer) δ 2.54 (12H, s, $N(CH_3)_2$), 3.28 (4H, m, NCH_2), 5.30 (2H, dd, J = 7.4, 2.4 Hz, CH), 6.16 (2H, d, J = 7.4 Hz, CH); ^{13}C NMR (400 MHz, C_6D_6) (major isomer) δ 14.2 (CH_3), 20.8 (CH_2), 31.7 (CH_2), 40.5 (NCH_3), 49.1 (NCH_2), 94.9 (CH), 100.2 (CH), 116.4

(C), 138.9 (CH), 143.1 (C), (minor isomer) δ 13.8 (CH_3), 20.1 (CH_2), 31.7 (CH_2), 53.4 (NCH_3), 53.0 (NCH_2), 95.6 (CH), 100.8 (CH), 119.7 (C), 139.3 (CH), 143.1 (C).

3c: **2c** (1.45 g, 5.03 mmol, 1.00 eq.) and KHMDS (1.08 g, 5.44 mmol, 1.08 eq.) were used. Yield: 0.678 g (68%); ^{1}H NMR (400 MHz, C_6D_6), (major isomer) *δ* 0.86 (6H, t, CH_3), 1.15 to 1.27 (8H, m, $(CH_2)_2$), 1.34 (4H, m, CH_2), 1.71 (4H, m, CH_2), 2.48 (12H, s, $N(CH_3)_2$), 5.21 (2H, dd, J = 7.4, 2.4 Hz, CH), 5.39 (2H, d, J = 2.4 Hz, CH), 6.07 (2H, d, J = 7.4 Hz, CH), (minor isomer) *δ* 2.53 (12H, s, $N(CH_3)_2$), 3.30 (4H, m, NCH_2), 5.29 (2H, dd, J = 7.4, 2.8 Hz, CH), 6.18 (2H, d, J = 7.4 Hz, CH); ^{13}C NMR (400 MHz, C_6D_6) (major isomer) δ 14.4 (CH_3), 23.1 (CH_2), 27.3 (CH_2), 29.5 (CH_2), 31.9 (CH_2), 40.5 (NCH_3), 49.3 (NCH_2), 95.0 (CH), 100.3 (CH), 116.5 (C), 138.9 (CH), 143.1 (C), (minor isomer) δ 14.4 (CH_3), 23.1 (CH_2), 26.6 (CH_2), 29.7 (CH_2), 31.7 (CH_2), 53.7 (NCH_3), 53.3 (NCH_2), 95.6 (CH), 100.8 (CH), 116.1 (C), 139.3 (CH), 143.1 (C).

3d: **2d** (1.83 g, 4.93 mmol, 1.00 eq.) and KHMDS (1.10 g, 5.50 mmol, 1.12 eq.) were used. Yield: 1.173 g (82%); ^{1}H NMR (400 MHz, C_6D_6), (major isomer) *δ* 0.92 (6H, t, CH_3), 1.27 to 1.39 (32H, m, $(CH_2)_9$), 1.75 (4H, m, CH_2), 2.50 (12H, s, $N(CH_3)_2$), 5.23 (2H, dd, J = 7.2, 2.1 Hz, CH), 5.40 (2H, d, J = 2.1 Hz, CH), 6.09 (2H, d, J = 7.2 Hz, CH), (minor isomer) *δ* 2.54 (12H, s, $N(CH_3)_2$), 3.30 (4H, m, NCH_2), 5.31 (2H, dd, J = 7.4, 2.4 Hz, CH), 6.20 (2H, d, J = 7.4 Hz, CH); ^{13}C NMR (400 MHz, C_6D_6) (major isomer) δ 14.4 (CH_3), 23.3 (CH_2), 27.7 (CH_2), 29.6 (CH_2), 29.9 (CH_2), 30.0_{77} (CH_2), 30.1_{57} (CH_2), 30.2_{00} (CH_2), 30.2_{07} (CH_2), 30.2_{17} (CH_2), 32.4 (CH_2), 40.5 (NCH_3), 49.4 (NCH_2), 95.0 (CH),

100.3 (CH), 116.5 (C), 138.9 (CH), 143.0 (C), (minor isomer) δ 27.5 (CH_2), 32.3 (CH_2), 53.7 (NCH_2), 96.0 (CH), 101.2 (CH), 119.7 (C), 139.6 (CH), 143.5 (C).

3e + 3a + 3d: **2a** (0.62 g, 2.5 mmol, 0.50 eq.), **2d** (0.92 g, 2.5 mmol, 0.50 eq.) and KHMDS (1.10 g, 2.76 mmol, 1.10 eq.) were used. Yield: 0.946 g (84%); ^{1}H NMR (400 MHz, C_6D_6), (major isomer) *δ* 0.90 (3H, t, CH_3), 0.95 (3H, m, CH_3), 1.26 to 1.37 (18H, m, $(CH_2)_9$), 1.69 (2H, m, CH_2), 1.73 (2H, m, CH_2), 2.48 (6H, s, $N(CH_3)_2$), 2.50 (6H, s, $N(CH_3)_2$), 5.21 (2H, m, J = 7.9, 2.4 Hz, CH), 5.39 (2H, m, J = 2.4 Hz, CH), 6.06 (2H, m, J = 7.9 Hz, CH), (minor isomer) *δ* 2.51 (6H, s, $N(CH_3)_2$), 2.54 (6H, s, $N(CH_3)_2$), 3.22 (2H, m, NCH_2), 3.32 (2H, m, NCH_2), 5.29 (2H, m, CH), 6.14 (1H, m, CH), 6.19 (1H, m, CH); ^{13}C NMR (400 MHz, C_6D_6) δ 12.1 (CH_3), 14.5 (CH_3), 22.7 (CH_2), 23.2 (CH_2), 27.7 (CH_2), 29.6 (CH_2), 29.9 (CH_2), 30.1 (CH_2), 30.1_{48} (CH_2), 30.1_{94} ($(CH_2)_2$), 30.2_{12} (CH_2), 32.4 (CH_2), 40.5 (CH_3), 49.3 (CH_2), 49.4 (CH_2), 51.4 (CH_2), 51.5 (CH_2), 94.9 (CH), 95.0 (CH), 100.0 (CH), 100.1 (CH), 100.3 (CH), 116.4 (C), 116.5 (C), 138.7 (CH), 138.9 (CH), 143.1 (C), 143.1 (C), (minor isomer) δ 11.6 (CH_3), 23.1_{79} (CH_2), 27.7 (CH_2), 29.6 (CH_2), 29.9 (CH_2), 30.1 (CH_2), 30.2 (CH_2), 30.2 (CH_2), 30.2 (CH_2), 30.2 (CH_2), 32.4 (CH_2), 40.5 (CH_3), 40.6 (CH_3), 49.4 (CH_2), 51.5 (CH_2), 95.0 (CH), 95.0 (CH), 100.1 (CH), 100.3 (CH), 116.4 (C), 116.5 (C), 138.7 (CH), 138.9 (CH), 143.1 (C), 143.1 (C).

3f + 3b + 3d: **2b** (0.65 g, 2.5 mmol, 0.50 eq.), **2d** (0.93 g, 2.5 mmol, 0.50 eq.) and KHMDS (1.11 g, 2.78 mmol, 1.11 eq.) were used. Yield: 1.000 g (85 %); ^{1}H NMR (400 MHz, C_6D_6), (major isomer) *δ* 0.82 (3H, t, CH_3), 0.92 (3H, m, CH_3), 1.27 to 1.38 (20H, m, CH_2 + $(CH_2)_9$), 1.66 (2H, m, CH_2), 1.75 (2H, m, CH_2), 2.49 (6H, s, $N(CH_3)_2$), 2.50

(6H, s, $N(CH_3)_2$), 5.21 (2H, m, J = 7.9, 2.4 Hz, CH), 5.39 (2H, m, J = 2.4 Hz, CH), 6.07 (2H, m, J = 7.9 Hz, CH), (minor isomer) δ 2.52 (6H, s, $N(CH_3)_2$), 2.54 (6H, s, $N(CH_3)_2$), 3.23 (2H, m, NCH_2), 3.33 (2H, m, NCH_2), 5.30 (2H, m, CH), 6.14 (1H, m, CH), 6.18 (1H, m, CH); ^{13}C NMR (400 MHz, C_6D_6) δ 14.2 (CH_3), 14.5 (CH_3), 20.8 (CH_2), 23.2 (CH_2), 27.7 (CH_2), 29.5 (CH_2), 29.9 (CH_2), 30.0 (CH_2), 30.1_{47} (CH_2), 30.1_{94} (CH_2), 30.2_{12} (CH_2), 31.7 (CH_2), 32.4 (CH_2), 40.5 (CH_3), 49.1 (CH_2), 49.3 (CH_2), 94.9 (CH), 95.0 (CH), 100.2 (CH), 100.3 (CH), 116.3_{56} (C), 116.4_{25} (C), 138.8 (CH), 143.0 (C), (minor isomer) δ 20.6 (CH_2), 27.6 (CH_2), 32.1 (CH_2), 53.4 (CH_2), 53.7 (CH_2), 95.9_{58} (CH), 95.9_{94} (CH), 100.2 (CH), 119.6_{21} (C), 119.6_{42} (C), 139.5_{88} (CH), 139.6_{19} (CH), 143.4 (C).

3g + **3c** + **3d**: **2c** (0.72 g, 2.5 mmol, 0.50 eq.), **2d** (0.93 g, 2.5 mmol, 0.50 eq.) and KHMDS (1.13 g, 2.83 mmol, 1.13 eq.) were used. Yield: 1.077 g (86%); ^1H NMR (400 MHz, C_6D_6), (major isomer) δ 0.86 (3H, t, CH_3), 0.92 (3H, m, CH_3), 1.21 to 1.38 (24H, m, $(CH_2)_3$ + $(CH_2)_9$), 1.71 (2H, m, CH_2), 1.75 (2H, m, CH_2), 2.48 (6H, s, $N(CH_3)_2$), 2.50 (6H, s, $N(CH_3)_2$), 5.22 (2H, m, J = 7.3, 2.5 Hz, CH), 5.39 (2H, m, J = 2.5 Hz, CH), 6.08 (2H, m, J = 7.3 Hz, CH), (minor isomer) δ 2.53 (6H, s, $N(CH_3)_2$), 2.55 (6H, s, $N(CH_3)_2$), 3.30 (2H, m, NCH_2), 3.33 (2H, m, NCH_2), 5.31 (2H, m, CH), 6.19 (2H, m, CH); ^{13}C NMR (400 MHz, C_6D_6) δ 14.3 (CH_3), 14.4 (CH_3), 23.1 (CH_2), 23.2 (CH_2), 27.3 (CH_2), 27.7 (CH_2), 29.5 (CH_2), 29.6 (CH_2), 29.9 (CH_2), 30.0_{75} (CH_2), 30.1_{55} (CH_2), 30.1_{88} (CH_2), 30.2_{05} (CH_2), 32.0 (CH_2), 32.4 (CH_2), 40.5 (CH_3), 49.3 (CH_2), 49.4 (CH_2), 95.1 (CH), 100.2_{95} (CH), 100.3_{24} (CH), 116.4_{84} (C), 116.5_{02} (C), 138.9 (CH), 143.0_{69} (C), 143.0_{87} (C), (minor isomer) δ 27.1 (CH_2), 27.5 (CH_2), 30.1 (CH_2), 53.7 (CH_2), 96.0 (CH), 101.2 (CH), 119.8 (C), 139.7 (CH), 143.6 (C).

3.3.3 – N,N-Dialkyl and N-Alkyl-N'-Dodecyl Dichloride Salts (4)

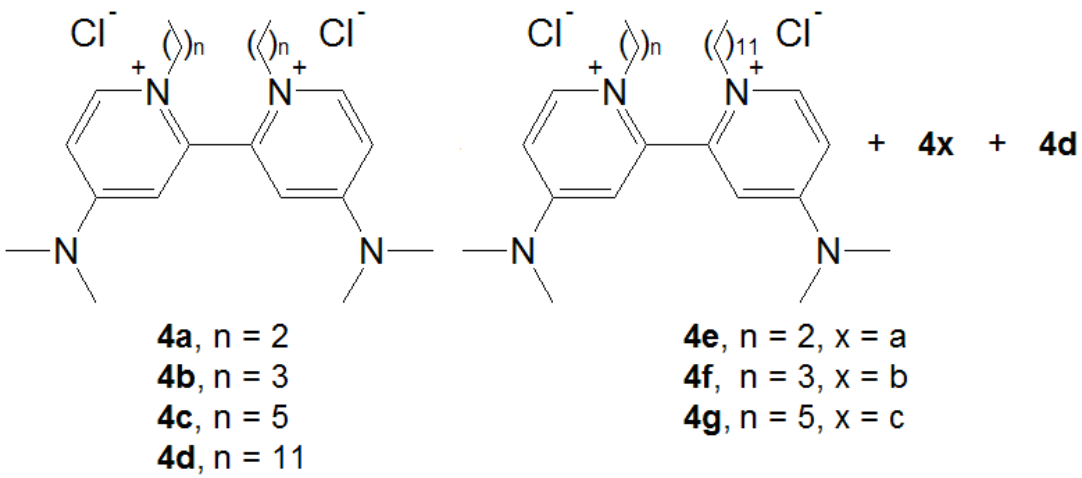


Figure 3.30: Left (a), structures of N,N-dipropyl (**4a**), N,N-dibutyl (**4b**), N,N-dihexyl (**4c**), and N,N-didodecyl (**4d**) -bis-2-(4-dimethylamino)pyridinium. Right (b), structures of N-propyl-N′-dodecyl (**4e**), N-butyl-N′-dodecyl (**4f**), and N-hexyl-N′-dodecyl (**4g**) -bis-2-(4-dimethylamino)pyridinium chloride in mixtures with **4a**, **4b**, and **4c**, respectively, and with **4d**.

To a hexanes (25 mL) solution of bis-pyridinylidenes **3a-d** or mixtures containing **3e-g** was added 0.85-0.95 equivalents of hexachloroethane (C_2Cl_6). The mixtures immediately warmed up upon addition of C_2Cl_6 to become khaki-brown suspensions. The mixtures were stirred overnight before being filtered, washed with hexanes (15 mL) and diethyl ether (15 mL), and dried *in vacuo* with gentle heating to afford the dichloride salt products **4a-d** and salt mixtures **4e-g** + **4a-c** + **4d** as khaki chalk-like powders in yields of 79-93% and 82-96% (calculated by assuming only **4e-g** are present), respectively.

4a: **3a** (0.547 g, 1.67 mmol, 1.00 eq.) and hexachloroethane (0.333 g, 1.41 mmol, 0.86 eq.) were used. Yield: 0.619 g, (93%); mp: 152.2-155.4°C; [Found: (ESI$^+$) (M-2 Cl)$^{2+}$

164.1313. $C_{20}H_{32}N_4Cl_2$ requires (M-2 Cl)/2, 164.1308]; ^{1}H NMR (400 MHz, CD_3CN) δ 0.85 (6H, t, CH_3), 1.75 (4H, m, CH_2), 3.24 (6H, s, CH_3NCH_3), 3.27 (6H, s, CH_3NCH_3), 3.71 (2H, m, NC*H*H), 4.07 (2H, m, NCH*H*), 7.11 (2H, dd, J = 7.6, 3.2 Hz, ArH), 7.26 (2H, d, J = 3.2 Hz, ArH), 8.44 (2H, d, J = 7.6 Hz, ArH); ^{13}C NMR (400 MHz, CD_3CN) δ 10.9 (CH_3), 24.7 (CH_2), 41.0 (NCH_3), 41.1 (NCH_3), 57.2 (NCH_2), 109.7 (CH), 112.8 (CH), 143.4 (C), 144.6 (CH), 157.2 (C); *m/z* (ESI^+) 363 [$(M-Cl)^+$, 61%], 327 (29), 385 (71), 243 (13), 207 (5), 164 (100).

4b: **3b** (0.572 g, 1.60 mmol, 1.00 eq.) and hexachloroethane (0.327 g, 1.38 mmol, 0.86 eq.) were used. Yield: 0.580 g (85%); mp: 130.1-133.0 °C; [Found: (ESI^+) $(M-2\ Cl)^{2+}$ 178.1470. $C_{22}H_{36}N_4Cl_2$ requires (M-2 Cl)/2, 178.1465]; ^{1}H NMR (400 MHz, CD_3CN) δ 0.83 (6H, t, CH_3), 1.25 (4H, m, CH_2), 1.71 (4H, m, CH_2), 3.26 (6H, s, CH_3NCH_3), 3.27 (6H, s, CH_3NCH_3), 3.75 (2H, m, NC*H*H), 4.16 (2H, m, NCH*H*), 7.15 (2H, dd, J = 7.7, 3.3 Hz, CH), 7.36 (2H, d, J = 3.3 Hz, CH), 8.56 (2H, d, J = 7.7 Hz, CH); ^{13}C NMR (400 MHz, CD_3CN) δ 13.7 (CH_3), 20.0 (CH_2), 33.3 (CH_2), 41.0 (NCH_3), 41.2 (NCH_3), 55.7 (NCH_2), 109.7 (CH), 112.8 (CH), 143.4 (C), 144.8 (CH), 157.2 (C); *m/z* (ESI^+) 391 [$(M-Cl)^+$, 41%], 355 (16), 292 (40), 235 (6), 178 (100).

4c: **3c** (0.703 g, 1.70 mmol, 1.00 eq.) and hexachloroethane (0.357 g, 1.51 mmol, 0.89 eq.) were used. Yield: 0.653 g (79%); mp: 115.3-118.8°C; [Found: (ESI^+) $(M-2\ Cl)^{2+}$ 206.1779. $C_{26}H_{44}N_4Cl_2$ requires (M-2 Cl)/2, 206.1778]; ^{1}H NMR (400 MHz, CD_3CN) δ 0.84 (6H, t, CH_3), 1.16-1.30 (12H, broad m, $(CH_2)_3$), 1.70 (4H, m, CH_2), 3.25 (6H, s, CH_3NCH_3), 3.27 (6H, s, CH_3NCH_3), 3.72 (2H, m, NC*H*H), 4.13 (2H, m, NCH*H*), 7.13

(2H, dd, J = 7.8, 3.0 Hz, CH), 7.34 (2H, d, J = 3.0 Hz, CH), 8.50 (2H, d, J = 7.8 Hz, CH); ^{13}C NMR (400 MHz, CD_3CN) δ 14.2 (CH_3), 23.0 (CH_2), 26.3 (CH_2), 31.2 (CH_2), 31.7 (CH_2), 41.0 (NCH_3), 41.2 (NCH_3), 55.9 (NCH_2), 109.7 (CH), 112.8 (CH), 143.4 (C), 144.7 (CH), 157.2 (C); *m/z* (ESI^+) 447 [$(M\text{-}Cl)^+$, 22%], 411 (9), 327 (17), 291 (4), 206 (100).

4d: **3d** (1.173 g, 2.02 mmol, 1.00 eq.) and hexachloroethane (0.401 g, 1.69 mmol, 0.84 eq.) were used. Yield: 1.230 g (93%); mp: 65-72°C [Found: (ESI^+) (M-2 Cl)$^{2+}$ 290.2715. $C_{38}H_{68}N_4Cl_2$ requires (M-2 Cl)/2, 290.2717]; ^{1}H NMR (400 MHz, CD_3CN) *δ* 0.88 (6H, t, CH_3), 1.20-1.32 (36H, broad m, $(CH_2)_9$), 1.72 (4H, m, CH_2), 3.25 (6H, s, $CH_3NC\mathit{H}_3$), 3.27 (6H, s, $C\mathit{H}_3NCH_3$), 3.74 (2H, m, NC*H*H), 4.12 (2H, m, NCH*H*), 7.13 (2H, dd, J = 7.7, 3.2 Hz, CH), 7.34 (2H, d, J = 3.2 Hz, CH), 8.50 (2H, d, J = 7.7 Hz, CH); ^{13}C NMR (400 MHz, CD_3CN) δ 14.4 (CH_3), 23.4 (CH_2), 26.7 (CH_2), 29.6 (CH_2), 30.0 (CH_2), 30.2 (CH_2), 30.3 ($3CH_2$), 31.3 (CH_2), 32.6 (CH_2), 41.1 (NCH_3), 41.2 (NCH_3), 56.0 (NCH_2), 109.7 (CH), 112.8 (CH), 143.4 (C), 144.7 (CH), 157.2 (C); *m/z* (ESI^+) 616 [$(M\text{-}Cl)^+$, 20%], 580 (4), 460 (3), 411 (4), 290 (100).

4e + 4a + 4d: Mixture **3e + 3a + 3d** (0.946 g, 2.08 mmol, 1.00 eq.) and hexachloroethane (0.464 g, 1.96 mmol, 0.94 eq.) were used. Yield: 1.053 g (96%); mp: 65-73°C; [Found: (ESI^+) (PrPr-2 Cl)$^{2+}$ 164.1307, (PrDo-2 Cl)$^{2+}$ 227.2014, (DoDo-2 Cl)$^{2+}$ 290.2716. $C_{20}H_{32}N_4Cl_2$ requires (PrPr-2 Cl)/2, 164.1308, $C_{29}H_{50}N_4Cl_2$ requires (PrDo-2 Cl)/2, 227.2012, $C_{38}H_{68}N_4Cl_2$ requires (DoDo-2 Cl)/2, 290.2717]; ^{1}H NMR (400 MHz, CD_3CN) *δ* 0.84 (3H, t, CH_3), 0.87 (3H, t, CH_3), 1.19-1.31 (18H, broad m, $(CH_2)_9$), 1.68-1.78 (4H,

m, CH_2 + CH_2), 3.26 (6H, s, CH_3NCH_3), 3.27 (6H, s, CH_3NCH_3), 3.70-3.78 (2H, m, NC*H*H), 4.09-4.18 (2H, m, NCH*H*), 7.16 (2H, m, CH), 7.38 (2H, m, CH), 8.58 (2H, m, CH); ^{13}C NMR (400 MHz, CD_3CN) δ 10.9 (CH_3), 14.4 (CH_3), 23.3 (CH_2), 24.7_{41} (CH_2), 24.7_{51} (CH_2), 26.6_{71} (CH_2), 26.6_{98} (CH_2), 29.6_{07} (CH_2), 29.6_{33} (CH_2), 30.0_{04} (CH_2), 30.0_{15} (CH_2), 30.0_{26} (CH_2), 30.1_{83} (CH_2), 30.2_{03} (CH_2), 30.2_{86} (CH_2), 30.3_{00} (CH_2), 31.2_{47} (CH_2), 31.2_{96} (CH_2), 32.5_{84} (CH_2), 32.5_{93} (CH_2), 41.0 (NCH_3), 41.2 (NCH_3), 55.8_{61} (NCH_2), 55.9_{19} (NCH_2), 57.1_{83} (NCH_2), 57.2_{23} (NCH_2), 109.6_{85} (CH), 109.7_{33} (CH), 112.9 (CH), 143.3_{42} (C), 143.3_{78} (C), 143.4_{09} (C), 143.4_{38} (C), 144.7_{46} (CH), 144.7_{85} (CH), 144.8_{27} (CH), 157.1_{75} (C), 157.1_{94} (C), 157.2_{18} (C), 157.2_{31} (C); *m/z* (ESI^+) 616 [$(DoDo\text{-}Cl)^+$, 24%], 580 (2), 460 (7), 363 [$(PrPr\text{-}Cl)^+$, 11%], 327 (4), 290 (100), 227 [$(PrDo\text{-}2\ Cl)^{2+}$, 4%], 164 (9).

4f + 4b + 4d: Mixture **3f + 3b + 3d** (1.000 g, 2.13 mmol, 1.00 eq.) and hexachloroethane (0.450 g, 1.90 mmol, 0.89 eq.) were used. Yield: 0.948 g (82%); mp: 116-123°C; [Found: (ESI^+) $(BuBu\text{-}2\ Cl)^{2+}$ 164.1307, $(BuDo\text{-}2\ Cl)^{2+}$ 234.2100, $(DoDo\text{-}2\ Cl)^{2+}$ 290.2730. $C_{22}H_{36}N_4Cl_2$ requires $(BuBu\text{-}2\ Cl)/2$, 178.1471, $C_{30}H_{52}N_4Cl_2$ requires $(BuDo\text{-}2\ Cl)/2$, 234.2091, $C_{38}H_{68}N_4Cl_2$ requires $(DoDo\text{-}2\ Cl)/2$, 290.2717]; ^{1}H NMR (400 MHz, CD_3CN) *δ* 0.85 (3H, t, CH_3), 0.88 (3H, t, CH_3), 1.21-1.32 (20H, broad m, CH_2 + $(CH_2)_9$), 1.66-1.74 (4H, m, CH_2 + CH_2), 3.23 (6H, s, CH_3NCH_3), 3.27 (6H, s, CH_3NCH_3), 3.67-3.75 (2H, m, NC*H*H), 4.03-4.12 (2H, m, NCH*H*), 7.09 (2H, m, CH), 7.23 (2H, m, CH), 8.36 (2H, m, CH); ^{13}C NMR (400 MHz, CD_3CN) δ 13.7 (CH_3), 14.4 (CH_3), 20.1 (CH_2), 23.4 (CH_2), 26.7 (CH_2), 29.6 (CH_2), 30.0 (CH_2), 30.2 (CH_2), 30.3 (CH_2), 31.3 (CH_2), 32.6 (CH_2), 33.3 (CH_2), 41.0 (NCH_3), 41.2 (NCH_3), 55.7 (NCH_2), 55.9 (NCH_2), 109.7 (CH),

112.7$_{93}$ (CH), 112.8$_{17}$ (CH), 143.4 (C), 144.7 (CH), 157.2 (C); *m/z* (ESI$^+$) 616 [(DoDo-Cl)$^+$, 12%], 460 (2), 391 [(BuBu-Cl)$^+$, 12%], 355 (7), 290 (100), 234 [(BuDo-2 Cl)$^{2+}$, 12%], 178 (34).

4g + 4c + 4d: Mixture **3g + 3c + 3d** (1.077 g, 2.17 mmol, 1.00 eq.) and hexachloroethane (0.453 g, 1.91 mmol, 0.88 eq.) were used. Yield: 1.069 g (87%); mp: 119-124°C; [Found: (E SI$^+$) (HexHex-2 Cl)$^{2+}$ 206.1776, (HexDo-2 Cl)$^{2+}$ 248.2250, (DoDo-2 Cl)$^{2+}$ 290.2722. $C_{26}H_{44}N_4Cl_2$ requires (HexHex-2 Cl)/2, 206.1778, $C_{32}H_{56}N_4Cl_2$ requires (HexDo-2 Cl)/2, 248.2247, $C_{38}H_{68}N_4Cl_2$ requires (DoDo-2 Cl)/2, 290.2717]; ^{1}H NMR (400 MHz, CD_3CN) δ 0.84 (3H, t, CH_3), 0.88 (3H, t, CH_3), 1.21-1.32 (24H, broad m, $(CH_2)_3$ + $(CH_2)_9$), 1.68-1.73 (4H, m, CH_2 + CH_2), 3.24 (6H, s, CH_3NCH_3), 3.27 (6H, s, CH_3NCH_3), 3.70-3.76 (2H, m, NC*H*H), 4.05-4.13 (2H, m, NCH*H*), 7.11 (2H, m, CH), 7.28 (2H, m, CH), 8.41 (2H, m, CH); ^{13}C NMR (400 MHz, CD_3CN) δ 14.2 (CH_3), 14.4 (CH_3), 20.0 (CH_2), 23.0 (CH_2), 23.4 (CH_2), 26.3 (CH_2), 26.7 (CH_2), 29.6 (CH_2), 30.0$_{28}$ (CH_2), 30.0$_{39}$ (CH_2), 30.2 (CH_2), 30.3 (CH_2), 31.2$_{02}$ (CH_2), 31.2$_{41}$ (CH_2), 31.7 (CH_2), 32.6 (CH_2), 41.0 (NCH_3), 41.2 (NCH_3), 55.9 (NCH_2), 109.7 (CH), 112.8 (CH), 143.4 (C), 144.6 (CH), 157.2 (C); *m/z* (ESI$^+$) 616 [(DoDo-Cl)$^+$, 11%], 447 [(HexHex-Cl)$^+$, 10%], 411 (5), 327 (9), 290 (100), 248 [(HexDo-2Cl)$^{2+}$, 9%], 164 (69).

3.3.4 – N,N-Dialkyl and N-Alkyl-N′-Dodecyl Hexafluorophosphate Salts (5)

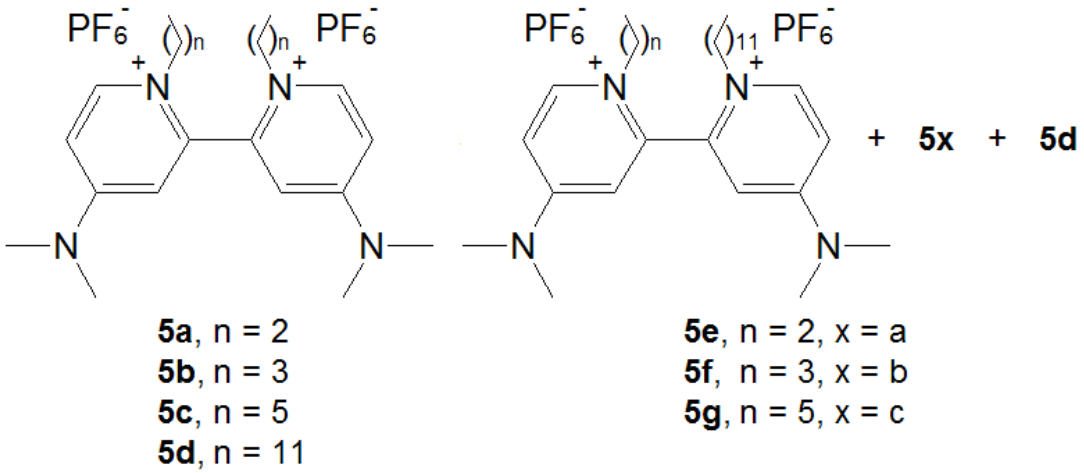


Figure 3.31: Left (a), structures of N,N-dipropyl (**5a**), N,N-dibutyl (**5b**), N,N-dihexyl (**5c**), and N,N-didodecyl (**5d**) -bis-2-(4-dimethylamino)pyridinium. Right (b), structures of N-propyl-N′-dodecyl (**5e**), N-butyl-N′-dodecyl (**5f**), and N-hexyl-N′-dodecyl (**5g**) -bis-2-(4-dimethylamino)pyridinium chloride in mixtures with **5a**, **5b**, and **5c**, respectively, and with **5d**.

The metathesis reaction was carried out by dissolving dichloride salts **4a-d** or dichloride salt mixtures **4e-g** + **4a-c** + **4d** in water (100 mg of salt per 5 mL of water), followed by the addition of ~2.3 equivalents of KPF_6 to the solutions. The mixtures were swirled vigorously and left to stand overnight or until the supernatant liquid in the mixtures appeared clear. A pinch (~10 mg) of KPF_6 was added to the settled mixtures, and if no further precipitate was observed, the mixtures were filtered (**5a**, **5b**, and mixture **5e** + **5a** + **5d**) or decanted (**5c**, **5d**, mixture **5f** + **5b** + **5d**, and mixture **5g** + **5c** + **5d**). The precipitates were then washed with hot water (60°C, 3 portions of 5 mL) and boiling ether (34°C, 3 portions of 5 mL). The products were dried *in vacuo* at 60°C, yielding hexafluorophosphate salts **5a-d** and salt mixtures **5e-g** + **5a-c** + **5d** as chalky reddish-

brown solids in yields of 44-90% and 61-86% (calculated by assuming only **5e-g** are present), respectively.

5a: **4a** (0.11 g, 0.27 mmol, 1.0 eq.) and potassium hexafluorophosphate (0.11 g, 0.60 mmol, 2.2 eq.) Yield: 0.089 g, (53%); mp: 220°C (decomposed); ^{1}H NMR (400 MHz, CD_3CN) δ 0.85 (6H, t, CH_3), 1.72 (4H, m, CH_2), 3.19 (6H, s, $CH_3NC\mathit{H}_3$), 3.26 (6H, s, $C\mathit{H}_3NCH_3$), 3.59-3.66 (2H, m, NC*H*H), 3.90-3.98 (2H, m, NCH*H*), 6.99 (2H, d, J = 3.0 Hz, CH), 7.02 (2H, dd, 7.6, 3.0 Hz, CH), 8.10 (2H, d, J = 7.6 Hz, CH); ^{13}C NMR (400 MHz, CD_3CN) δ 10.7 (CH_3), 24.6 (CH_2), 40.9 (NCH_3), 41.0 (NCH_3), 57.2 (NCH_2), 109.7 (CH), 112.3 (CH), 143.3 (C), 144.1 (CH), 157.2 (C).

5b: **4b** (0.11 g, 0.25 mmol, 1.0 eq.) and potassium hexafluorophosphate (0.11 g, 0.59 mmol, 2.4 eq.) were used. Yield: 0.073 g (45%); mp: 220°C (decomposed); ^{1}H NMR (400 MHz, CD_3CN) δ 0.85 (6H, t, CH_3), 1.24 (4H, m, CH_2), 1.69 (4H, m, CH_2), 3.19 (6H, s, $CH_3NC\mathit{H}_3$), 3.26 (6H, s, $C\mathit{H}_3NCH_3$), 3.60-3.67 (2H, m, NC*H*H), 3.94-4.02 (2H, m, NCH*H*), 7.00 (2H, d, J = 3.1 Hz, CH), 7.02 (2H, dd, 7.5, 3.1 Hz, CH), 8.10 (2H, d, J = 7.5 Hz, CH); ^{13}C NMR (400 MHz, CD_3CN) δ 13.6 (CH_3), 20.0 (CH_2), 33.2 (CH_2), 40.9_{51} (NCH_3), 40.9_{88} (NCH_3), 55.7 (NCH_2), 109.7 (CH), 112.3 (CH), 143.3 (C), 144.1 (CH), 157.2 (C).

5c: **4c** (0.12 g, 0.25 mmol, 1.0 eq.) and potassium hexafluorophosphate (0.10 g, 0.55 mmol, 2.2 eq.) were used. Yield: 0.078 g (44%); mp: 77-79°C; ^{1}H NMR (400 MHz, CD_3CN) δ 0.85 (6H, t, CH_3), 1.21-1.33 (12H, broad m, $(CH_2)_3$), 1.70 (4H, broad m, CH_2),

3.19 (6H, s, $CH_3NC\mathit{H}_3$), 3.26 (6H, s, $C\mathit{H}_3NCH_3$), 3.58-3.65 (2H, m, NC*H*H), 3.93-4.01 (2H, m, NCH*H*), 7.00 (2H, d, J = 3.1 Hz, CH), 7.02 (2H, dd, 7.5, 3.1 Hz, CH), 8.10 (2H, d, J = 7.5 Hz, CH); ^{13}C NMR (400 MHz, CD_3CN) δ 14.1 (CH_3), 23.0 (CH_2), 26.3 (CH_2), 31.1 (CH_2), 31.7 (CH_2), 40.9 (NCH_3), 41.0 (NCH_3), 55.9 (NCH_2), 109.7 (CH), 112.3 (CH), 143.3 (C), 144.1 (CH), 157.2 (C).

5d: **4d** (0.17 g, 0.25 mmol, 1.0 eq.) and potassium hexafluorophosphate (0.11 g, 0.59 mmol, 2.3 eq.) were used. Yield: 0.198 g (90%); mp: 65-68°C; ^{1}H NMR (400 MHz, CD_3CN) *δ* 0.88 (6H, t, CH_3), 1.21-1.27 (36H, broad m, $(CH_2)_9$), 1.69 (4H, broad m, CH_2), 3.19 (6H, s, $CH_3NC\mathit{H}_3$), 3.26 (6H, s, $C\mathit{H}_3NCH_3$), 3.59-3.66 (2H, m, NC*H*H), 3.93-4.00 (2H, m, NCH*H*), 6.99 (2H, d, J = 3.0 Hz, CH), 7.02 (2H, dd, 7.6, 3.0 Hz, CH), 8.10 (2H, d, J = 7.6 Hz, CH); ^{13}C NMR (400 MHz, CD_3CN) δ 14.4 (CH_3), 23.4 (CH_2), 26.6 (CH_2), 29.6 (CH_2), 29.9_{80} (CH_2), 30.0_{35} (CH_2), 30.1_{82} (CH_2), 30.2_{96} (CH_2), 30.3_{04} (CH_2), 31.7 (CH_2), 32.6 (CH_2), 40.9 (NCH_3), 41.0 (NCH_3), 56.0 (NCH_2), 109.7 (CH), 112.3 (CH), 143.3 (C), 144.1 (CH), 157.2 (C).

5e + 5a + 5d: Mixture **4e + 4a + 4d** (0.14 g, 0.26 mmol, 1.0 eq.) and potassium hexafluorophosphate (0.11 g, 0.60 mmol, 2.3 eq.) were used. Yield: 0.164 g (86%); mp: 75-77°C; ^{1}H NMR (400 MHz, CD_3CN) *δ* 0.85 (3H, t, CH_3), 0.89 (3H, t, CH_3), 1.21-1.33 (18H, broad m, $(CH_2)_9$), 1.68-1.75 (4H, m, CH_2 + CH_2), 3.19 (6H, s, $CH_3NC\mathit{H}_3$), 3.26 (6H, s, $C\mathit{H}_3NCH_3$), 3.58-3.66 (2H, m, NC*H*H), 3.90-4.00 (2H, m, NCH*H*), 6.99 (2H, m, CH), 7.02 (2H, m, CH), 8.10 (2H, m, CH); ^{13}C NMR (400 MHz, CD_3CN) δ 10.8 (CH_3), 14.3 (CH_3), 23.4 (CH_2), 24.7 (CH_2), 26.6 (CH_2), 29.5_{53} (CH_2), 29.9_{69} (CH_2), 29.9_{84} (CH_2),

30.0_{39} (CH_2), 30.1_{83} (CH_2), 30.2_{98} (CH_2), 31.1_{83} (CH_2), 31.2_{14} (CH_2), 32.6 (CH_2), 40.9_{74} (NCH_3), 40.9_{98} (NCH_3), 41.0_{18} (NCH_3), 55.9_{03} (NCH_2), 55.9_{49} (NCH_2), 57.3 (NCH_2), 109.7_{00} (CH), 109.7_{37} (CH), 112.3_{04} (CH), 112.3_{18} (CH), 112.3_{49} (CH), 143.3 (C), 144.1_{27} (C), 144.1_{54} (C), 157.1_{35} (C).

5f + 5b + 5d: Mixture **4f + 4b + 4d** (0.27 g, 0.50 mmol, 1.0 eq.) and potassium hexafluorophosphate (0.22 g, 1.2 mmol, 2.4 eq.) were used. Yield: 0.231 g (61%); mp: 72-74°C; ^{1}H NMR (400 MHz, CD_3CN) δ 0.83-0.90 (6H, m, CH_3 + CH_3), 1.21-1.32 (20H, broad m, CH_2 + $(CH_2)_9$), 1.64-1.70 (4H, m, CH_2 + CH_2), 3.19 (6H, s, $CH_3NC\mathit{H}_3$), 3.26 (6H, s, $C\mathit{H}_3NCH_3$), 3.59-3.67 (2H, m, NC*H*H), 3.93-4.00 (2H, m, NCH*H*), 7.00 (2H, m, CH), 7.02 (2H, m, CH), 8.10 (2H, m, CH); ^{13}C NMR (400 MHz, CD_3CN) δ 13.7 (CH_3), 14.4 (CH_3), 20.0 (CH_2), 23.4 (CH_2), 26.6 (CH_2), 29.5_{77} (CH_2), 29.9_{92} (CH_2), 30.0_{45} (CH_2), 30.2 (CH_2), 30.3_{05} (CH_2), 30.3_{15} (CH_2), 31.1_{85} (CH_2), 31.2_{15} (CH_2), 32.6 (CH_2), 33.2 (CH_2), 40.9_{67} (NCH_3), 41.0_{13} (NCH_3), 55.8 (NCH_2), 56.0 (NCH_2), 109.8 (CH), 112.3 (CH), 143.3 (C), 144.1 (C), 157.2 (C).

5g + 5c + 5d: Mixture **4g + 4c + 4d** (0.30 g, 0.51 mmol, 1.0 eq.) and potassium hexafluorophosphate (0.22 g, 1.2 mmol, 2.3 eq.) were used. Yield: 0.310 g (77%); mp: 74-75°C; ^{1}H NMR (400 MHz, CD_3CN) δ 0.83-0.90 (6H, m, CH_3 + CH_3), 1.21-1.33 (24H, broad m, $(CH_2)_3$ + $(CH_2)_9$), 1.68 (4H, m, CH_2 + CH_2), 3.19 (6H, s, $CH_3NC\mathit{H}_3$), 3.26 (6H, s, $C\mathit{H}_3NCH_3$), 3.59-3.66 (2H, m, NC*H*H), 3.93-4.00 (2H, m, NCH*H*), 6.99 (2H, m, CH), 7.02 (2H, m, CH), 8.10 (2H, m, CH); ^{13}C NMR (400 MHz, CD_3CN) δ 14.2 (CH_3), 14.4 (CH_3), 23.0 (CH_2), 23.4 (CH_2), 26.3 (CH_2), 26.6 (CH_2), 29.5_{79} (CH_2), 29.9_{96} (CH_2), 30.0_{49}

(CH_2), 30.2 (CH_2), 30.3 (CH_2), 31.1_{52} (CH_2), 31.1_{93} (CH_2), 31.7 (CH_2), 326 (CH_2), 40.9_{87} (NCH_3), 41.0_{31} (NCH_3), 56.0 (NCH_2), 109.8 (CH), 112.3 (CH), 143.3 (C), 144.1 (C), 157.2 (C).

3.3.5 – 2D NMR Assignments

Table 3.5: ^{13}C, ^{1}H, ^{1}H-^{1}H COSY, and ^{1}H-^{13}C HMBC NMR Assignments for (*Z*)-N,N-dipropyl-bis-2-(4-dimethylamino)pyridinylidene (**3a**) in C_6D_6. VT - Found via Variable Temperature NMR.

Position	δ_C, mult.	δ_H, coupl. (J in Hz)	COSY	HMBC
a	138.7, CH	6.03, d (7.2)	b	b, c, e, h, i
b	100.1, CH	5.18, dd (7.2, 2.2)	a, c	a, c
c	95.0, CH	5.38, d (2.2)	b	b, h, i
d	40.6, CH_3	2.48, s	---	c, d, h
e	51.5, CH_2	2.92, broad ^{VT}	f ^{VT}	N/A
f	22.7, CH_2	1.69, m	e, g	e, g
g	12.1, CH_3	0.90, t	f	e, f
h	143.1, C	---	---	---
i	116.4, C	---	---	---

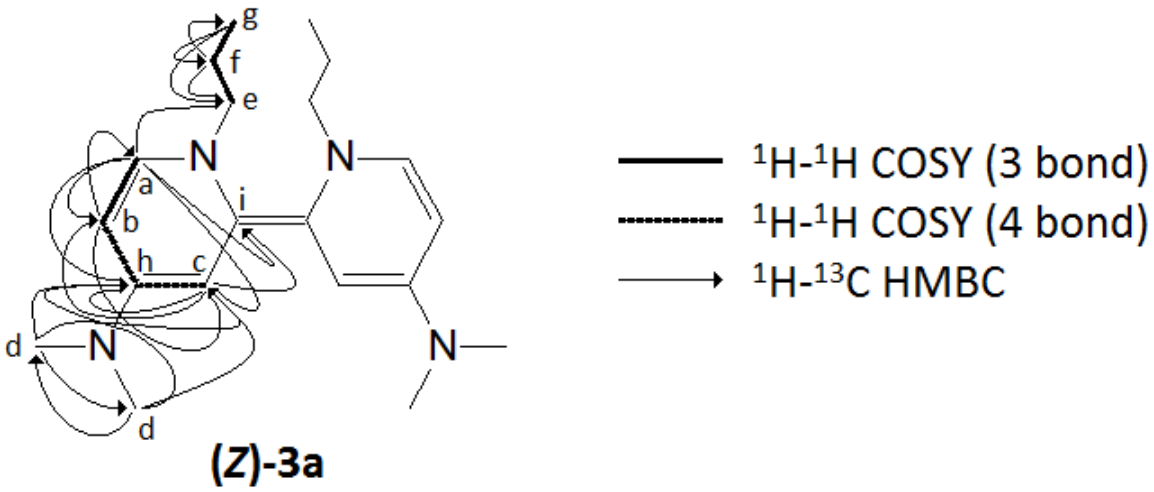


Figure 3.32: Structure of (***Z*)-3a** illustrating all assigned 2D NMR correlations for ^{1}H-^{1}H COSY and ^{1}H-^{13}C HMBC.

Table 3.6: ^{13}C, ^{1}H, ^{1}H-^{1}H COSY, and ^{1}H-^{13}C HMBC NMR Assignments for (*E*)-N,N-dipropyl-bis-2-(4-dimethylamino)pyridinylidene (**3a**) in C_6D_6. HSQC - Found via ^{1}H-^{13}C Heteronuclear Single Quantum Coherence NMR.

Position	δ_C, mult.	δ_H, coupl. (J in Hz)	COSY	HMBC
a	139.6, CH	6.14, d (7.5)	b	b, h, i
b	101.1, CH	5.28, dd (7.5, 2.6)	a	N/A
c	96.0, CH	5.17, d (2.6) ^{HSQC}	N/A	a, b, i
d	40.6, CH_3	2.51, s	---	d, h
e	55.4, CH_2	3.21, m	f	a, i
f	23.2, CH_2	1.62, m ^{HSQC}	e, g	e, f, g
g	11.6, CH_3	0.81, t ^{HSQC}	f	e, f
h	143.5, C	---	---	---
i	119.7, C	---	---	---

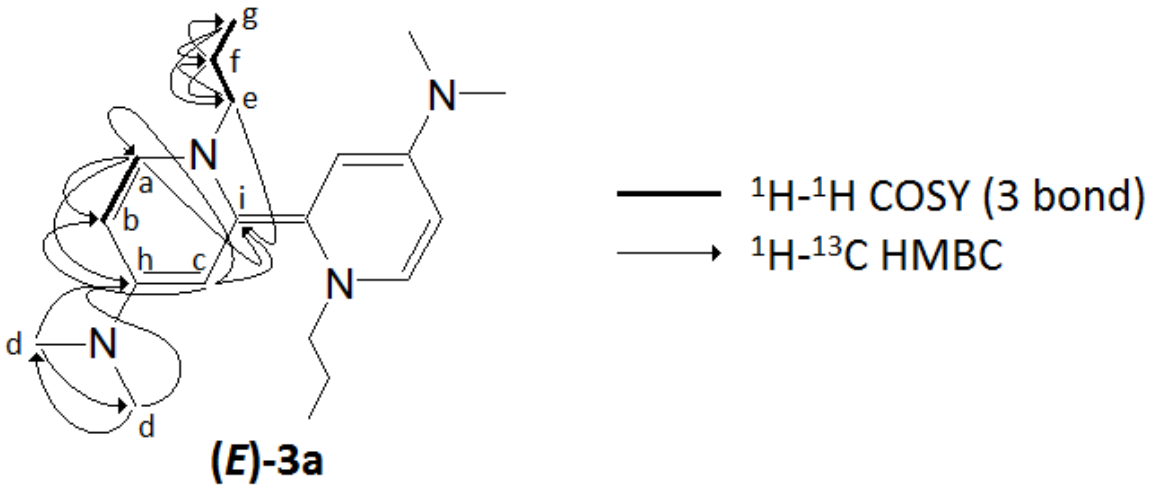


Figure 3.33: Structure of (***E*)-3a** illustrating all assigned 2D NMR correlations for ^{1}H-^{1}H COSY and ^{1}H-^{13}C HMBC.

Table 3.7: ^{13}C, ^{1}H, ^{1}H-^{1}H COSY, and ^{1}H-^{13}C HMBC NMR Assignments for N,N-dipropyl-2-(4-dimethylamino)pyridinium chloride (**4a**) in CD_3CN.

Position	δ_C, mult.	δ_H, coupl. (J in Hz)	COSY	HMBC
a	144.6, CH	8.44, d (7.6)	b	b, e_1, e_2, h, i
b	109.7, CH	7.11, dd (7.6, 3.2)	a, c	c
c	112.8, CH	7.26, d (3.2)	b	b, i
d_1	41.1, CH_3	3.27, s	d_2	d_2, h
d_2	41.0, CH_3	3.24, s	d_1	d_1, h
e_1	57.2, CH_2	3.91, dt (144, 8)	e_2, f	a, f, g, i
e_2	57.2, CH_2	3.88, dt (144, 8)	e_1, f	a, f, g, i
f	24.7, CH_2	1.75, m	e_1, e_2, g	e_1, e_2, g
g	10.9, CH_3	0.85, t	f	e_1, e_2, f
h	157.2, C	---	---	---
i	143.4, C	---	---	---

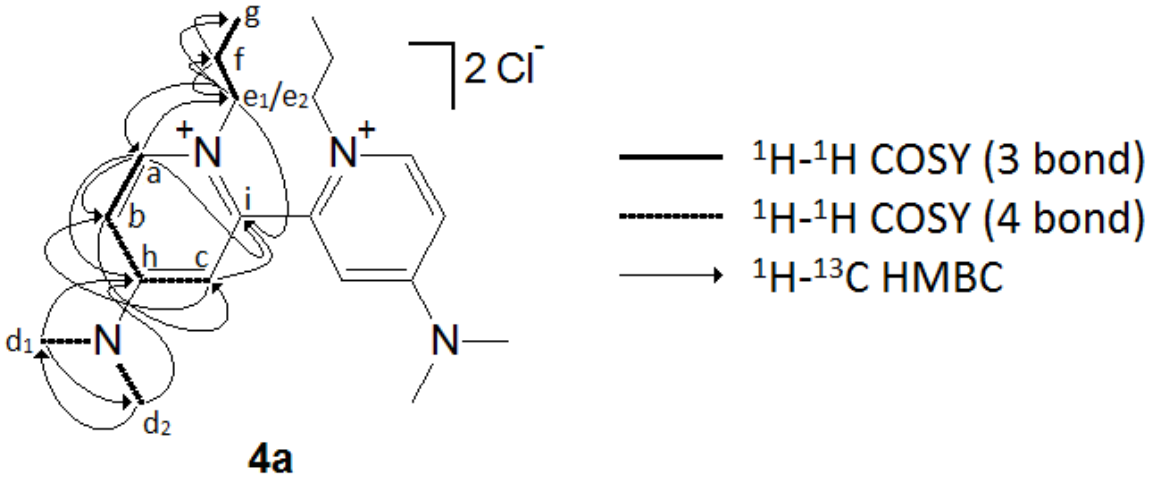


Figure 3.34: Structure of **4a** illustrating all assigned 2D NMR correlations for ^{1}H-^{1}H COSY and ^{1}H-^{13}C HMBC.

3.3.6 – Cyclic Voltammetry Spectra

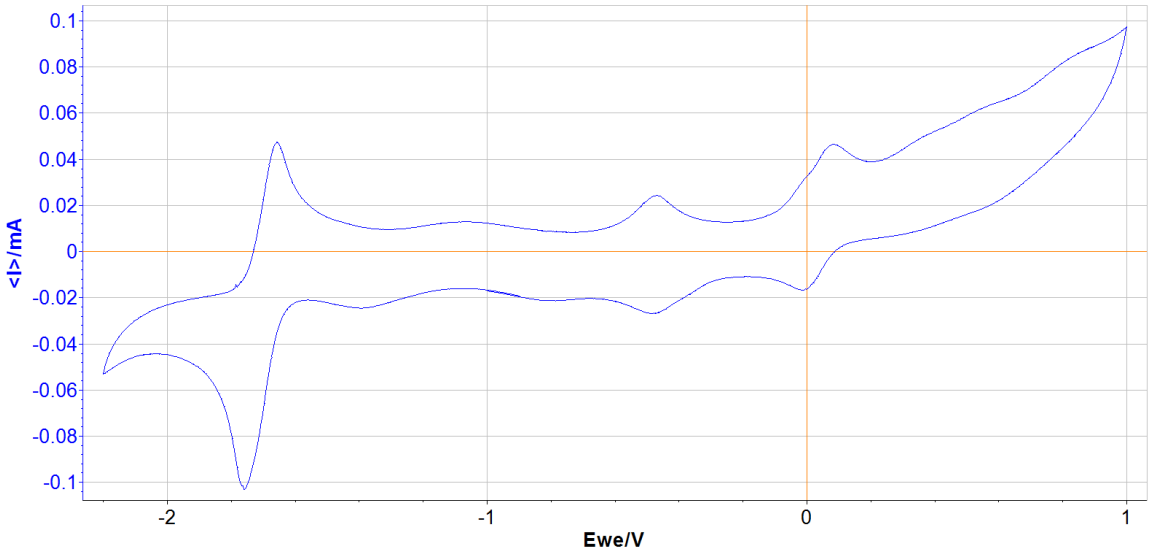


Figure 3.35: CV spectrum of **4a** + Fc in 0.1 M TBAH in DMF at 50 mV/s.

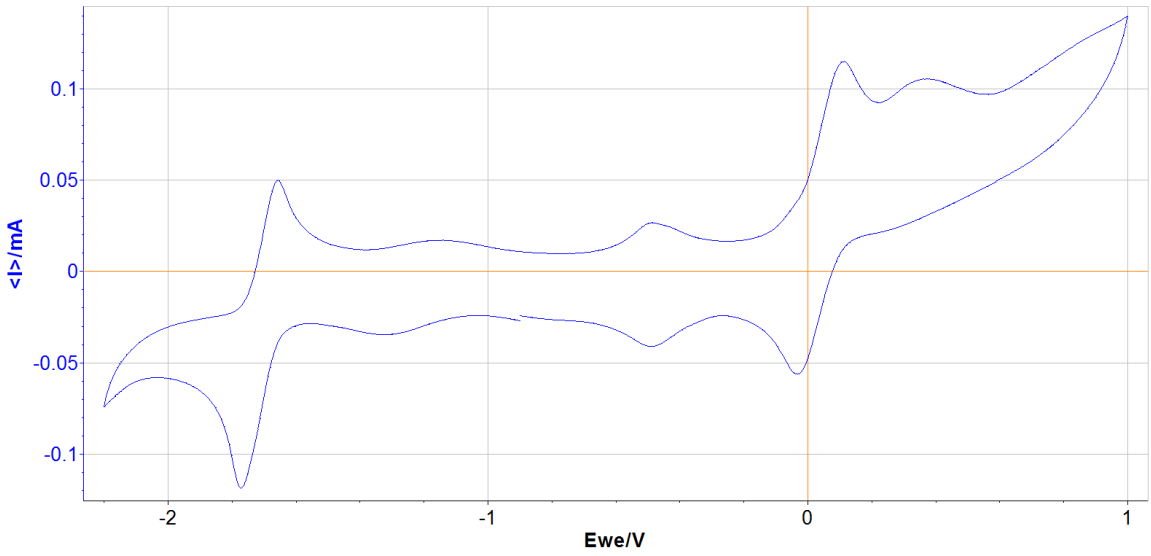


Figure 3.36: CV spectrum of **4b** + Fc in 0.1 M TBAH in DMF at 50 mV/s.

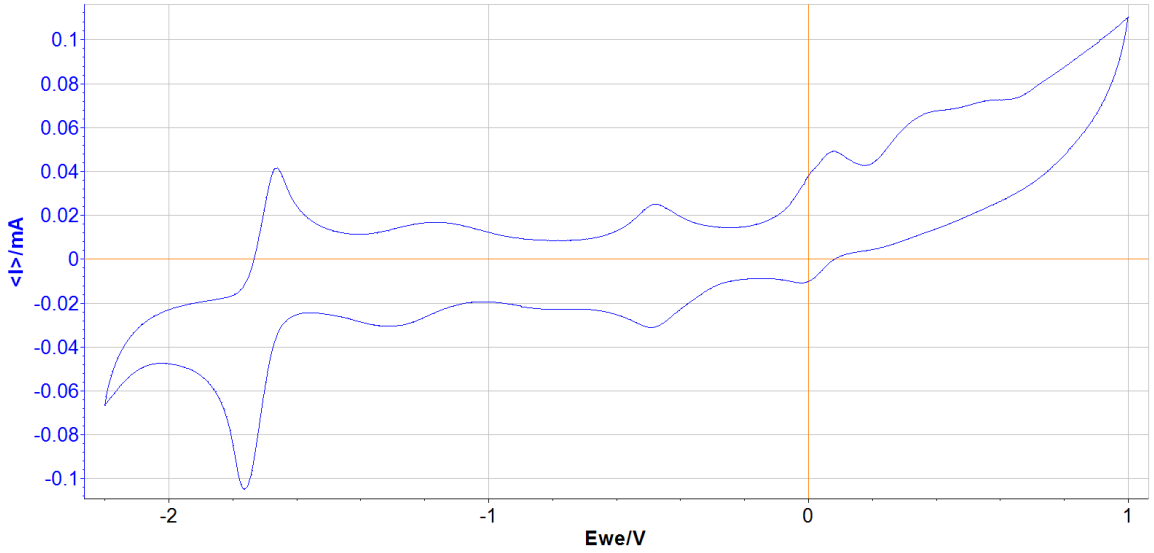


Figure 3.37: CV spectrum of **4c** + Fc in 0.1 M TBAH in DMF at 50 mV/s.

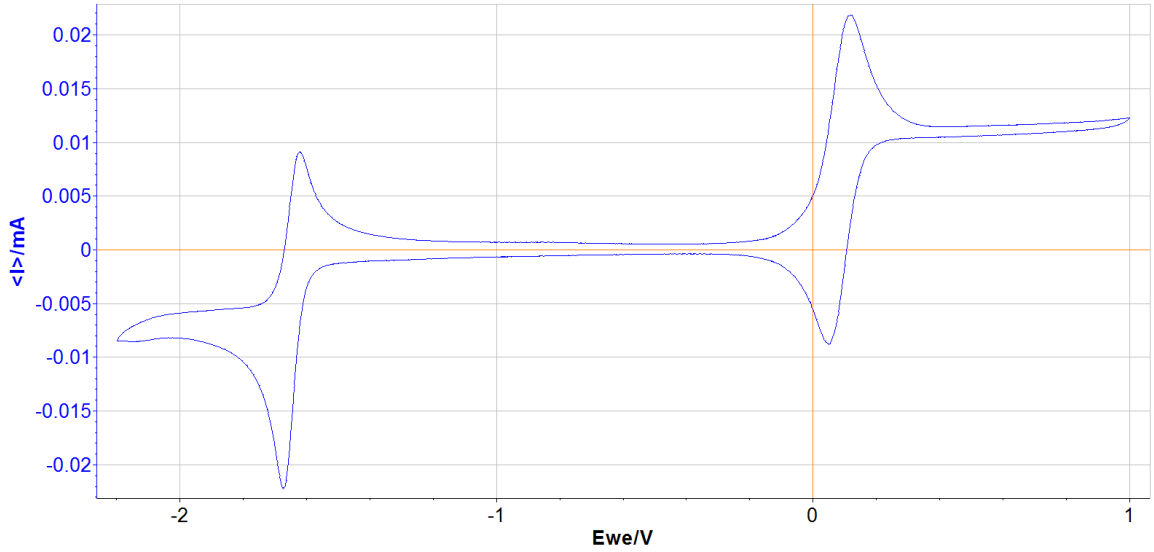


Figure 3.38: CV spectrum of **5a** + Fc in 0.1 M TBAH in DMF at 10 mV/s with ZIR correction.

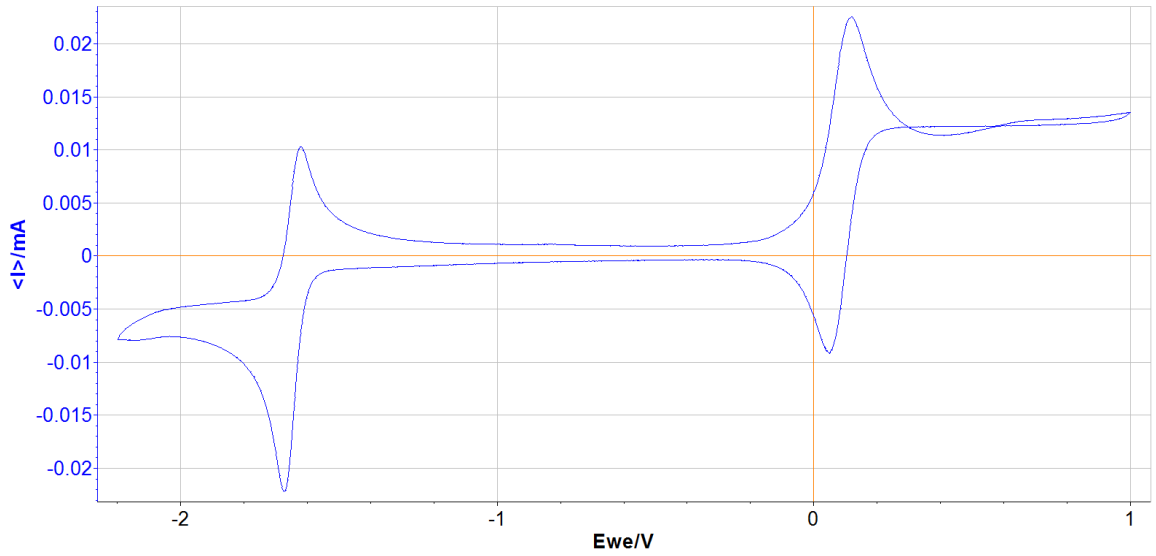


Figure 3.39: CV spectrum of **5b** + Fc in 0.1 M TBAH in DMF at 10 mV/s with ZIR correction.

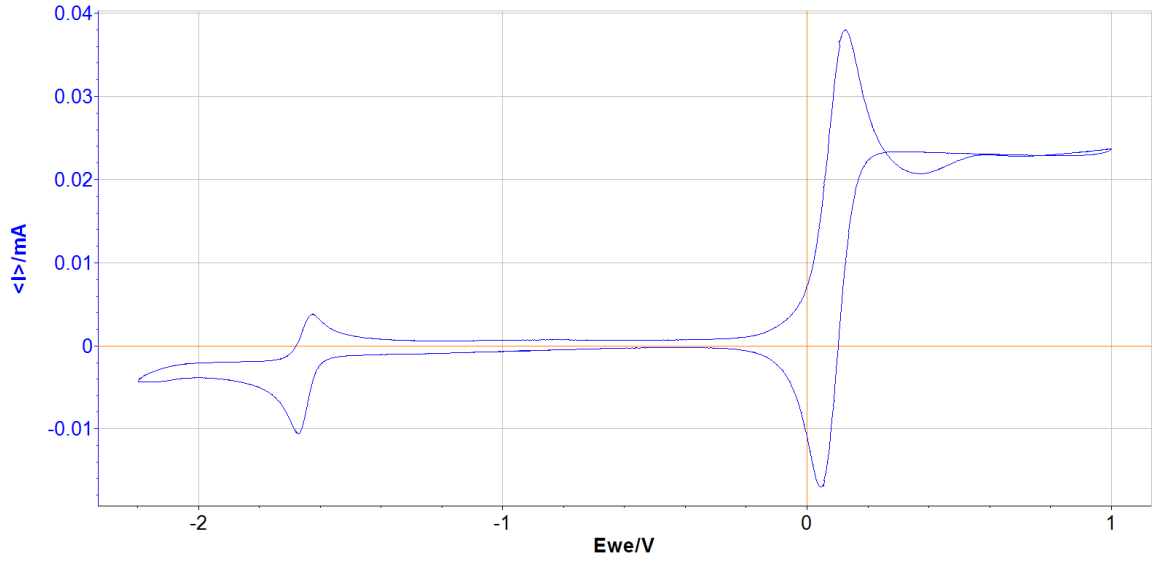


Figure 3.40: CV spectrum of **5c** + Fc in 0.1 M TBAH in DMF at 10 mV/s with ZIR correction.

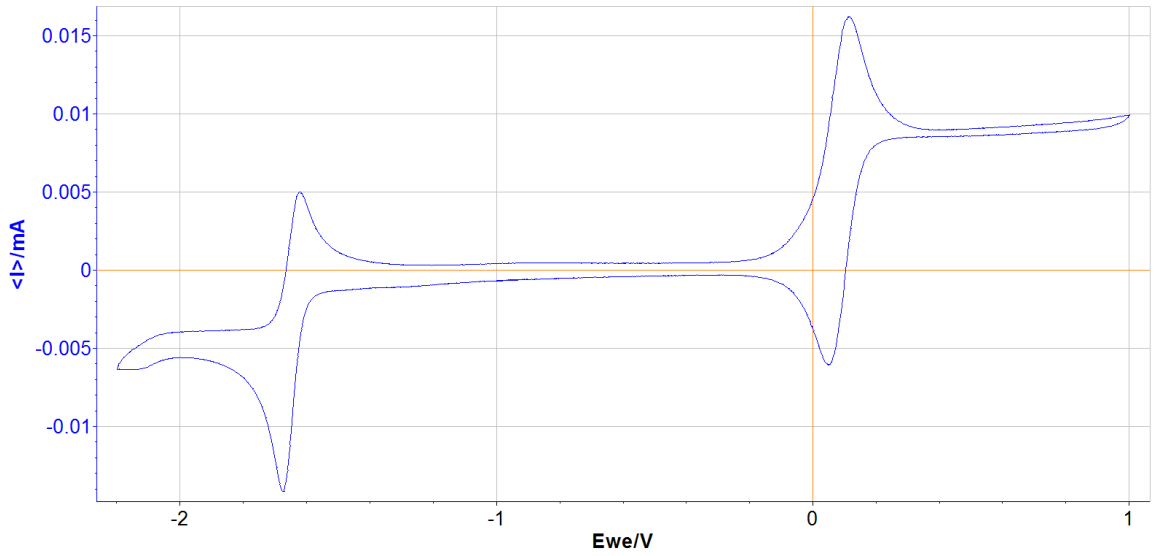


Figure 3.41: CV spectrum of **5d** + Fc in 0.1 M TBAH in DMF at 10 mV/s with ZIR correction.

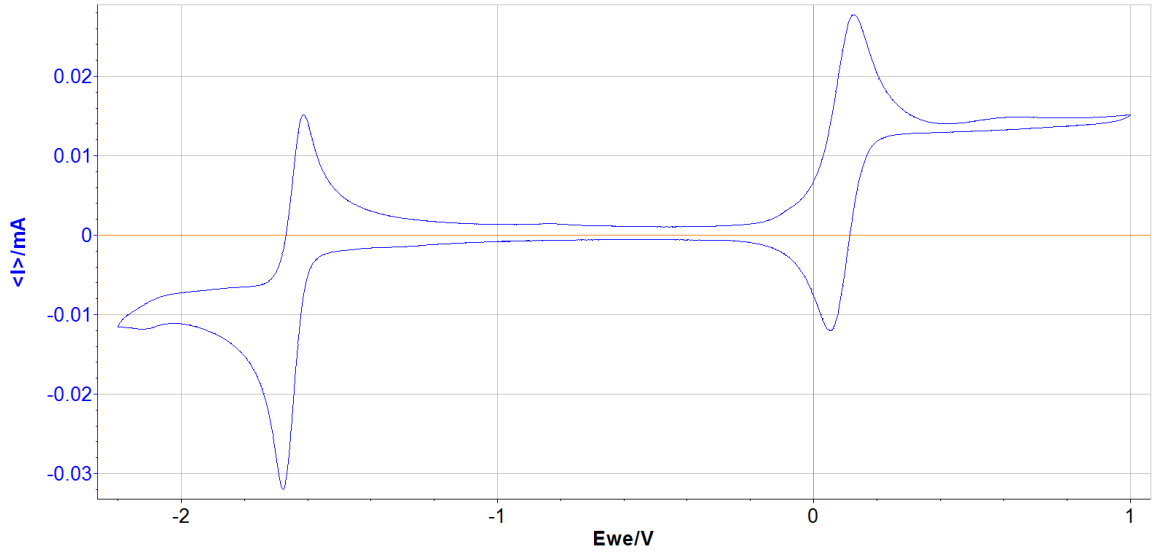


Figure 3.42: CV spectrum of **5e+5a+5d** + Fc in 0.1 M TBAH in DMF at 10 mV/s with ZIR correction.

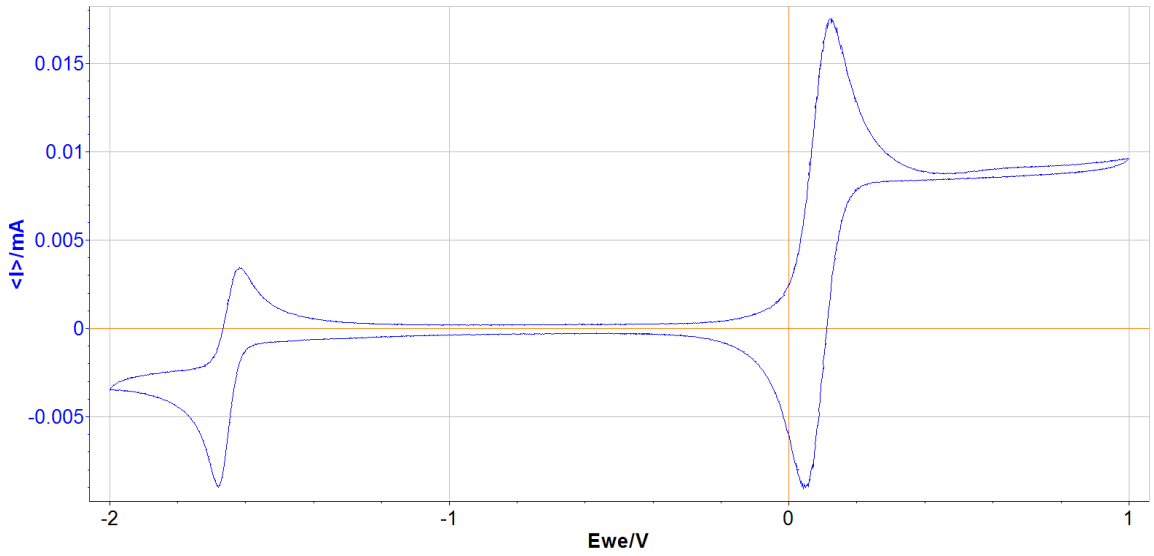


Figure 3.43: CV spectrum of **5f+5b+5d** + Fc in 0.1 M TBAH in DMF at 10 mV/s with ZIR correction.

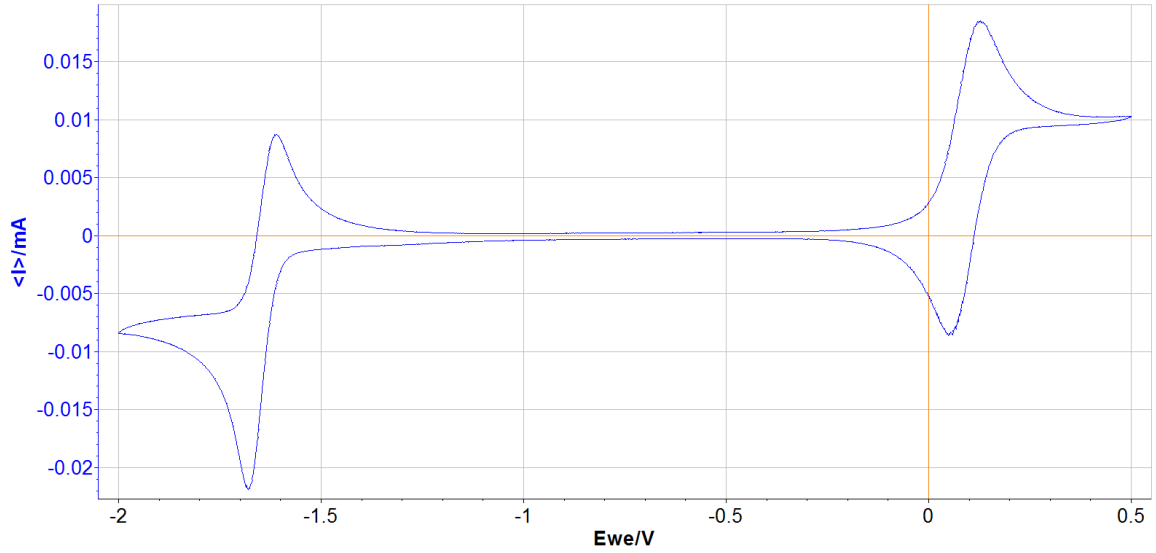
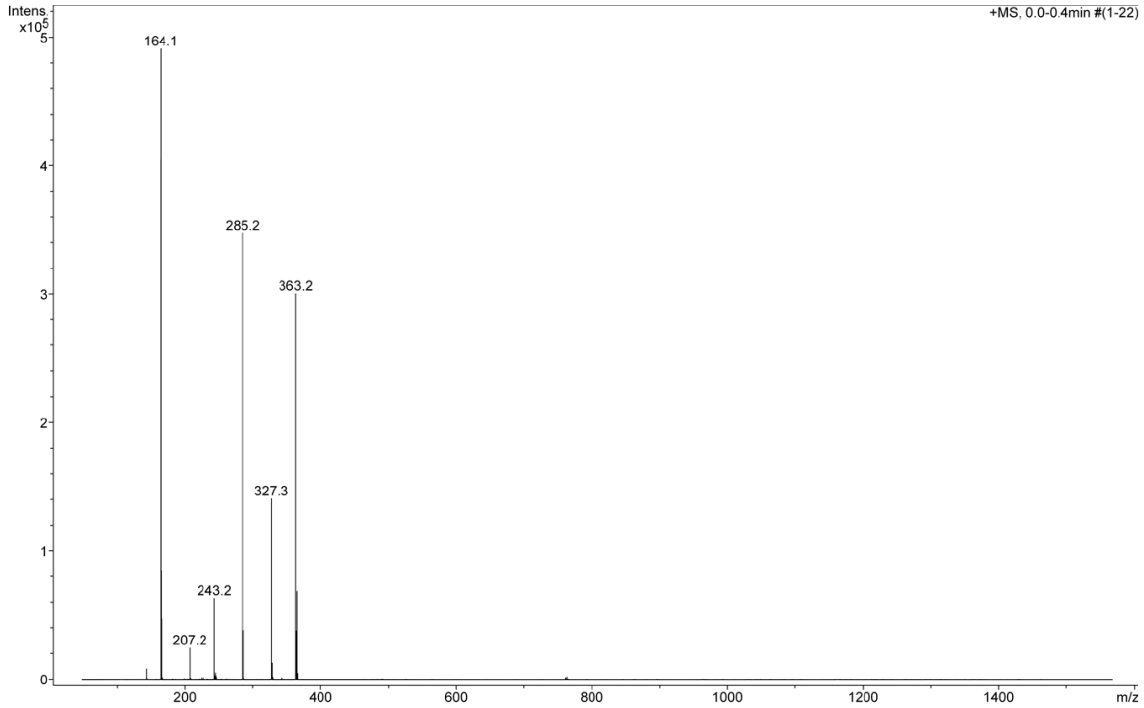


Figure 3.44: CV spectrum of **5g+5c+5d** + Fc in 0.1 M TBAH in DMF at 10 mV/s with ZIR correction.

3.3.7 – Electrospray Ion Mass Spectra



Acquisition Parameter					
Source Type	ESI	Ion Polarity	Positive	Set Corrector Fill	52 V
Scan Range	n/a	Capillary Exit	100.0 V	Set Pulsar Pull	398 V
Scan Begin	50 m/z	Hexapole RF	130.0 V	Set Pulsar Push	398 V
Scan End	1500 m/z	Skimmer 1	55.0 V	Set Reflector	1300 V
		Hexapole 1	26.0 V	Set Flight Tube	9000 V
				Set Detector TOF	1960 V

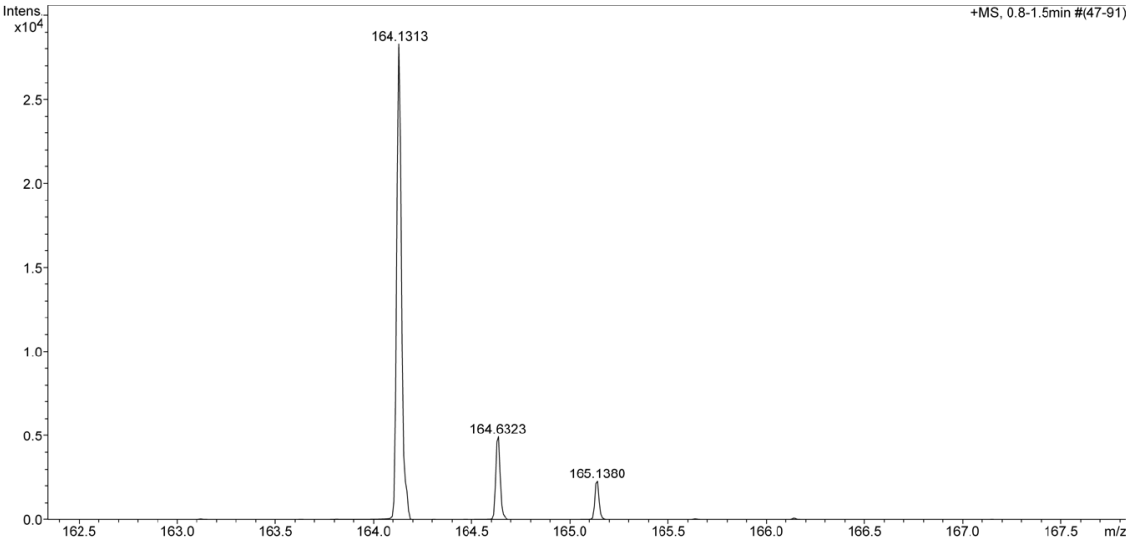


Figure 3.45: Top (a); Low-resolution mass spectrum of **4a**. Bottom (b); High-resolution mass spectrum of **4a**.

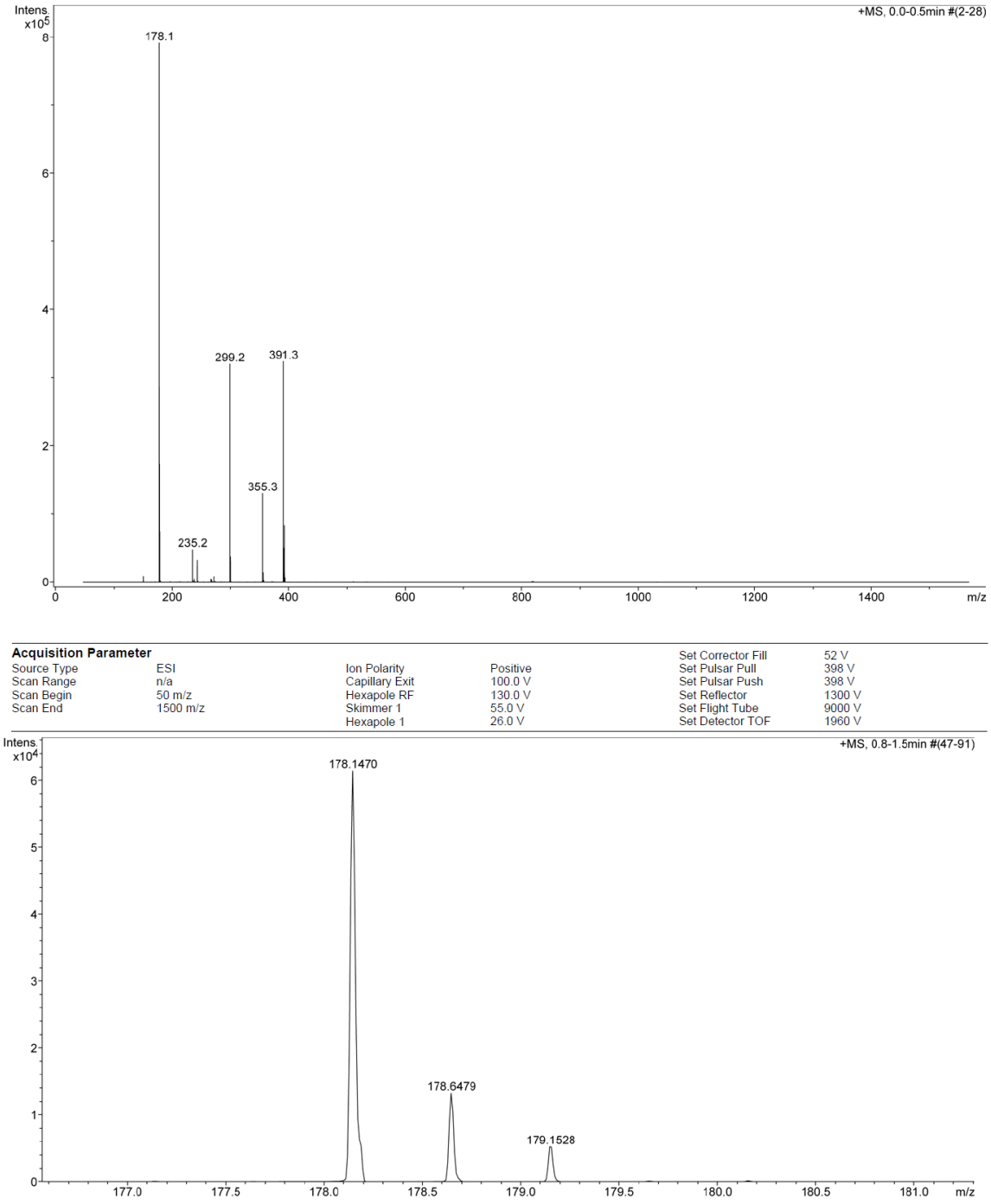


Figure 3.46: Top (a); Low-resolution mass spectrum of **4b**. Bottom (b); High-resolution mass spectrum of **4b**.

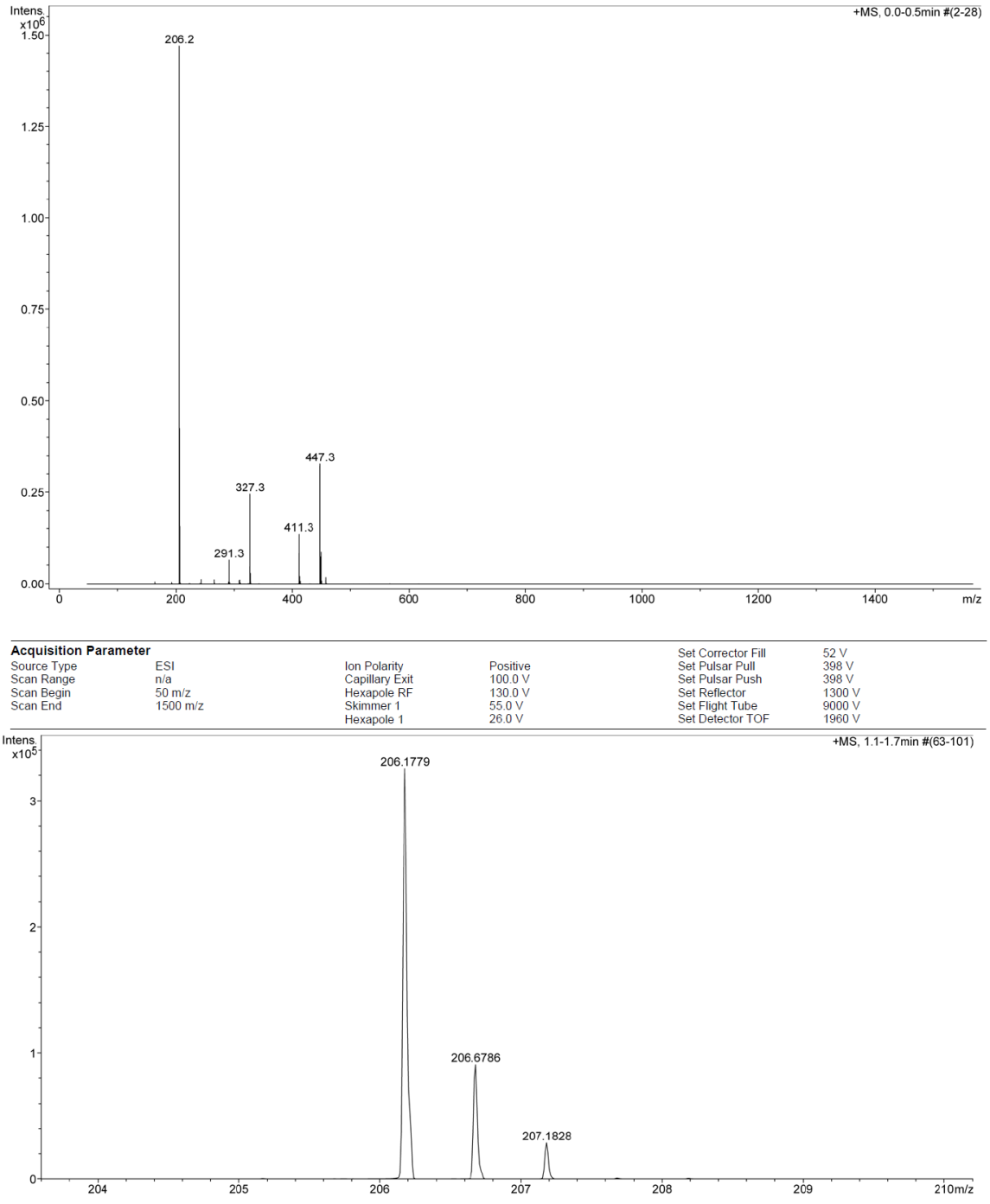


Figure 3.47: Top (a); Low-resolution mass spectrum of **4c**. Bottom (b); High-resolution mass spectrum of **4c**.

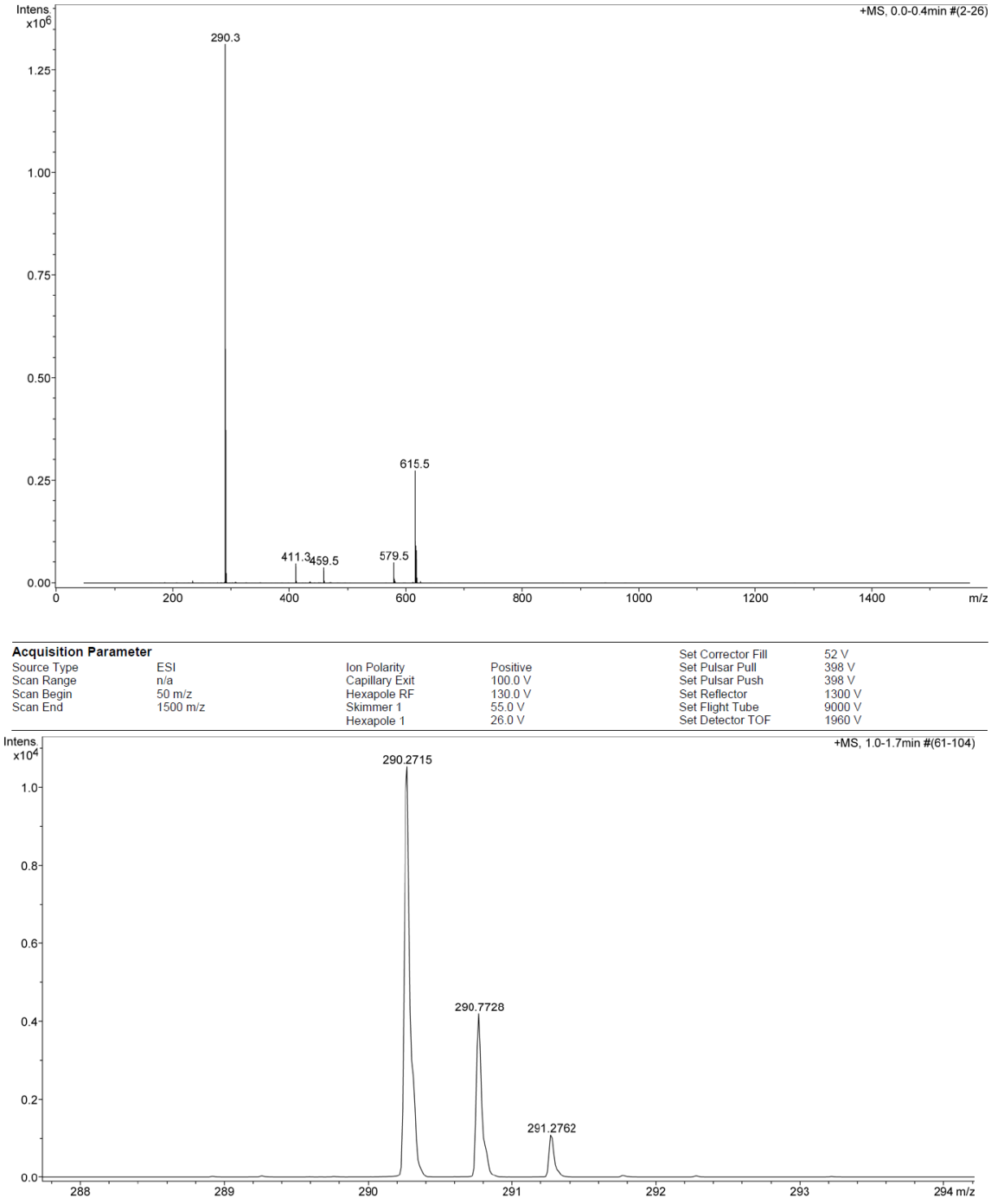
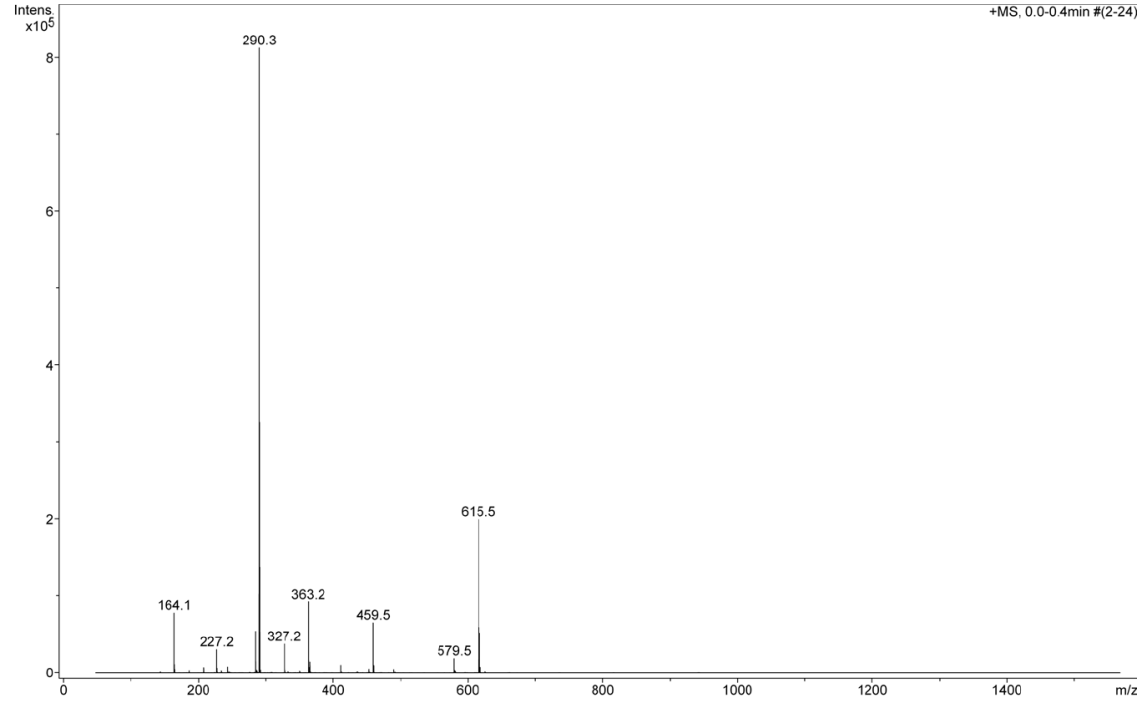


Figure 3.48: Top (a); Low-resolution mass spectrum of **4d**. Bottom (b); High-resolution mass spectrum of **4d**.



Acquisition Parameter					
Source Type	ESI	Ion Polarity	Positive	Set Corrector Fill	52 V
Scan Range	n/a	Capillary Exit	100.0 V	Set Pulsar Pull	398 V
Scan Begin	50 m/z	Hexapole RF	130.0 V	Set Pulsar Push	398 V
Scan End	1500 m/z	Skimmer 1	55.0 V	Set Reflector	1300 V
		Hexapole 1	26.0 V	Set Flight Tube	9000 V
				Set Detector TOF	1960 V

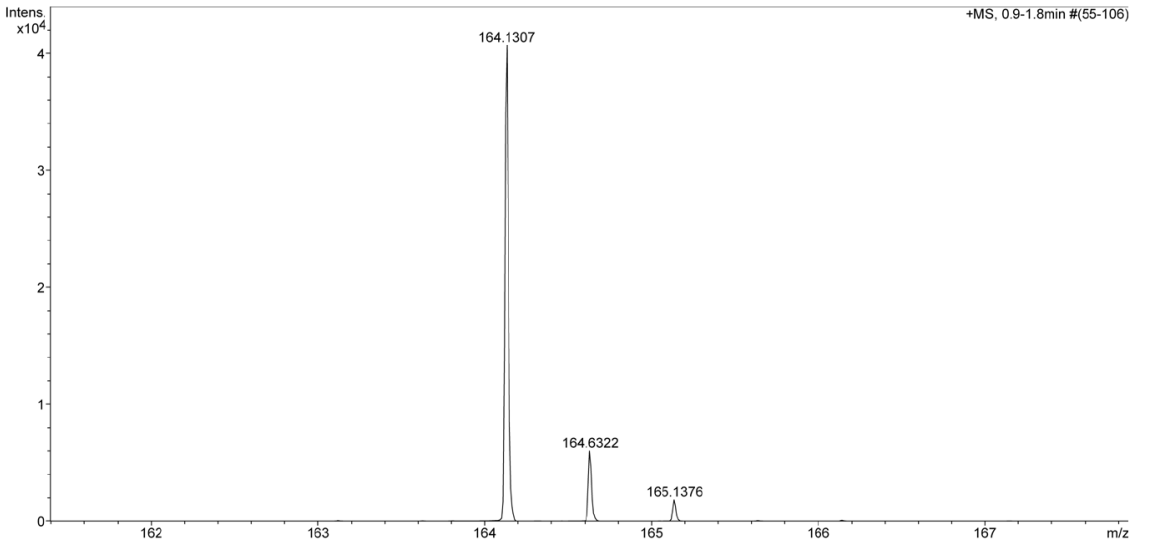


Figure 3.49: Top (a); Low-resolution mass spectrum of **4e**+**4a**+**4d**. Bottom (b); High-resolution mass spectrum of **4a** in sample **4e**+**4a**+**4d**.

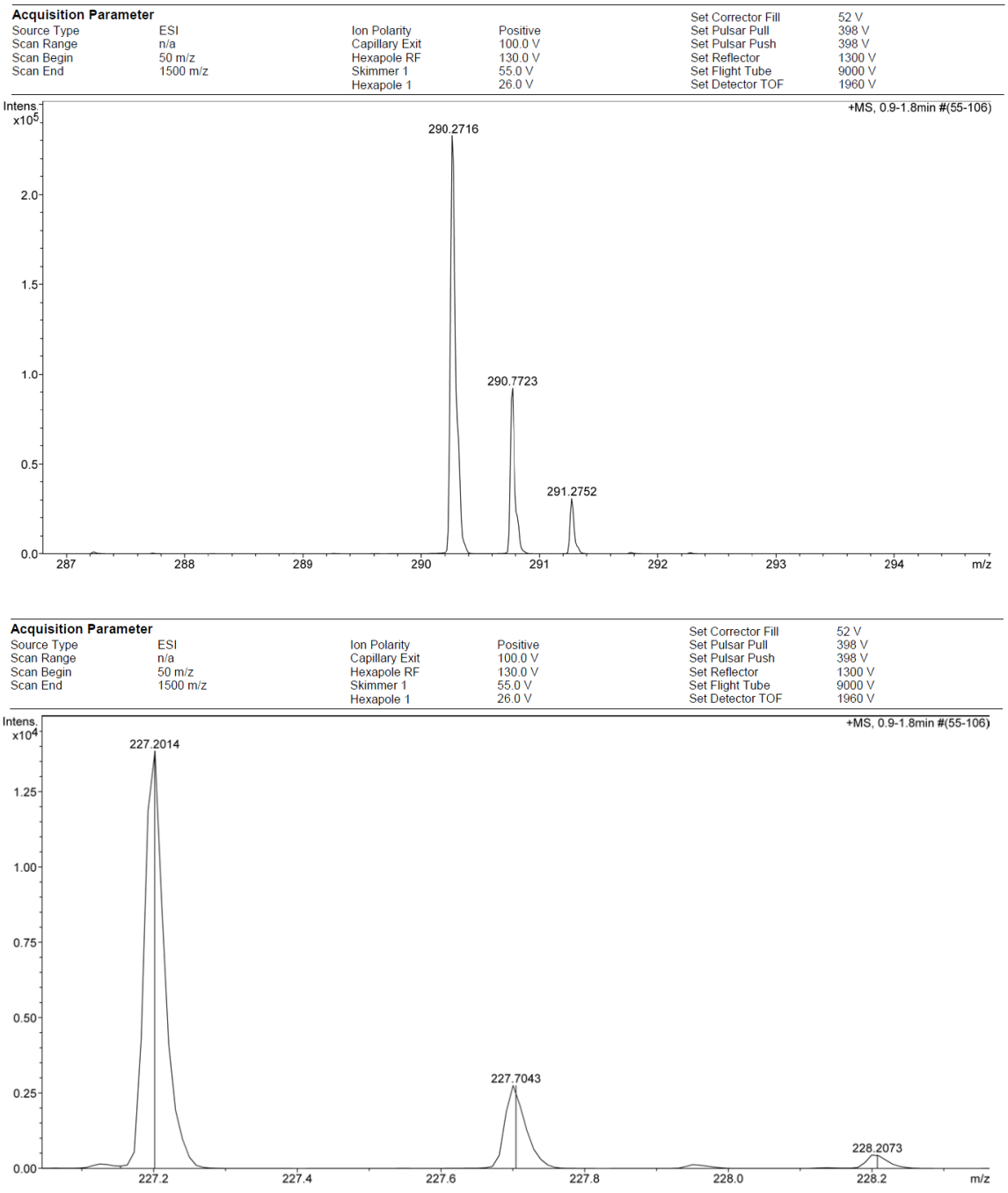


Figure 3.50: Top (a); High-resolution mass spectrum of **4d** in sample **4e+4a+4d**. Bottom (b); High-resolution mass spectrum of **4e** in sample **4e+4a+4d**.

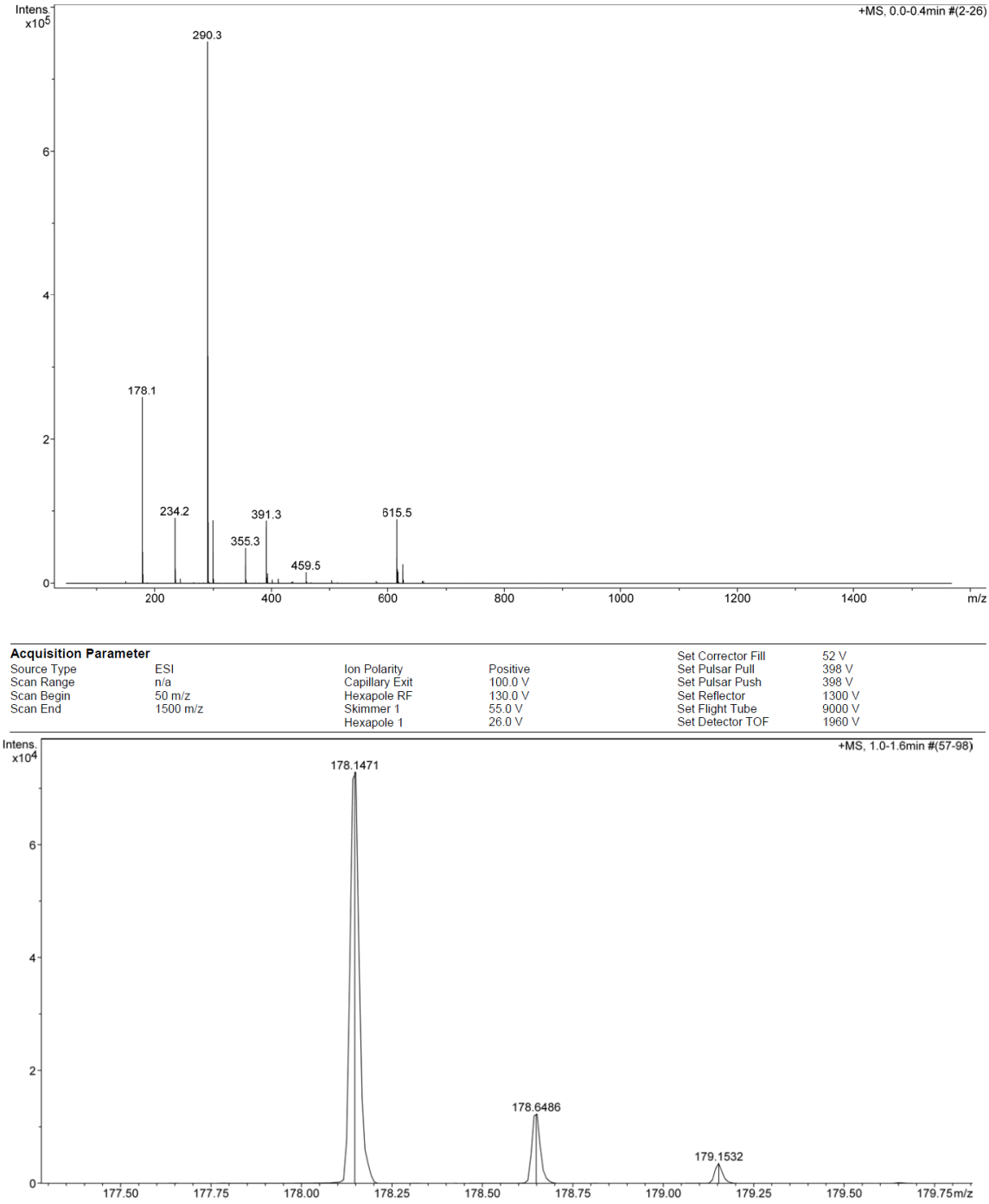


Figure 3.51: Top (a); Low-resolution mass spectrum of **4f**+**4b**+**4d**. Bottom (b); High-resolution mass spectrum of **4b** in sample **4f**+**4b**+**4d**.

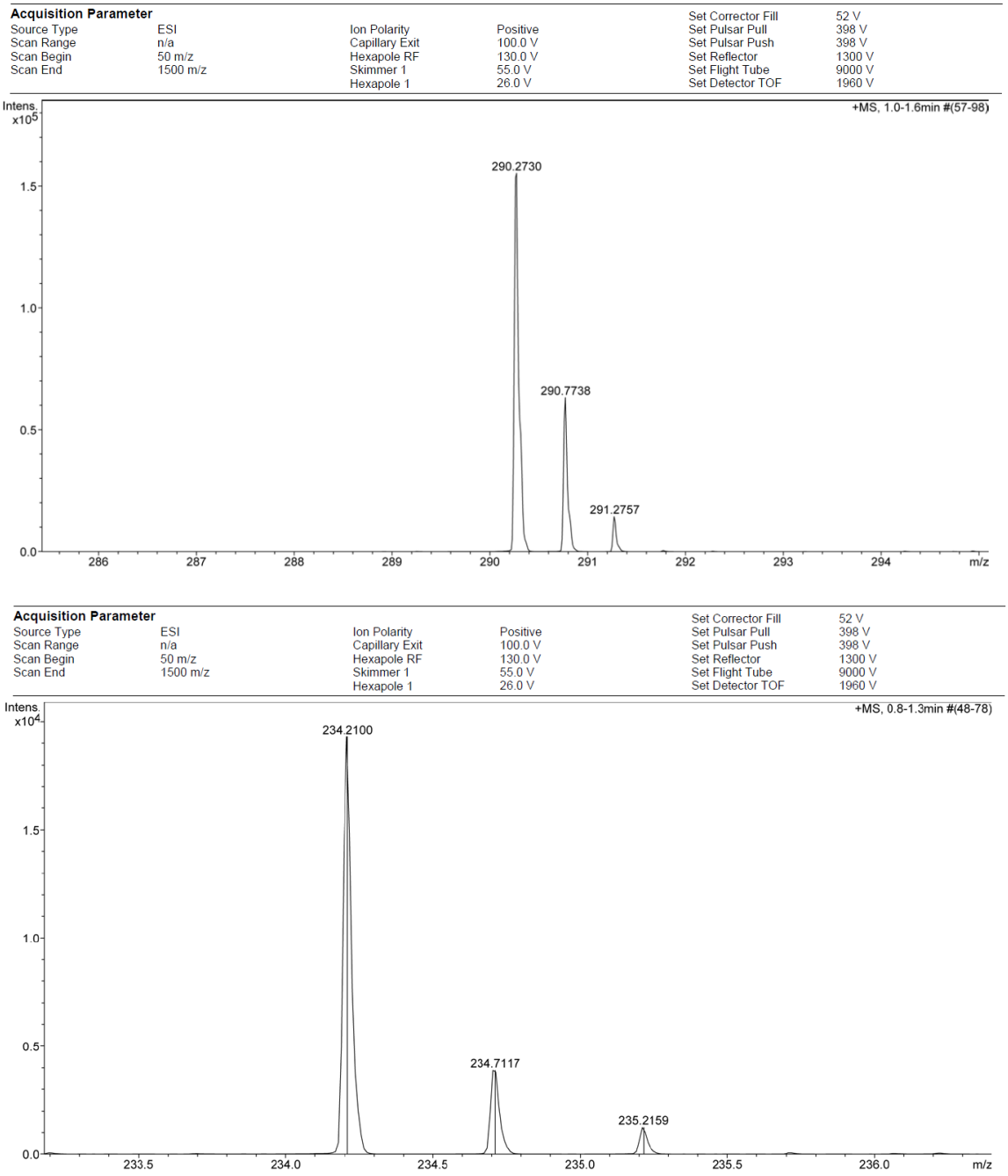


Figure 3.52: Top (a); High-resolution mass spectrum of **4d** in sample **4f+4b+4d**. Bottom (b); High-resolution mass spectrum of **4f** in sample **4f+4b+4d**.

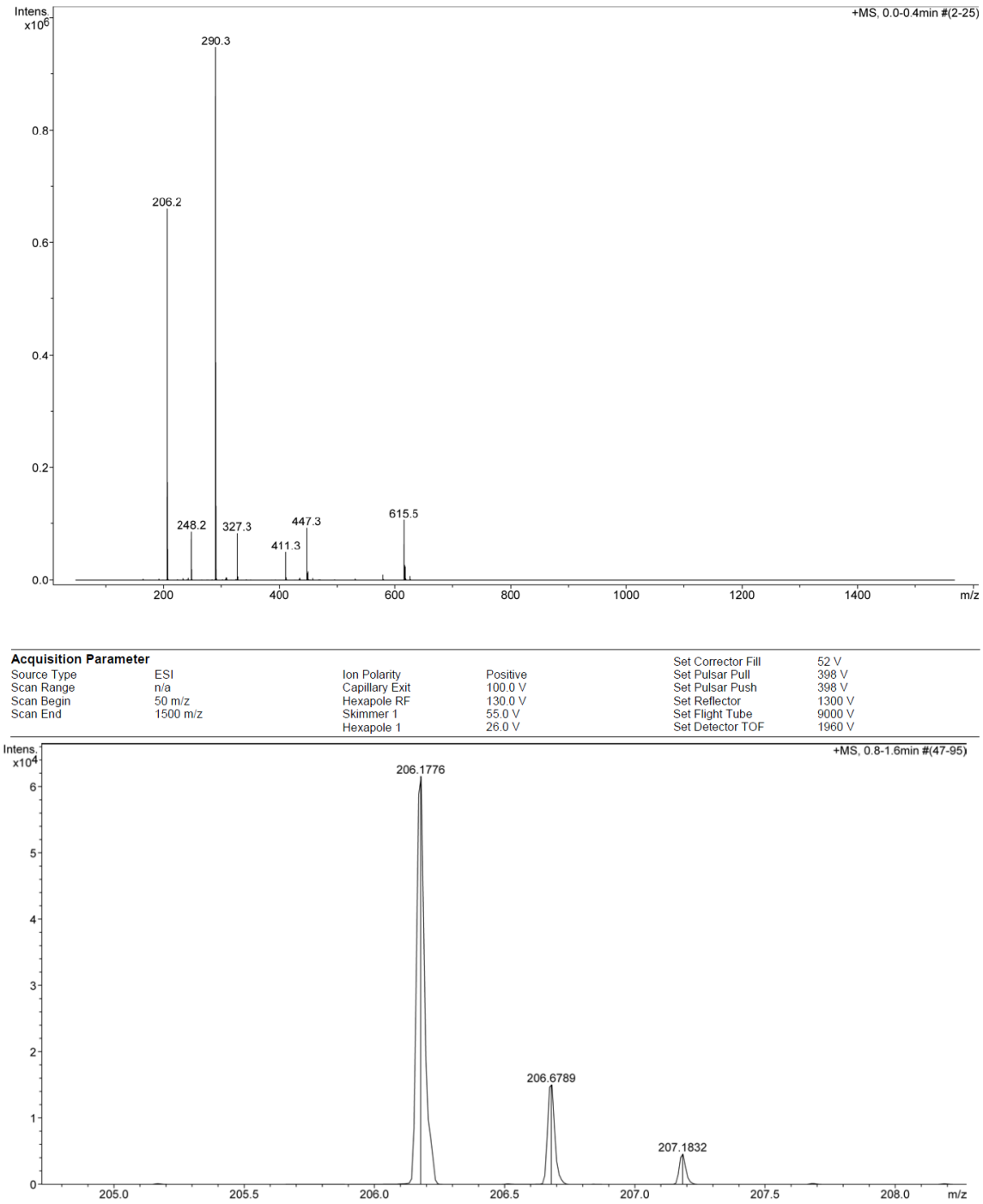


Figure 3.53: Top (a); Low-resolution mass spectrum of **4g**+**4c**+**4d**. Bottom (b); High-resolution mass spectrum of **4c** in sample **4g**+**4c**+**4d**.

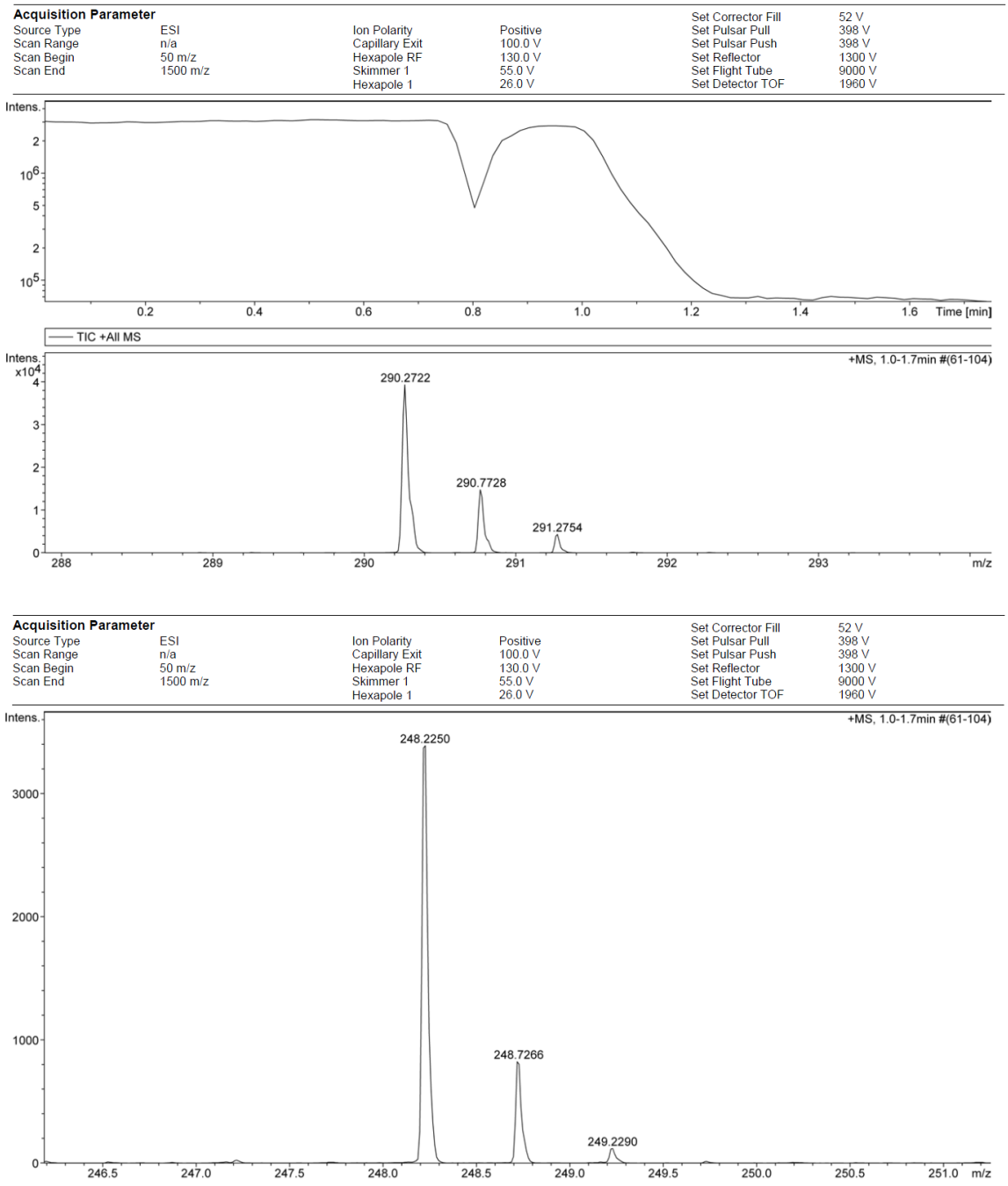
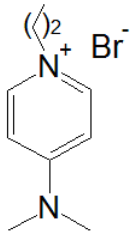


Figure 3.54: Top (a); High-resolution mass spectrum of **4d** in sample **4g+4c+4d**. Bottom (b); High-resolution mass spectrum of **4g** in sample **4g+4c+4d**.

3.3.8 – 1D and 2D NMR Spectra



2a

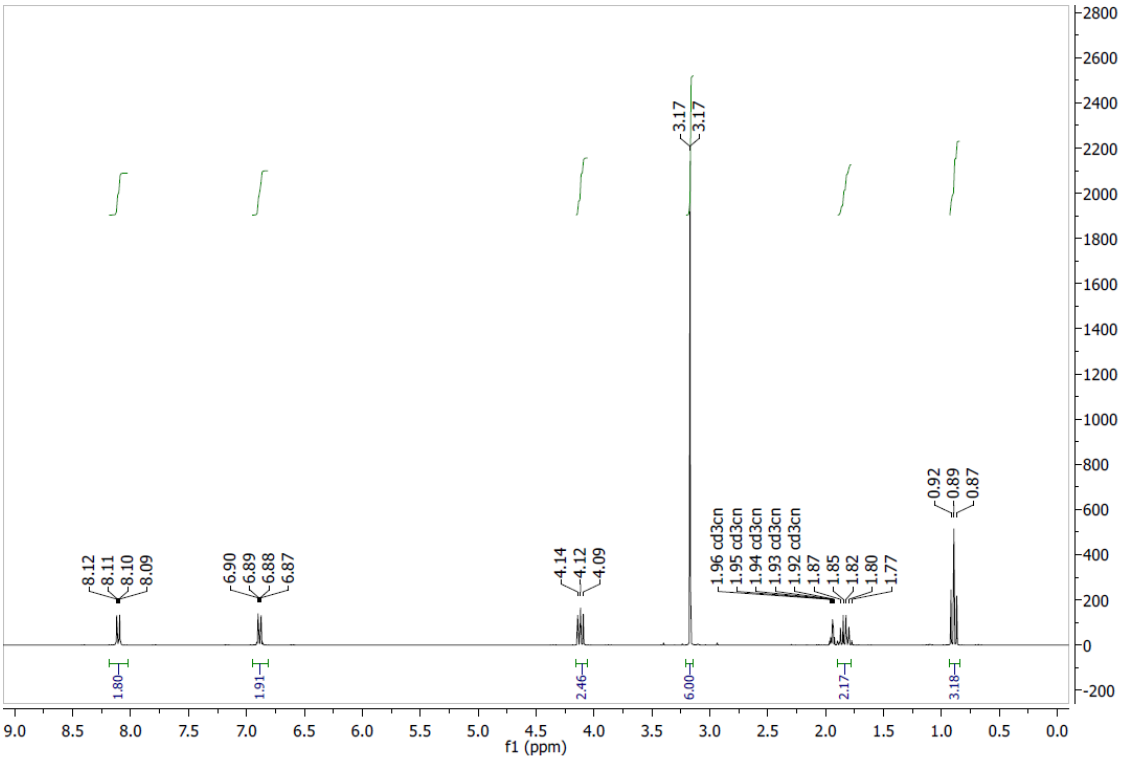


Figure 3.55: ^{1}H NMR spectrum of **2a** in CD_3CN (300 MHz).

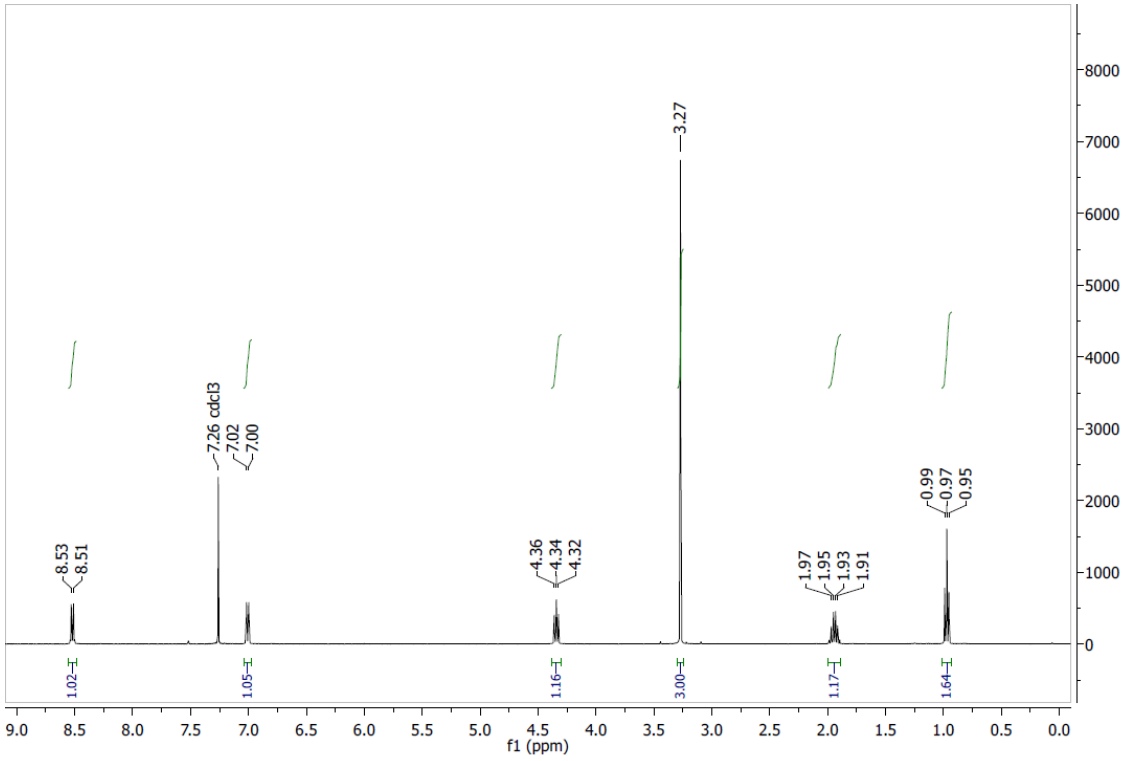


Figure 3.56: ^{1}H NMR spectrum of **2a** in $CDCl_3$ (400 MHz).

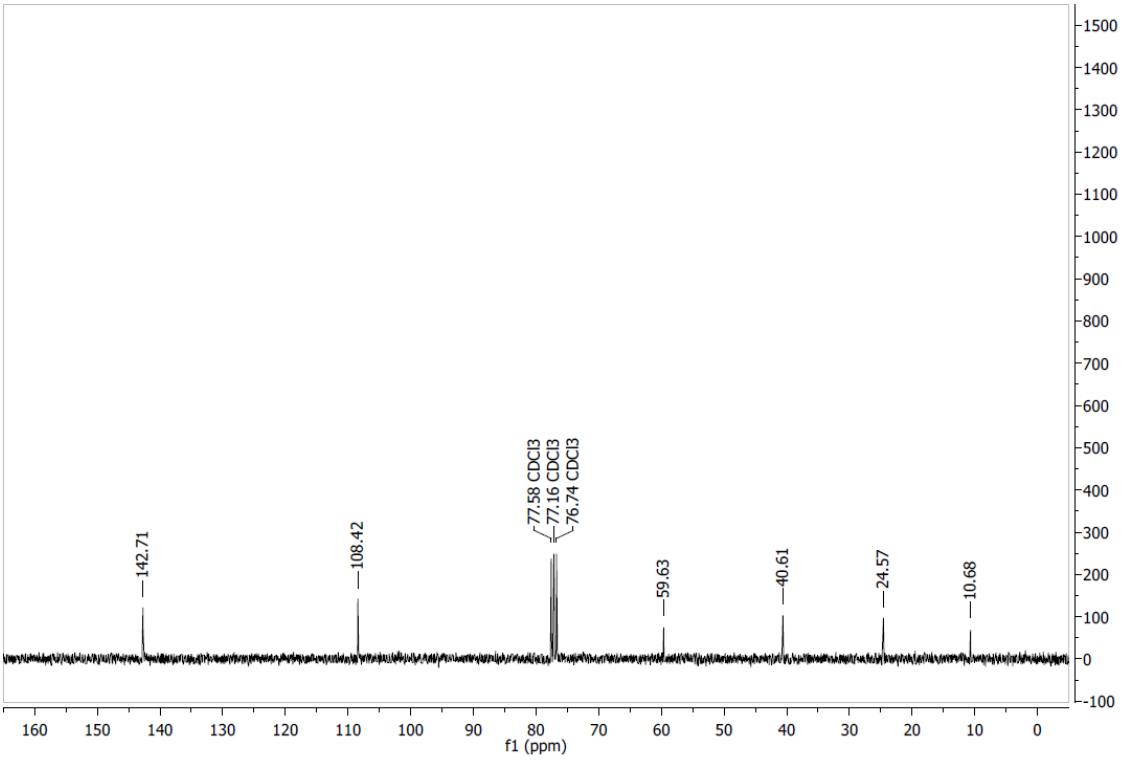
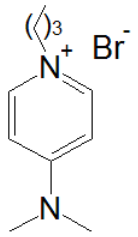


Figure 3.57: ^{13}C NMR spectrum of **2a** in $CDCl_3$ (400 MHz).



2b

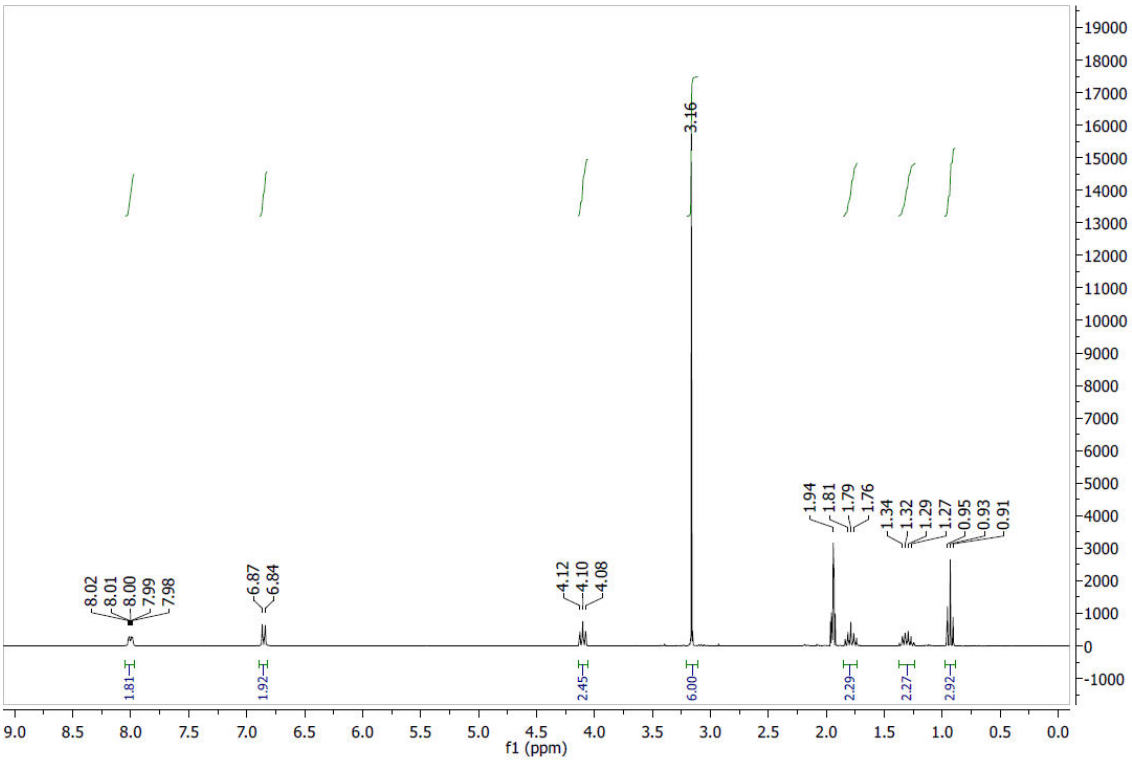


Figure 3.58: ^{1}H NMR spectrum of **2b** in CD_3CN (300 MHz).

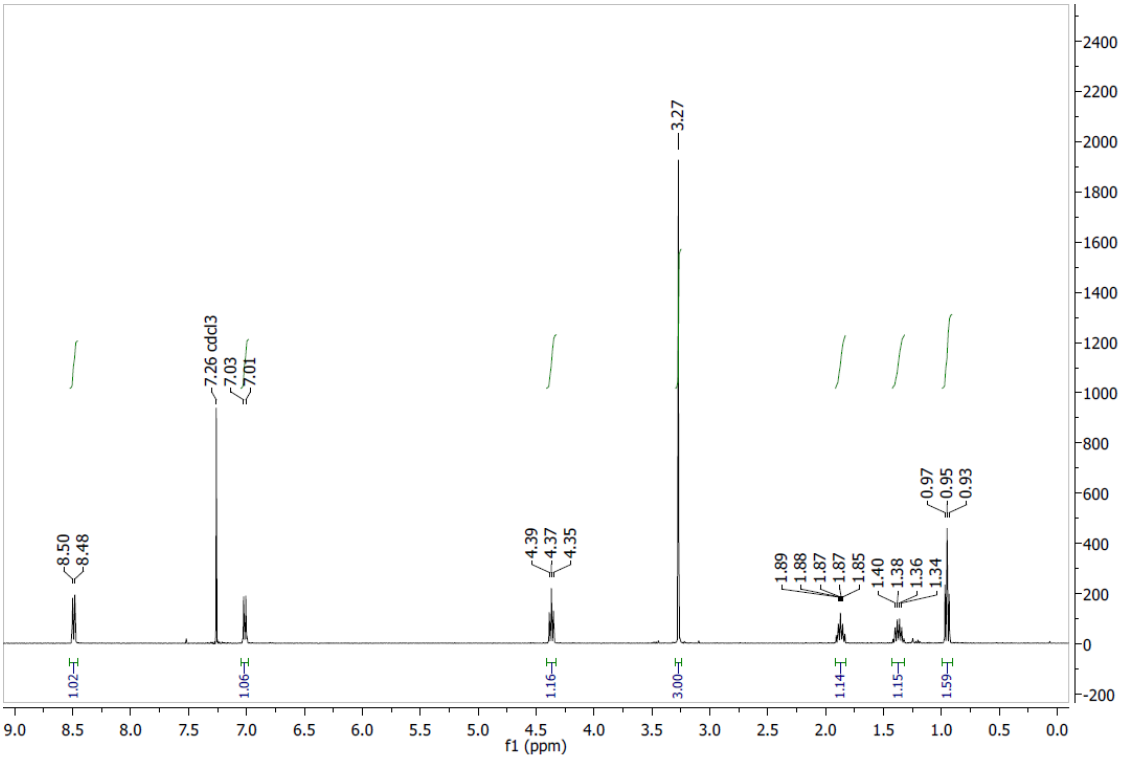


Figure 3.59: ^{1}H NMR spectrum of **2b** in $CDCl_3$ (400 MHz).

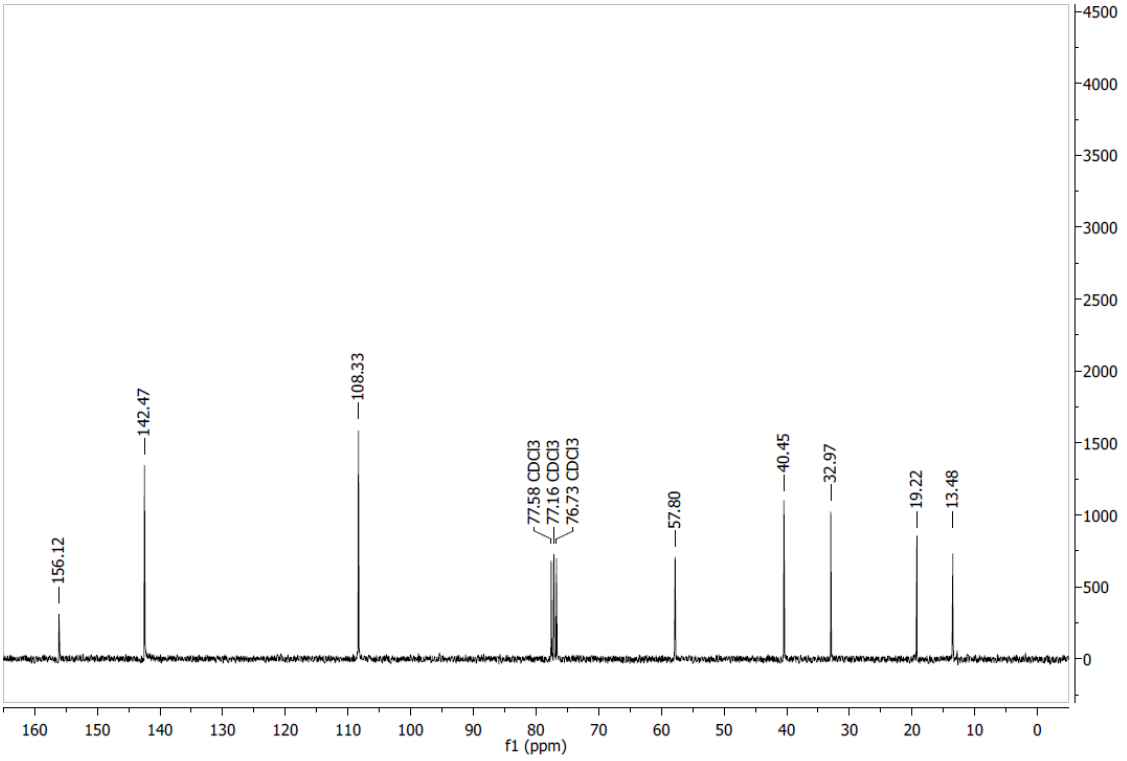
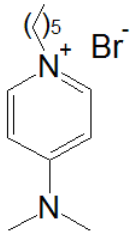


Figure 3.60: ^{13}C NMR spectrum of **2b** in $CDCl_3$ (400 MHz).



2c

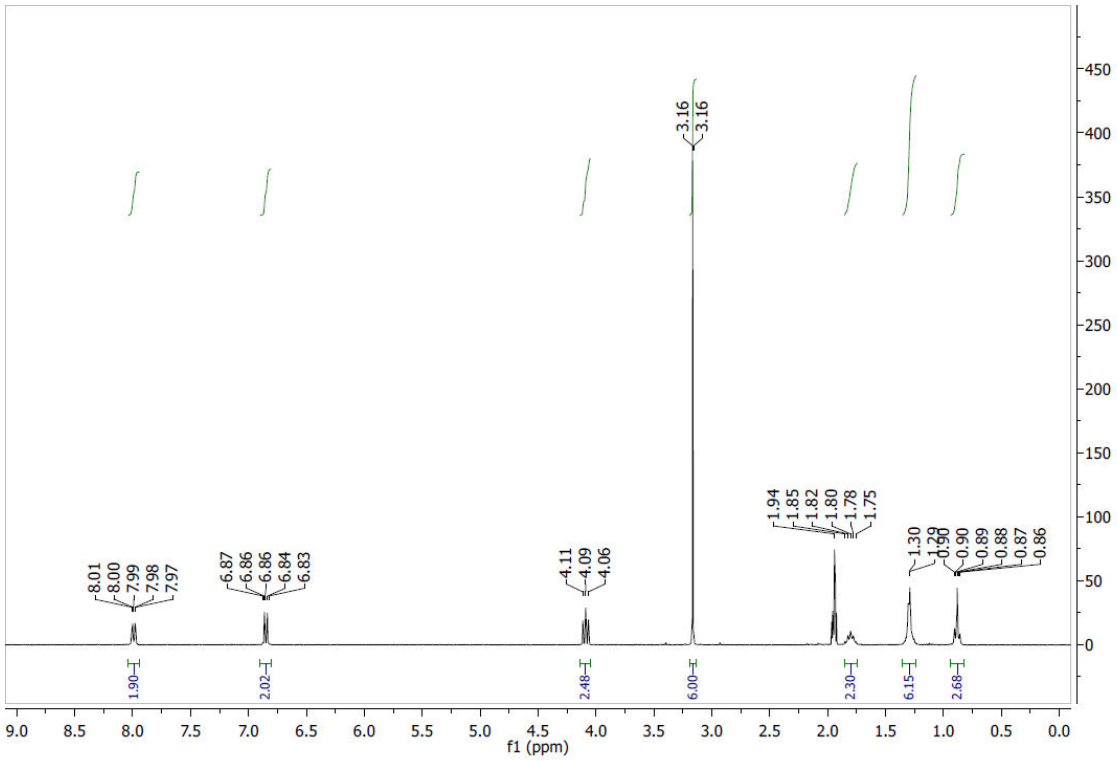


Figure 3.61: ^{1}H NMR spectrum of **2c** in CD_3CN (300 MHz).

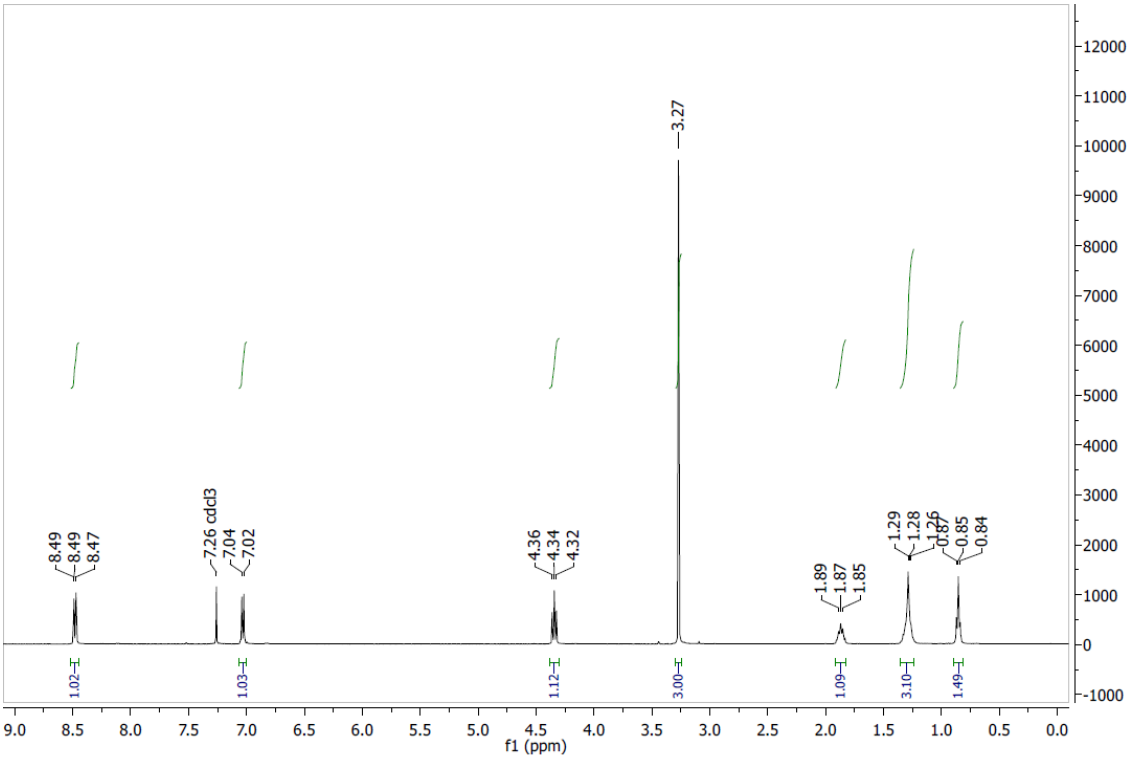


Figure 3.62: ^{1}H NMR spectrum of **2c** in $CDCl_3$ (400 MHz).

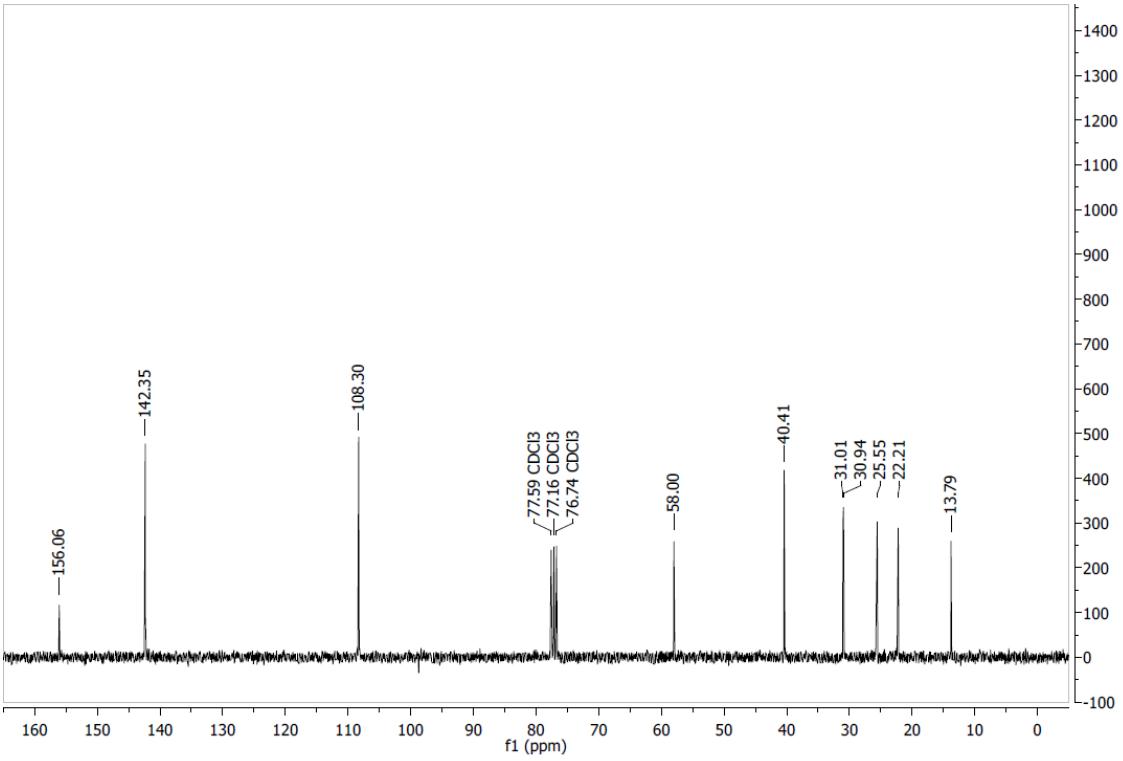
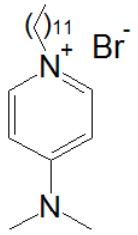


Figure 3.63: ^{13}C NMR spectrum of **2c** in $CDCl_3$ (400 MHz).



2d

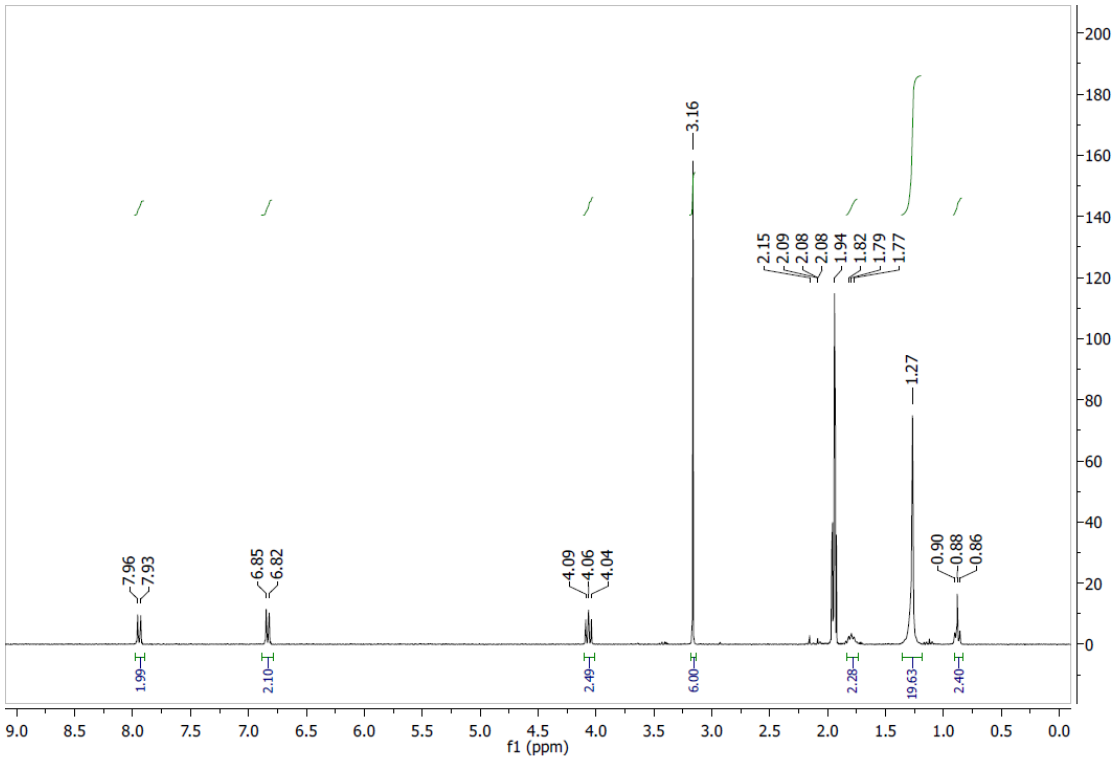


Figure 3.64: ^{1}H NMR spectrum of **2d** in CD_3CN (300 MHz).

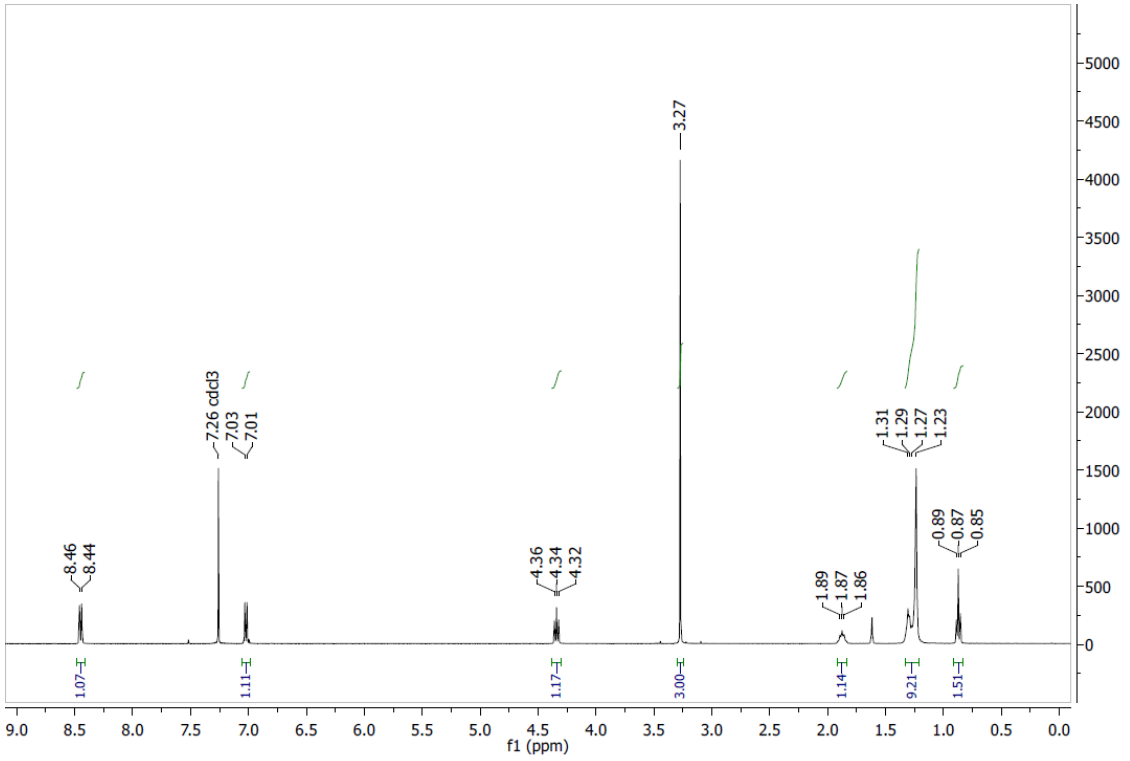


Figure 3.65: ^{1}H NMR spectrum of **2d** in $CDCl_3$ (400 MHz).

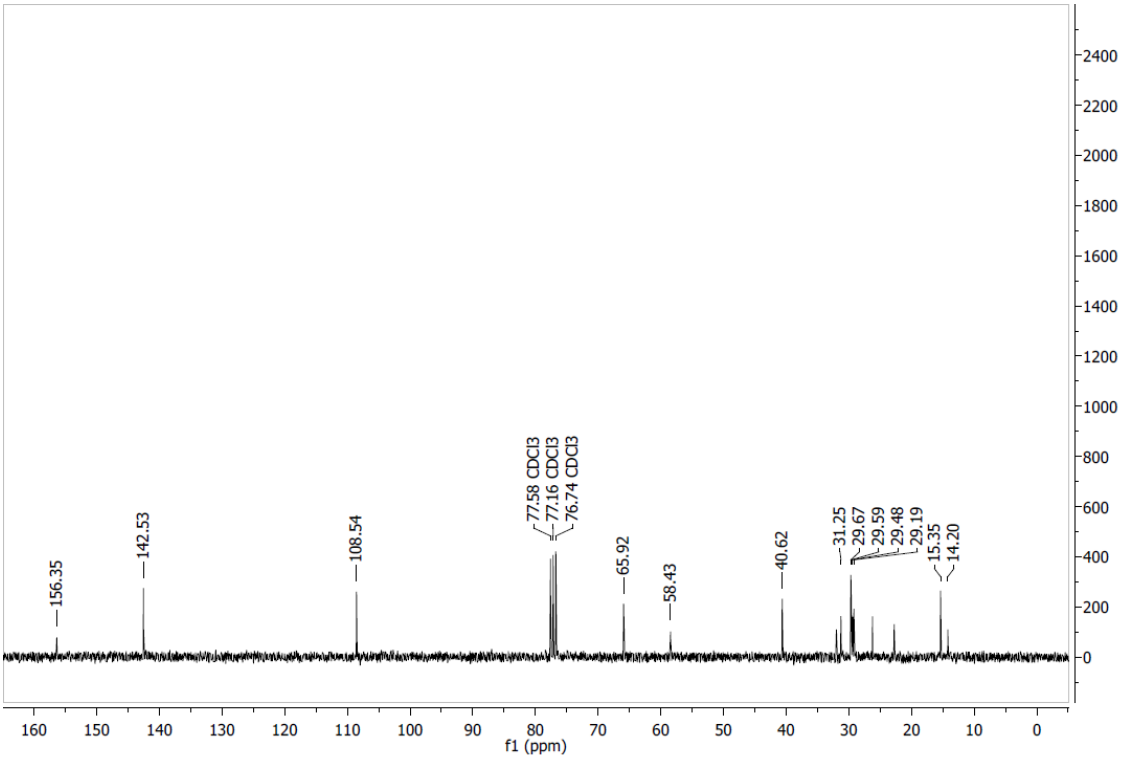
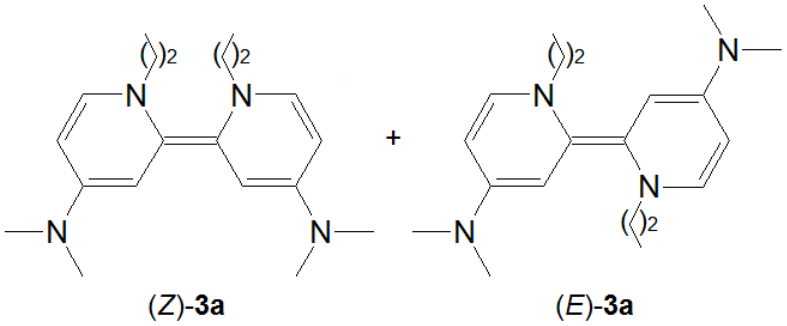


Figure 3.66: ^{13}C NMR spectrum of **2d** in $CDCl_3$ (400 MHz).



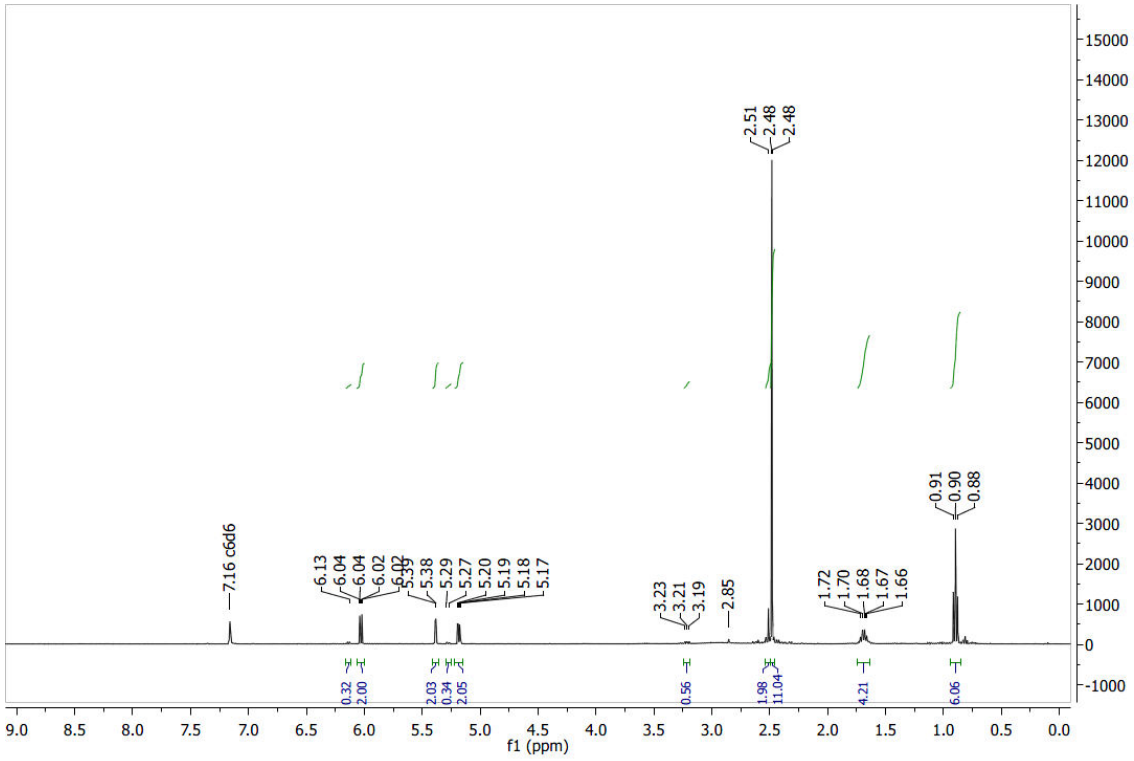


Figure 3.67: ^{1}H NMR spectrum of **3a** in C_6D_6 (400 MHz).

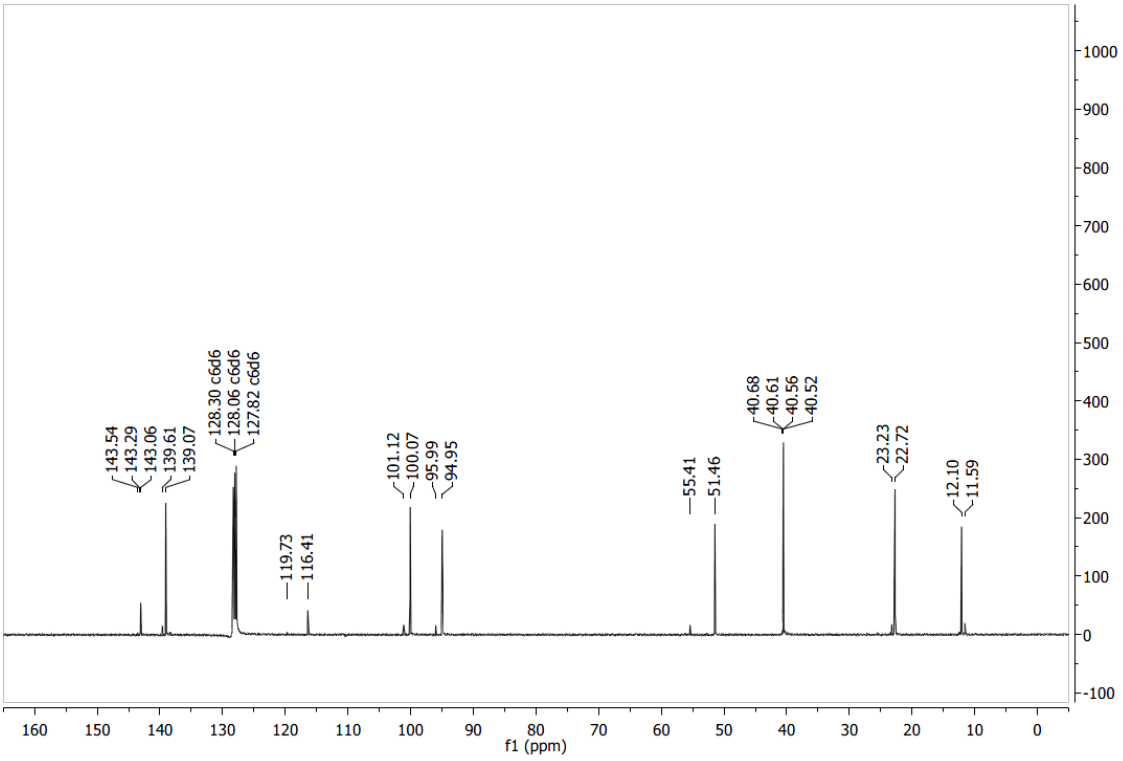


Figure 3.68: ^{13}C NMR spectrum of **3a** in C_6D_6 (400 MHz).

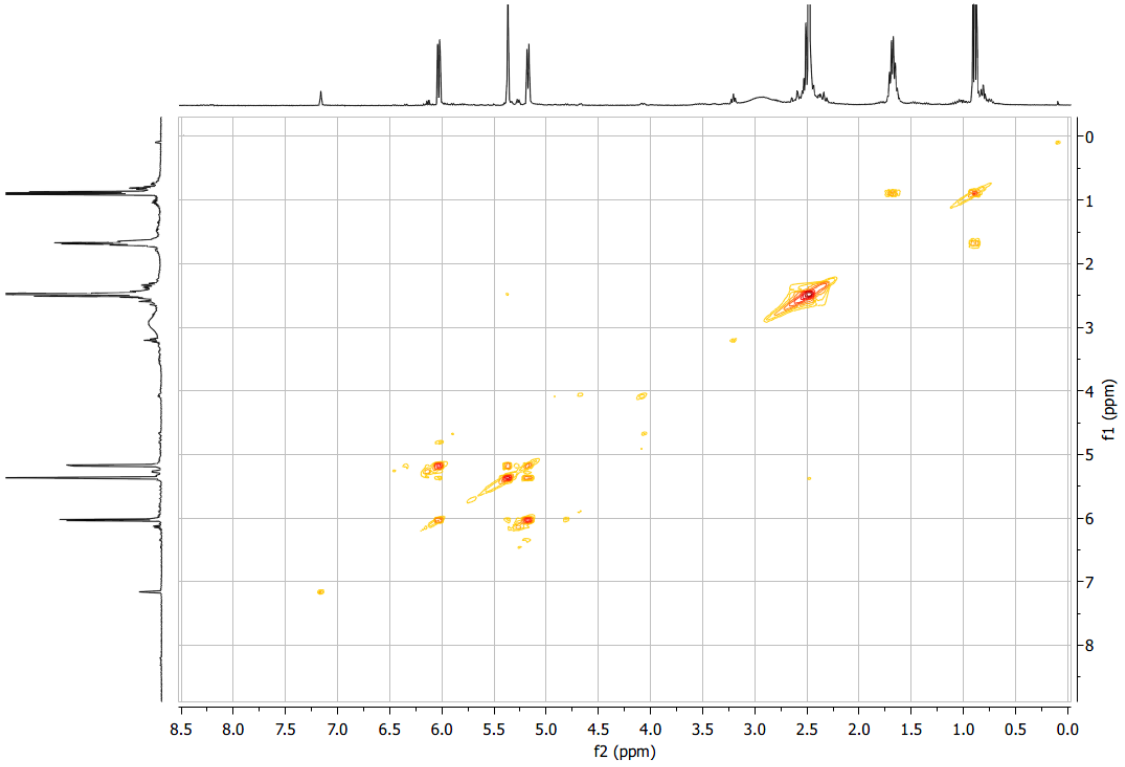


Figure 3.69: ^{1}H-^{1}H COSY NMR spectrum of **3a** in C_6D_6 (400 MHz).

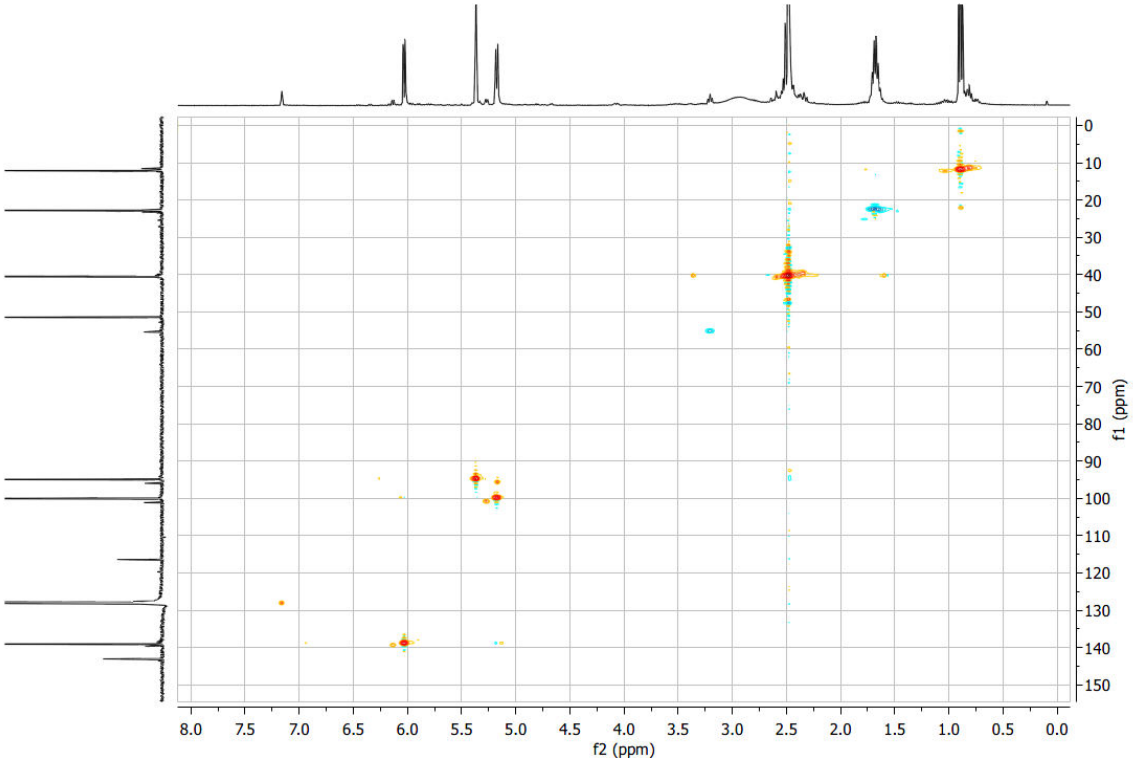


Figure 3.70: ^{1}H-^{13}C HSQC NMR spectrum of **3a** in C_6D_6 (400 MHz).

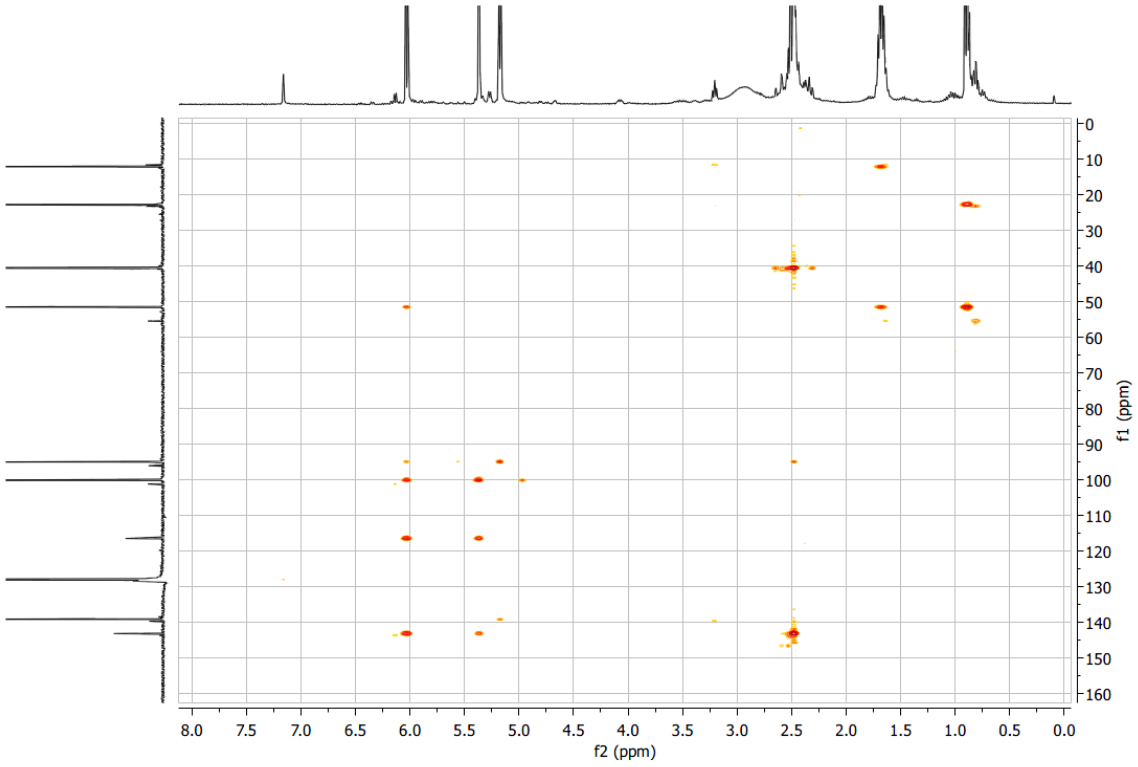
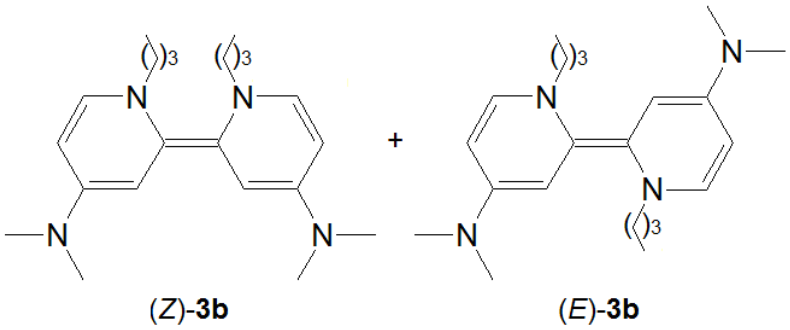


Figure 3.71: ^{1}H-^{13}C HMBC NMR spectrum of **3a** in C_6D_6 (400 MHz).



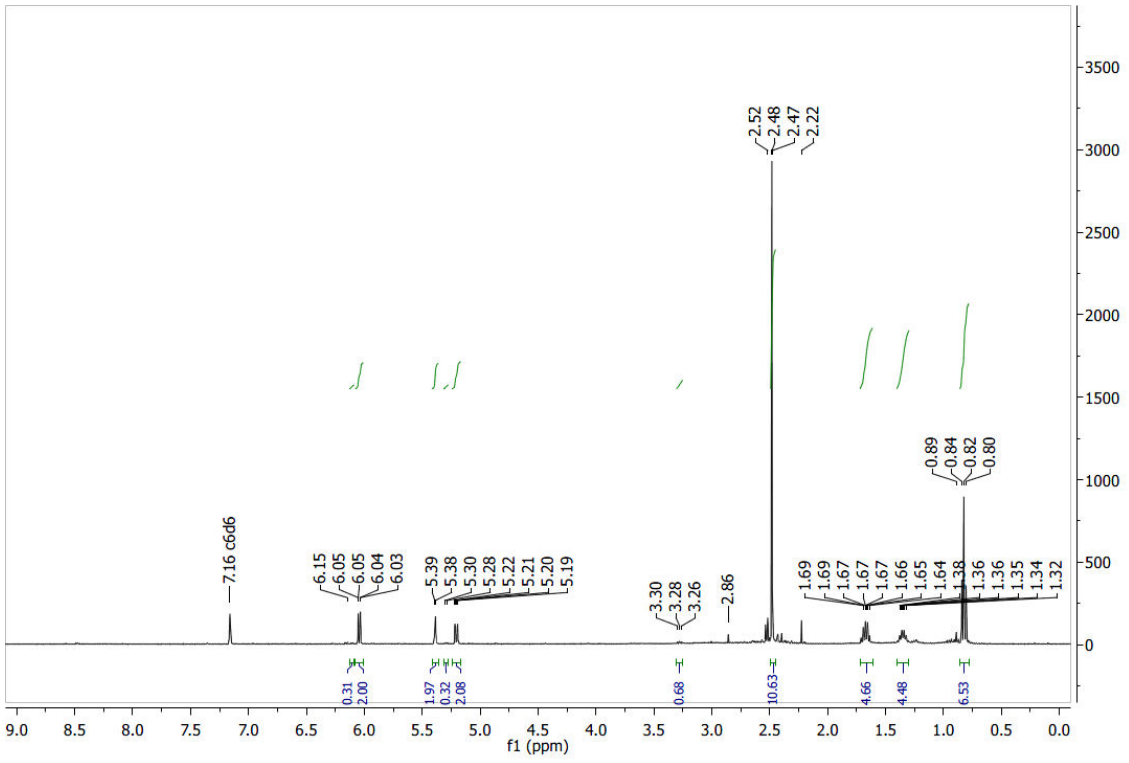


Figure 3.72: ^{1}H NMR spectrum of **3b** in C_6D_6 (400 MHz).

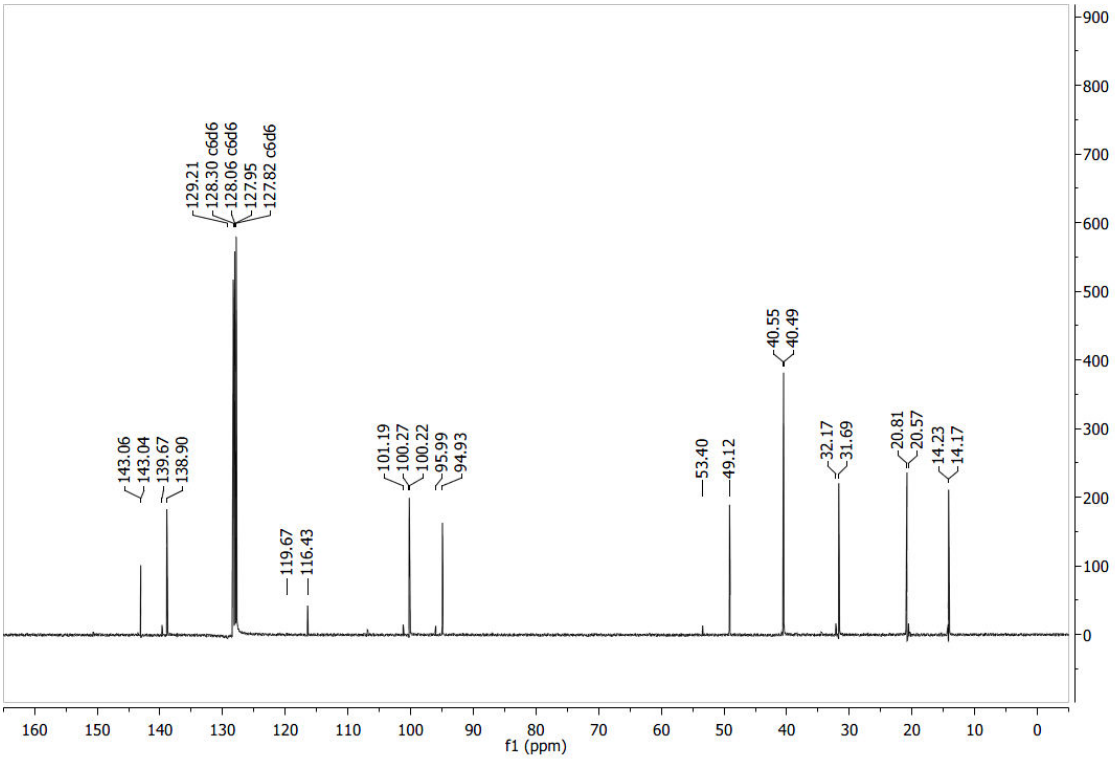
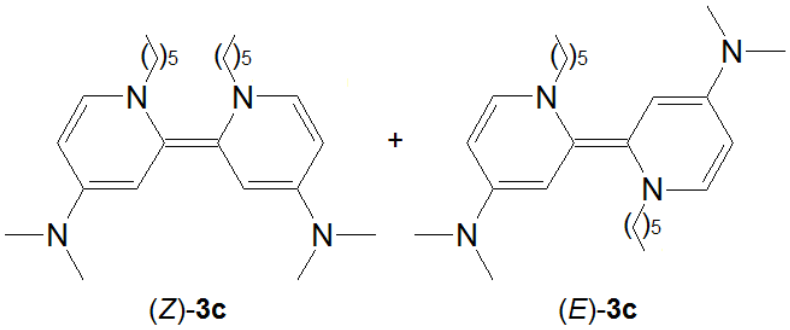


Figure 3.73: ^{13}C NMR spectrum of **3b** in C_6D_6 (400 MHz).



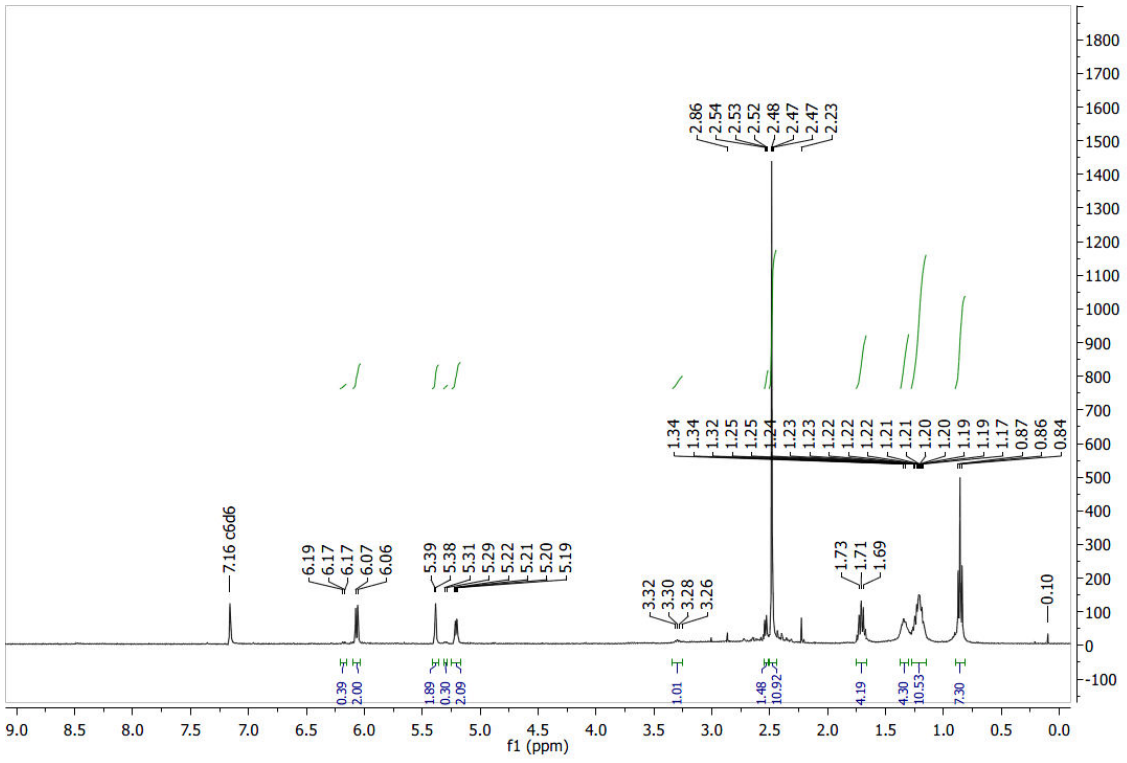


Figure 3.74: ^{1}H NMR spectrum of **3c** in C_6D_6 (400 MHz).

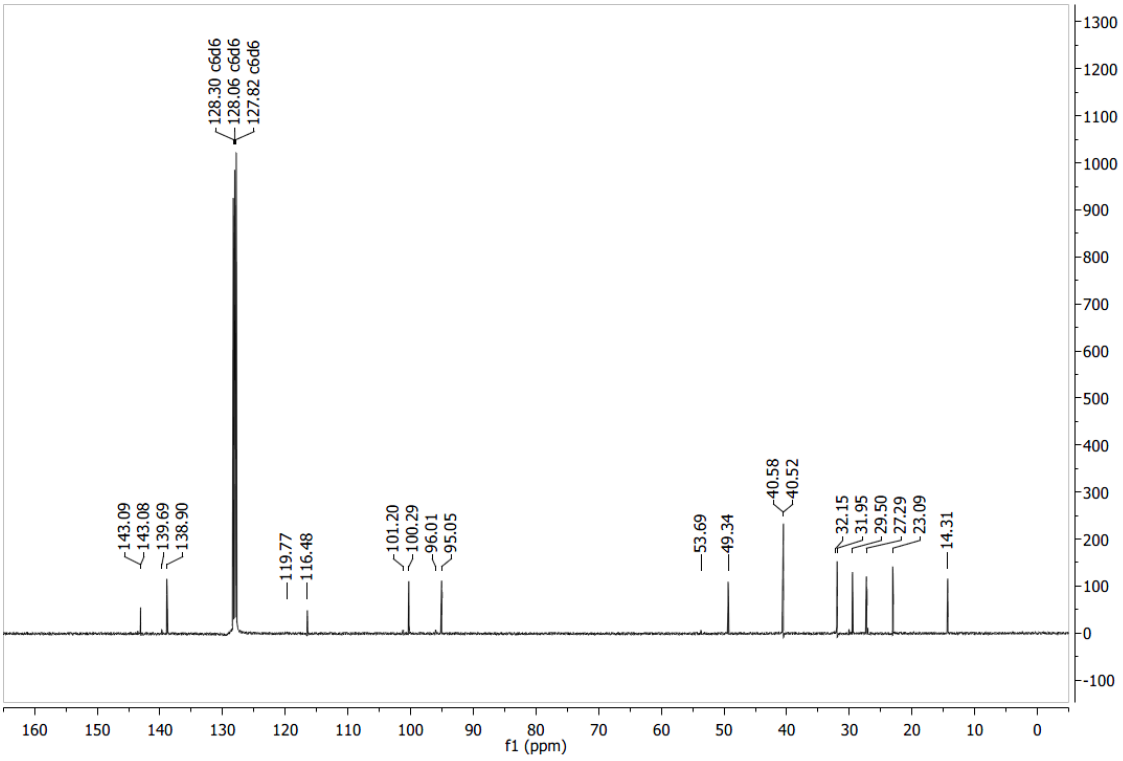
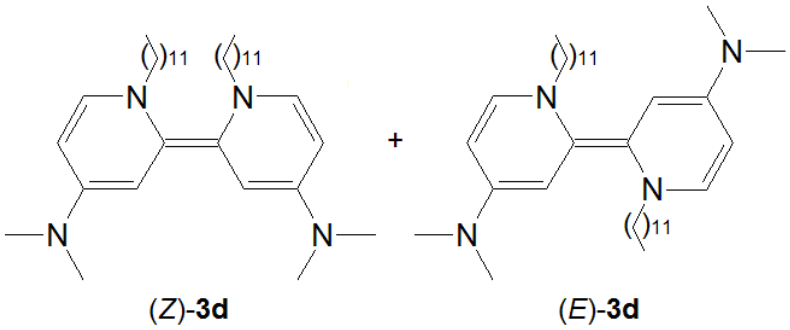


Figure 3.75: ^{13}C NMR spectrum of **3c** in C_6D_6 (400 MHz).



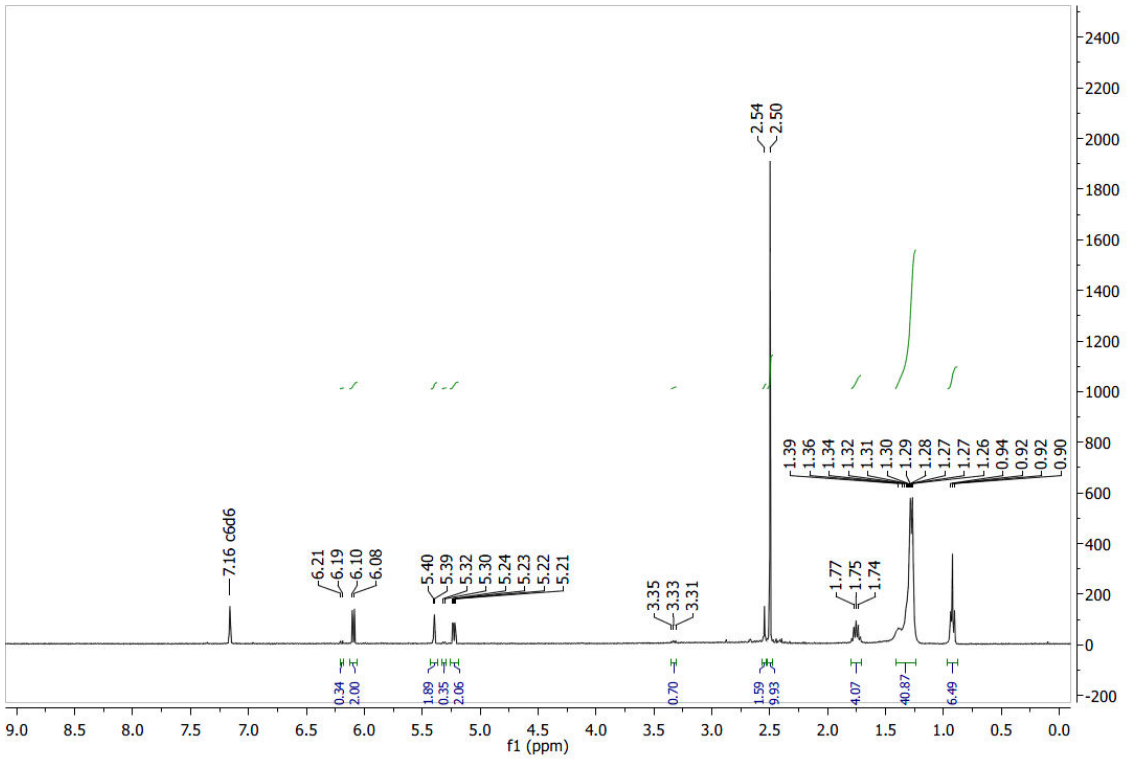


Figure 3.76: ^{1}H NMR spectrum of **3d** in C_6D_6 (400 MHz).

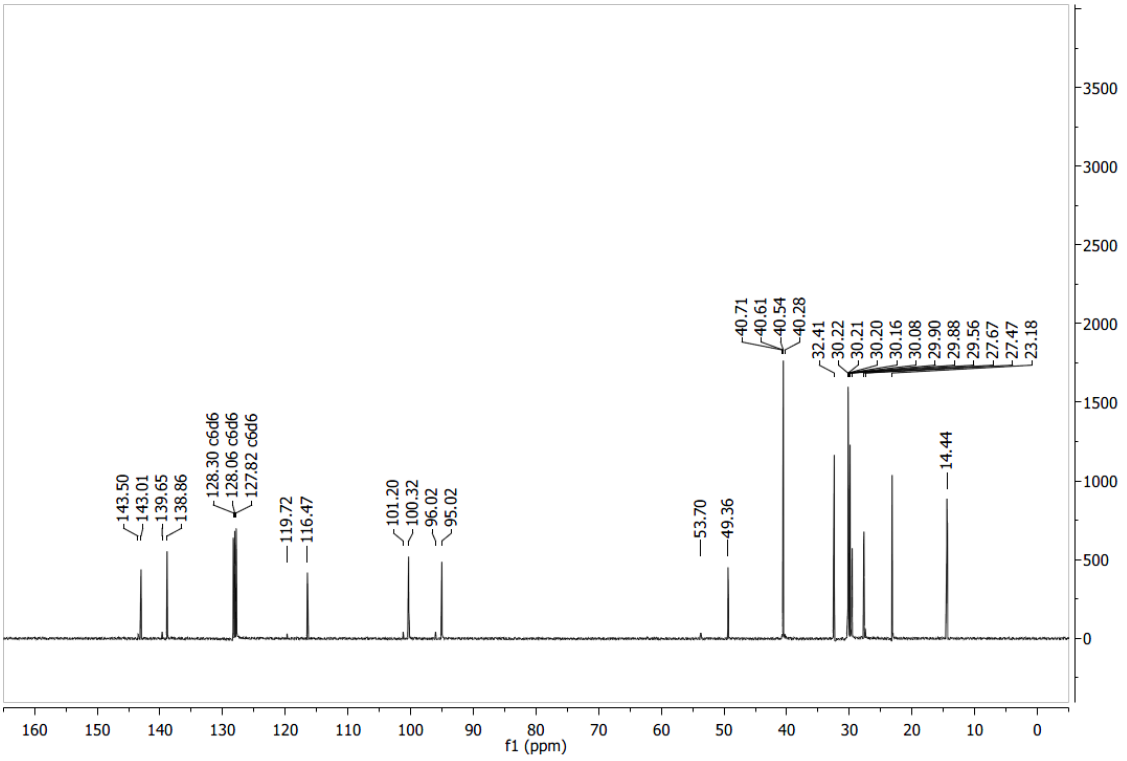
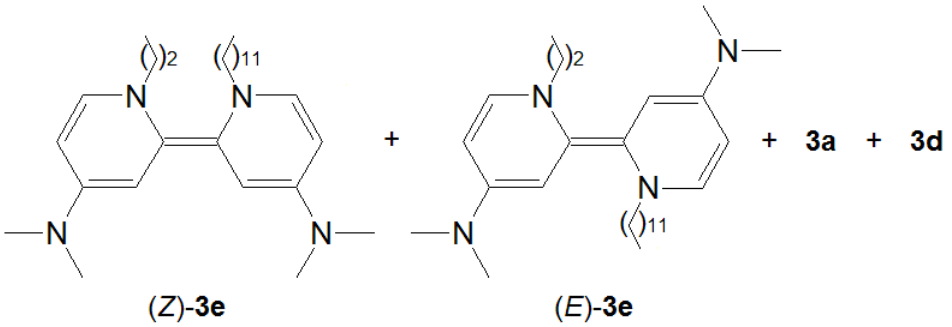


Figure 3.77: ^{13}C NMR spectrum of **3d** in C_6D_6 (400 MHz).



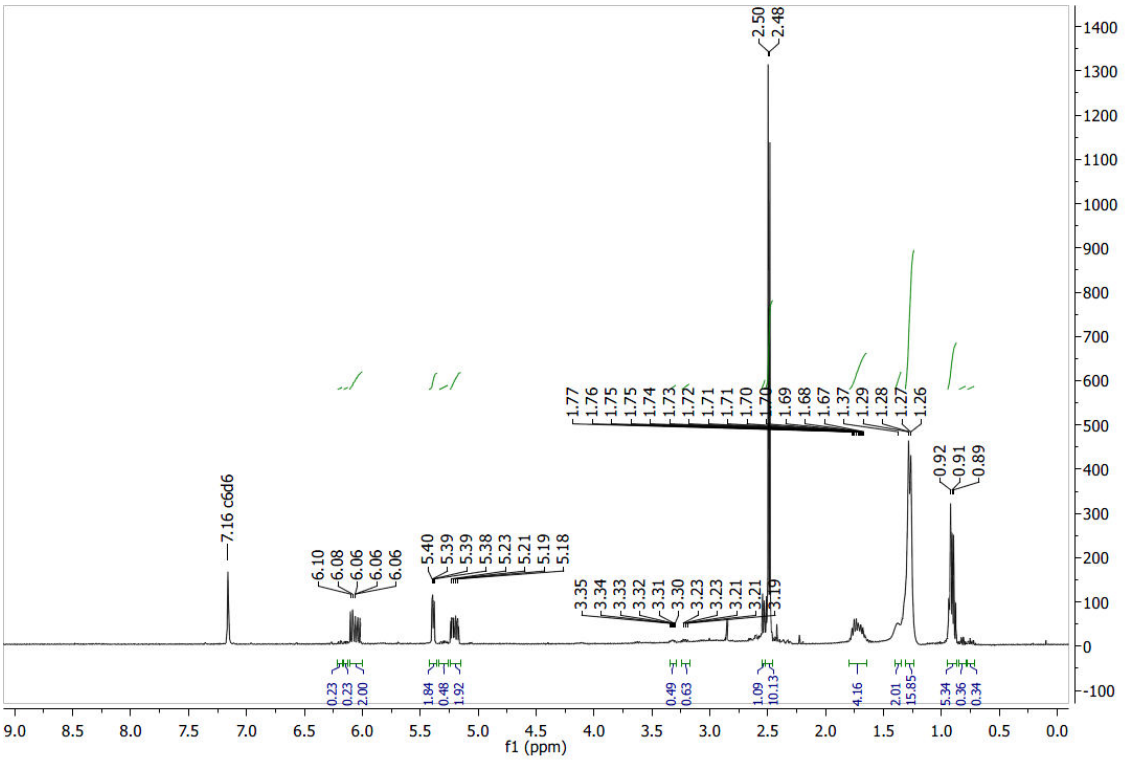


Figure 3.78: ^{1}H NMR spectrum of **3a**, **3d**, and **3e** unknown mixture in C_6D_6 (400 MHz).

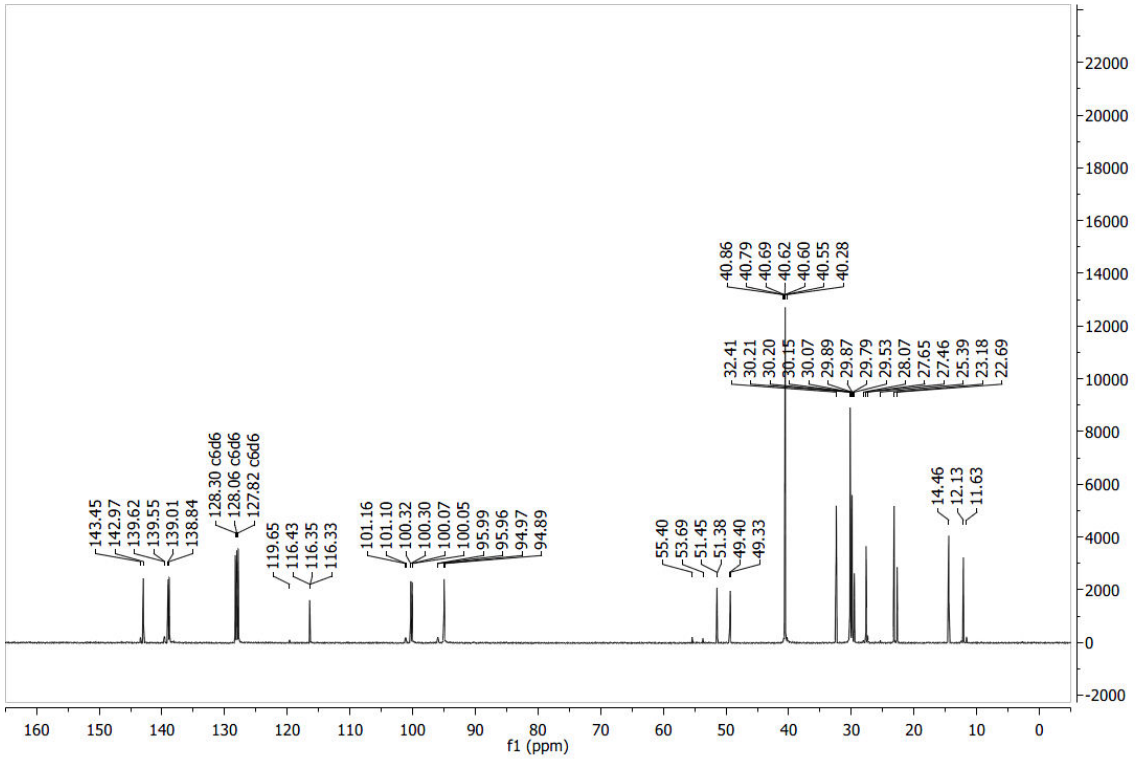
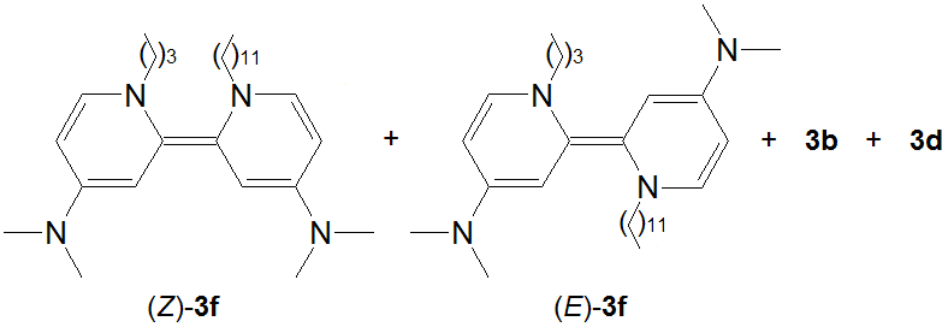


Figure 3.79: ^{13}C NMR spectrum of **3a**, **3d**, and **3e** unknown mixture in C_6D_6 (400 MHz).



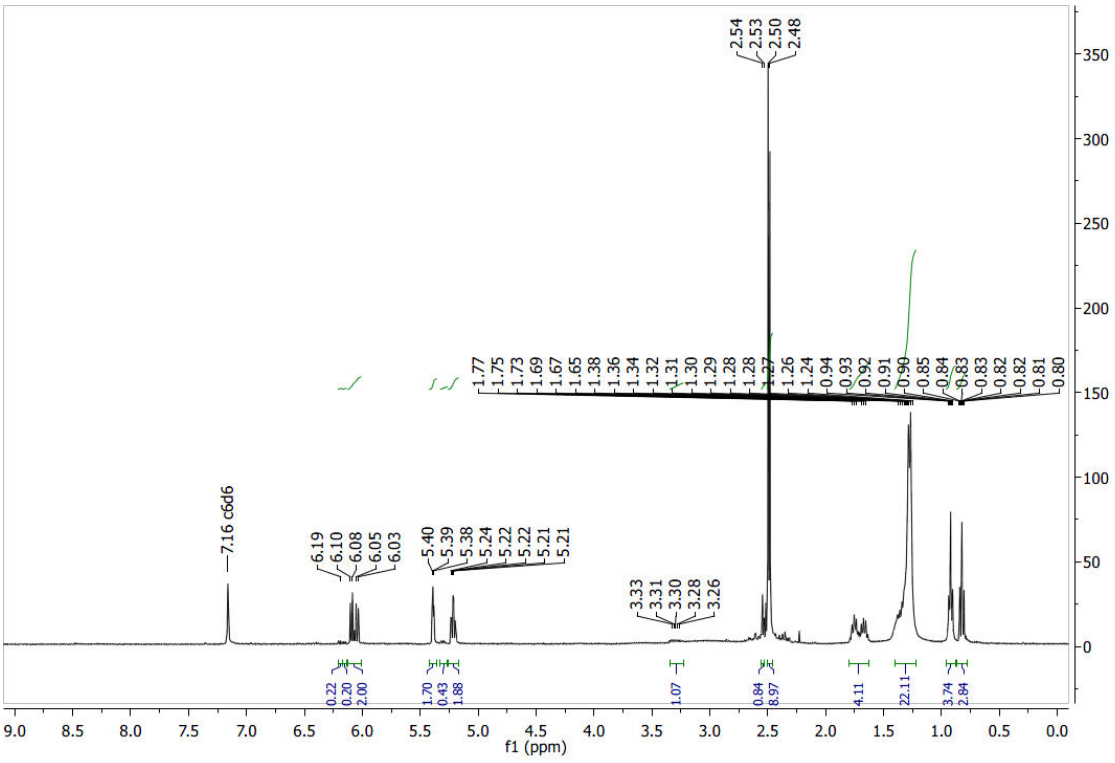


Figure 3.80: ^{1}H NMR spectrum of **3b**, **3d**, and **3f** unknown mixture in C_6D_6 (400 MHz).

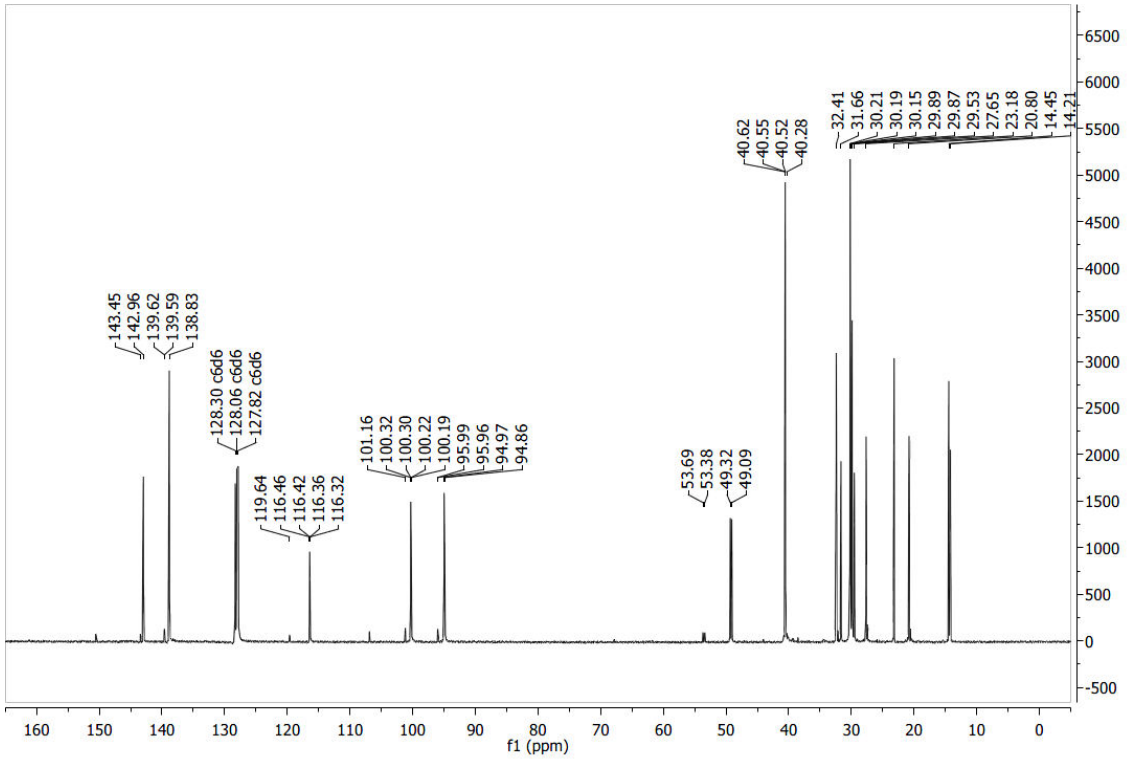
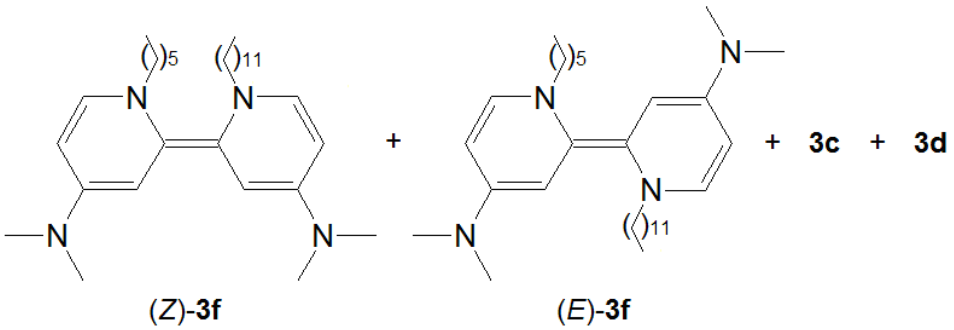


Figure 3.81: ^{13}C NMR spectrum of **3b**, **3d**, and **3f** unknown mixture in C_6D_6 (400 MHz).



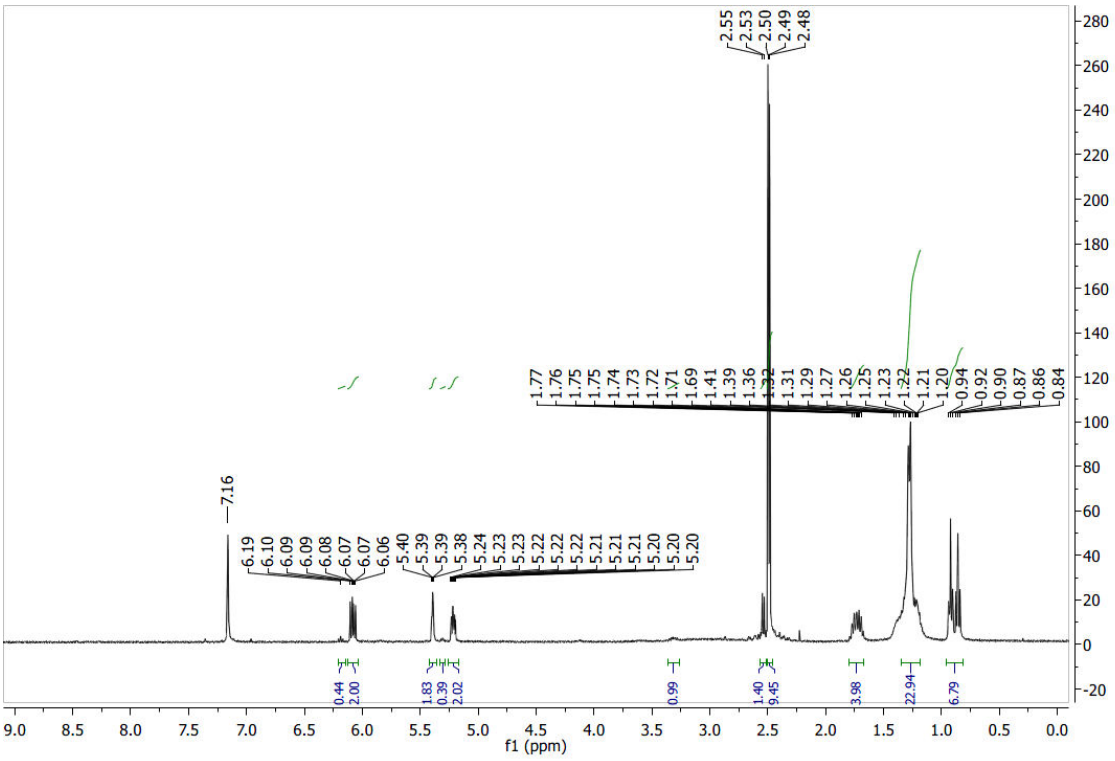


Figure 3.82: ^{1}H NMR spectrum of **3c**, **3d**, and **3g** unknown mixture in C_6D_6 (400 MHz).

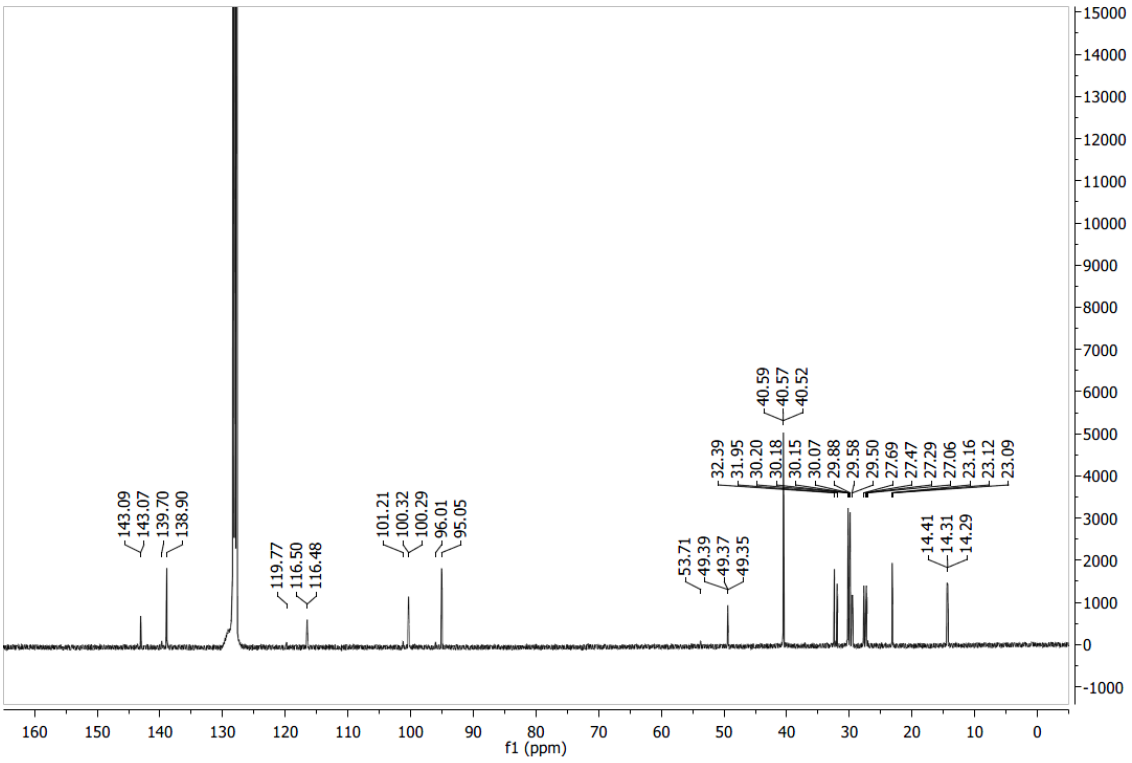
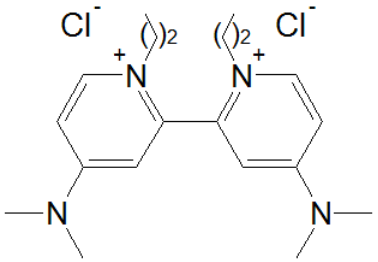


Figure 3.83: ^{13}C NMR spectrum of **3c**, **3d**, and **3g** unknown mixture in C_6D_6 (400 MHz).



4a

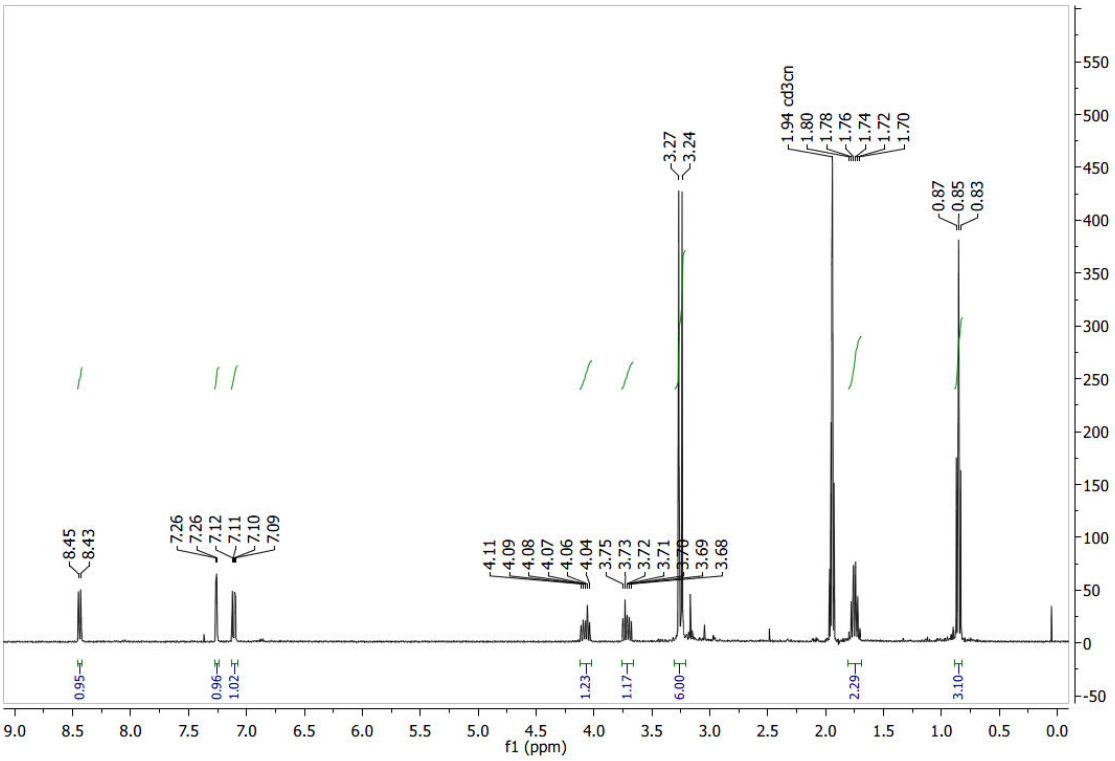


Figure 3.84: ^{1}H NMR spectrum of **4a** in CD_3CN (400 MHz).

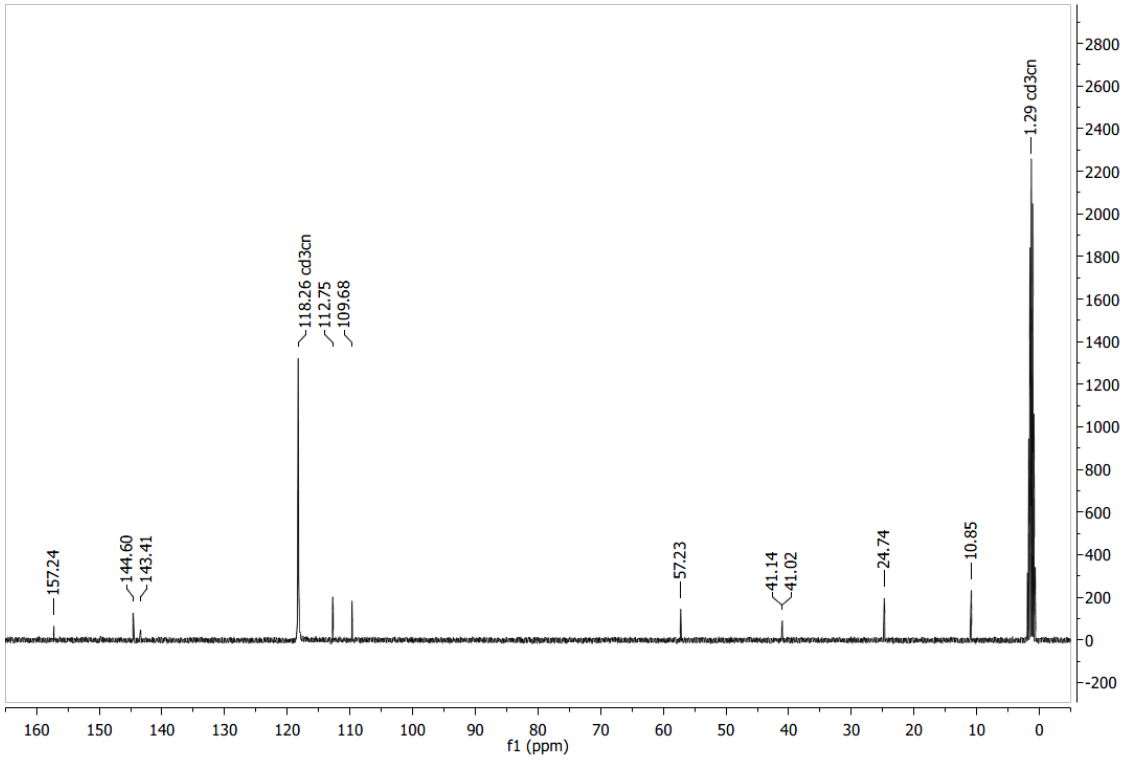


Figure 3.85: ^{13}C NMR spectrum of **4a** in CD_3CN (400 MHz).

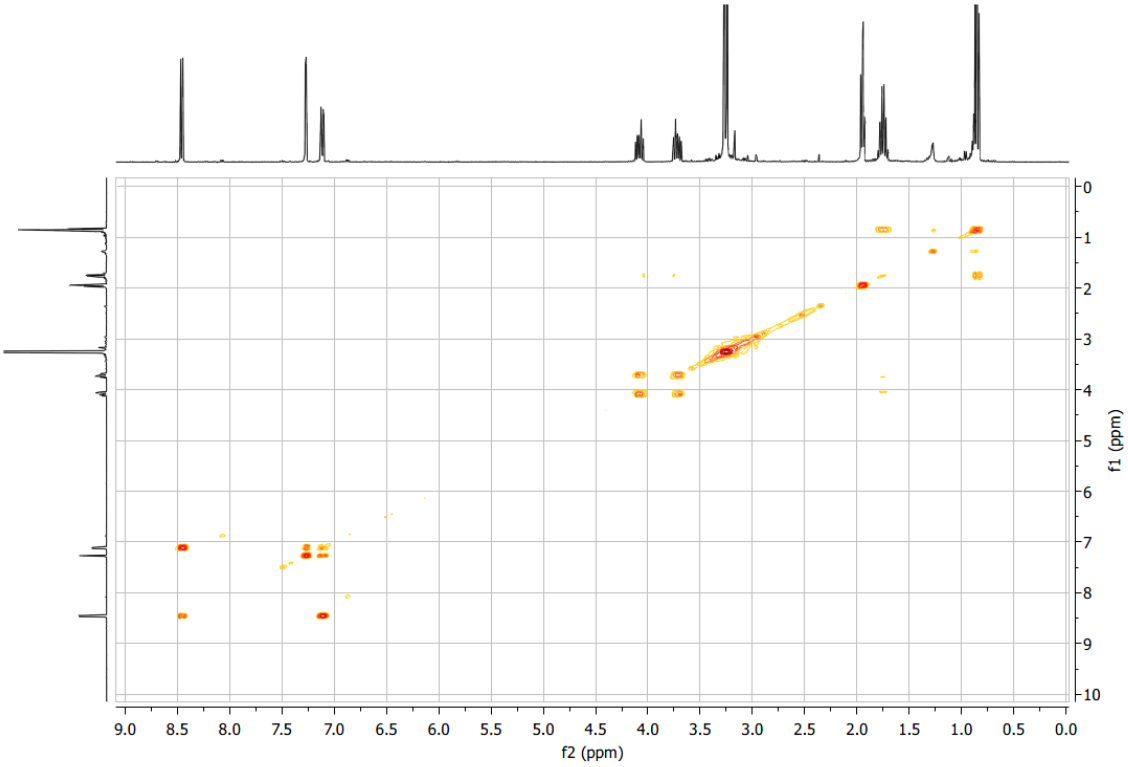


Figure 3.86: ^{1}H-^{1}H COSY NMR spectrum of **4a** in CD_3CN (400 MHz).

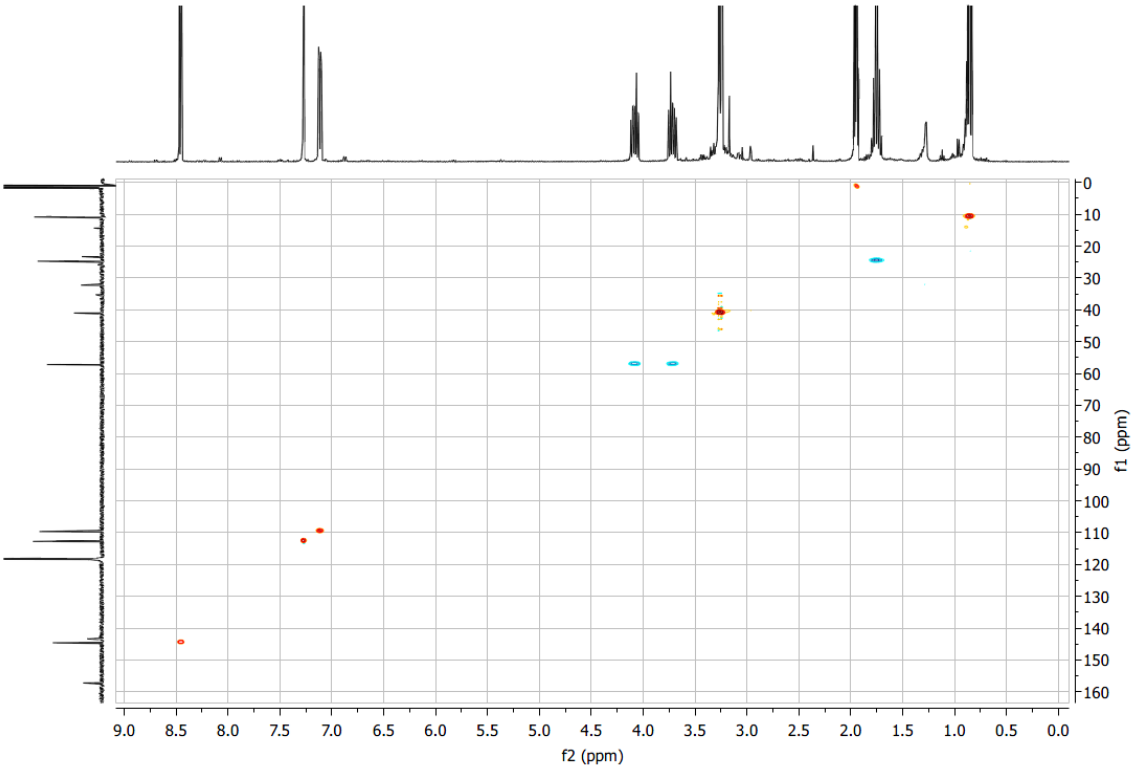


Figure 3.87: ^{1}H-^{13}C HSQC NMR spectrum of **4a** in CD_3CN (400 MHz).

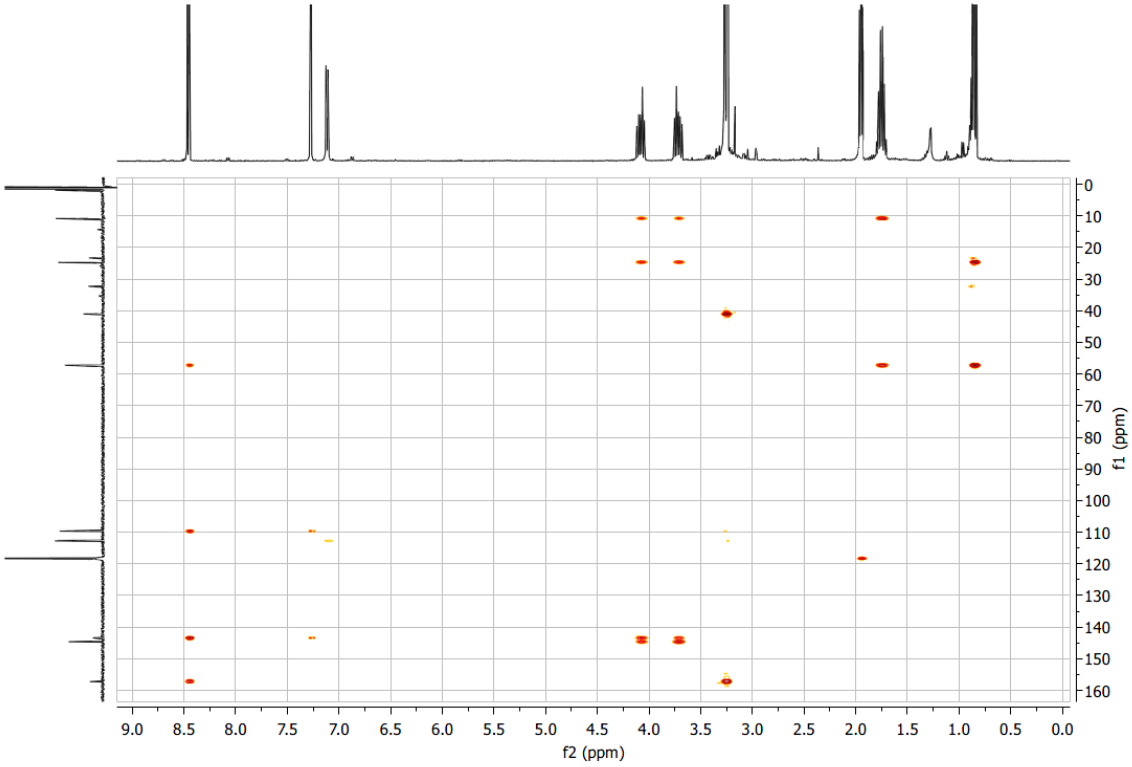
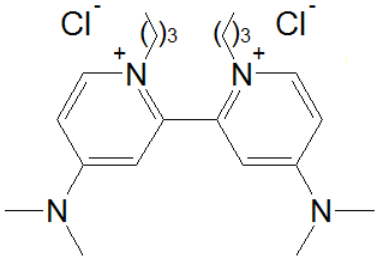


Figure 3.88: ^{1}H-^{13}C HMBC NMR spectrum of **4a** in CD_3CN (400 MHz).



4b

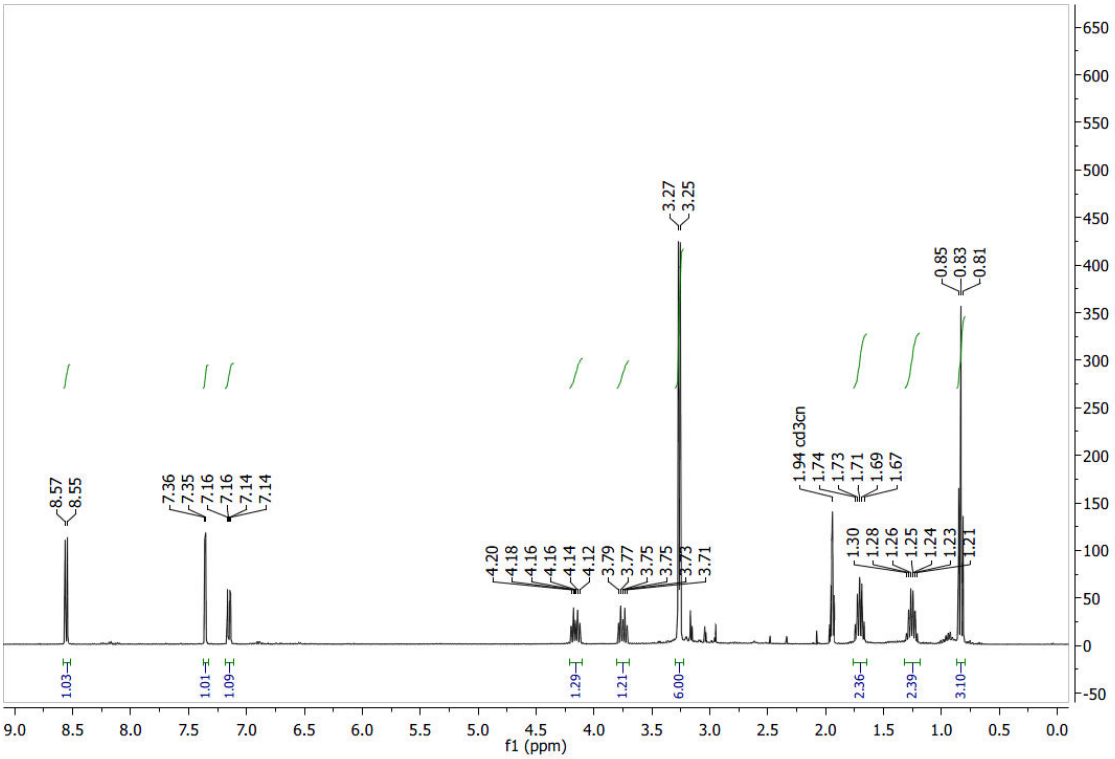


Figure 3.89: ^{1}H NMR spectrum of **4b** in CD_3CN (400 MHz).

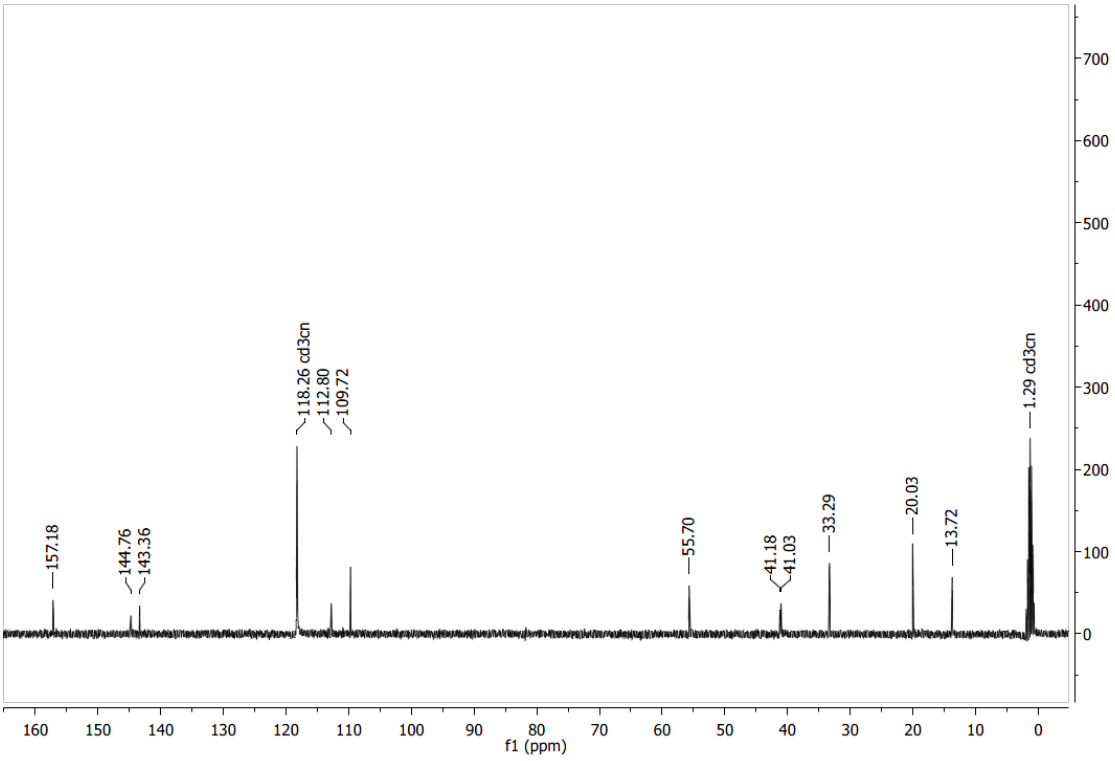
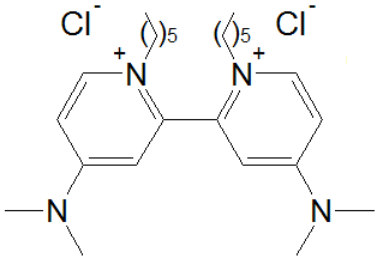


Figure 3.90: ^{13}C NMR spectrum of **4b** in CD_3CN (400 MHz).



4c

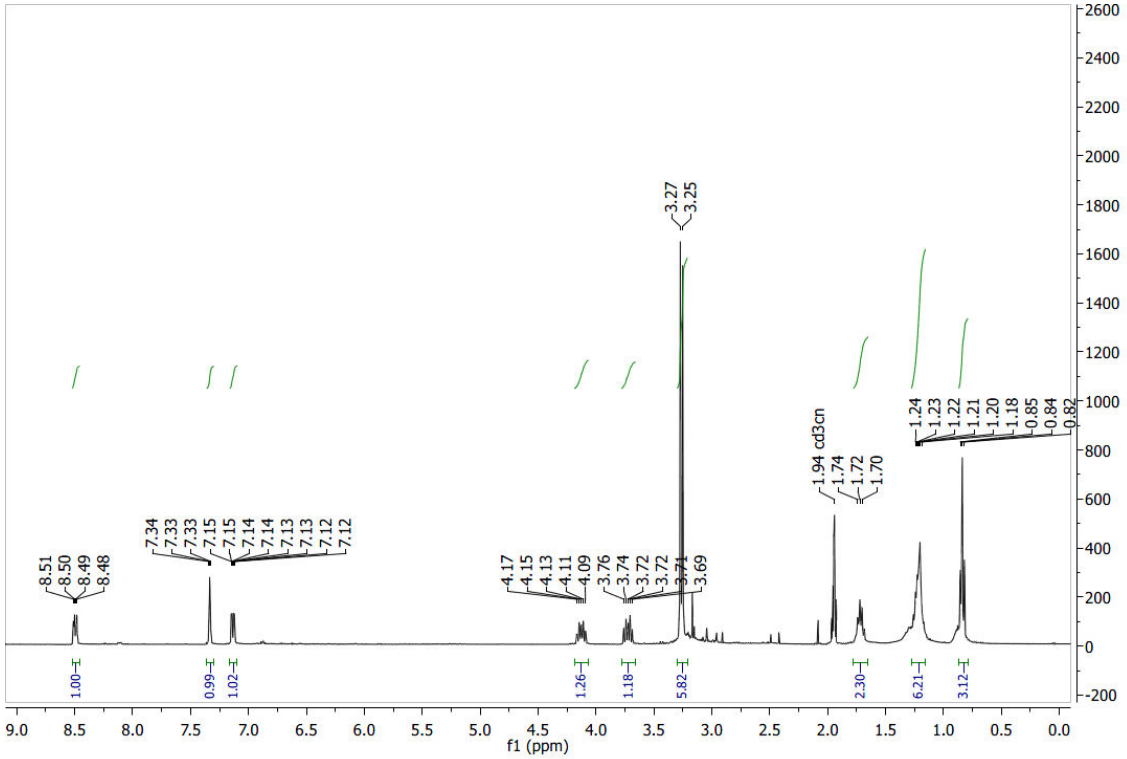


Figure 3.91: ^{1}H NMR spectrum of **4c** in CD_3CN (400 MHz).

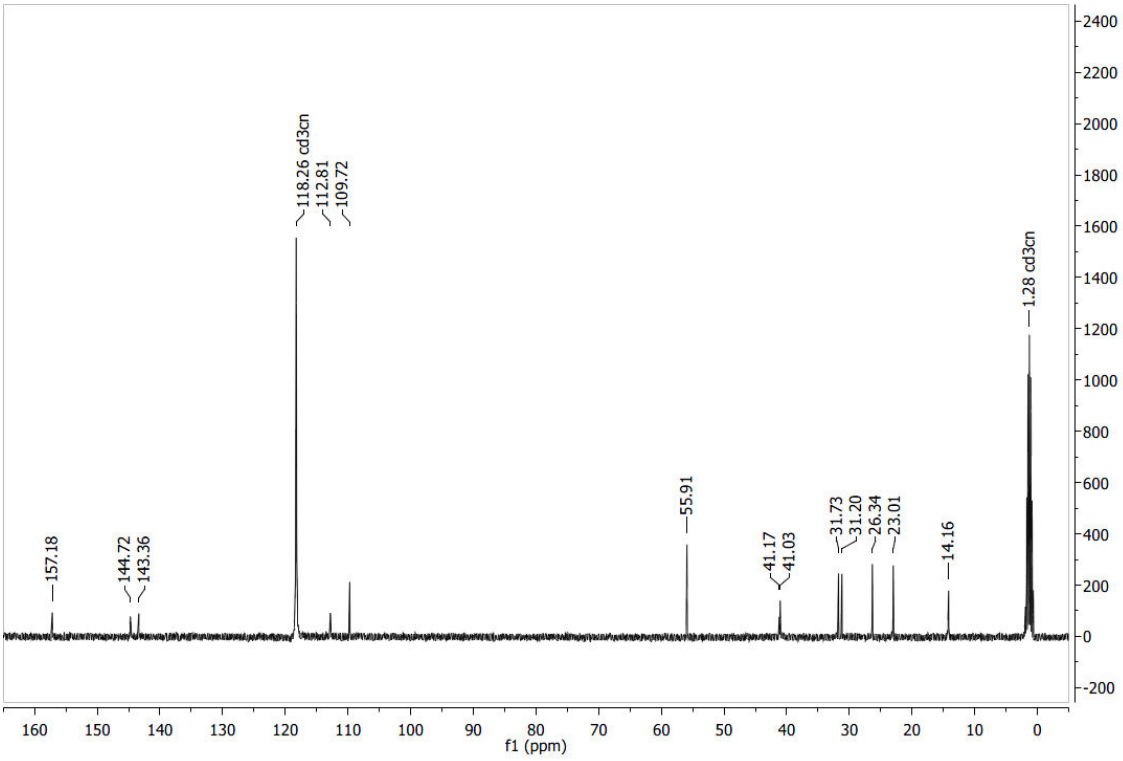
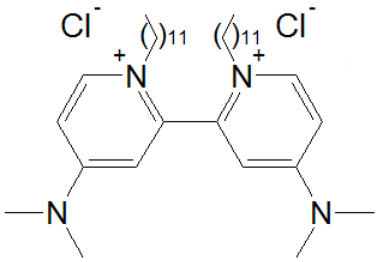


Figure 3.92: ^{13}C NMR spectrum of **4c** in CD_3CN (400 MHz).



4d

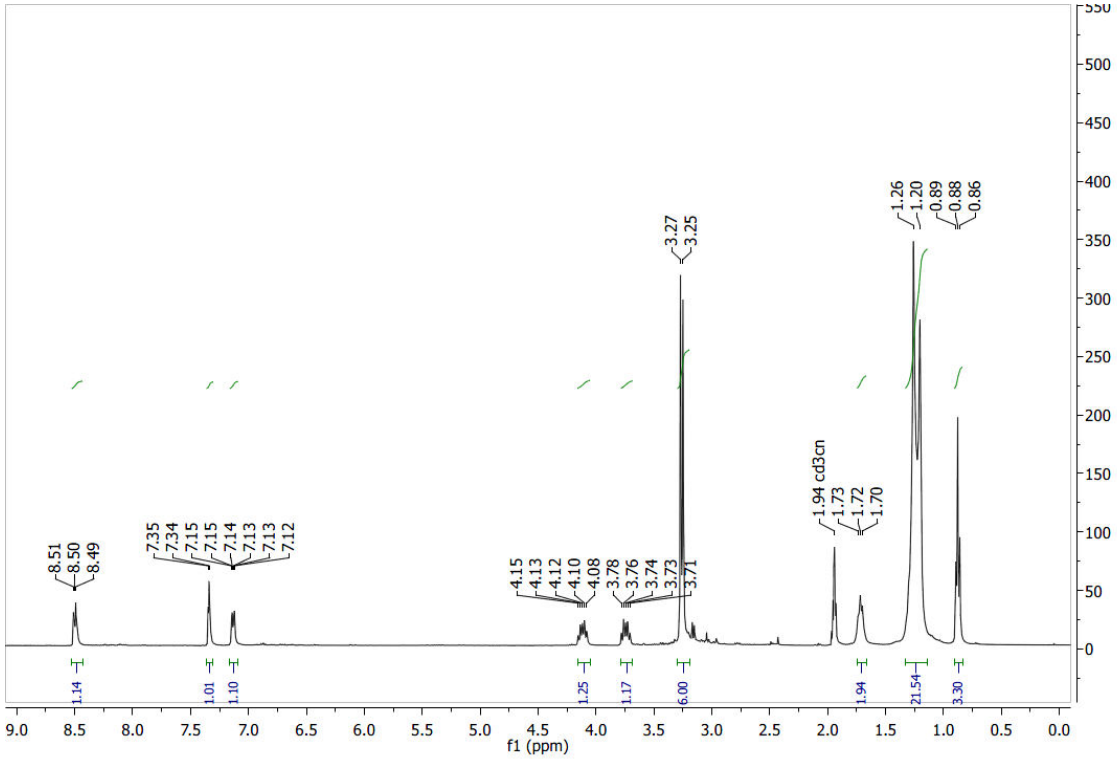


Figure 3.93: ^{1}H NMR spectrum of **4d** in CD_3CN (400 MHz).

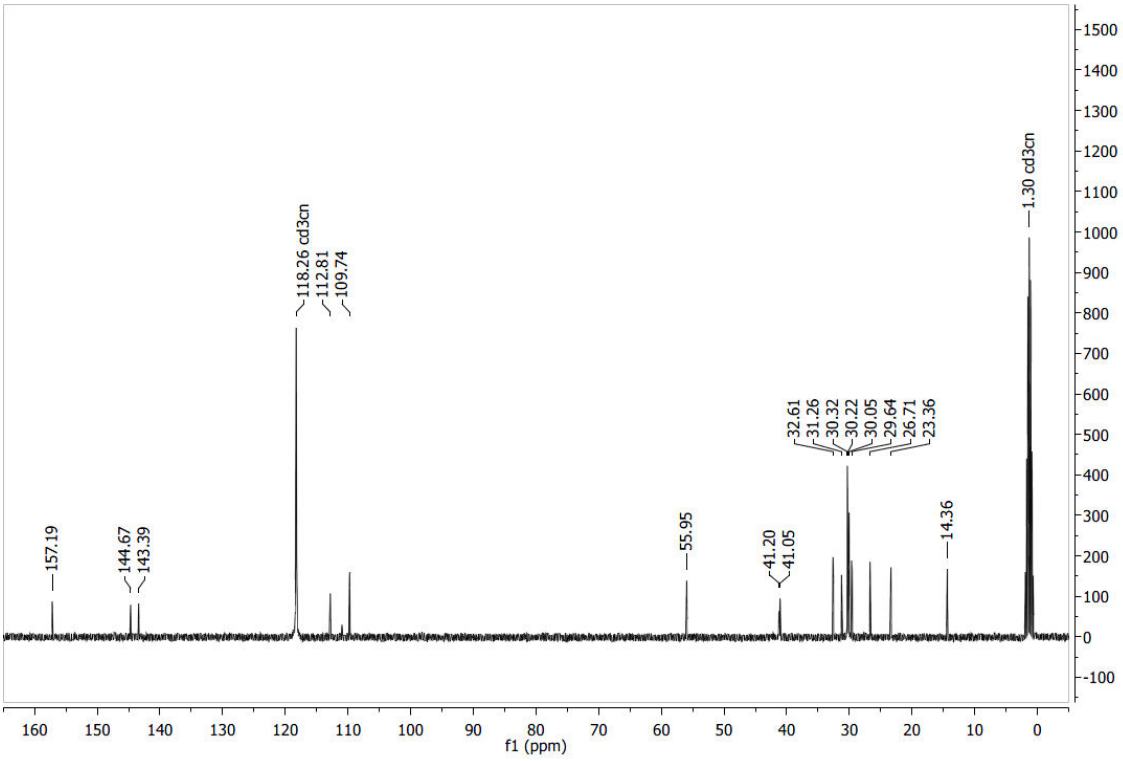
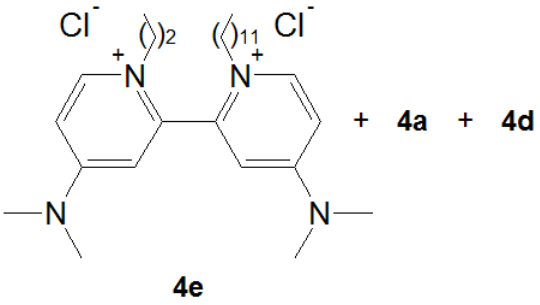


Figure 3.94: ^{13}C NMR spectrum of **4d** in CD_3CN (400 MHz).



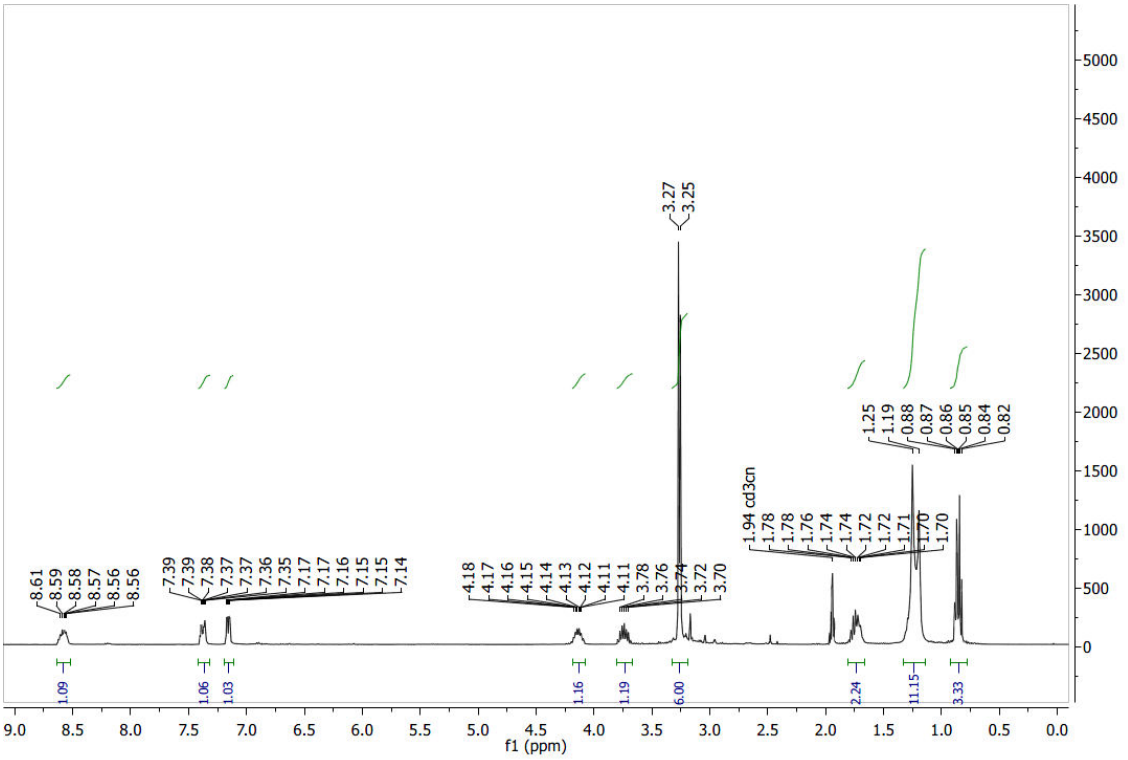


Figure 3.95: ^{1}H NMR spectrum of **4a**, **4d**, and **4e** unknown mixture in C_6D_6 (400 MHz).

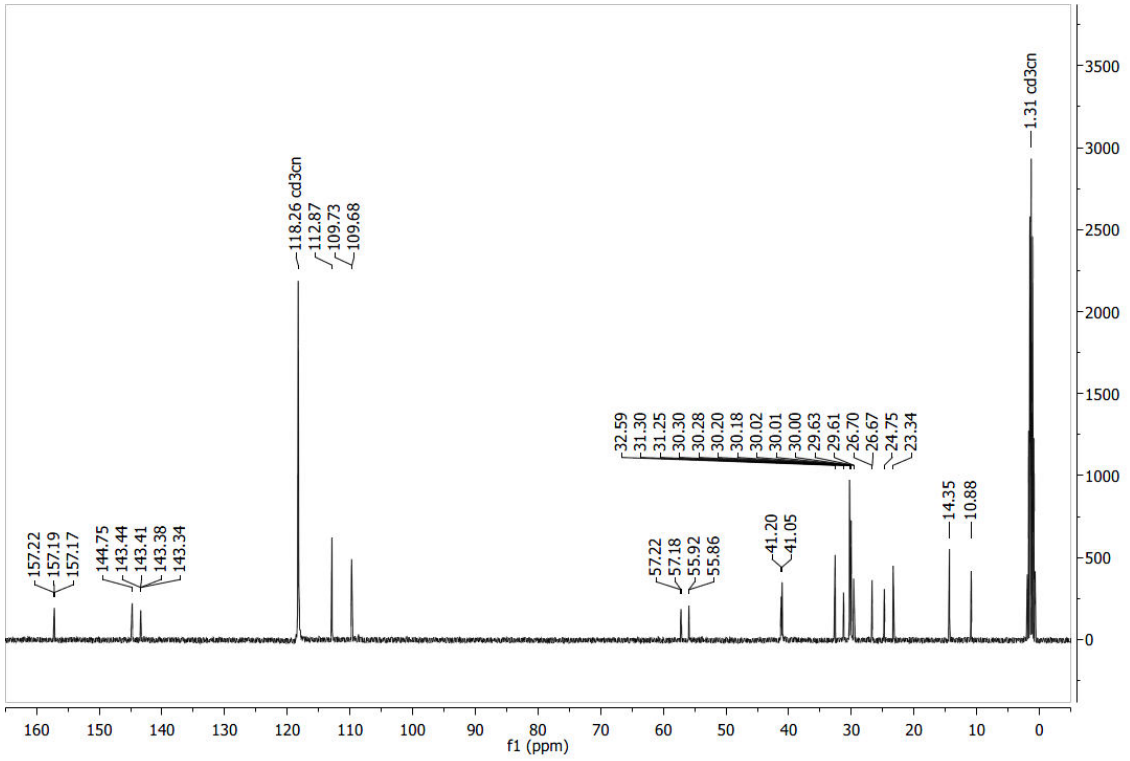
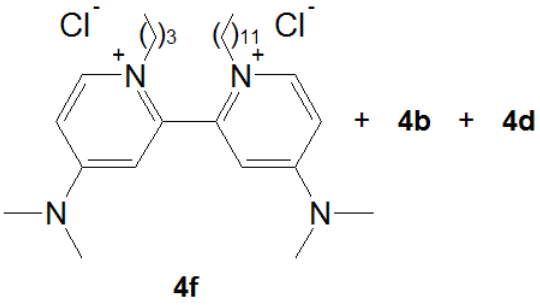


Figure 3.96: ^{13}C NMR spectrum of **4a**, **4d**, and **4e** unknown mixture in C_6D_6 (400 MHz).



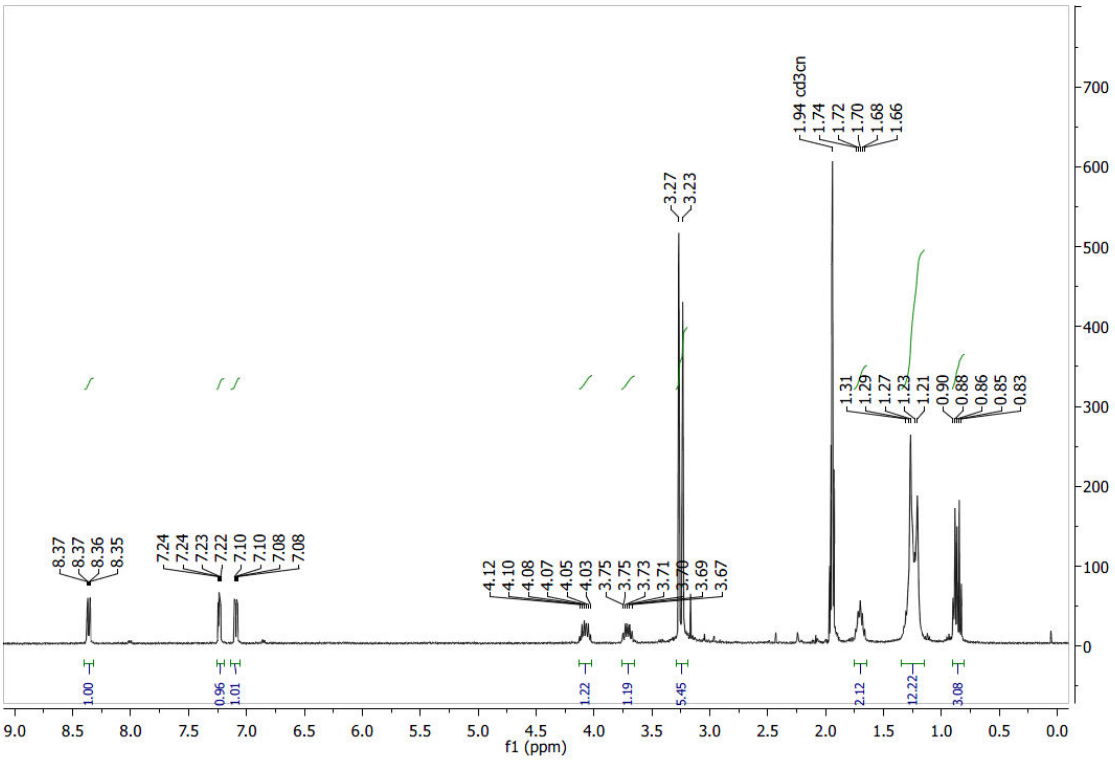


Figure 3.97: ^{1}H NMR spectrum of **4b**, **4d**, and **4f** unknown mixture in C_6D_6 (400 MHz).

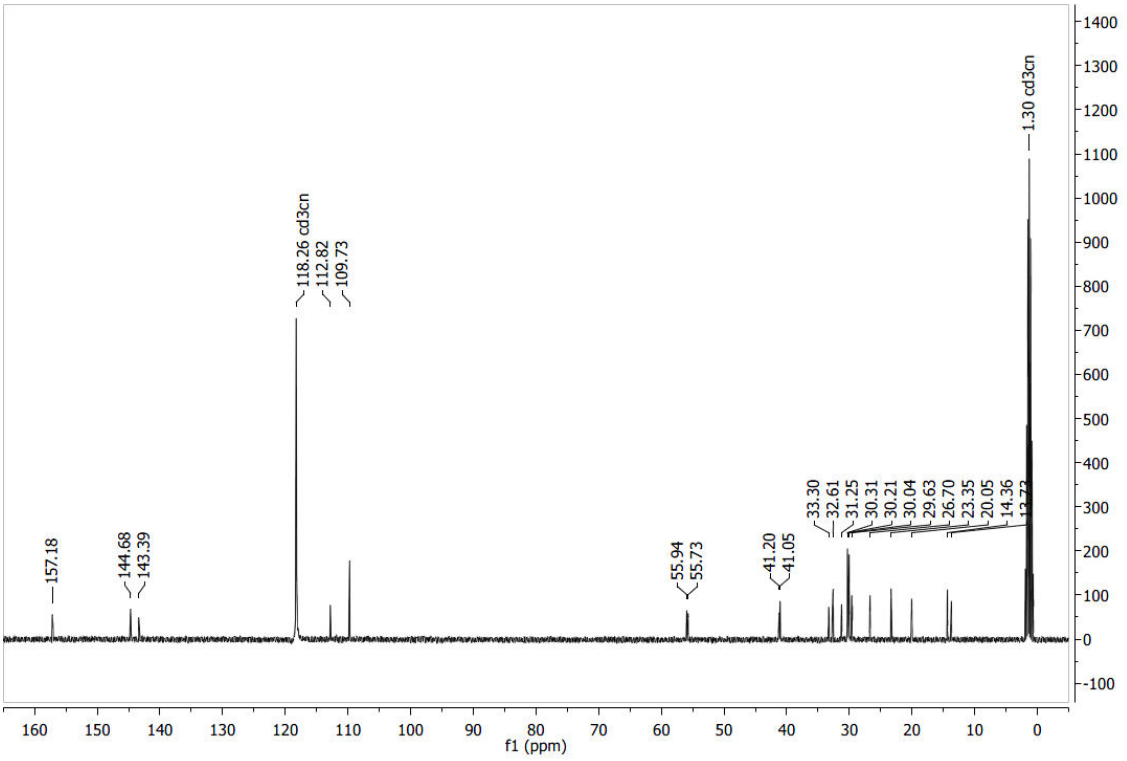
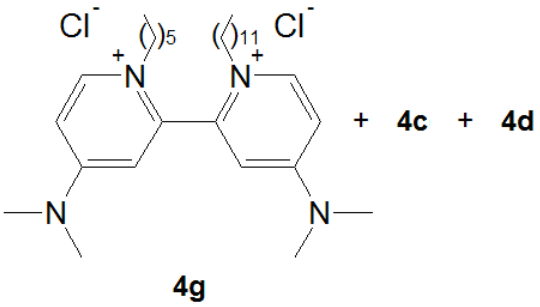


Figure 3.98: ^{13}C NMR spectrum of **4b**, **4d**, and **4f** unknown mixture in C_6D_6 (400 MHz).



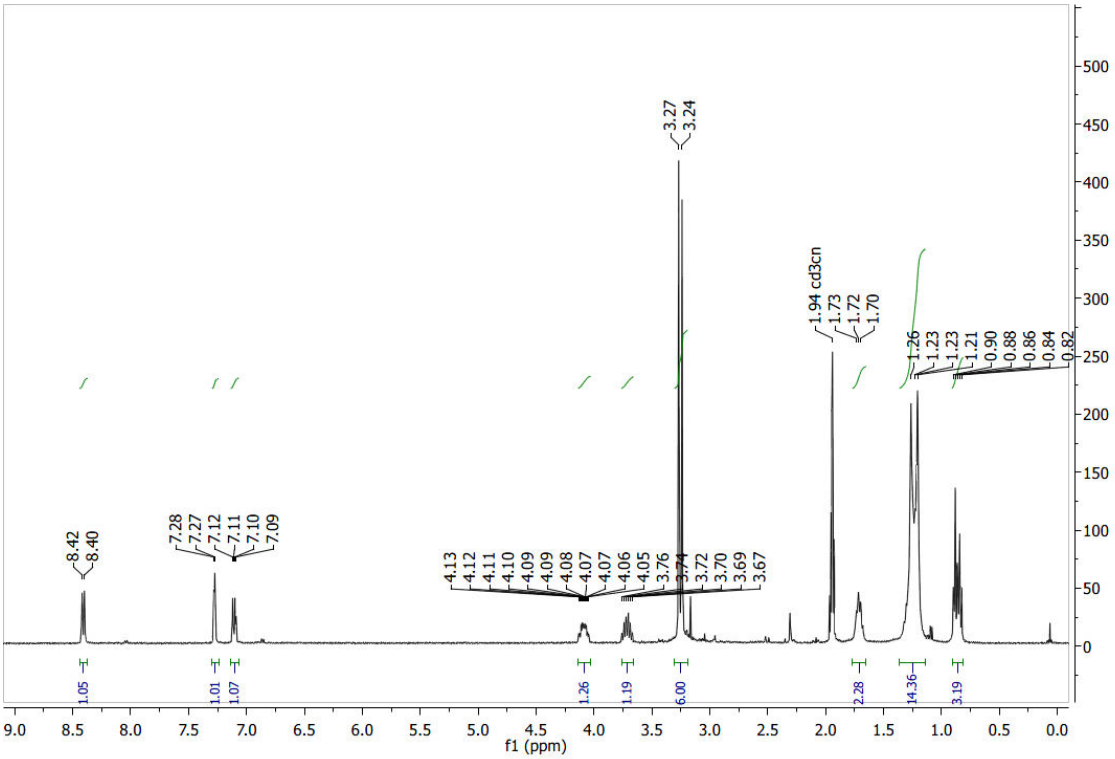


Figure 3.99: ^{1}H NMR spectrum of **4c**, **4d**, and **4g** unknown mixture in C_6D_6 (400 MHz).

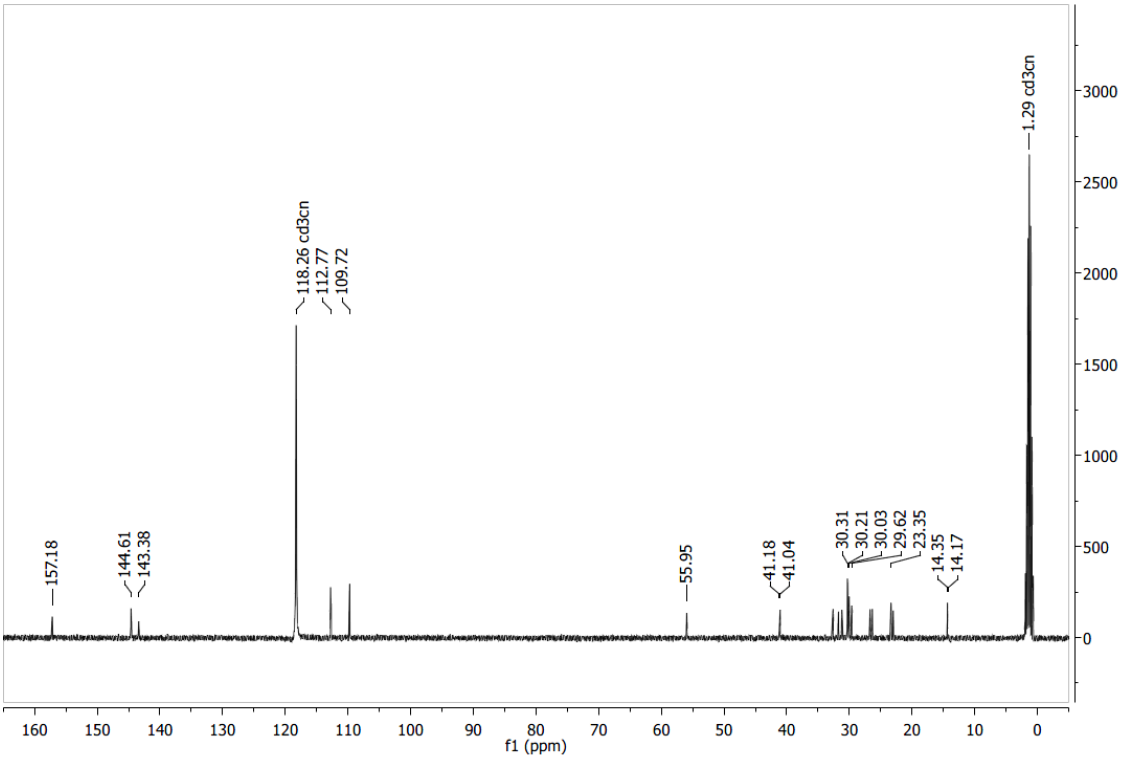
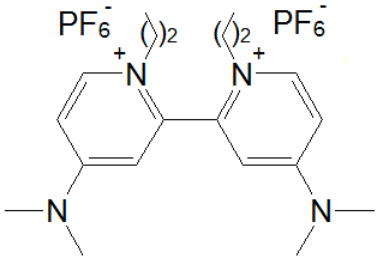


Figure 3.100: ^{13}C NMR spectrum of **4c**, **4d**, and **4g** unknown mixture in C_6D_6 (400 MHz).



5a

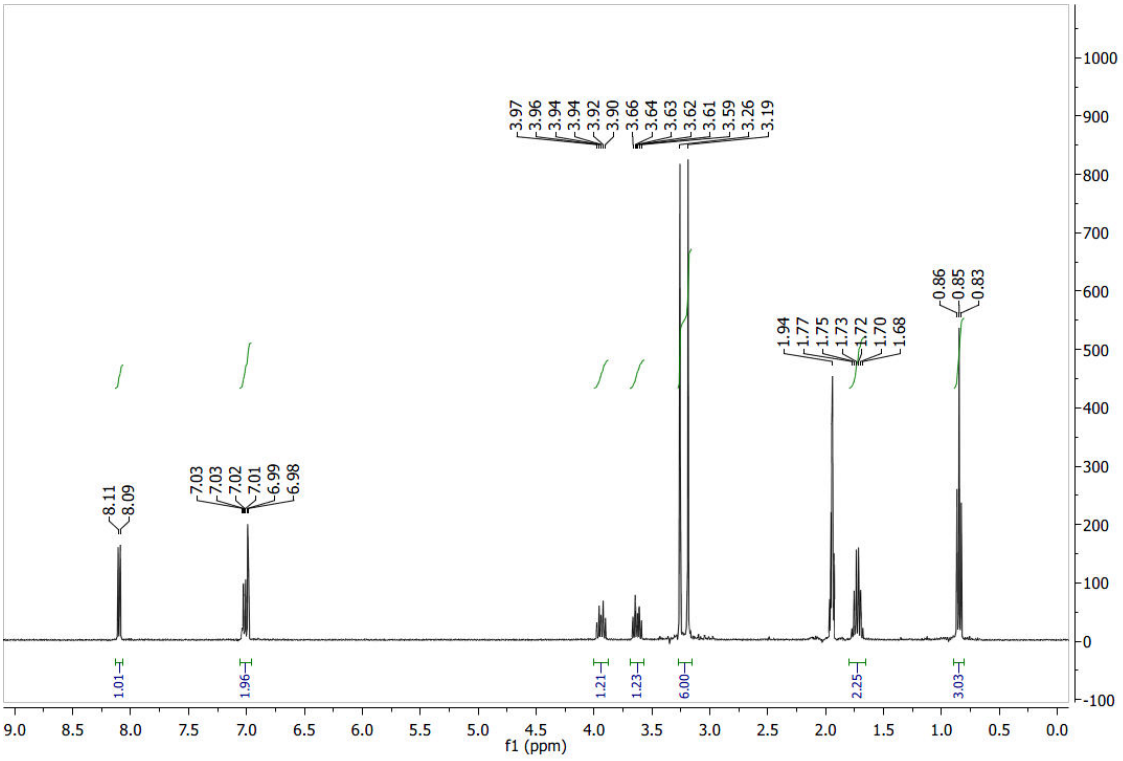


Figure 3.101: ^{1}H NMR spectrum of **5a** in CD_3CN (400 MHz).

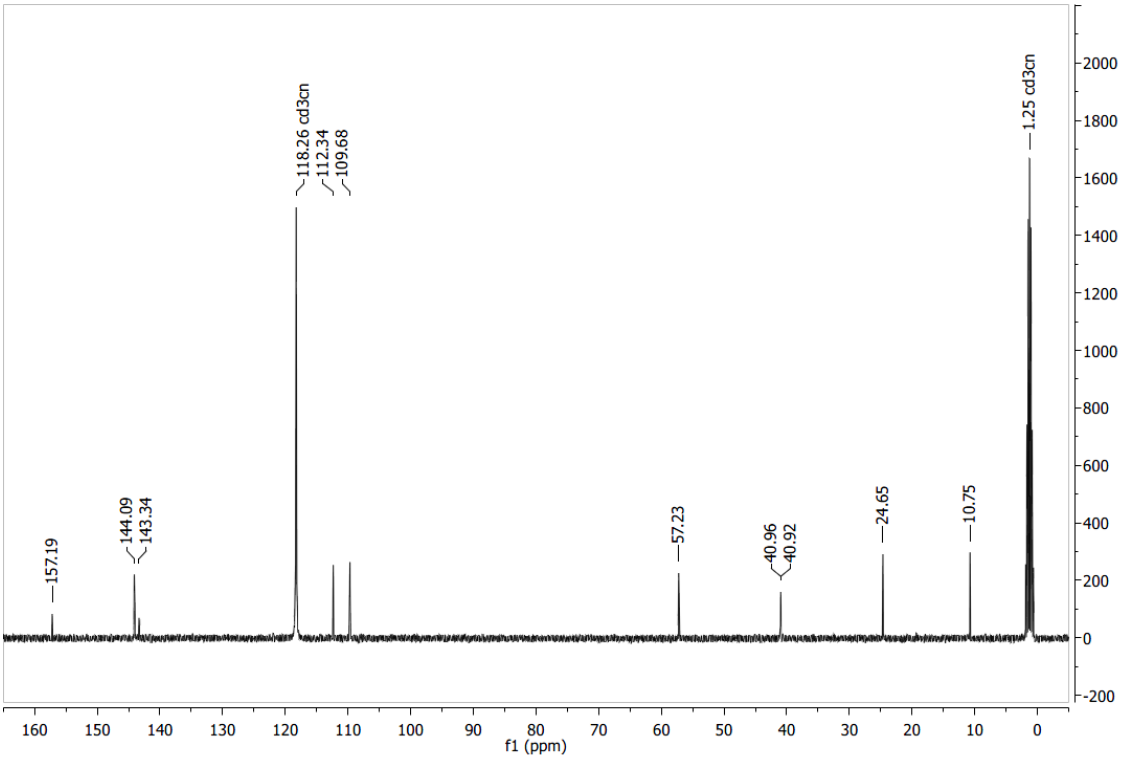
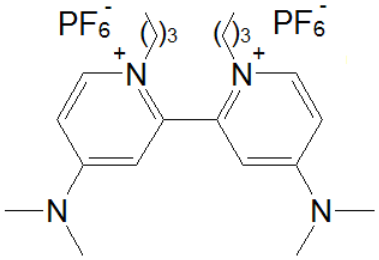


Figure 3.102: ^{13}C NMR spectrum of **5a** in CD_3CN (400 MHz).



5b

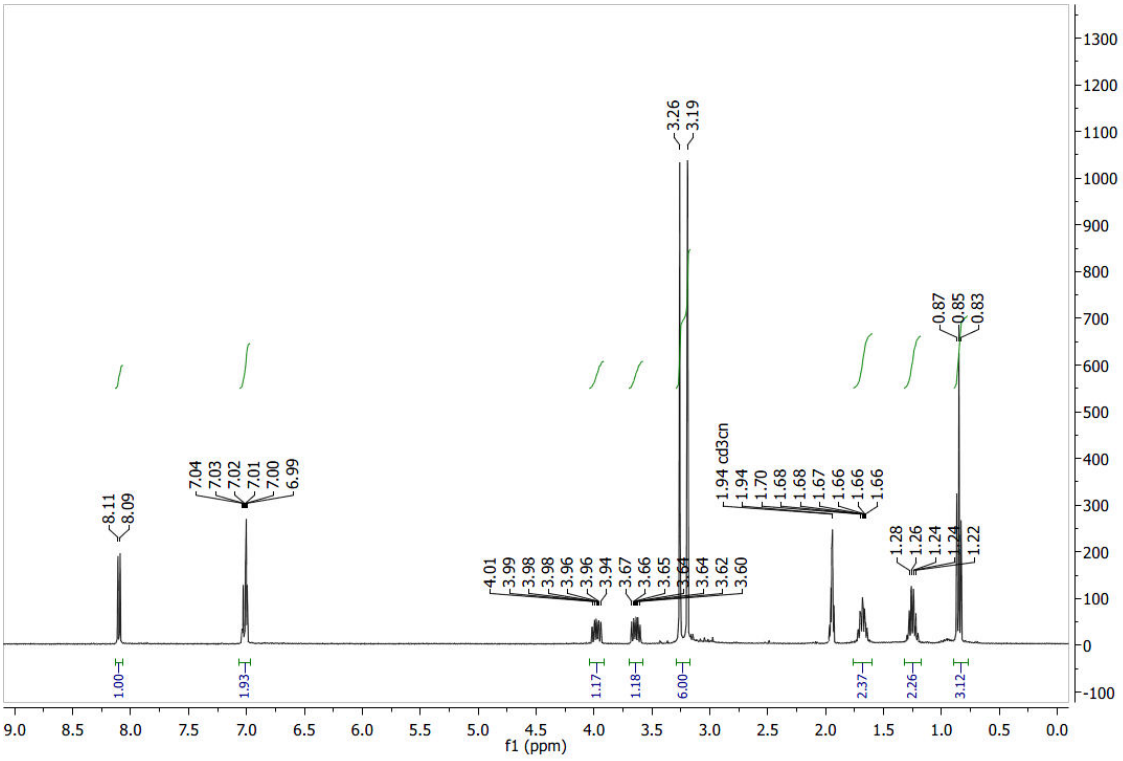


Figure 3.103: ^{1}H NMR spectrum of **5b** in CD_3CN (400 MHz).

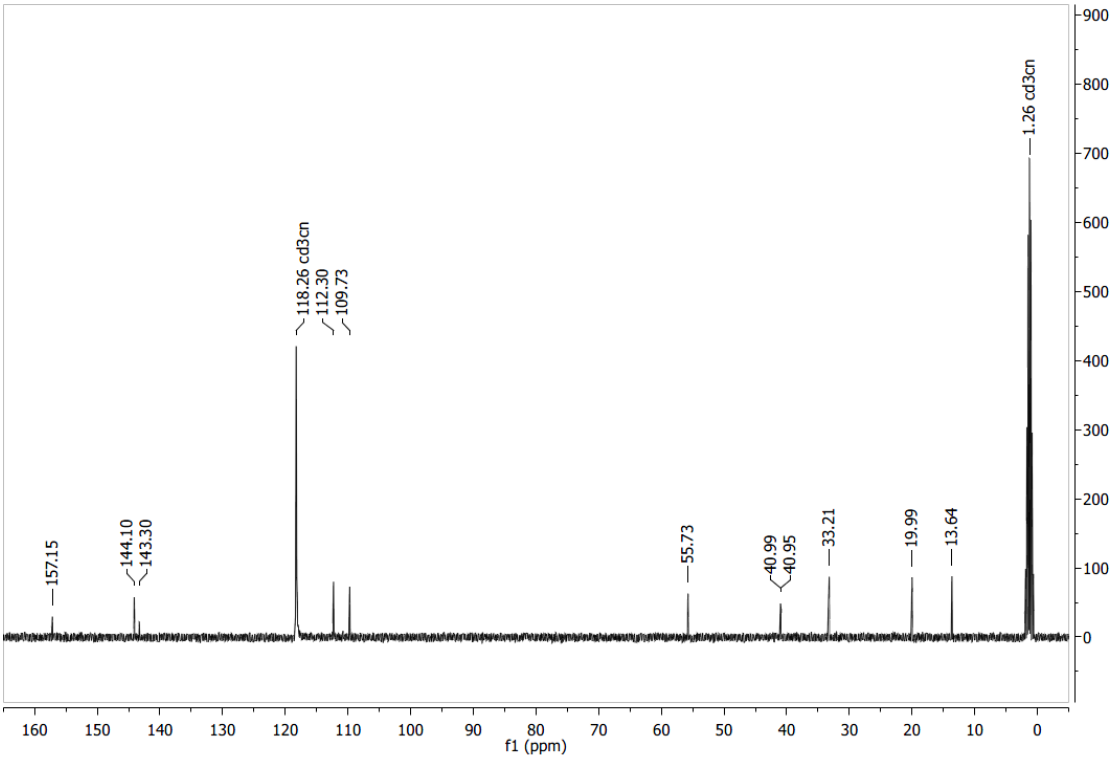
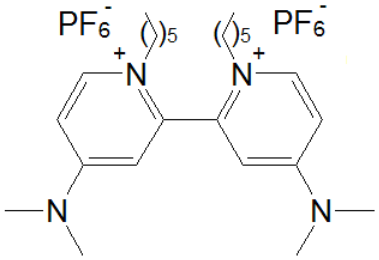


Figure 3.104: ^{13}C NMR spectrum of **5b** in CD_3CN (400 MHz).



5c

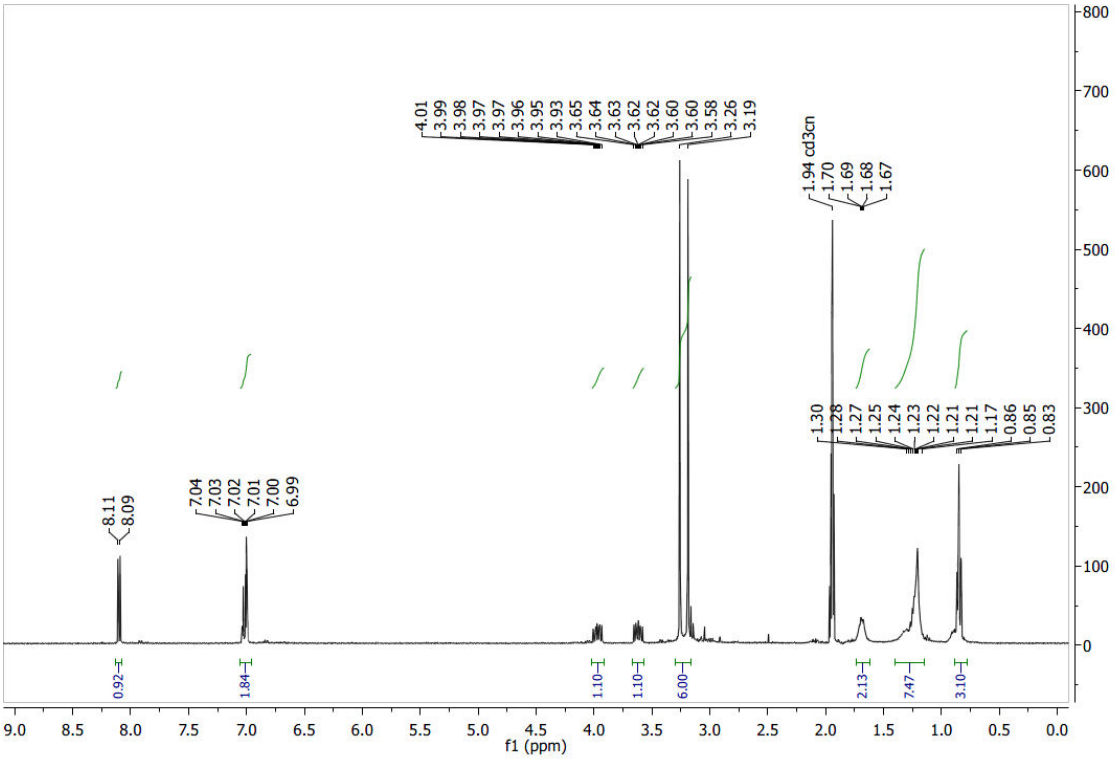


Figure 3.105: ^{1}H NMR spectrum of **5c** in CD_3CN (400 MHz).

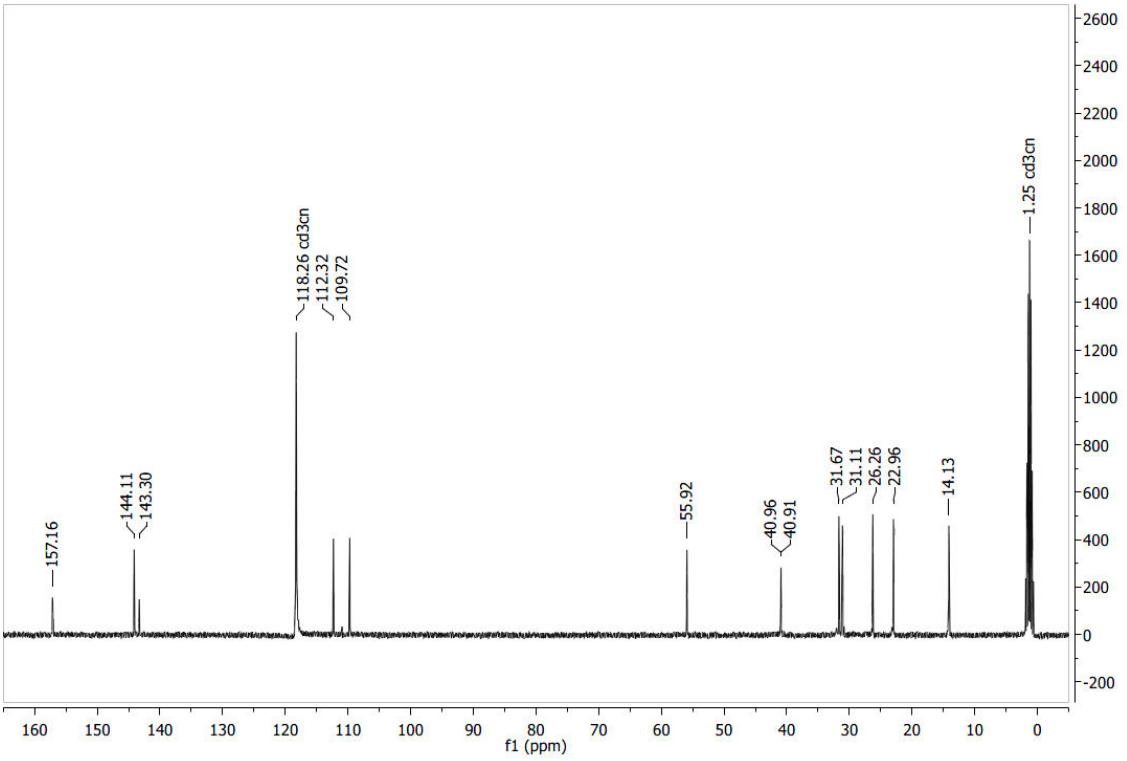
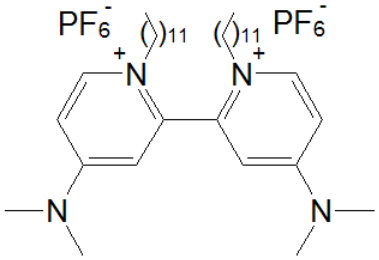


Figure 3.106: ^{13}C NMR spectrum of **5c** in CD_3CN (400 MHz).



5d

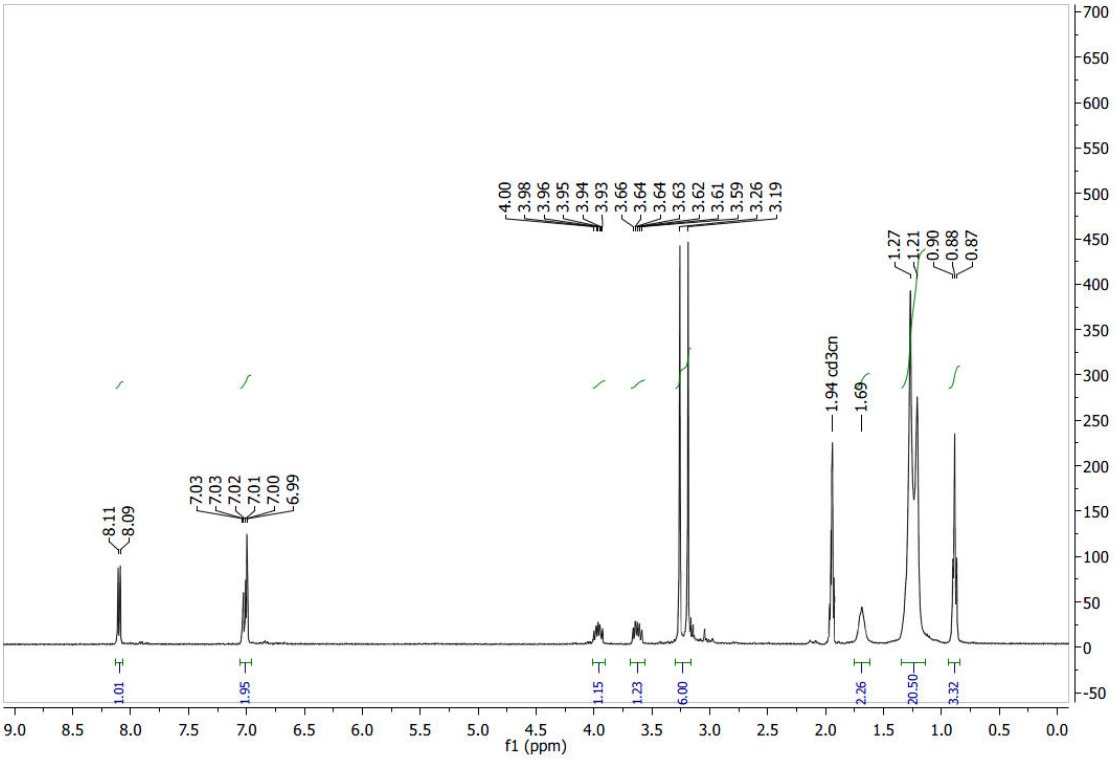


Figure 3.107: ^{1}H NMR spectrum of **5d** in CD_3CN (400 MHz).

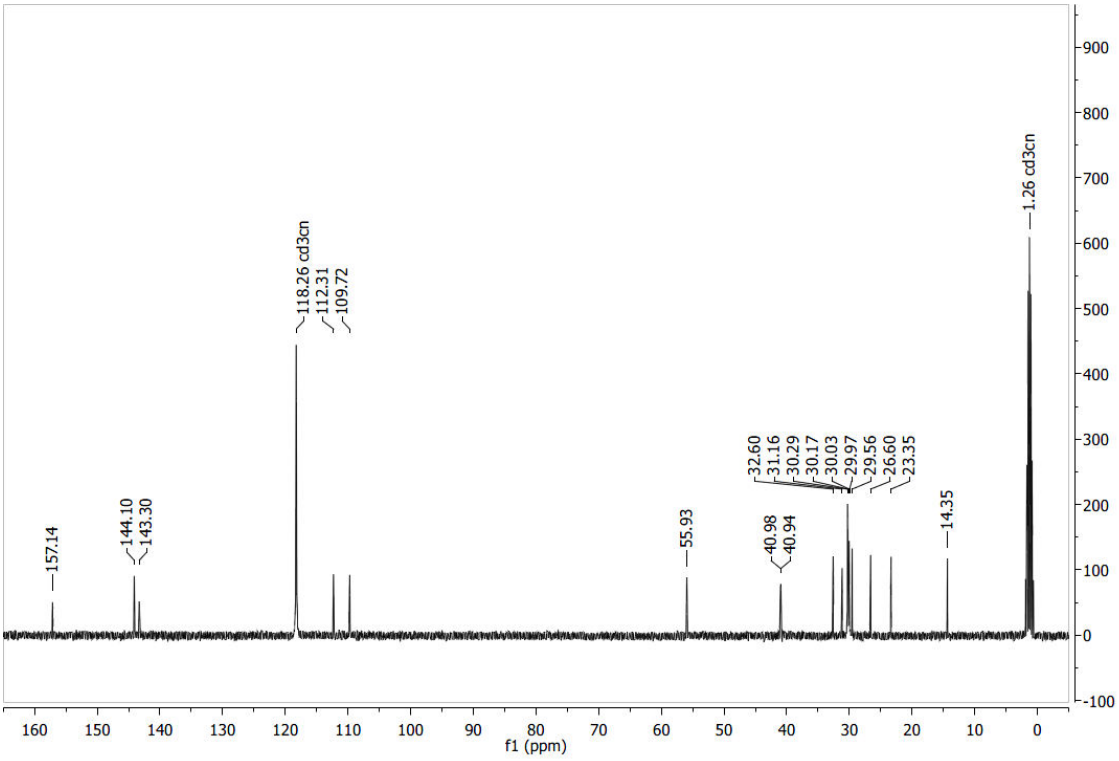
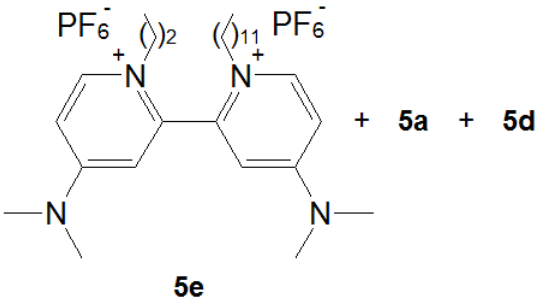


Figure 3.108: ^{13}C NMR spectrum of **5d** in CD_3CN (400 MHz).



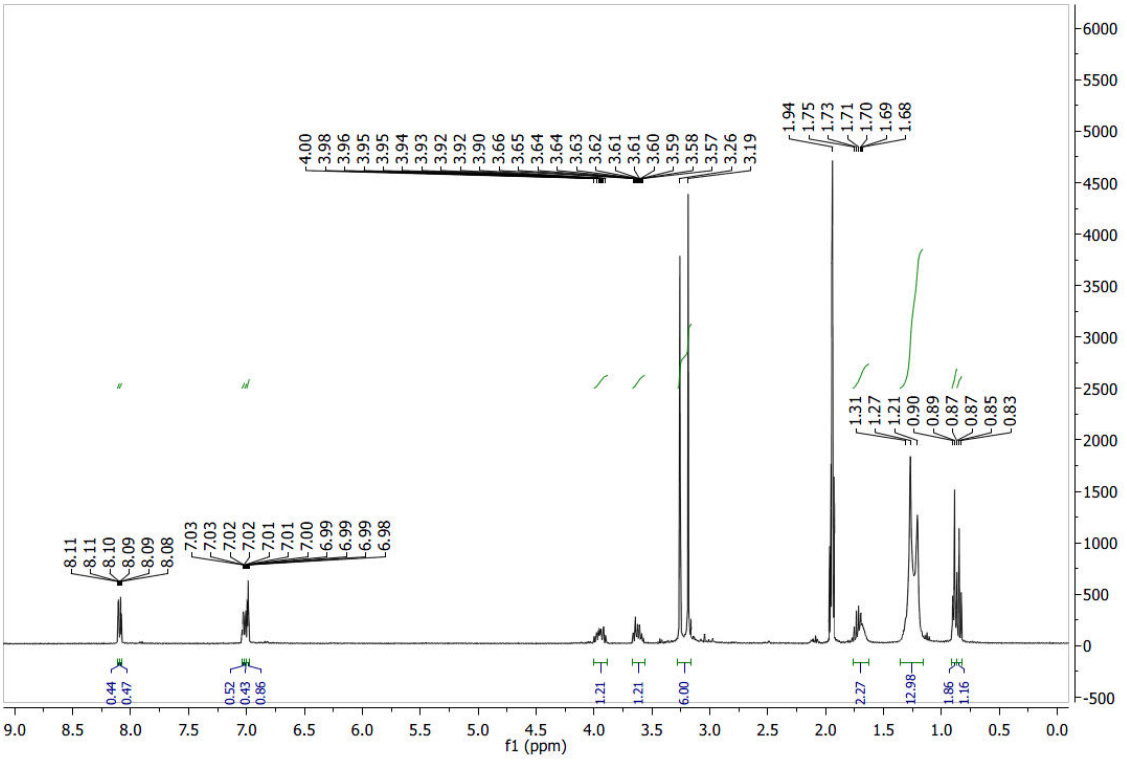


Figure 3.109: ^{1}H NMR spectrum of **5a**, **5d**, and **5e** unknown mixture in C_6D_6 (400 MHz).

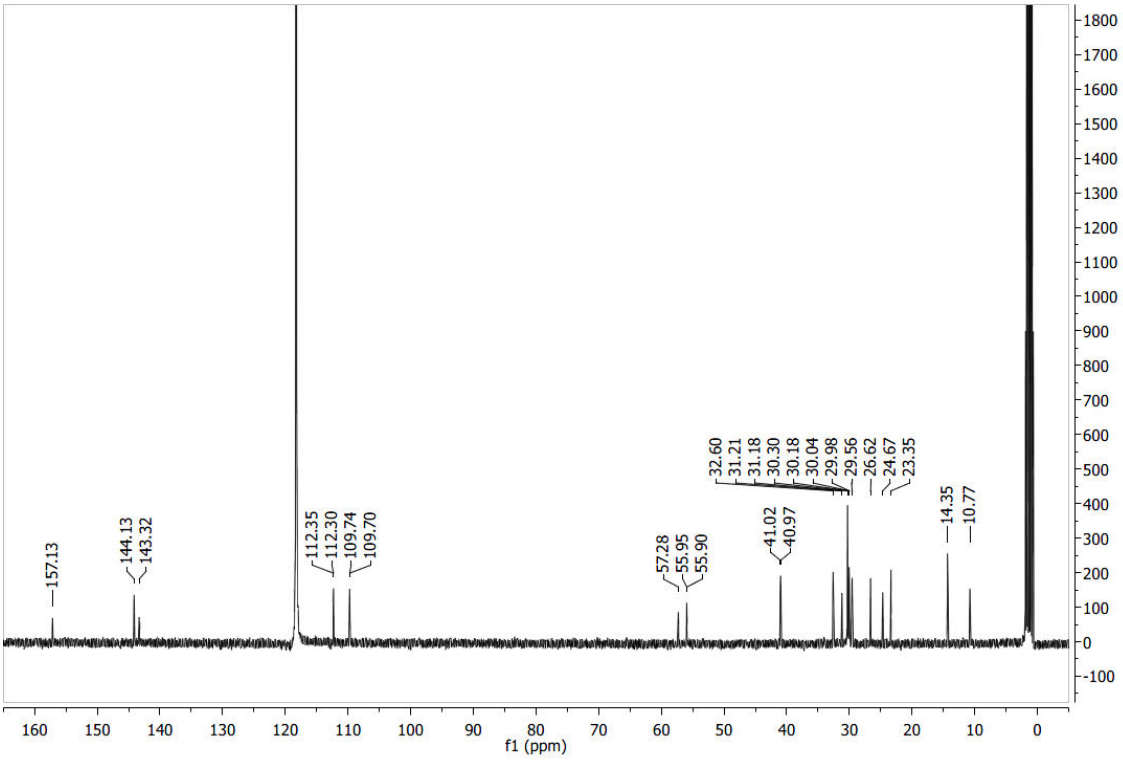
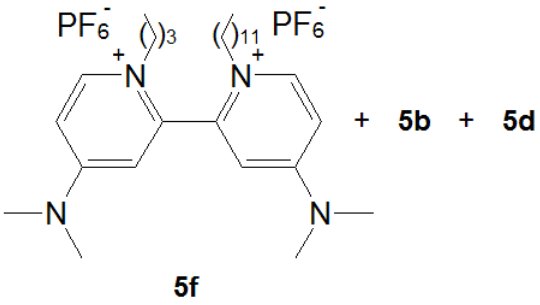


Figure 3.110: ^{13}C NMR spectrum of **5a**, **5d**, and **5e** unknown mixture in C_6D_6 (400 MHz).



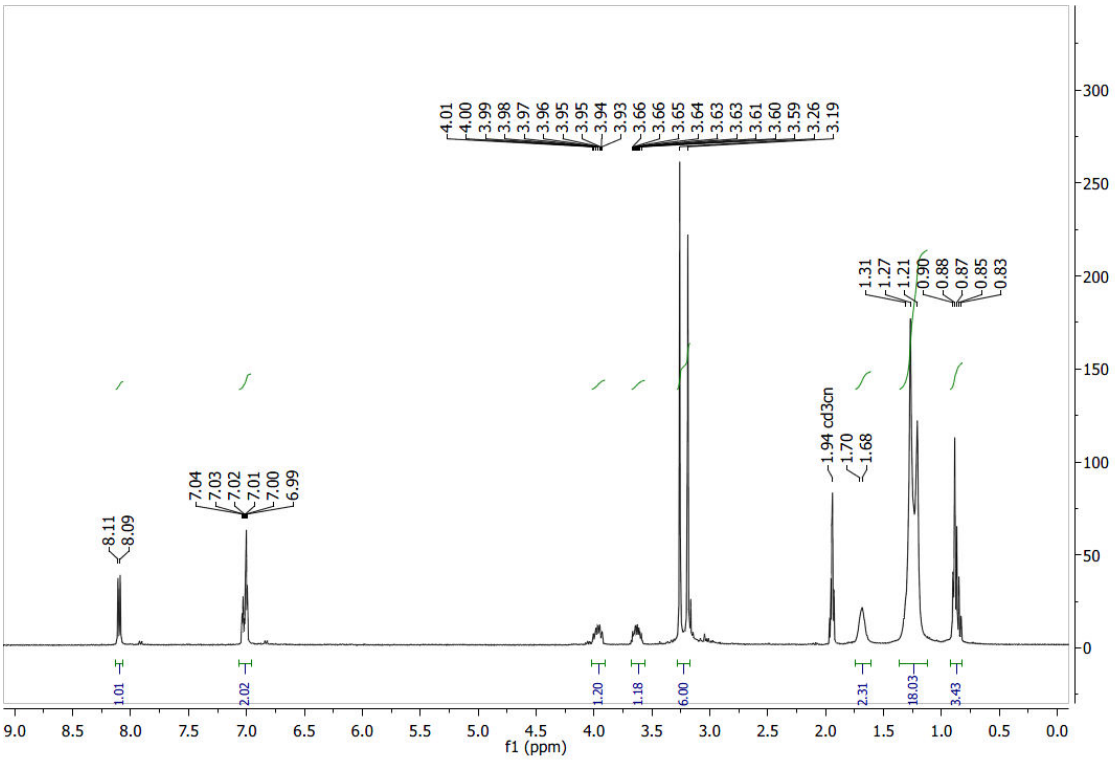


Figure 3.111: ^{1}H NMR spectrum of **5b**, **5d**, and **5f** unknown mixture in C_6D_6 (400 MHz).

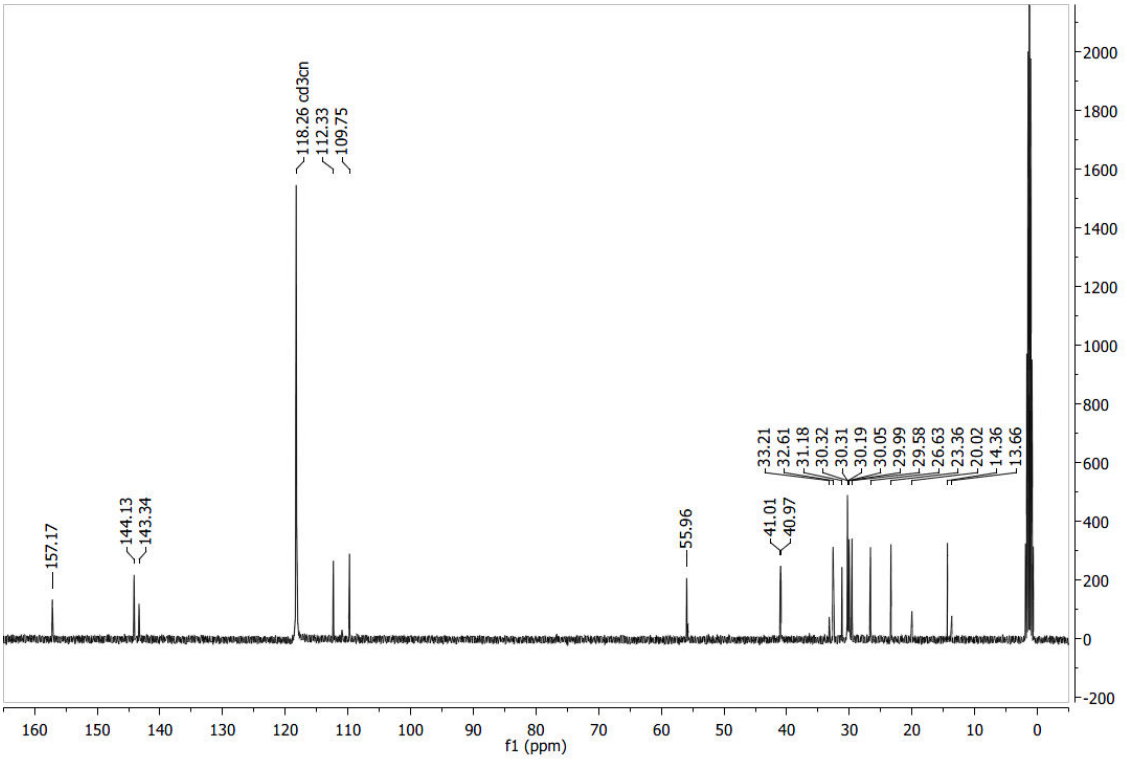
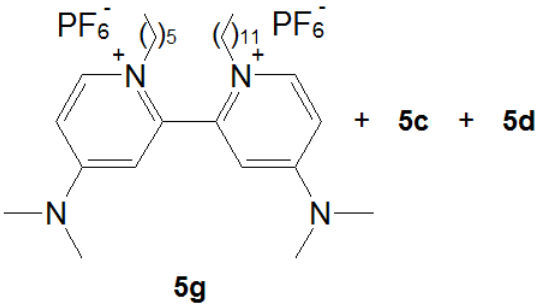


Figure 3.112: ^{13}C NMR spectrum of **5b**, **5d**, and **5f** unknown mixture in C_6D_6 (400 MHz).



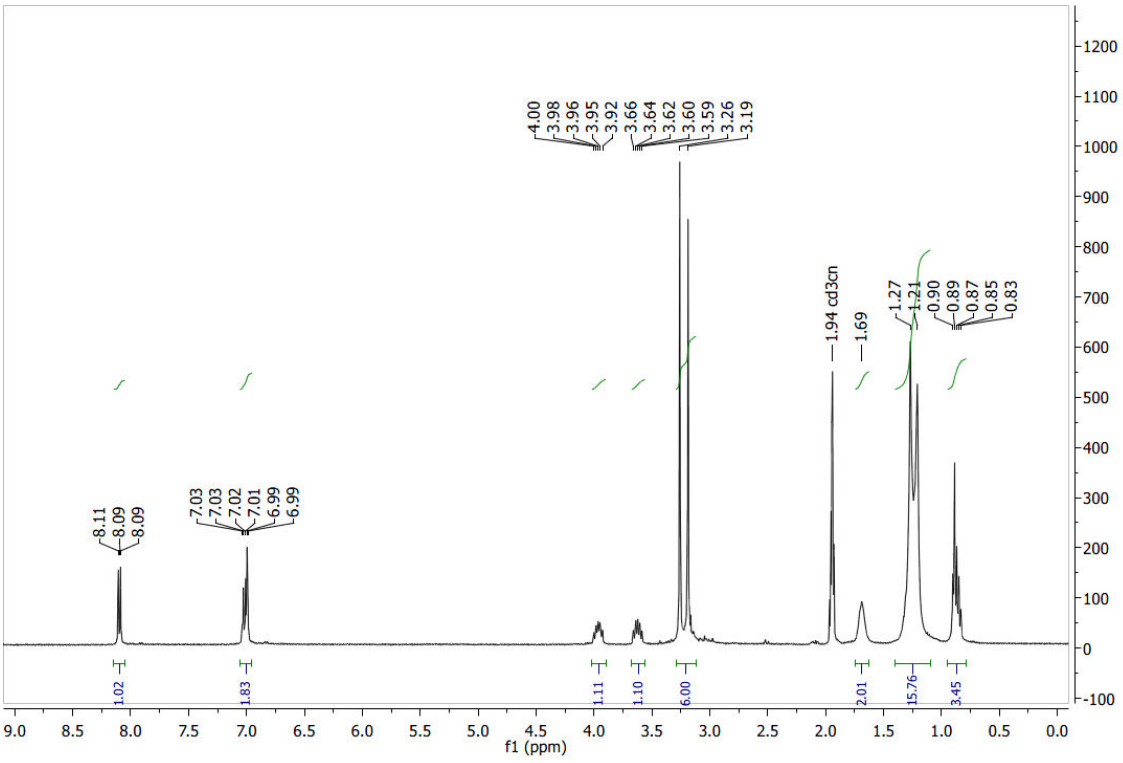


Figure 3.113: ^{1}H NMR spectrum of **5c**, **5d**, and **5g** unknown mixture in C_6D_6 (400 MHz).

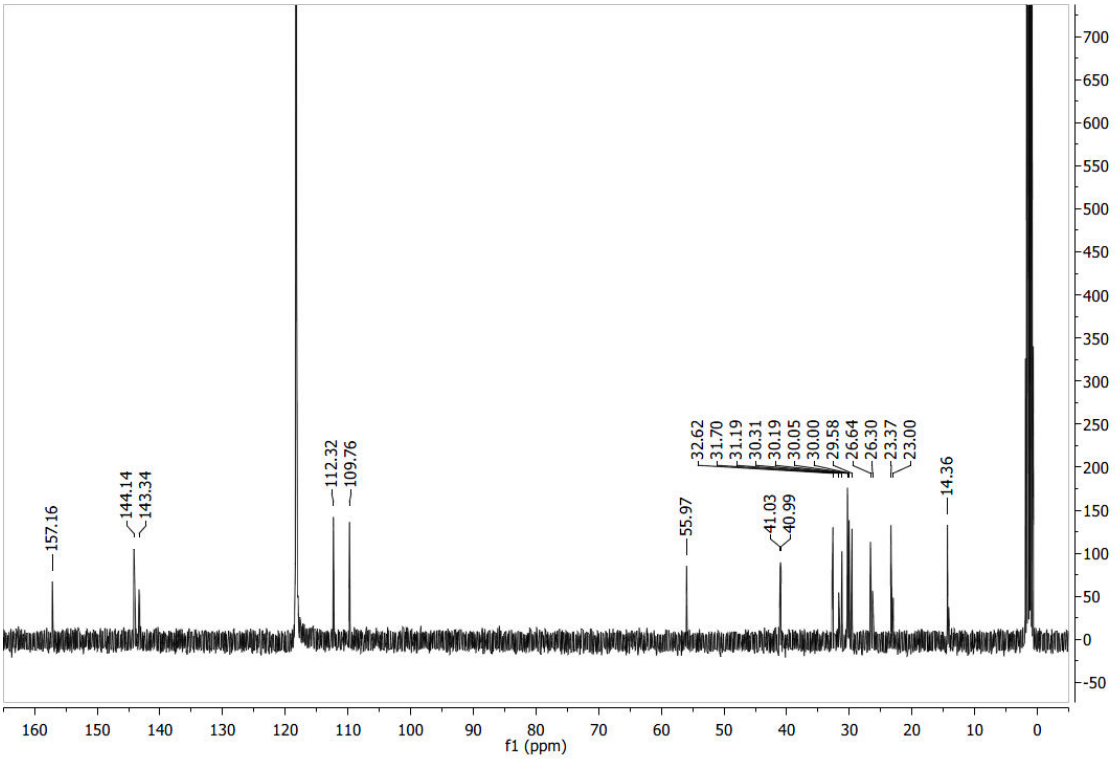


Figure 3.114: ^{13}C NMR spectrum of **5c**, **5d**, and **5g** unknown mixture in C_6D_6 (400 MHz).

Bibliography

1. Linden, D. *Linden's Handbook of Batteries*, **2002**: The McGraw-Hill Companies, Inc., 1.3-1.18.

2. Volta and the "pile". *Electrochem.cwru.edu* **July 5**, **2013**, <http://electrochem.cwru.edu/encycl/art-v01-volta.htm>.

3. Science and Celebrity: Humphry Davy's Rising Star. *Chemheritage.org* **July 5**, **2013**, <http://www.chemheritage.org/discover/media/magazine/articles/26-4-science-and-celebrity.aspx?page=1>.

4. Russell, C. A. Sir Humphry Davy. *Endeavour* **1978**, *2*, 161-164.

5. Kurzweil, P. Gaston Planté and his invention of the lead-acid battery - The genesis of the first practical rechargeable battery. *J. Power Sources* **2010**, *195*, 4424-4434.

6. Broussely, M.; Biensan, P.; Simon, B. Lithium insertion into host materials: the key to success for Li ion batteries. *Electrochim. Acta* **1999**, *45*, 3-22.

7. Scrosati, B. History of lithium batteries. *J. of Solid State Electrochem.* **2011**, *15*, 1623-1630.

8. Conte, F. V. Battery and battery management for hybrid electric vehicles: a review. *Elektrotechnik und informationstechnik* **2006**, *123*, 424-431.

9. Dunn, B.; Kamath, H.; Tarascon, J. Electrical Energy Storage for the Grid: A Battery of Choices. *Science* **2011**, *334*, 928-935.

10. World Batteries Market. *MarketResearch.com* **July 5**, **2013**, <http://www.marketresearch.com/Freedonia-Group-Inc-v1247/Batteries-7174630/>.

11. Aguirre, K.; Eisenhardt, L.; Lim, C. *Lifecycle Analysis Comparison of a Battery Electric Vehicle and a Conventional Gasoline Vehicle* **2012**: Institute of the Environment and Sustainability.

12. Linden, D. *Linden's Handbook of Batteries*, **2002**: The McGraw-Hill Companies, Inc., 23.1-23.88.

13. Boyes, J. D. *Energy Storage Systerms Program Report for FY99* **2000**: Sandia National Laboratories.

14. Perrin, M.; Saint-Drenan, Y. M.; Mattera, F., et al. Lead–acid batteries in stationary applications: competitors and new markets for large penetration of renewable energies. *J. Power Sources* **2005**, *144*, 402-410.

15. Linden, D. *Linden's Handbook of Batteries*, **2002**: The McGraw-Hill Companies, Inc., 35.1-35.94.

16. Scrosati, B. *Lithium Batteries : Advanced Technologies and Applications.* **2013**: John Wiler & Sons, Inc.

17. Linden, D. *Linden's Handbook of Batteries*, **2002**: The McGraw-Hill Companies, Inc., 6.1-6.23.

18. Armand, M.; Tarascon, J. Building better batteries. *Nature* **2008**, *451*, 652-657.

19. Bard, J. A.; Faulkner, R. L. *Electrochemical Methods: Fundamentals and Applications*, **2001**: John Wiley & Sons, Inc., 1-43.

20. Linden, D. *Linden's Handbook of Batteries*, **2002**: The McGraw-Hill Companies, Inc., A.1-A.13.

21. Linden, D. *Linden's Handbook of Batteries*, **2002**: The McGraw-Hill Companies, Inc., 2.1-2.37.

22. Bard, J. A.; Faulkner, R. L. *Electrochemical Methods: Fundamentals and Applications*, **2001**: John Wiley & Sons, Inc., 44-86.

23. Linden, D. *Linden's Handbook of Batteries*, **2002**: The McGraw-Hill Companies, Inc., B.1-B.2.

24. Light, T. S. Standard solution for redox potential measurements. *Anal. Chem.* **1972**, *44*, 1038-1039.

25. Roemmele, T. L.; Boeré, R. T. Electrochemistry of redox-active Group 15/16 heterocyles. *Coordination Chemistry Reviews* **2000**, *210*, 369-445.

26. Abutarbush, S. M. *Saunders Comprehensive Veterinary Dictionary. 3.* **2007**: Elsevier, Inc.

27. Bard, J. A.; Faulkner, R. L. *Electrochemical Methods: Fundamentals and Applications*, **2001**: John Wiley & Sons, Inc., 808-813.

28. Hernández-Burgos, K.; Rodríguez-Calero, G. G.; Zhou, W., et al. Increasing the Gravimetric Energy Density of Organic Based Secondary Battery Cathodes Using Small Radius Cations (Li^+ and Mg^{2+}). *J. Am. Chem. Soc.* **2013**, *135*, 14532-14535.

29. Aurbach, D.; Markovsky, B.; Rodkin, A., et al. An analysis of rechargeable lithium-ion batteries after prolonged cycling. *Electrochim. Acta* **2002**, *47*, 1899-1911.

30. Gu, W. B.; Wang, C. Y. Thermal‐Electrochemical Modeling of Battery Systems. *J. Electrochem. Soc.* **2000**, *147*, 2910-2922.

31. Park, J. *Principles and Applications of Lithium Secondary Batteries.***2012**: Wiley-VCH.

32. Snihir, I.; Rey, W.; Verbitskiy, E., et al *Battery open-circuit voltage estimation by a method of statistical analysis* **2005**: EURANDOM.

33. A Guide to Understanding Battery Specifications. *web.mit.edu* **December 14**, **2014**, <http://web.mit.edu/evt/summary_battery_specifications.pdf>.

34. Murphy, J. A.; Garnier, J.; Park, S. R., et al. Super-Electron Donors: Bis-pyridinylidene Formation by Base Treatment of Pyridinium Salts. *Org. Lett.* **2008**, *10*, 1227-1230.

35. Comments on the History of Lithium-Ion Batteries. *Electrochem.org* **July 16**, **2013**, <http://www.electrochem.org/dl/ma/201/pdfs/0259.pdf>.

36. Väyrynen, A.; Salminen, J. Lithium ion battery production. *The Journal of Chemical Thermodynamics; Thermodynamics of Sustainable Processes* **2012**, *46*, 80-85.

37. Lisbona, D.; Snee, T. A review of hazards associated with primary lithium and lithium-ion batteries. *Process Saf. Environ. Prot.* **2011**, *89*, 434-442.

38. Broussely, M.; Archdale, G. Li-ion batteries and portable power source prospects for the next 5-10 years. *J. Power Sources* **2004**, *136*, 386-394.

39. Linden, D. *Linden's Handbook of Batteries*, **2002**: The McGraw-Hill Companies, Inc., 22.3-22.24.

40. Zhang, W. A review of the electrochemical performance of alloy anodes for lithium-ion batteries. *J. Power Sources* **2011**, *196*, 13-24.

41. Fergus, J. W. Recent developments in cathode materials for lithium ion batteries. *J. Power Sources* **2010**, *195*, 939-954.

42. Zhang, S. S. A review on electrolyte additives for lithium-ion batteries. *J. Power Sources* **2006**, *162*, 1379-1394.

43. Wang, Y.; Cao, G. Developments on Nanostructured Cathode Materials for High-Performance Lithium-Ion Batteries. *Advanced Materials* **2008**, *20*, 2251-2269.

44. Singhal, A.; Skandan, G.; Amatucci, G., et al. Nanostructured electrodes for next generation rechargeable electrochemical devices. *J. Power Sources* **2004**, *129*, 38-44.

45. Noorden, T. V. The rechargeable revolution: A better battery. *Nature* **2014**, *507*, 26-28.

46. Tuck, C. D. S. Rechargeable lithium battery, WO1991000624 A1, **1991**.

47. Georgopoulos, P. Current collector assembly for an electrochemical cell, US5422201 A, **1995**.

48. Johnson, L. G. Regenerative ion exchange fuel cell, US8568921 B1, **2013**.

49. Portet, C.; Taberna, P. L.; Simon, P., et al. Modification of Al Current Collector/Active Material Interface for Power Improvement of Electrochemical Capacitor Electrodes. *J. Electrochem. Soc.* **2006**, *153*, A649-A653.

50. Portet, C.; Taberna, P. L.; Simon, P., et al. Modification of Al current collector surface by sol–gel deposit for carbon–carbon supercapacitor applications. *Electrochimica Acta* **2004**, *49*, 905-912.

51. Johnson, B. A.; White, R. E. Characterization of Commercially Available Lithium-Ion Batteries. *J. Power Sources* **1998**, *70*, 48-54.

52. Iwakuraa, C.; Fukumotoa, Y.; Inouea, H., et al. Electrochemical characterization of various metal foils as a current collector of positive electrode for rechargeable lithium batteries. *J. Power Sources* **1997**, *68*, 301-303.

53. Whitehead, A. H.; Schreiber, M. Current Collectors for Positive Electrodes of Lithium-Based Batteries. *J. Electrochem. Soc.* **2005**, *152*, A2105-A2113.

54. Wu, H.; Lee, E.; Wu, N., et al. Effects of current collectors on power performance of $Li_4Ti_5O_{12}$ anode for Li-ion battery. *J. Power Sources* **2012**, *197*, 301-304.

55. Gyenge, E.; Jung, J.; Mahato, B. Electroplated reticulated vitreous carbon current collectors for lead-acid batteries: opportunities and challenges. *J. Power Sources* **2003**, *113*, 388-395.

56. Chung, S.; Manthiram, A. Lithium-sulfur batteries with superior cycle stability by employing porous current collectors. *Electrochim. Acta* **2013**, *107*, 569-576.

57. Nakamura, T.; Okano, S.; Yaguma, N., et al. Electrochemical performance of cathodes prepared on current collector with different surface morphologies. *J. Power Sources* , .

58. Jiang, S. P.; Love, J. G.; Apateanu, L. Effect of contact between electrode and current collector on the performance of solid oxide fuel cells. *Solid State Ionics* **2003**, *160*, 15-26.

59. Dasgupta, S.; Jacobs, J. K. Current collector for lithium ion battery, US5547782 A, **1996**.

60. Koksbang, R.; Olsen, I. I. Electroconductive polymers, lightweight lithium batteries, US5368959 A, **1994**.

61. Wang, Q.; Wang, D.; Wang, B. Preparation and Electrochemical Performance of $LiFePO_4$-based Electrode Using Three-Dimensional Porous Current Collector. *Int. J. Electrochem. Sci.* **2012**, *7*, 8753-8760.

62. Arbizzani, C.; Lazzari, M.; Mastragostino, M. Lithiation/Delithiation Performance of Cu_6Sn_5 with Carbon Paper as Current Collector. *J. Electrochem. Soc.* **2005**, *152*, A259-A294.

63. Hu, L.; Choi, J. W.; Yang, Y., et al. Highly conductive paper for energy-storage devices. *Proceedings of the National Academy of Sciences* **2009**, *106*, 21490-21494.

64. Huang, B.; Kang, G.; Ni, Y. Electrically Conductive Fibre Composites Prepared from Polypyrrole-Engineered Pulp Fibres. *Can. J. Chem. Eng.* **2005**, *83*, 896-903.

65. Takahashi, M.; Tobishima, S.; Takei, K., et al. Reaction behavior of $LiFePO_4$ as a cathode material for rechargeable lithium batteries. *Solid State Ionics* **2002**, *148*, 283-289.

66. Andersson, A. S.; Thomas, J. O.; Kalska, B., et al. Thermal Stability of $LiFePO_4$-Based Cathodes. *Electrochemical and Solid-State Letters* **2000**, *3*, 66-68.

67. Matsui, H.; Nakamura, T.; Kobayashi, Y., et al. Open-circuit voltage study on $LiFePO_4$ olivine cathode. *J. Power Sources* **2010**, *195*, 6879-6883.

68. Chong, J.; Xun, S.; Song, X., et al. Towards the understanding of coatings on rate performance of $LiFePO_4$. *J. Power Sources* **2012**, *200*, 67-76.

69. Doeff, M.; Wilcox, J.; Yu, R., et al. Impact of carbon structure and morphology on the electrochemical performance of $LiFePO_4$/C composites. *Journal of Solid State Electrochemistry* **2008**, *12*, 995-1001.

70. Delacourt, C.; Poizot, P.; Levasseur, S., et al. Size Effects on Carbon-Free $LiFePO_4$ Powders: The Key to Superior Energy Density. *Electrochemical and Solid-State Letters* **2006**, *9*, A352-A355.

71. Oh, S. W.; Bang, H. J.; Myung, S., et al. The Effect of Morphological Properties on the Electrochemical Behavior of High Tap Density C – $LiFePO_4$ Prepared via Coprecipitation. *J. Electrochem. Soc.* **2008**, *155*, A414-A420.

72. Dominko, R.; Bele, M.; Gaberscek, M., et al. Impact of the Carbon Coating Thickness on the Electrochemical Performance of $LiFePO_4$ / C Composites. *J. Electrochem. Soc.* **2005**, *152*, A607-A610.

73. Zhang, W. Structure and performance of $LiFePO_4$ cathode materials: A review. *J. Power Sources* **2011**, *196*, 2962-2970.

74. Street, G. B.; Clarke, T. C.; Krounbi, M., et al. Preparation and characterization of neutral and oxidized polypyrrole films. *Molecular Crystals and Liquid Crystals* **1982**, *83*, 253-264.

75. Sato, K.; Yamaura, M.; Hagiwara, T., et al. Study on the electrical conduction mechanism of polypyrrole films. *Synth Met* **1991**, *40*, 35-48.

76. Brédas, J.; Thémans, B.; André, J. Bipolarons in polypyrrole chains. *Phys. Rev. B* **1983**, *27*, 7827-7830.

77. Thiéblemont, J. C.; Planche, M. F.; Petrescu, C., et al. Stability of chemically synthesized polypyrrole films. *Synth Met* **1993**, *59*, 81-96.

78. Child, A. D.; Kuhn, H. H. Enhancement of the thermal stability of chemically synthesized polypyrrole. *Synth Met* **1997**, *84*, 141-142.

79. Ding, C.; Qian, X.; Yu, G., et al. Dopant effect and characterization of polypyrrole-cellulose composites prepared by in situ polymerization process. *Cellulose* **2010**, *17*, 1067-1077.

80. Wang, Q.; Sun, J.; Yao, X., et al. Thermal stability of $LiPF_6$/EC + DEC electrolyte with charged electrodes for lithium ion batteries. *Thermochimica Acta* **2005**, *437*, 12-16.

81. Li, W.; Lucht, B. L. Inhibition of the Detrimental Effects of Water Impurities in Lithium-Ion Batteries. *Electrochemical and Solid-State Letters* **2007**, *10*, A115-A117.

82. Street, G.; Clarke, T.; Geiss, R., et al. Characterization of Polypyrrole. *Journal de Physique Colloques* **1983**, *44*, C3-599-C3-606.

83. Jakab, E.; Mészáros, E.; Omastová, M. Thermal decomposition of polypyrroles. *Journal of Thermal Analysis and Calorimetry* **2007**, *88*, 515-521.

84. Kohlman, R.; Zibold, A.; Tanner, D., et al. Limits for Metallic Conductivity in Conducting Polymers. *Phys. Rev. Lett.* **1997**, *78*, 3915-3918.

85. Wang, H.; Leaukosol, N.; He, Z., et al. Microstructure, distribution and properties of conductive polypyrrole/cellulose fiber composites. *Cellulose* **2013**, *20*, 1587-1601.

86. Ding, M. S.; Xu, K.; Zhang, S. S., et al. Change of Conductivity with Salt Content, Solvent Composition, and Temperature for Electrolytes of $LiPF_6$ in Ethylene Carbonate-Ethyl Methyl Carbonate. *J. Electrochem. Soc.* **2001**, *148*, A1196-A1204.

87. Guyomard, D.; Tarascon, J. M. High voltage stable liquid electrolytes for $Li_{1+x}Mn_2O_4$/carbon rocking-chair lithium batteries. *J. Power Sources* **1995**, *54*, 92-98.

88. Ding, M. S.; Xu, K.; Zhang, S. S., et al. Change of Conductivity with Salt Content, Solvent Composition, and Temperature for Electrolytes of $LiPF_6$ in Ethylene Carbonate-Ethyl Methyl Carbonate. *J. Electrochem. Soc.* **2001**, *148*, A1196-A1204.

89. Warren, M. *Electronic and Structural Effects on the Electrochemistry of Polypyrrole* **2005**: The University of British Columbia.

90. Tamm, J.; Alumaa, A.; Hallik, A., et al. Influence of Anions on Electrochemical Properties of Polypyrrole-Modified Electrodes. *Russian J. Electrochem.* **2002**, *38*, 182-187.

91. Lekgoathi, M. D. S.; Vilakazi, B. M.; Wagener, J. B., et al. Decomposition kinetics of anhydrous and moisture exposed $LiPF_6$ salts by thermogravimetry. *J. Fluorine Chem.* **2013**, *149*, 53-56.

92. Eshetu, G. G.; Grugeon, S.; Gachot, G., et al. LiFSI vs. $LiPF_6$ electrolytes in contact with lithiated graphite: Comparing thermal stabilities and identification of specific SEI-reinforcing additives. *Electrochim. Acta* **2013**, *102*, 133-141.

93. Amine, K.; Liu, J.; Belharouak, I. High-temperature storage and cycling of C-$LiFePO_4$/graphite Li-ion cells. *Electrochemistry Communications* **2005**, *7*, 669-673.

94. Cho, E.; Mun, J.; Chae, O. B., et al. Corrosion/passivation of aluminum current collector in bis(fluorosulfonyl)imide-based ionic liquid for lithium-ion batteries. *Electrochemistry Communications* **2012**, *22*, 1-3.

95. Lux, S. F.; Chevalier, J.; Lucas, I. T., et al. HF Formation in $LiPF_6$-Based Organic Carbonate Electrolytes. *ECS Electrochemistry Letters* **2013**, *2*, A121-A123.

96. Rao, L.; Newman, J. Heat-• Generation Rate and General Energy Balance for Insertion Battery Systems. *J. Electrochem. Soc.* **1997**, *144*, 2697-2704.

97. Aurbach, D.; Talyosef, Y.; Markovsky, B., et al. Design of electrolyte solutions for Li and Li-ion batteries: a review. *Electrochim. Acta* **2004**, *50*, 247-254.

98. Dahbi, M.; Ghamouss, F.; Tran-Van, F., et al. Comparative study of EC/DMC LiTFSI and $LiPF_6$ electrolytes for electrochemical storage. *J. Power Sources* **2011**, *196*, 9743-9750.

99. Abouimrane, A.; Ding, J.; Davidson, I. J. Liquid electrolyte based on lithium bis-fluorosulfonyl imide salt: Aluminum corrosion studies and lithium ion battery investigations. *J. Power Sources* **2009**, *189*, 693-696.

100. Krause, L. J.; Lamanna, W.; Summerfield, J., et al. Corrosion of aluminum at high voltages in non-aqueous electrolytes containing perfluoroalkylsulfonyl imides; new lithium salts for lithium-ion cells. *J. Power Sources* **1997**, *68*, 320-325.

101. Dupré, N.; Cuisinier, M.; Guyomard, D. Electrode/Electrolyte Interface Studies in Lithium Batteries Using NMR. *Interface-Electrochemical Society* **2011**, *20*, 61.

102. Zhang, Y.; Wang, C.; Tang, X. Cycling degradation of an automotive $LiFePO_4$ lithium-ion battery. *J. Power Sources* **2011**, *196*, 1513-1520.

103. Skotheim, T. A. *Handbook of conducting polymers.* **1997**: CRC press.

104. Liu, G.; Xun, S.; Vukmirovic, N., et al. Polymers with tailored electronic structure for high capacity lithium battery electrodes. *Adv Mater* **2011**, *23*, 4679-4683.

105. Helm, R. V.; Lanum, W. J.; Cook, G. L., et al. Purification and Properties of Pyrrole, Pyrrolidine, Pyridine and 2-Methylpyridine. *J. Phys. Chem.* **1958**, *62*, 858-862.

106. Ni, Y.; Huang, B.; Kang, G. Electrically conductive paper composite, US7943066, **2011**.

107. Peppel, W. J. Preparation and Properties of the Alkylene Carbonates. *Ind. Eng. Chem.* **1958**, *50*, 767-770.

108. Pachauri, R. K.; Allen, M. R.; Barros, V. R., et al *Climate Change 2014 Synthesis Report: Summary for Policymakers* **2014**: Intergovernmental Panel on Climate Change.

109. *Policy Implications of Greenhouse Warming : Mitigation, Adaptation, and the Science Base.* **1992**: National Academy Press.

110. National Academy, o. E. *America's Energy Future : Technology and Transformation.* **2009**: National Academies Press.

111. *CO_2 Emissions From Fuel Combustion.* **2013**: International Energy Agency.

112. *Canada's Emissions Trends.* **2013**: Environment Canada.

113. Hanjalic, K.; van de Krol, R.; Lekic, A. *Sustainable Energy Technologies: Options and Prospects. 23,* **2008**: Springer.

114. Hekkert, M. P.; Hendriks, F. H. J. F.; Faaij, A. P. C., et al. Natural gas as an alternative to crude oil in automotive fuel chains well-to-wheel analysis and transition strategy development. *Energy Policy* **2005**, *33*, 579-594.

115. Burnham, A.; Han, J.; Clark, C. E., et al. Life-Cycle Greenhouse Gas Emissions of Shale Gas, Natural Gas, Coal, and Petroleum. *Environ. Sci. Technol.* **2012**, *46*, 619-627.

116. Weisser, H. The security of gas supply—a critical issue for Europe? *Energy Policy* **2007**, *35*, 1-5.

117. Hultman, N. E.; Koomey, J. G.; Kammen, D. M. What History Can Teach Us about the Future Costs of U.S. Nuclear Power. *Env. Sci. & Tech.* **2007**, *41*, 2088-2093.

118. Bushnell, J. *Water and Power: Hydroelectric Resources in the Era of Comperitions in the Western U.S.***1998**: University of California Energy Institute.

119. Evans, A.; Strezov, V.; Evans, T. J. Assessment of sustainability indicators for renewable energy technologies. *Renewable and Sustainable Energy Reviews* **2009**, *13*, 1082-1088.

120. Denholm, P.; Ela, E.; Kirby, B., et al *The Role of Energy Storage with Renewable Electricity Generation* **2010**: National Renewable Energy Laboratory.

121. Milligan, M.; Lew, D.; Jordan, G., et al *How do Wind and Solare Power Affect Grid Operations: The Western Wind and Solar Integration Study* **2009**: National Renewable Energy Laboratory.

122. Halamay, D. A.; Brekken, T. K. A.; Simmons, A., et al. Reserve Requirement Impacts of Large-Scale Integration of Wind, Solar, and Ocean Wave Power Generation. *Sustainable Energy, IEEE Transactions on* **2011**, *2*, 321-328.

123. Blumsack, S.; Fernandez, A. Ready or not, here comes the smart grid! *Energy; 7th Biennial International Workshop "Advances in Energy Studies"* **2012**, *37*, 61-68.

124. Moslehi, K.; Kumar, R. *Smart Grid - a reliability perspective* **2010**: Innovative Smart Grid Technologies.

125. Budischak, C.; Sewell, D.; Thomson, H., et al. Cost-minimized combinations of wind power, solar power and electrochemical storage, powering the grid up to 99.9% of the time. *J. Power Sources* **2013**, *225*, 60-74.

126. Ibrahim, H.; Ilinca, A.; Perron, J. Energy storage systems—Characteristics and comparisons. *Renewable and Sustainable Energy Reviews* **2008**, *12*, 1221-1250.

127. Divya, K. C.; Østergaard, J. Battery energy storage technology for power systems—An overview. *Electr. Power Syst. Res.* **2009**, *79*, 511-520.

128. Thaller, L. H. Energy storage system, US3996064, **1976**.

129. Shigematsu, T. *Redox Flow Battery for Energy Storage* **2011**: Sumito Electric.

130. Chen, H.; Cong, T. N.; Yang, W., et al. Progress in electrical energy storage system: A critical review. *Progress in Natural Science* **2009**, *19*, 291-312.

131. Kaneko, H.; Nozaki, K.; Wada, Y., et al. Vanadium redox reactions and carbon electrodes for vanadium redox flow battery. *Electrochim. Acta* **1991**, *36*, 1191-1196.

132. Weber, A. Z.; Meyers, J. P.; Gostick, J. T. Redox flow batteries: a review. *J. Appl. Electrochem.* **2011**, *41*, 1137-1164.

133. Wang, W.; Luo, Q.; Li, B., et al. Recent Progress in Redox Flow Battery Research and Development. *Adv. Funct. Mater.* **2013**, *23*, 970-986.

134. Hall, P. J.; Bain, E. J. Energy-storage technologies and electricity generation. *Energy Policy* **2008**, *36*, 4352-4355.

135. Dyer, C. K. Fuel cells for portable applications. *J. Power Sources* **2002**, *106*, 31-34.

136. Unisearch, L. Novel vanadium halide redox flow battery, EP1618624 A1, **2006**.

137. 3.2 V $LiFePO_4$ Cell Product Specifications. *evamerica.com* **December 14**, **2014**, <http://www.evamerica.com/fluxpbcell072811.pdf>.

138. Li, L.; Kim, S.; Xai, G., et al *Advanced Redox Flow Batteries for Stationary Electrical Energy Storage* **2012**: Pacific Northwest National Laboratory.

139. Wessells, C.; Ruffo, R.; Huggins, R. A., et al. Investigations of the Electrochemical Stability of Aqueous Electrolytes for Lithium Battery Applications. *Electrochemical and Solid-State Letters* **2010**, *13*, A59-A61.

140. Yang, Z.; Zhang, J.; Kintner-Meyer, M. C. W., et al. Electrochemical Energy Storage for Green Grid. *J. Am. Chem. Soc.* **2011**, *111*, 3577-3613.

141. Ponrouch, A.; Marchante, E.; Courty, M., et al. In search of an optimized electrolyte for Na-ion batteries. *Energy Environ. Sci.* **2012**, *5*, 8572-8583.

142. Liu, Q.; Sleightholme, A. E. S.; Shinkle, A. A., et al. Non-aqueous vanadium acetylacetonate electrolyte for redox flow batteries. *Electrochemistry Communications* **2009**, *11*, 2312-2315.

143. Li, Z.; Li, S.; Liu, S., et al. Electrochemical Properties of an All-Organic Redox Flow Battery Using 2,2,6,6-Tetramethyl-1-Piperidinyloxy and N-Methylphthalimide. *Electrochemical and Solid-State Letters* **2011**, *14*, A171-A173.

144. Brushett, F. R.; Vaughey, J. T.; Jansen, A. N. An All-Organic Non-aqueous Lithium-Ion Redox Flow Battery. *Adv. Energy Mater.* **2012**, *2*, 1390-1396.

145. Shin, S.; Yun, S.; Moon, S. A review of current developments in non-aqueous redox flow batteries: characterization of their membranes for design perspective. *RSC Adv.* **2013**, *3*, 9095-9116.

146. Oriji, G.; Katayama, Y.; Miura, T. Investigation on V(IV)/V(V) species in a vanadium redox flow battery. *Electrochim. Acta* **2004**, *49*, 3091-3095.

147. Alkhayri, F. M. *Toward an All-Organic Non-Aqueous Redox Flow Battery Based on 2,2,6,6-Tetramethyl-1-Piperidinyloxy and a Bispyridinylidene* **2014**: University of New Brunswick.

148. Murphy, J. A. Discovery and Development of Organic Super-Electron-Donors. *J. Org. Chem.* **2014**, *79*, 3731-3746.

149. Murphy, J. A.; Garnier, J.; Kennedy, A. R., et al. Structure and reactivity in neutral organic electron donors derived from 4-dimethylaminopyridine. *Beilstein J. Org. Chem.* **2010**, *6*, No. 73.

150. Sadoc, J. F.; Charvolin, J. Frustration in bilayers and topologies of liquid crystals of amphiphilic molecules. *J.Phys.France* **1986**, *47*, 683-691.

151. Myers, D. *Surfactant Science and Technology. 3rd.* **2006**: John Wiley & Sons, Inc.

152. Causin, V.; Saielli, G. Effect of asymmetric substitution on the mesomorphic behaviour of low-melting viologen salts of bis(trifluoromethanesulfonyl)amide. *J. Mater. Chem.* **2009**, *19*, 9153-9162.

153. Brown, R. J. C.; Brown, R. F. C. Melting Point and Molecular Symmetry. *J. Chem. Educ.* **2000**, *77*, 724.

154. Westwell, M. S.; Searle, M. S.; Wales, D. J., et al. Empirical Correlations between Thermodynamic Properties and Intermolecular Forces. *J. Am. Chem. Soc.* **1995**, *117*, 5013-5015.

155. Yalkowsky, S. H. Solubility and partitioning V: dependence of solubility on melting point. *J. Pharm. Sci.* **1981**, *70*, 971-973.

156. Delaney, J. S. Predicting aqueous solubility from structure. *Drug Discov. Today* **2005**, *10*, 289-295.

157. Spectral Database for Organic Compounds - SDBS No. 5723. *dbs.db.aist.go.jp* **December 14**, **2014**.

158. Spectral Database for Organic Compounds - SDBS No. 3869. *dbs.db.aist.go.jp* **December 14**, **2014**.

159. Spectral Database for Organic Compounds - SDBS No. 1225. *dbs.db.aist.go.jp* **December 14**, **2014**.

160. Spectral Database for Organic Compounds - SDBS No. 1526. *dbs.db.aist.go.jp* **December 14**, **2014**.

161. Spectral Database for Organic Compounds - SDBS No. 1738. *dbs.db.aist.go.jp* **December 14**, **2014**.

162. MPA160 and MPA161 DigiMelt Student Melting Point System. *thinksrs.com* **December 14**, **2014**, <http://www.thinksrs.com/downloads/PDFs/Manuals/MPA160m.pdf>.

163. Garnier, J.; Thomson, D. W.; Zhou, S., et al. Hybrid super electron donors – preparation and reactivity. *Beilstein Journal of Organic Chemistry* **2012**, *8*, 994-1002.

164. Aranzaes, J. R.; Daniel, M.; Astruc, D. Metallocenes as references for the determination of redox potentials by cyclic voltammetry — Permethylated iron and cobalt sandwich complexes, inhibition by polyamine dendrimers, and the role of hydroxy-containing ferrocenes. *Can. J. Chem.* **2006**, *84*, 288-299.

165. Spectral Database for Organic Compounds - SDBS No. 5567. *dbs.db.aist.go.jp* **December 14**, **2014**.

166. Gottlieb, H. E.; Kotlyar, V.; Nudelman, A. NMR Chemical Shifts of Common Laboratory Solvents as Trace Impurities. *J. Org. Chem.* **1997**, *62*, 7512-7515.

167. Zhang, D.; Telo, J. P.; Liao, C., et al. Experimental and Computational Studies of Nuclear Substituted 1,1'-Dimethyl-2,2'-Bipyridinium Tetrafluoroborates. *J Phys Chem A* **2007**, *111*, 13567-13574.

168. Macomber, R. S. *A Complete Introduction to Modern NMR Spectroscopy*, **1998**: John Wiley & Sons, Inc., 68-87.

169. Macomber, R. S. *A Complete Introduction to Modern NMR Spectroscopy*, **1998**: John Wiley & Sons, Inc., 215-243.

170. Perrin, C. L.; Dwyer, T. J. Application of two-dimensional NMR to kinetics of chemical exchange. *Chem. Rev.* **1990**, *90*, 935-967.

171. Macomber, R. S. *A Complete Introduction to Modern NMR Spectroscopy*, **1998**: John Wiley & Sons, Inc., 88-103.

172. Minch, M. J. Orientational dependence of vicinal proton-proton NMR coupling constants: The Karplus relationship. *Concepts Magn. Reson.* **1994**, *6*, 41-56.

173. Lemieux, R. U.; Nagabhushan, T. L.; Paul, B. Relationship of ^{13}C to Vicinal ^{1}H Coupling to the Torsion Angle in Uridine and Related Structures. *Can. J. Chem.* **1972**, *50*, 773-776.

174. Alkorta, I.; Elguero, J.; Roussel, C., et al. *Advances in Heterocyclic Chemistry*, **2012**: Academic Press, 1-188.

175. Inctroduction to Chemical Exchange with the Mexico Program. *chemistry.mcmaster.ca* **December 14**, **2014**, <http://www.chemistry.mcmaster.ca/bain/Intro.pdf>.

176. Williams, D.; Fleming, I. *Spectroscopic Methods In Organic Chemistry.*: McGraw-Hill Education (India) Pvt Limited.

177. Casarini, D.; Foresti, E.; Gasparrini, F., et al. Conformational studies by dynamic NMR. 50. Atropisomerism in hindered naphthyl sulfoxides: structure, stereodynamics, and chiral resolution. *J. Org. Chem.* **1993**, *58*, 5674-5682.

178. Ho, C. S.; Lam, C.; Chan, M., et al. Electrospray Ionisation Mass Spectrometry: Principles and Clinical Applications. *The Clinical Biochemist Reviews* **2003**, *24*, 3-12.

179. Kissinger, P. T.; Heineman, W. R. Cyclic voltammetry. *J. Chem. Educ.* **1983**, *60*, 702.

180. Nicholson, R. S. Theory and Application of Cyclic Voltammetry for Measurement of Electrode Reaction Kinetics. *Anal. Chem.* **1965**, *37*, 1351-1355.

181. Garnier, J.; Kennedy, A. R.; Berlouis, L. E. A., et al. Structure and reactivity in neutral organic electron donors derived from 4-dimethylaminopyridine. *Beilstein Journal of Organic Chemistry* **2010**, *6*, 73.

182. Klingler, R. J.; Kochi, J. K. Electron-transfer kinetics from cyclic voltammetry. Quantitative description of electrochemical reversibility. *J. Phys. Chem.* **1981**, *85*, 1731-1741.

183. Evans, D. H.; O'Connell, K. M.; Petersen, R. A., et al. Cyclic voltammetry. *J. Chem. Educ.* **1983**, *60*, 290.

184. Analytical Electrochemistry: The Basic Concepts. *asdlib.org* **December 14**, **2014**, <http://www.asdlib.org/onlineArticles/ecourseware/Kelly_Potentiometry/PDF-4-Reversibility.pdf>.

185. Tsierkezos, N. Cyclic Voltammetric Studies of Ferrocene in Nonaqueous Solvents in the Temperature Range from 248.15 to 298.15 K. *Journal of Solution Chemistry* **2007**, *36*, 289-302.

186. Paul, A.; Laurila, T.; Vuorinen, V., et al. *Thermodynamics, Diffusion and the Kirkendall Effect in Solids*, **2014**: Springer International Publishing, 115-139.

187. Zhang, L.; Yi, F.; Zhang, X., et al. Optimization of the Synthesis and Characterizations of the Functionalized Ionic Liquids. *Hua xue shi jie = Chemical world.* **2013**, *54*, 46-51.

188. Crosthwaite, J. M.; Muldoon, M. J.; Dixon, J. K., et al. Phase transition and decomposition temperatures, heat capacities and viscosities of pyridinium ionic liquids. *The Journal of Chemical Thermodynamics; Ionic Liquids* **2005**, *37*, 559-568.

189. Jerchel, D.; Fischer, H.; Thomas, K. Synthesen mit Pyridyl-pyridinium-halogeniden: Einführung von Halogen, der Thiol- und Thioäthergruppe in die 4-Stellung des Pyridinkerns. *Chemische Berichte* **1956**, *89*, 2921-2933.

Julien Martin

11544 Route 144, St Léonard, NB, E3E 2M8
(506) 261-9651 or (506) 423-6775
julien.daniel.martin@gmail.com

Summary of Qualifications:

- Academic laboratory research experience in electrochemistry, synthetic organic chemistry, and materials research.
- Adept with air-free techniques and preparations, purification/isolation processes, electrochemical technologies, spectroscopic studies, and analytical chemical methodologies.
- Teaching experience in general chemistry and analytical chemistry laboratories.
- Thorough, high attention to detail, quick learner, and highly adaptive.
- Completely fluent in both English and French, spoken and written.

Education:

Master in Chemistry (completing)	University of New Brunswick, (2015)
Bachelor of Science Major in Chemistry	University of New Brunswick, 2010
Grade Twelve Diploma	École Grande-Rivière, New Brunswick, 2006

Research Projects:

Preparation and Characterization of Macroporous Layered Double Hydroxide Thin Films
Undergraduate chemistry 4000 thesis completed under Dr. Gilles Villemure at UNB (2009-2010)

- Used electrophoretic and electrochemical deposition experiments to produce macroporous materials with high surface areas.
- Acquired experience with electron microscopy techniques and electroanalytical experiements.

Synthesis and Testing of Conductive Polymer Composite Materials in Lithium Ion Batteries
Research assistant project turned MSc Thesis project under Dr. Adam Dyker at UNB (2010-2014)

- Conducted time-consuming battery test experiments in an organized and precise manner.
- Extensive amounts of data were processed with Excel to extract relevant information.

Synthesis, Isolation, and Characterization of "Super Electron Donor" Organic Reducing Agents.
MSc Thesis project under Dr. Adam Dyker at UNB (2011-2014)

- Developed a robust isolation technique for a number of highly-sensitive liquid compounds.
- Became highly adept in air-free techniques and preparation of equipment for sensitive chemistry.

Teaching Experiences:

Teaching Assistant in Analytical Chemistry Laboratory Courses at UNB, Fredericton
Helped teach 5 lab courses under Dr. James Tong and Dr. Noureddin E. Kassimi (2011-2012)

- Operated spectrometers and other instruments, independently taught many experimental procedures, helped prepare reagents and clean apparatuses, and assisted in marking.
- Required in-depth knowledge of analytical chemistry to properly assist students, in addition to patience, kindness, and understanding.

Teaching Assistant in General Chemistry Laboratory Courses at UNB, Fredericton
Helped teach 7 lab courses under Dr. Valerie Reeves and Dr. James Tait (2011-2014)

- Taught experimental procedures to separate student groups, helped organize and prepare experiment sessions, and organized and handled large amounts of student report marking.
- Built trust with the students through fairness and understanding, supplemented by in-depth knowledge of each experiment and adaptability to rapidly-changing situations.

Other Services and Duties:

- Volunteer research assistant under Dr. Gilles Villemure of UNB Fredericton (Summer 2010).
- Graduate student representative on the Chemistry Safety Committee of UNB (2012-2013).
- Graduate assistant for maintaining the Solvent Dispensing System in Toole Hall (2012-2013).
- Treasurer of the Chemistry Graduate Student Association of UNB Fredericton (2013-2014).

References:

Dr. Adam Dyker	Assistant Professor Department of Chemistry University of New Brunswick	cadyker@unb.ca (506) 453-4981 - Office (506) 444-1902 - Cell
Dr. James Tait	Instructor Department of Chemistry Fredericton, New Brunswick	jtait@unb.ca (506) 453-4871 - Office
Dr. Valerie Reeves	Senior Instructor Department of Chemistry University of New Brunswick	vreeves@unb.ca (506) 458-7241 - Office (506) 476-5945 - Cell